Dissertation

Epitaxy and thickness scaling of ferroelectric $Al_{1-x}Sc_xN$ - towards next-generation memory and computing devices

submitted by **Georg Schönweger** (born in Meran, Italy)
in partial fulfillment of the requirements for the degree of Doctor of Engineering (Dr.-Ing.)

Kiel University
Faculty of Engineering
Kiel, Germany
March, 2024

First Examiner:	Prof. Dr. Hermann Kohlstedt
Second Examiner:	Prof. Dr. Fabian Lofink
Third Examiner:	Prof. Dr. Dr. Oliver Ambacher

Date of Examination: 10.07.2024

Eidesstattliche Erklärung

Ich, Georg Schönweger, versichere an Eides statt durch meine untenstehende, dass ich die vorstehende Arbeit selbständig und ohne unzulässige fremde Hilfe angefertigt und alle Stellen, die ich wörtlich oder dem Sinne nach aus Veröffentlichungen entnommen habe, als solche kenntlich gemacht habe und mich auch keiner anderen als der angegebenen Literatur oder sonstiger Hilfsmittel bedient habe.

Ich versichere an Eides statt, dass ich die vorgenannten Angaben nach bestem Wissen und Gewissen gemacht habe und dass die Angaben der Wahrheit entsprechen und ich nichts verschwiegen habe.

Die Strafbarkeit einer falschen eidesstattlichen Versicherung ist mir bekannt, namentlich die Strafandrohung gemäß § 156 StGB bis zu drei Jahren Freiheitsstrafe oder Geldstrafe bei vorsätzlicher Begehung der Tat bzw. gemäß § 163 Abs.1 StGB bis zu einem Jahr Freiheitsstrafe oder Geldstrafe bei fahrlässiger Begehung. Ich versichere, dass mir bisher kein akademischer Grad entzogen wurde. Weiterhin erkläre ich hiermit, dass diese Arbeit unter Einhaltung der Regeln guter wissenschaftlicher Praxis der Deutschen Forschungsgemeinschaft entstanden ist und die Doktorarbeit in dieser Form weder vollständig noch in Teilen in einem anderen Prüfungsverfahren bereits vorgelegen hat, veröffentlicht wurde oder zur Veröffentlichung eingereicht wurde.

Ort, Datum	Georg Schönweger

Abstract

Information technology including the recent advance of artificial intelligence (AI) demands a huge amount of electrical power. Next-generation devices based on the ferroelectric effect could potentially lower this demand. The field-driven switching of the polarization by the application of an electric field promises lowest energy consumption as well as it allows for various device concepts. Such devices are suitable for detaching from the classical Von-Neumann architecture by merging memory and computation (in-memory) and thus lowering the latency gap between those. Additionally, they allow for addressing neuromorphic architectures by emulating the functionality of synapses and neurons found in the human brain on device level. However, after the discovery of ferroelectricity $\approx$ 100 years ago, ferroelectric random access memory (FeRAM) is up to now the only commercial available memory product which is based on the ferroelectric switching. This is mainly due to the poor Complementary Metal Oxide Semiconductor (CMOS)-compatibility of classical ferroelectric materials such as the perovskites and the related integration and scalability issues.

This situation changed after the discovery of ferroelectricity in the CMOS-compatible fluorite-type structures in 2013, which resulted in the demonstration of various types of highly scaled ferroelectricity-based memory and computation devices which are close to commercialization. This was followed by the discovery of ferroelectricity in CMOS-compatible wurtzite-type $Al_{1-x}Sc_xN$ in 2019, on which this doctoral thesis is building up. The structure and chemistry of the fluorite- and wurtzite-type ferroelectrics and their respective electrical response differs fundamentally, thus potential advantages and disadvantages in terms of device applications can be expected. The goal of this doctoral thesis is to gain a fundamental understanding of the switching phenomena in $Al_{1-x}Sc_xN$ and to identify suitable applications. To achieve this, first the sputter-deposition of epitaxial ferroelectric $Al_{1-x}Sc_xN$ onto GaN/sapphire templates was established, which addresses the integration of ferroelectricity into III-N technology by using a structurally fully compatible material (all-wurtzite). On the other hand, this allows to investigate the impact of the structure (i.e. epitaxial strain, mosaicity, as-deposited pinned polarity) of the usually fiber-textured grown $Al_{1-x}Sc_xN$ thin films on the electrical response to gain a better fundamental understanding of the switching event. At a later stage of my work, ferroelectricity in single-crystal metal organic chemical vapor (MOCVD) deposited $Al_{0.85}Sc_{0.15}N$ was revealed, which is expected to facilitate the integration of wurtzite-type ferroelectricity into III-N devices, as it is the standard growth method of such heterostructures. This not only guides towards an active functional high-quality barrier material feasible for e.g. building up or depleting a two-

dimensional-electron gas (2DEG) in high-electron mobility transistors (HEMTs). The single-crystal quality also allows for sophisticated atomically resolved scanning transmission microscopy (STEM) investigations of the switching event and the associated polarization domain evolution. For sputter-deposited films, the introduction of intermediate ultrathin (10 nm) epitaxial Pt electrodes into the $Al_{1-x}Sc_xN$/GaN heterostructures results in a more uniform and less leaky electrical response, as well as it provides a smooth template for the growth of ultrathin epitaxial $Al_{1-x}Sc_xN$. Thus, Pt/GaN templates were used to investigate the thickness scalability of ferroelectric $Al_{1-x}Sc_xN$. Interestingly, only a minor dependence of the coercive field on the $Al_{1-x}Sc_xN$ film thickness was revealed and switching of 10 nm thin films could be demonstrated. This was compared to a thickness study on $Al_{1-x}Sc_xN$ films grown non-epitaxially on $Pt/SiO_2/Si$ templates. The growth using silicon substrates resulted in a higher coercive field to breakdown field ratio, which was related to a more favourable thermal expansions coefficient match between $Al_{1-x}Sc_xN$ and the substrate. A minor decrease of the coercive field with decreasing film thickness below 10 nm was related to depolarization fields and allowed for ferroelectric switching of ≈4 nm (8 to 9 unit cells) thin films at ≈1 V. Thus, the switching voltage is already compatible with the on-chip voltage supply of integrated circuits (ICs). Furthermore, atomically resolved stable partial switching of ultralow volumes suggests the feasibility of multi-bit operation also for highly scaled devices - an issue which is currently faced for the fluorite-type ferroelectrics. Further STEM investigations of sputtered as well as MOCVD-grown $Al_{1-x}Sc_xN$ thin films reveal the occurrence of inclined polarization domain boundaries. This together with electrical investigations suggest the presence of conductive polarization domain walls in wurtzite-type materials - a phenomena which can be exploited to build memristive two-terminal devices.

Zusammenfassung

Die Informationstechnologie einschließlich der in jüngster Zeit stark voranschreitenden künstliche Intelligenz (KI) verlangt nach einer enormen Menge an elektrischer Energie. Elektrische Bauteile der nächsten Generation, welche auf dem ferroelektrischem Effekt beruhen, könnten diesen Bedarf verringern. Das durch ein elektrisches Feld steuerbare Schalten der Polarisation verspricht einen geringen Leistungsverbrauch und ermöglicht diverse Bauteilkonzepte. Solche Konzepte sind geeignet, um sich von der klassischen Von-Neumann-Architektur zu lösen, indem die Speicher- und Recheneinheit näher zusammenrückt (in-memory) und so die Latenz zwischen beiden verringert wird. Auch können neuromorphe Konzepte adressiert werden, z.B. indem auf Bauteilebene die Funktionalität der Basiseinheiten des menschlichen Gehirns - Neuronen und Synapsen - nachgebildet werden. Trotz dass die Entdeckung des ferroelektrischen Effekts bereits 100 Jahre zurück liegt, sind ferroelektrische *random access memories* (FeRAM) die aktuell einzigen kommerziell erhältlichen Speicherbausteine, welche auf ferroelektrischem Schalten beruhen. Dies liegt vorallem an der mangelnden komplementärer Metalloxid-Halbleiter (CMOS)-Kompatibilität von klassischen ferroelektrischen Materialien wie den Perowskiten und deren Integrations- und Skalierungsschwierigkeiten.

Diese Situation hat sich nach der Entdeckung von Ferroelektrizität in den CMOS-kompatiblen Fluorit-Strukturen (HfO_2) in 2013 geändert und es folgten diverse Demonstrationen von hoch skalierten Rechen/Speicherbauteilen, welche dicht vor der Kommerzialisierung stehen. Die Entdeckung von Ferroelektrizität in CMOS-kompatiblen Wurtzite-Strukturen ($Al_{1-x}Sc_xN$) folgte in 2019, worauf diese Arbeit aufbaut. Aufgrund der unterschiedlichen Chemie und Struktur und der daraus resultierenden unterschiedlichen elektrische Eigenschaften beider Materialklassen ergeben sich Vor- und Nachteile in Bezug auf mögliche Anwendungen. Das Ziel dieser Arbeit ist es, ein fundamentales Verständnis für das ferroelektrische Schalten in $Al_{1-x}Sc_xN$ zu erarbeiten sowie geeignete Anwendungen auszumachen. Um dies zu erreichen, wurde zuerst ein Prozess entwickelt mit welchem per Kathodenzerstäubung ferroelektrisches $Al_{1-x}Sc_xN$ epitaktisch auf GaN/Saphir abgeschieden werden konnte, was die Integration von Ferroelektrizität in die III-N Technologie durch Nutzung eines strukturell kompatiblem Ferroelektrikum forciert. Zudem ermöglicht dies das Untersuchen des Einflusses der Struktur (z.B. epitaxiale Dehnung, Mosaizität, aufgewachsene gepinnte Polarität) der normalerweise mit Fasertextur wachsenden $Al_{1-x}Sc_xN$ Dünnfilme auf die elektrischen Eigenschaften, um somit des Schaltverhalten besser zu verstehen. Zu einem späteren Zeitpunkt dieser Arbeit wurde in mit Metallorganischer Chemischer Gasphasenabscheidung (MOCVD) gewachsenen $Al_{0.85}Sc_{0.15}N$ Dünnfilmen Ferroelektrizität nachgewiesen

und untersucht. Dies vereinfacht die Integration von Wurtzite-Ferroelektrika in III-N Bauteile, für welche MOCVD die Standard Wachstumsmethode ist. Außerdem könnte somit ferroelektrisches $Al_{1-x}Sc_xN$ in z.B. *high electron mobility transistors* (HEMTs) gleichzeitig als aktives (Aufbau des leitenden Kanals durch Polarisationsdiskontinuität) und funktionales (dynamisches und nicht-flüchtiges An & Ausschalten des Kanals) Barrierematerial fungieren. Rastertransmissionselektronenmikroskopie (STEM) der einkristallinen Dünnfilme ermöglicht es, die Struktur und Polarität mikroskopisch (atomar) als auch makroskopisch aufzulösen und gibt Auskunft über Nukleation und Wachstum von Polarisations-Domänen hervorgerufen durch ferroelektrischem Schalten. Bei mit Kathodenzerstäubung abgeschiedenen $Al_{1-x}Sc_xN$ Dünnfilmen bewirkt die Einbringung eines epitaxialen ultradünnen (10 nm) Pt Dünnfilms als Zwischenschicht in $Al_{1-x}Sc_xN$/GaN Heterostrukturen ein homogeneres und weniger mit Leckströmen behaftetes ferroelektrisches Schalten. Deshalb und aufgrund der geringen Oberflächenrauheit wurden Pt/GaN/Saphir Substrate genutzt, um die Skalierbarkeit der Schichtdicke von ferroelektrischen $Al_{1-x}Sc_xN$ zu untersuchen. Interessanterweise wurde nur eine schwache Abhängigkeit des Koerzitivfeldes von der $Al_{1-x}Sc_xN$ Filmdicke im Bereich von 100 nm bis 10 nm beobachtet. Die Skalierung wurde mit einer Dickenserie von $Al_{1-x}Sc_xN$, welches nicht-epitaxial auf $Pt/SiO_2/Si$ abgeschieden wurde, verglichen und es stellte sich heraus, dass letztere aufgrund des passenderen thermischen Ausdehnungskoeffizienten von Silizium im Vergleich zu Saphir elektrisch stabiler sind. Eine geringfügige Abnahme des Koerzitivfeldes bei Filmdicken unterhalb 10 nm wurde mit dem Aufkommen von Depolarisationsfeldern in Zusammenhang gebracht und ermöglichte das ferroelektrische Schalten von $\approx$ 4 nm (8 bis 9 Einheitszellen) dünnen $Al_{1-x}Sc_xN$ Filmen bei einer Spannung von $\approx$ 1 V. Somit ist die Schaltspannung bereits kompatibel mit der Betriebsspannung von integrierten Schaltkreisen (ICs). Weiters deutet das per STEM atomar aufgelöste, stabile partielle Schalten von ultrakleinen Volumen darauf hin, dass auch in hoch skalierten Bauteilen mehrere Zwischenwerte in eine Zelle gespeichert werden können (*multi-bit operation*) - eine Eigenschaft welche hoch skalierte Ferroelektrika mit Fluorit-Struktur aktuell nur mehr eingeschränkt aufweisen. Darüber hinaus decken STEM Untersuchungen das Aufkommen von stabilen Polarisations-Domänenwänden mit signifikanter horizontaler Komponente in $Al_{1-x}Sc_xN$ Dünnfilmen auf. Dies in Zusammenhang mit elektrischen Untersuchungen deutet auf das Vorhandensein von leitfähigen Domänenwänden in Ferroelektrika mit Wurtzite-Struktur hin - ein Phänomen welches memristive Funktionalität in Kondensatorstrukturen ermöglicht.

Contents

Chapter 1

Introduction

In recent times information technology involves more and more brain- and bio-inspired paradigms, both being far off from the very digital character of classical computing devices. This is especially evident considering the growing impact of artificial intelligence (AI) in almost every area of life. Early disease recognition, human-like chat partners, artistic image generation and manipulation, speech recognition and voice generators or self driving cars are just a few examples of nowadays available AI-based systems implemented mostly by using deep learning (DL) algorithms including artificial neural networks (ANN).[AZH+21, NW23, LBH15] While this concepts mimic human-brain functionalities, they are still implemented via classical digital information technology which uses Boolean logic and separates memory and computation (von Neumann model). As a result, the computation power and thus the energy needed for nowadays AI systems is very high, adversely affecting the environmental footprint.[MK22] This is in strong contrast to the comparably high energy-efficiency of the human brain, which co-locates memory and analogue-like data processing.[DMM95] The power consumption of the human brain consisting of $\approx 10^{11}$ neurons and $\approx 10^{15}$ synapses amounts to ≈ 20 W, while a digital implementation of an ANN with the same number of neurons and synapses would consume ≈ 7.9 MW.[MK22] Thus, the potential savings in terms of energy are enormous and it would be a natural consequence to implement brain-inspired data processing not on a digital but on a brain-like architecture.

There are various visions on how to realize such architectures, with one of them trying to mimic the behaviour of synapses and neurons on the hardware level using new electronic devices (i.e. neuromorphic engineering). For the realization of such devices, ferroelectric materials are very promising due to their ability of polarization retention and inversion by the intended application of a sufficiently high electric field. This allows in principle to integrate (non-volatile) memory functionality into processing devices, e.g. in the form of a ferroelectric field effect transistors (FeFET)[KKD20],

eventually merging memory and computation. Furthermore, partial and accumulative polarization switching in FeFETs enables mimicking synaptic weights and the integrate-and-fire functionality of neurons.[MMS20, KCJ21, KL23] Similarly, it allows for an analogue-like conductivity modulation of two-terminal devices such as ferroelectric tunnel junctions (FTJs), which make them ideal candidates for simulating synapses and their corresponding weights.[CMM$^+$22]. Such partial switching is not only useful for neuromorphic applications, but could also enhance non-volatile memory functionality of FeFETs or of ferroelectric random access memories (FeRAMs). Similar as for commercial FLASH memories, partial switching allows in principle to store multiple states into a single cell, eventually increasing the storage density.[PLH21] However, ferroelectric-based memory (FeRAM, FeFET) outperforms FLASH memory with respect to read and write times and energies (microsecond and nJ/bit range vs. nanosecond and fJ/bit range), which would be beneficial for reducing the latency gap between memory and computation as well as for reducing the power consumption in general.[LLC$^+$23, KKOJ23]

All ferroelectricity-based device concepts have strict requirements on the material properties of the ferroelectric. A strong polarization retention and a high cycling endurance is essential wherever a high reliability and a long life-time is required. Furthermore, in order to achieve a high storage density and a low power consumption, the film thickness as well as the lateral dimensions should be as small as possible. However, scaling down the dimensions of classical ferroelectrics such as the perovskites is often accompanied by a degradation or even total loss of the ferroelectric properties, while the integration into CMOS-technology remains challenging.[CDLS04, PCK$^+$03, QWC$^+$21] Since the discovery of ferroelectricity $\approx$ 100 years ago, huge progress with respect to the ferroelectric, piezoelectric, pyroelectric and dielectric properties of ferroelectric materials has been made, eventually resulting in many of nowadays improved commercially available sensors, actuators and capacitors.[SDE$^+$06] However, FeRAMs, where each cell consists of a transistor and an external ferroelectric capacitor (1T-1C), are up to now still the only commercially available memory devices which rely on the ferroelectric effect.[Bon90]

At the moment of writing, this situation is believed to change due to the recent emergence of the fluorite-type ferroelectrics $\approx$ 12 years ago and the wurtzite-type ferroelectrics $\approx$ 4 years ago.[BMB$^+$11, FWL$^+$19] Both materials are CMOS compatible and already well established in industry due to their enhanced pizeoelectric ($Al_{1-x}Sc_xN$) and dielectric (HfO_2) properties. Furthermore, to switch the polarization of this materials, comparably high electric fields ($E_c = 1 - 3$ MV/cm for the fluorite- and $E_c = 2 - 6$ MV/cm for the wurtzite-type ferroelectrics) are required, which promises long reten-

tion times and permits in principle to aggressively scale-down the device-dimensions while still maintaining an adequate memory window.[MSM+21, SPMH22] In fact, highly-scaled HfO_2-based FeFETs were demonstrated recently and the endurance, retention and downscaling issues reported so far for classical ferroelectrics seem to be solved.[KKOJ23, SRK+21] However, the entrance of HfO_2-based FeFETs into the commercial market is still pending. This is mainly due to device-to-device and cycle-to-cycle variability, which gets more prominent in highly scaled devices where the device size approaches the typical grain size (some tens of nanometers).[MSM+21, LLC+23] This can be related to the polymorphism and the typically polycrystalline structure of the fluorite-type ferroelectrics, potentially resulting in grain-to-grain variations due to inhomogeneities in structure, size, orientation and/or local doping of the individual grains.[MOM+17] Additionally, ferroelectricity in HfO_2-based materials requires typically post-annealing and exhibits wake-up behaviour, i.e. the ferroelectricity emerges only after initial cycling[SPMH22].

In this context, $Al_{1-x}Sc_xN$ promises uniform ferroelectric properties also for highly scaled devices due to the preferred highly c-axis oriented (i.e. highly textured) growth and the very stable ferroelectric wurtzite phase.[KKOJ23, MSM+21] The remarkable temperature stability with a Curie-temperature above 1100 °C allows to address high temperature applications.[IWY+21]. No post-annealing is required and ferroelectricity is present from the very first cycle, thus simplifying the integration into devices in comparison to HfO2-based ferroelectrics. Furthermore, ferroelectric $Al_{1-x}Sc_xN$ can be grown epitaxially on the structurally compatible wurtzite-type III-N materials like GaN and the integration of ferroelectric functionality into GaN-based high electron mobility transistors (FeHEMTs) using $Al_{1-x}Sc_xN$ was recently demonstrated.[WWH+23, CNN+22] This opens a completely new perspective on power electronic device functionality, e.g. in the form of non-volatile memory or dynamically changing the normally-on behaviour of HEMTs into the favourable normally-off behaviour.[YOY+23] Two-terminal devices as well as three terminal 2D-FeFETs using ferroelectric $Al_{1-x}Sc_xN$ were recently demonstrated as well.[WWM+23, LZW+21, KOF+23] While the demonstration of such devices is impressive and gives a prospect on possible applications, aspects such as reliability, endurance, the feasibility of industrial integration at reasonable manufacturing costs, dimensional miniaturization and power consumption have to be addressed in order to enter the commercial market. Thus, fundamental research on the basic material properties is required in order to understand and improve the ferroelectric behaviour of $Al_{1-x}Sc_xN$. In this context, especially the understanding and may suppression of leakage currents appearing at the high fields required for ferroelectric switching are essential from a device-perspective.

Therefore, in the course of this work, the focus first lies on epitaxial growth of the usually fiber-textured ferroelectric $Al_{1-x}Sc_xN$ on GaN templates with and without intermediate epitaxial Pt electrode (see chapter 4.2 and 4.1). This allows not only to investigate the impact of the structure on the electrical response with respect to e.g. leakage, coercive field and polarization, but also to investigate the feasibility and the fundamental properties of this ferroelectric III-N heterostructure in general. Latter forms a base for future power- and optoelectronic devices enhanced by ferroelectric functionality. This is strengthened by the followed investigation on single-crystal ferroelectric $Al_{1-x}Sc_xN$/GaN heterostructures grown by metal organic chemical vapor deposition (MOCVD), which is the standard growth method for III-N devices.

The second focus of this work lies on the thickness reduction of $Al_{1-x}Sc_xN$ thin films, which is required for low voltage and thus low power operation in order to be competitive or to outperform current technologies and for reaching compatibility to the on-chip voltage supply of advanced integrated circuits (ICs). Therefore, the impact of thickness reduction on the ferroelectric response and structure is investigated in detail (see chapter 4.4). Finally, through the investigation of ferroelectricity in $Al_{1-x}Sc_xN$ films with thicknesses down to 4 nm, the polarization domain evolution, the partial switching capability of ultralow volumes as well as switching voltages as low as 1 V are revealed (see chapter 4.5). Additionally, this guided towards the observation of hysteretic leakage current contributions likely arising due to charged domain wall formation and conduction upon ferroelectric switching, which is strenghtened by the TEM investigations on the single-crystal quality MOCVD-grown $Al_{1-x}Sc_xN$. While simple leakage currents in ferroelectrics are generally considered to be unfavourable (e.g. in terms of power consumption or device failure), the domain wall conduction (DWC) phenomena present e.g. in classical ferroelectrics resulted in the emergence of an own class of devices which is suitable for targeting memory as well as neuromorphic applications (DWC-based devices).[JZ19, SS23]

Chapter 2

Fundamentals

2.1 Ferroelectricity

Ferroelectricity can arise exclusively in materials with a polar space group and thus with a spontaneous polarization. At higher temperatures (i.e. above the material-specific Curie temperature) the spontaneous polarization typically disappears and a non-polar phase becomes energetically favourable. Ferroelectricity implies the polarization inversion between at least two stable states by the application of an electric field. Therefore, while all materials with a polar space group are pyroelectrics as well as piezoelectrics, not all of them are ferroelectrics.[RDL$^+$] Also the wurtzite-type materials were considered to be only pyroelectric until the year 2019, in which Fichtner et. al demonstrated ferroelectric switching in $Al_{1-x}Sc_xN$ experimentally.[FWL$^+$19] This can be regarded as the birth of the ferroelectric wurtzite-type family which up to now got expanded by $Al_{1-x}B_xN$, $Ga_{1-x}Sc_xN$, $Al_{1-x}Y_xN$, $Zn_{1-x}Mg_xO$and recently also by undoped AlN.[HHX$^+$21, WWWM21, WML$^+$23, FBZ$^+$21, HSO$^+$23] All of these materials have in common that the electric field required to invert the polarization is comparably high and close to the electrical breakdown field. This typically goes hand in hand with the appearance of leakage currents at fields close to the switching field. This enriches the investigation of ferroelectricity in the wurtzite-type materials and may explains why ferroelectricity in this material class has been discovered only recently. Therefore, in this chapter, the focus first lies on the characterization of ferroelectrics in general. Special attention is given to the clear identification of the ferroelectric switching event and its distinction to only resistive and capacitive effects. Later, the switching dynamics in ferroelectrics involving domain nulceation and growth are discussed. This is followed by an introduction to the basic ferroelectric properties of $Al_{1-x}Sc_xN$. Finally, the chapter ends with an overview of the current state of the art of ferroelectric-based

memory devices and their prospects in terms of future applications with special focus on the fluorite- and wurtzite-type ferroelectrics.

2.1.1 Basic ferroelectric properties and characterization

Polarization in dependence of the electric field ($P-E$) loops are at the core of ferroelectric characterization. They directly reveal the key properties such as the remanent polarization (P_r) and the coercive field (E_c). The latter is defined as the electric field, which is required to obtain zero net polarization. P_r is defined as the retaining net polarization without the application of an external electrical field.[Dam98] Its sign and so the direction of the polarization depends on the history of the material and can be changed by the application of an electric field higher than the material-specific and frequency-dependent E_c.[JLZ13] The shape of the hysteresis reflects the switching dynamics and allows directly to distinguish between abruptly- (very steep slope, narrow switching field range) and slowly (moderate slope, broader switching field range) switching ferroelectric materials.

$P-E$ loops are typically obtained by applying a voltage signal (e.g. of triangular, trapezoidal or sinusoidal waveform) to a ferroelectric capacitor while measuring the current response, as illustrated in Figure 2.1.

Prior to the actual hysteresis measurement, it is convenient to preset the polarization state by pre-poling the capacitor. The polarization can then be deduced from the displacement of the charges at the electrodes screening the polarization (i.e. the displacement current) upon application of an electric field.[JLZ13] At fields far apart from E_c (no FE-switching), the displacement current is solely a consequence of dielectric polarization and is denoted as i_c. This effect occurs in any dielectric capacitor, its extent is proportional to the area of the capacitor (A), the relative permittivity (ε_r) and to the change of the electric field with time (dE/dt) and can be calculated by equation 2.1:[AMMK18]

$$i_c(t) = \varepsilon_0 \varepsilon_r A \frac{dE}{dt} \tag{2.1}$$

with ε_0 the vacuum permittivity. Thus, for a voltage signal with triangular waveform, a constant positive and a constant negative displacement current i_c appears for increasing and decreasing fields respectively, as depicted in Figure 2.1b. In the vicinity of E_c, the polarization starts to invert, therefore the charges screening the prior polarization state at the respective electrodes need to invert as well, resulting in a displacement current (i_f) solely due to the ferroelectric switching event. This current peaks typically at E_c, followed by a decrease to zero as soon as the polarization inverted

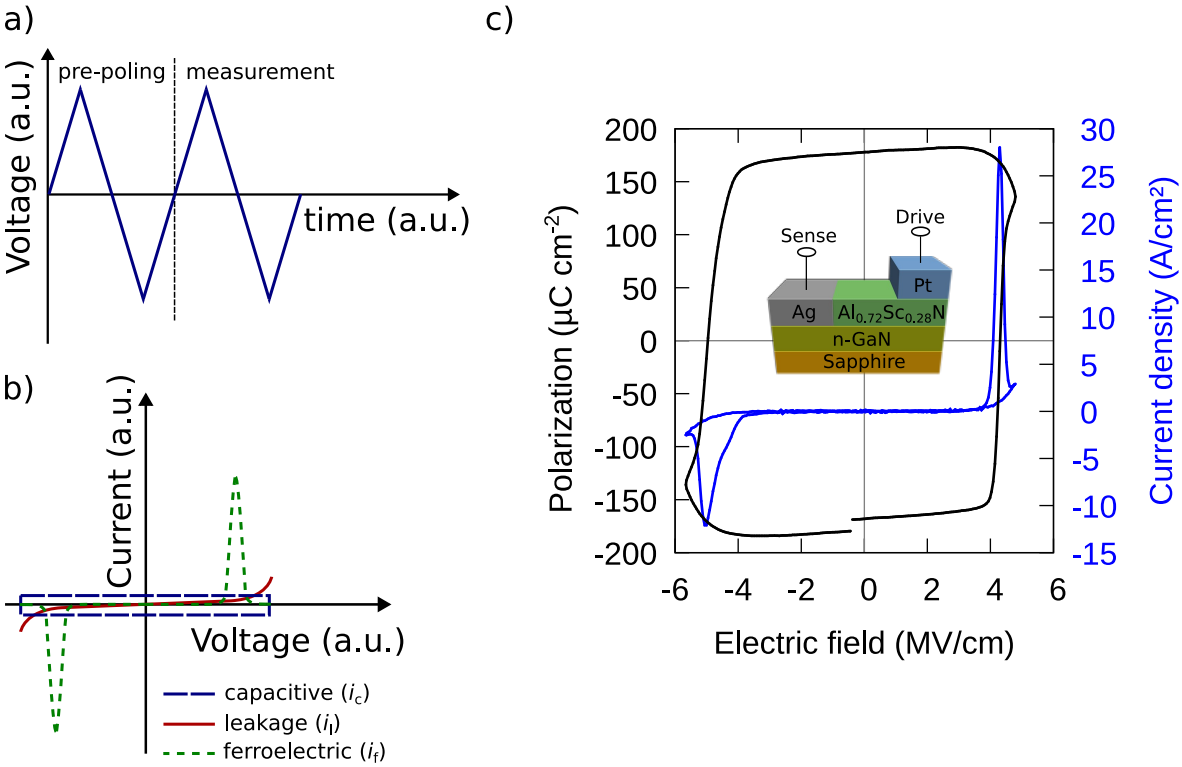

Figure 2.1: a) Voltage signal with triangular waveform used to perform dynamic hysteresis measurements. The pre-poling defines the polarization state of the ferroelectric prior to the actual measurement. b) Possible individual current responses of a ferroelectric capacitor upon application of a voltage signal as depicted in a). c) An exemplary $P-E$ hysteresis loop (black) of an $Al_{1-x}Sc_xN$ based ferroelectric capacitor and its associated apparent polarization. The measured current response (blue) is a superposition of ferroelectric and dielectric displacement- as well as leakage currents. The measurement was performed by using a signal with triangular waveform at 1.5 kHz. In addition, the visible asymmetry is related to the difference in top- and bottom-electrode materials (Pt and n-GaN). [SPI+22] John Wiley & Sons. © 2022 The Authors. Advanced Functional Materials published by Wiley-VCH GmbH.

completely (see Figure 2.1b). The associated accumulating charges per area correspond to the polarization P at time t and the respective electric field E, which can therefore be calculated by equation 2.2:[Dam98]

$$P(t) = \frac{1}{A}\int_0^t i_f(t)\mathrm{d}t \tag{2.2}$$

By plotting $P(t)$ in dependence of $E(t)$ for one period T of the measurement signal, the typical hysteretic $P-E$ loop is obtained. However, in reality the measured current corresponds to a superposition of the individual currents as sketched in Fig. 2.1b. For a symmetric voltage signal (e.g. triangular waveform) it follows $\int_0^T i_c(t)\mathrm{d}t = 0$. Thus,

the enclosed area of the $P-E$ loop is not changing due to i_c and the polarization at zero field is still reflecting the intrinsic P_r value. However, a constant i_c results in a tilting of the $P-E$ loop. At higher fields, in addition to the dielectric and ferroelectric displacement currents, typically non-linear leakage currents (i_l) arising e.g. due to Schottky emission, Pool-Frenkel emission or Fowler–Nordheim tunneling can contribute to the overall current response (see Figure 2.1b). $P-E$ loops which are affected by leakage can be misinterpreted, i.e. in the sense that the ferroelectric nature is not directly evident ($i_l > i_f$) and P_r is easily overestimated as well as E_c may can't be determined correctly.[MWP+05] On the other hand, measured $P-E$ loops of leaky dielectric capacitors can be easily misinterpreted to be ferroelectric.[YIV+11, Sco07] The current response and the associated $P-E$ loop of an exemplary ferroelectric $Al_{1-x}Sc_xN$ based capacitor (device structure sketched in the inset) consisting of a superposition of all of the discussed individual currents is depicted in Figure 2.1c. Clearly, the displacement current peaks due to true ferroelectric switching are visible. The field at which the current peaks coincides with E_c, where also the slope of the $P-E$ loop is highest. In comparison to the ferroelectric displacement current, the dielectric displacement current at lower fields ($E < E_c$) is small and therefore not visible in the current response, although a slight tilting of the $P-E$ loop is evident. However, the overall current increases after reaching the local minima of the current peak at $E > E_c$. Furthermore, when sweeping back from the maximum applied field, the current is not dropping back to the constant dielectric displacement current. Both phenomena are clear indications of leakage current contributions. Thus, the polarization obtained via equation 2.2 is overestimated and not reflecting the true polarization of this ferroelectric capacitor. To correct the $P-E$ loop for leakage and dielectric displacement contributions, one can perform the positive-up negative-down (PUND) or the dynamic leakage compensation correction (DLCC) method.[BJK+93, MWP+05]

A typical PUND sequence, in this case consisting of a train of voltage signals with triangular waveform, is depicted in Figure 2.2a.

The first voltage signal presets the polarization of the ferroelectric. During the second signal, the polarization in a true ferrolectric will switch (SW), resulting in the current response $i_{p2} = i_f + i_l + i_c$. In the subsequent voltage signal with same polarity, the polarization of the ferroelectric will not switch again (NSW) and the current response amounts to $i_{p3} = i_l + i_c$. The same holds true for the opposite polarity (signal 4 and 5) and the ferroelectric displacement currents can be separated from dielectric and leakage contributions ($i_f = i_{p2}+i_{p4}-(i_{p3}+i_{p5})$). The integration over time of i_f results in the corrected $P-E$ loop and allows for extraction of the intrinsic P_r and E_c values. Furthermore, the PUND technique is helpful to distinguish between

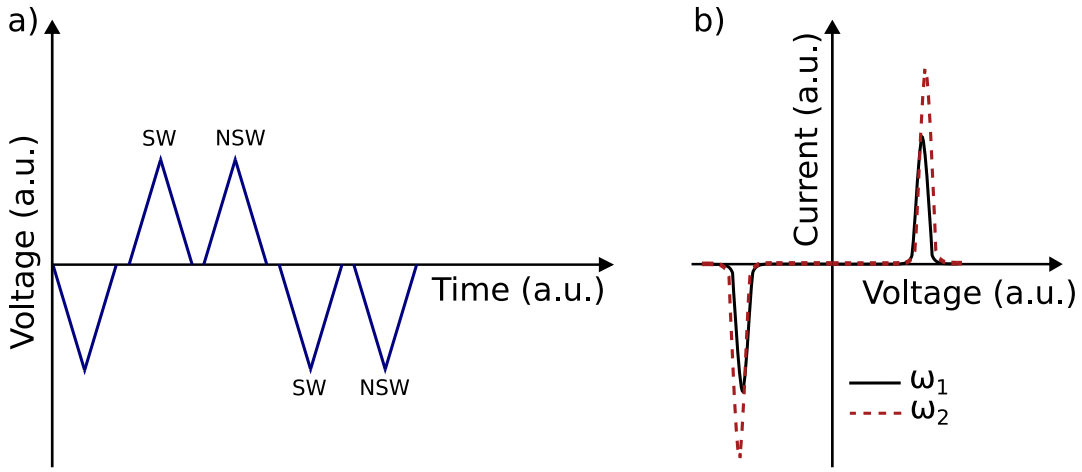

Figure 2.2: a) Typical PUND voltage signal sequence. The switching (SW) and non-switching (NSW) voltage signals are labeled respectively. b) Ferroelectric displacement currents sketched for two frequencies (ω_1, ω_2 with $\omega_2 > \omega_1$). The displacement current as well as E_c (peak position) increases with increasing frequency.

real ferroelectricity and solely non-linear resistive or/and capacitive effects.[Sco07]

In contrast to PUND, the DLLC method corrects for i_l by the subtraction of two switching cycles measured at different frequencies (ω). Since the charges required to screen the polarization inversion are frequency independent ($q_f = i_f/\omega = const$), the current i_f has to increase with frequency ($i_f \propto \omega$) in order to properly screen the intrinsic polarization of the ferroelectric material, as sketched in Figure 2.2b. On the other hand, the leakage current is in good approximation only dependent on the voltage amplitude, but not on the frequency. Therefore, by subtracting the current response of two switching cycles measured at different frequencies $i(\omega_2) - i(\omega_1)$ with $\omega_2 > \omega_1$, the leakage compensated current response (i_{comp}) can be calculated by equation 2.3:[MWP+05]

$$i_{comp}(\omega) = i_f + i_c = \frac{\omega}{\omega_2 - \omega_1}(i(\omega_2) - i(\omega_1)) \tag{2.3}$$

This allows in principle to calculate the leakage free current response for any frequency (ω). However, for the DLCC method it is assumed that the peak shape of i_f is not dependent on the frequency, which implies a frequency independent E_c. This is certainly not the case for real ferroelectrics, as the polarization inversion involves the time-dependent nucleation and growth of polarization domains, which will be discussed in the following section. Therefore, equation 2.3 is suggested as a first order approximation and the frequencies ω_1 and ω_2 should be chosen to be close in order to keep the impact of the frequency low. The leakage free $P - E$ loop can than be calculated by the integration of i_{comp} over time using equation 2.2.

The relative permittivity is strongly enhanced by the presence of the permanent dipoles and their inversion upon ferroelectric switching.[Bö04] As a result, ε_r in dependence of the electric field ($\varepsilon_r - E$) loops of ferroelectrics typically exhibit a butterfly-shaped hysteresis, as depicted in Figure 2.3a. Similar as for $P - E$ loops, no or only a minor hysteresis is obtained when measuring non-switching (i.e. pre-poling the capacitor to the subsequent field direction of the actual measurement) $\varepsilon_r - E$ loops of ferroelectric capacitors. If both effects are present, this is a clear fingerprint of true ferroelectricity.

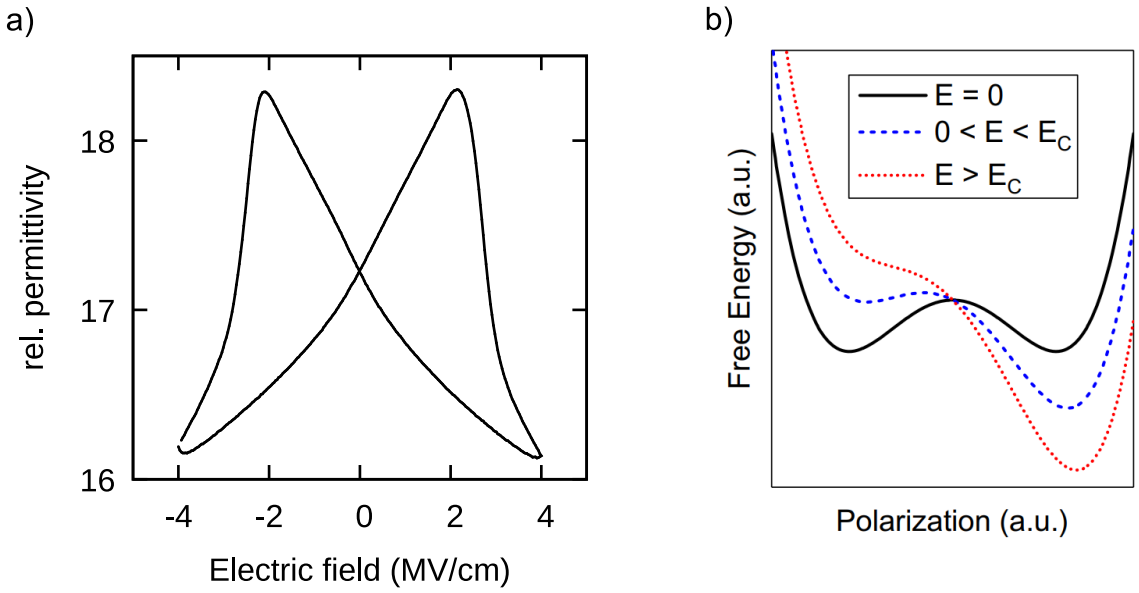

Figure 2.3: a) Typical butterfly-shaped $\varepsilon_r - E$ loop indicating ferroelectric switching in a 100 nm thin $Al_{1-x}Sc_xN$ based capacitor. Measured using a small amplitude AC signal of 100 kHz and 0.1 V overlaid by a DC bias voltage swept with steps of 0.5 V and a delay of 100 ms in between. b) Landau free energy double well potential for different electric fields.[PKH+17] Reproduced with permission from Springer Nature.

The ε_r response on the electric field can be measured by the application of an AC voltage with high frequency (> 1 kHz) and small amplitude which is superimposed by a stepwise increasing DC offset voltage. The AC signal in conjunction with an LCR meter allows to determine the capacitance C in dependence of the DC bias field from which for the parallel-plate capacitor configuration ε_r can be deduced via equation 2.4

$$\varepsilon_r = \frac{Cd}{\varepsilon_0 A} \tag{2.4}$$

with d the thickness of the dielectric layer and A the area of the capacitor. The common explanation for the butterfly-shape of $\varepsilon_r - E$ loops refers to the polarization

domains and the associated domain wall movement. The presence of domains and domain walls destabilizes the lattice and the associated shallower potential well for atomic displacement results in an enhancement of ε_r. Thus, for increasing E with $E < E_c$, the initial rise of ε_r can be explained by the activation of pinned domains (i.e. pinned domains at defect sides become mobile) and the creation of new domains. In the vicinity of E_c, the maximum in ε_r can be correlated to a domain state with highest disorder, while the drop of ε_r at fields above E_c can be related to the decrease in domain density due to polarization switching. Increasing further the electric field should in principle result in a single domain state with ε_r reaching its minimum and becoming constant.[Dam98, BLGW99, CBSB97]

However, the coercive field of $Al_{1-x}Sc_xN$ is high compared to classical ferroelectrics and the unipolar state (i.e. only one polarization direction present in the material) is very stable. Thus, an initial rise of ε_r can hardly be explained by the creation or depinning of polarization domains at electrical fields well below E_c. The distinct butterfly-shaped ε_r hysteresis observed for $Al_{1-x}Sc_xN$ is explainable by considering the Landau theory. A bias field creates an asymmetry in the Landau free energy double well potential - see Fig. 2.3b. In particular, this results in a flattening of the potential well which describes the switching side (i.e. the acting electric field is anti parallel to the polarization direction) and in a steepening of the potential well which describes the non-switching side (i.e. acting electric field is parallel to the polarization direction). Thus, before switching, the displacement of the atoms at electric fields below E_c is facilitated and the relative permittivity is enhanced. After polarization switching ($E > E_c$), ε drops drastically due to the steeper potential well of the non-switching side.[PKH$^+$17, MSM$^+$21]

Furthermore, it is well-known that not only polarization domains-, but also several other effects contribute to the field-dependence of ε_r, e.g. the movement of charged defects and the related building-up of a space charge region (SCR)[LS09] or the piezoelectric effect[AP09]. In general, the via a bias field adjustable permittivity makes ferroelectrics highly interesting for tunable microwave applications, e.g. in the form of varactors.[SDE$^+$06].

2.1.2 Ferroelectric domains

Ferroelectric materials feature at least two stable polarization directions within their crystal lattice. Regions with a specific polarization direction (domains) typically form which are separated by an interface (domain wall) to adjacent regions with different polarization direction. Such splitting into domains occurs e.g. when a material is

cooled to below the Curie temperature, where the transitions from the paraeletric into the ferroelectric phase occurs, since the individual polarization directions are in principle energetically equivalent.[Dam98, EGMB20]

Based on the classical considerations of Kittel in 1946 for ferromagnets which were adapted briefly later for ferroelectrics, a stray field (and so a depolarization field E_{dep}) appears in theory also for ferroelectrics if the polarization is unscreened (Figure 2.4a).[Kit46, MF53] Similar as in ferromagnets, such a stray field and its associated energy can be reduced by the formation of domains with opposite polarity, as sketched in Figure 2.4b.

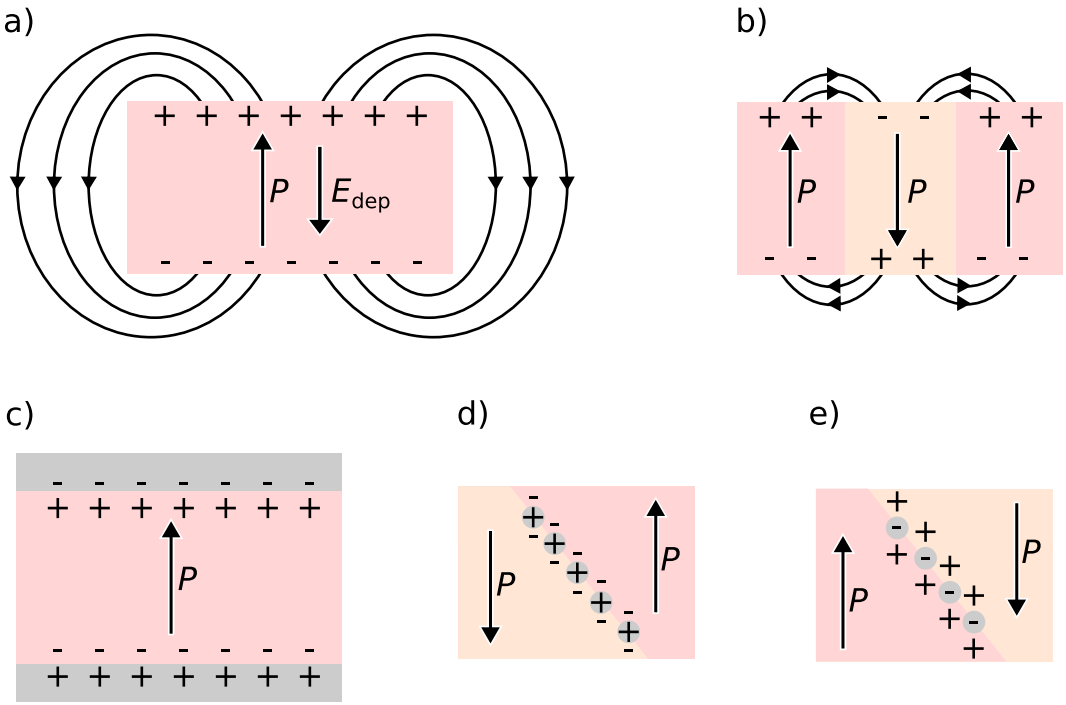

Figure 2.4: a) Sketch of an unipolar (single domain) unscreened ferroelectric and the associated stray field resulting in the depolarization field (E_{dep}) b) The formation of domains with different polarization directions results in a stray field reduction - based on classical considerations from Kittel. c) Sketch of a single domain without the occurrence of stray fields as the polarization is screened - e.g. due to the charges provided by electrodes (sketched in gray). d) Sketch of an inclined domain wall and the associated compensating charges in tail-to-tail (polarization pointing apart from each other) and e) head-to-head (polarization pointing towards each other) configuration.

However, an increasing number of domains comes at the cost of an energetically unfavourable increase in domain wall density. The minimization of these energies with respect to the domain width (w) results in the well-known equation[CSRS12]

$$w = \sqrt{\frac{\sigma}{U}d} \tag{2.5}$$

with σ the energy density per unit area of the domain wall, U the volume energy density of the domain and d the film thickness.

Nevertheless, if the polarization is screened, the stray field is absent and a single domain state is energetically stable, as depicted in Figure 2.4c. Consequently, after poling or inverting the polarization of a ferroelectric capacitor by the application of a sufficiently high enough electric field ($E > E_c$) with subsequent removal of the field, a domain configuration with net polarization ($P_r > 0$) can remain stable due to the screening charges present at the electrodes. Furthermore, a single domain state can also be stable without the presence of electrodes. In contrast to magnetism, electrical charges are monopols and can be screened easily by available charges which are present e.g. in the plasma during sputter-deposition. As an example, the as-deposited polarity of $Al_{1-x}Sc_xN$ is typically fully Nitrogen (N)-polar (i.e. no domains are present right after deposition).[FWL+19] The domain dynamics are further complicated by the necessary occurrence of defects, e.g. the interface to the electrodes, topography, grain-boundaries, dopants, vacancies, and so on. This defects can hinder domain wall movement as well as act as nucleation center for inversion domains or as pinning centers.[Dam98]

The domain dynamics in ferroelectrics often match what is referred to as the Kolmogorov–Avrami–Ishibashi (KAI) model[IT71, SRM98], which considers domain nucleation and propagation upon ferroelectric switching. In this theory, the limiting factor for polarization inversion is the domain wall movement and so the domain growth (domain wall motion limited switching). The volume fraction V_f switched at the time t is then expressed via equation 2.6:

$$V_f = 1 - exp\left\{-\left(\frac{t}{t_0}\right)^n\right\} \tag{2.6}$$

with t_0 the characteristic switching time and n the Avrami exponent, which is closely related to the dimensionality D of the growing domains. In the case of a random distribution of pre-existing nucleation sites it follows $n = D$, while in the case of a continuous constant nucleation rate it follows $n = 1 + D$.[YHM+23] From this the frequency (f) dependence of E_c (which can be defined as the field where $V_f = 0.5$) follows the formula

$$E_c = f^{D/\alpha} \tag{2.7}$$

with $\alpha \approx 6$.[DRS05]

A more recent approach to describe the domain dynamics was established by Tagantsev et al.[TSS+02] Here, the limiting factor is not the domain propagation but the nucleation of domains (NLS). The domain evolution for the KAI and the NLS model are sketched in Figure 2.5.

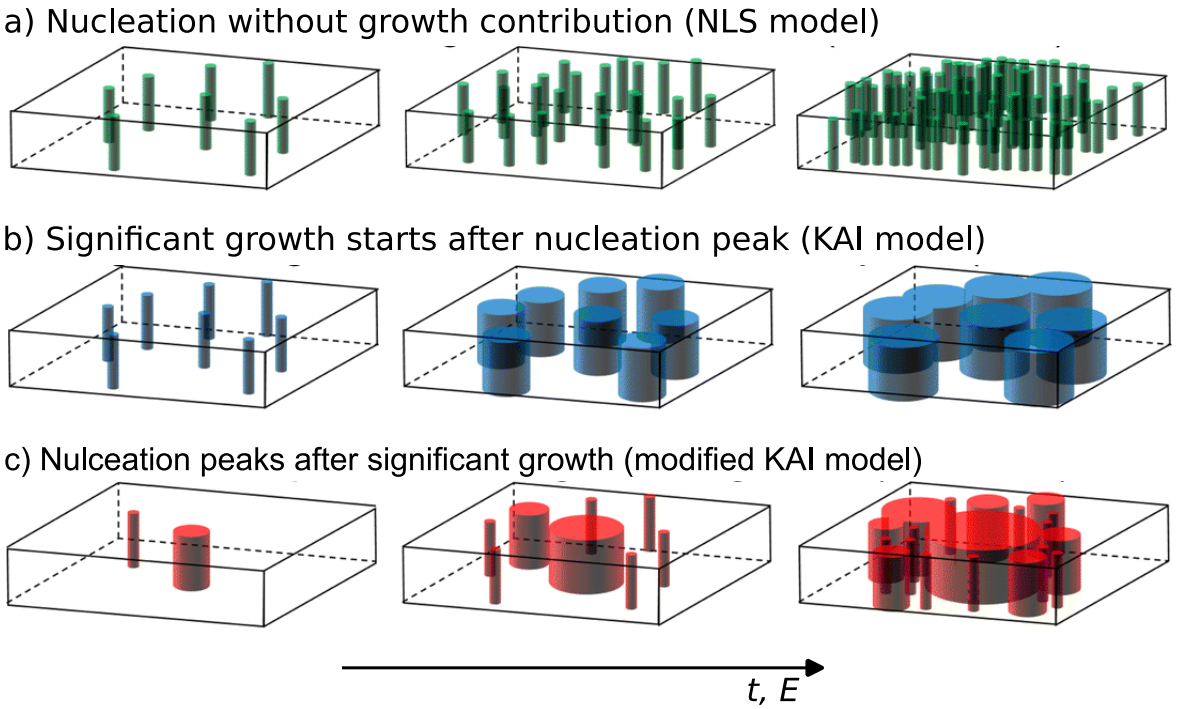

Figure 2.5: Sketch of domain evolution with time t and electric field E (increasing from left to right) a) for the nucleation limited switching and b) for the domain wall motion limited switching. An extended KAI model for describing the wurtzite-type ferroelectric domain dynamics is sketched in c). Reproduced from Ref. [YHM+23] with permission from the Royal Society of Chemistry.

The validity of the respective model can be proven by fitting the transient current of the individual ferroelectric material in dependence of time and electrical field to e.g. equation 2.6 in the case of KAI switching dynamics. However, due to the fact that the KAI model assumes an infinite crystal as well as unrestricted domain growth, it is more appropriate to describe domain dynamics in single crystals or epitaxial films. This way, as an example, epitaxial PZT thin films were suggested to follow the KAI model[SKN+05], while polycrystalline PZT and HfO_2 thin films were suggested to follow the NLS model[TSS+02, MSM+12, GSJ+18]. However, for the wurtzite-type ferroelectrics $Al_{1-x}Sc_xN$ and $Al_{1-x}B_xN$ neither the KAI nor the NLS model could appropriately describe the domain dynamics and a modified KAI model was proposed, which considers simultaneous non-linear nucleation and growth, as sketched in Fig. 2.5c.[YHM+23] Note that the shape of the domains is not necessarily cylindrical, but

can also be e.g. cone-like, as sketched in Fig. 2.4.

From a device perspective, the switching speed as well as the domain evolution during switching are of greatest interest. Former determines the maximum operation speed while latter is especially interesting in terms of stable partial switching capabilities of highly-scaled multi-storage or neuromorphic devices. In this context, due to the small-signal amplitude and frequency dependence of polarization domains (and so of ε_r), such domain dynamics can in principle be investigated by performing Rayleigh-analysis (see chapter 2.1.1).[Eit07, ZHH+21b, BBKK22, MPG+23]

Furthermore, the (partial) inversion of the polarization may involve the formation of polarization discontinuities between two adjacent domains. Such discontinuities are typically screened by mobile charges (i.e. charged domain walls) and are suitable for current transport (i.e. conductive domain walls).[EGMB20] A sketch of charged domain walls in tail-to-tail and head-to-head configuration are presented in Figure 2.4d and e. The density of charged domain walls and so the overall resistivity of the ferroelectric can be modulated by exploiting the time and field dependence of the ferroelectric switching process. This enables in principle nanoscaled memristive devices capable of addressing neuromorphic concepts.[SZS+17, WMH+22, SS23, MLW+20]

2.2 Ferroelectricity in $Al_{1-x}Sc_xN$

In the course of this doctoral thesis, a comprehensive review on the structural and ferroelectric properties of $Al_{1-x}Sc_xN$ was published. This review provides an introduction to ferroelectric $Al_{1-x}Sc_xN$, summarises the results of our own studies as well as others and reflects the state-of-the-art.[SIF23] This chapter includes an excerpt of this review discussing the basic ferroelectric properties of $Al_{1-x}Sc_xN$. The included part was solely written by myself. Epitaxy and thickness scaling of ferroelectric $Al_{1-x}Sc_xN$ were the main focus of this doctoral thesis, thus their discussion is included in the form of own publications in chapter 4. The possible applications of $Al_{1-x}Sc_xN$ in terms of state-of-the-art ferroelectric memory devices are discussed in chapter 2.3.

This chapter was published in Emerging Ferroelectric Materials and Devices, Vol 114, G. Schönweger, Md. R. Islam, S. Fichtner, Structural and ferroelectric properties of $Al_{1-x}Sc_xN$, 80-82, Copyright 2023, with permission from Elsevier. Slight adaptions consisting of changing in-chapter references and the inclusion of Fig. 2.7 were made.

Polarization in dependence of the electric field ($P - E$) loops for the up to now most studied wurtzite-type material $Al_{1-x}Sc_xN$ are depicted in Figure 2.6a, revealing its fundamental ferroelectric properties. The material features a high remanent polarization (P_r) as well as a high coercive field (E_c). In combination with the square-

like shape of the hysteresis, the latter promises long retention times, meaning no loss of polarization over time. Early work demonstrated virtually constant remenant polarization for at least 10^5 s in $Al_{1-x}Sc_xN$ [FWL+19], which was later confirmed by Wang et. al.[WWV+21, WWMM22] Drury et. al. investigated retention at elevated temperatures up to 400 °C for 10^3 s and observed negligible (< 2 %) changes in apparent polarization. This changes were likely arising from leakage current variations before and after the dwell time of the respective temperature, thus no true polarization loss is expected.[DYZ+22] The distinct polarization states and the stability with time and temperature of $Al_{1-x}Sc_xN$ are beneficial in terms of device applications, e.g. for ferroelectric-based non-volatile memory and neuromorphic computing devices. Recently, impressive 10 years of data retention was extrapolated for an $Al_{1-x}Sc_xN$ based two-dimensional channel ferroelectric field effect transistor (FeFET).[KOF+23].

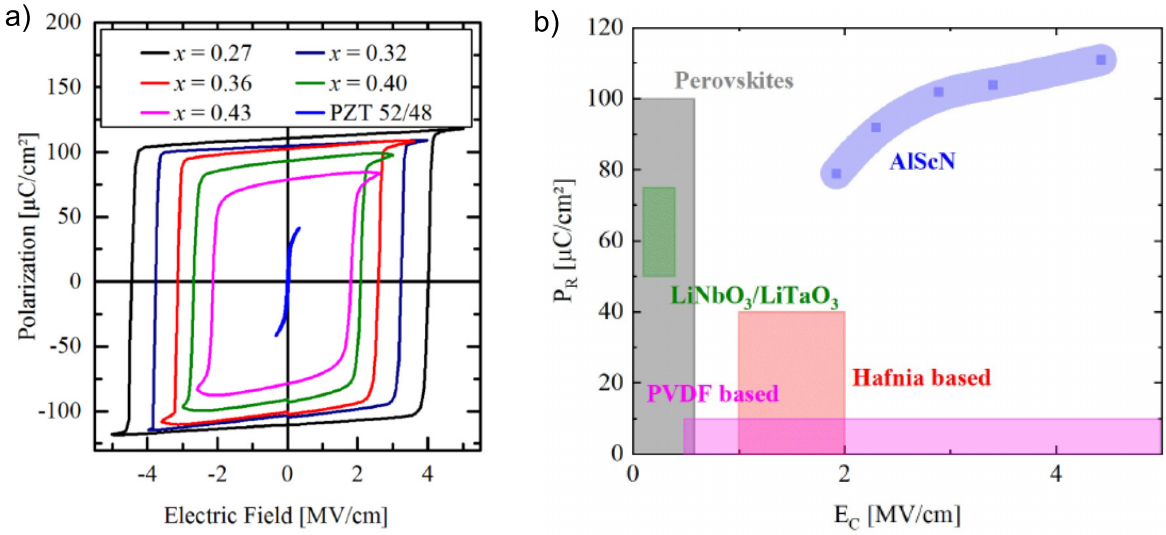

Figure 2.6: a) $P - E$ loops for various Scandium concentrations (x) and in comparison to PZT. Reprinted from [FWL+19], with the permission of AIP Publishing. b) P_r and E_c for various material classes. © [2020] IEEE. Reprinted, with permission, from [FLW+20]

The high remanent polarization in combination with the high coercive field separates $Al_{1-x}Sc_xN$ from classical- as well as from the relatively new Hafnia-based fluorite-structured ferroelectrics, as depicted in Fig. 2.6b. The narrow hysteresis-loop of $PbZr_{0.52}Ti_{0.48}O_3$ (PZT 52/48) depicted in Fig. 2.6a highlights further the difference of $Al_{1-x}Sc_xN$ to such classical ferroelectrics. The much larger P_r values range between 80 to 130 $\mu C/cm^2$ and E_c values range between 2 and 6 MV/cm, both are adjustable by changing the scandium concentration x. Chemically, the inclusion of Sc atoms destabilizes the wurtzite-structure due to the different coordination numbers between Al atoms in the wurtzite-type AlN and Sc atoms in the cubic ScN.[WIK+22, BFPS21] Addition-

ally, the more ionic bonding-type of Sc-N compared to the more covalent bonding-type of Al-N was suggested to disturb the wurtzite structure further.[YMG+22] Structurally, an increase in x results in an increase of the internal parameter u (the relative distance in c-direction from a metal to a nitrogen atom - see Fig. 2.7). This goes hand in hand with a decrease in the dipole moment, explaining the decrease in P_r with increasing x. The structural and chemical changes with increasing scandium content result in a lowering of the energy barrier for switching between the two polarization states.[MSM+21] Thus, if the barrier is low enough, meaning that E_c is lower than the electrical breakdown field, the material can undergo the transition from one polarity state into the other by the application of an electric field, i.e. the material becomes ferroelectric.

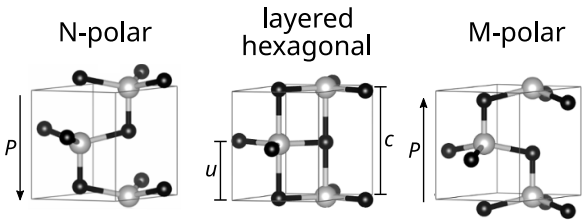

Figure 2.7: The two stable polarization states in ferroelectric $Al_{1-x}Sc_xN$ and the intermediate layered hexagonal structure. Black dots depict nitrogen atoms, grey dots depict Al/Sc atoms. [SPI+22] John Wiley & Sons. © 2022 The Authors. Advanced Functional Materials published by Wiley-VCH GmbH.

The scandium concentration has to be in a certain range for $Al_{1-x}Sc_xN$ to be ferroelectric. The maximum value is determined by the concentration at which the transition from the polar wurtzite structure into the non-polar cubic structure occurs. Akiyama et. al. reported that the transition starts at $x = 0.42$, above which a mixture between wurtzite- and cubic structure coexists up to $x = 0.45$, followed by a solely cubic structure.[AKK+08] This agrees well with the reported $x_{max} = 0.43$ of Fichtner et. al.[FWL+19] In contrast, the minimum scandium concentration for $Al_{1-x}Sc_xN$ to be ferroelectric is not restricted to a fixed value, since the energy barrier for switching is also highly dependent on film stress and temperature as well as on epitaxial strain if grown epitaxially. All of these parameters can destabilize the wurtzite-structure and thus facilitate ferroelectric switching, eventually resulting in a lowering of E_c.[FWL+19, SPI+22, GLI+23, YNF+22] As an example, even in undoped AlN, ferroelectricity was experimentally demonstrated at temperatures above 100 °C.[ZHH+21a] However, the electrical breakdown field is also dependent on strain/stress, temperature and scandium concentration. Furthermore, the band gap of $Al_{1-x}Sc_xN$ decreases with increasing scandium concentration.[DEG13] As a consequence, the electrical breakdown resistance decreases as well with increasing x.[Wan] Similarly, temperature and

strain/stress influence the breakdown resistance.[ZHH+21a, YMO+22a, YMO+22b] Ferroelectric switching can only occur if E_c is below the breakdown field. Thus, the combination of scandium concentration, stress/strain and temperature determine the (ferro)electric response of $Al_{1-x}Sc_xN$.

Here the included excerpt of the review "Structural and ferroelectric properties of $Al_{1-x}Sc_xN$" ends.[SIF23]
The full review can be found online - https://doi.org/10.1016/bs.semsem.2023.09.017

2.3 State-of-the-art of ferroelectricity-based memory devices

The field driven switching of the polarization in ferroelectricity-based memory devices promises lowest energy consumption. Furthermore, the readout of the (partially switched) polarization state - representing e.g. a (multi-level) memory state - can be accomplished in several ways; by measuring the ferroelectric displacement current (e.g. FeRAM), by sensing the field effect induced by the polarization screening charges (e.g. FeFET, FeHEMT) or by measuring polarization dependent currents which go through the ferroelectric material (i.e. memristive devices in the form of ferroelectric tunnel junctions, ferroelectric diodes and domain-wall-conduction-based devices). Exploiting ferroelectricity thus allows for a broad range of device concepts (see Fig. 2.8) and various demonstrator devices which prove the basic memory or computation functionality can be found in literature.

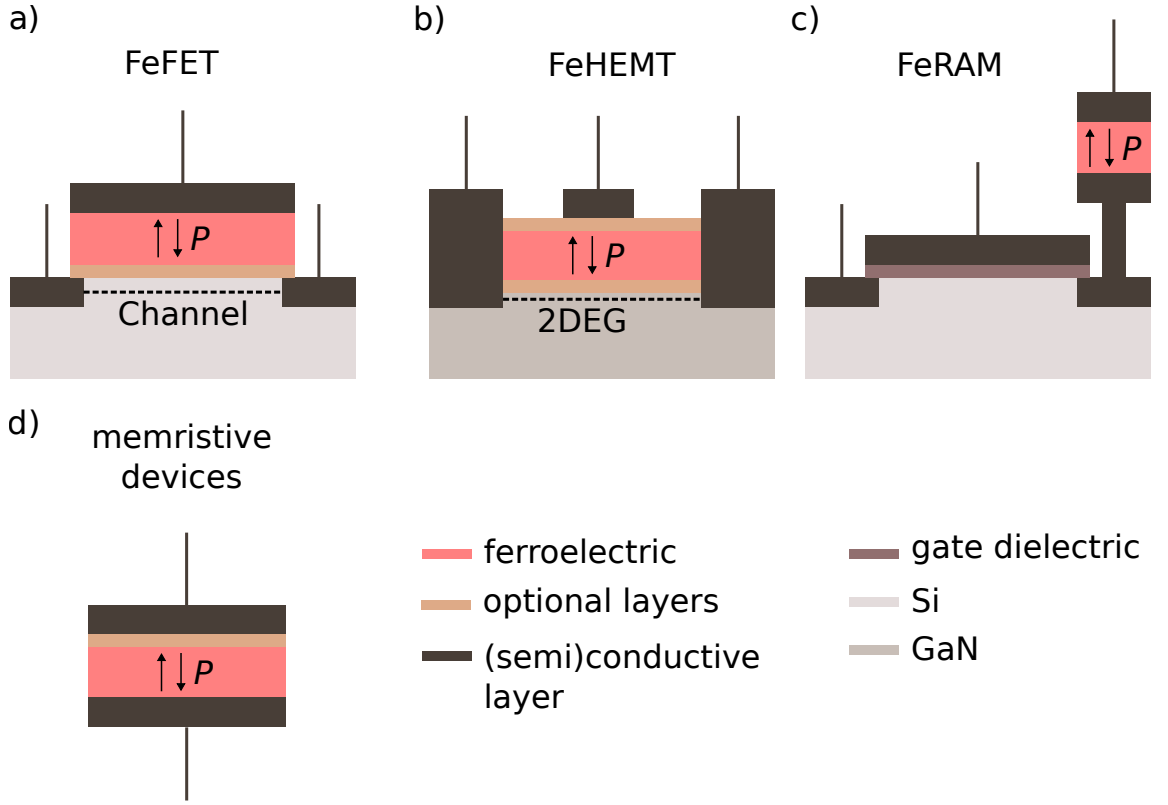

Figure 2.8: Basic structure of ferroelectricity-based non-volatile memory devices concepts - a) FeFET, b) FeHEMT, c) FeRAM and d) ferroelectricity-based memristive devices.

However, FeRAM are up to now the only ferroelectricity-based memory devices which entered the commercial market.[Bon90] In this chapter, first a short summary

on how FeRAM evolved and why up to now it serves only a niche market is given. This is followed by a discussion on why and how the fluorite-type and wurtzite-type ferroelectrics potentially enhance ferroelectricity-based devices capable of entering a much broader commercial market. The state-of-the-art of wurtzite- and fluorite-type ferroelectricity-based devices such as FeRAM, FeFETs, FeHEMTs, as well as two-terminal devices are presented. The peculiarities of the two ferroelectric material classes and the potential advantages in regard to the respective devices are discussed.

The commercialisation of FeRAM in the early 1990s was enabled by the success of integrating ferroelectric PZT via RF-sputtering into a CMOS process. This is facilitated by the fact that the ferroelectric capacitor consisting of only poorly CMOS compatible materials is spatially separated from the actual CMOS transistor (1T-1C). This resembles the design of volatile dynamic random access memories (DRAM), but for FeRAM the capacitor is a ferroelectric and can therefore hold its state also without power supply (non-volatile memory). Furthermore, ferroelectric switching involves higher displacement currents compared to the ones resulting from simple capacitor charging in DRAM. In principle, this allows to scale down the lateral dimensions more aggressively, while still maintaining adequate readout currents, eventually resulting in higher cell densities.[SSM18] However, perovskite-based FeRAM got stuck at a 130 nm CMOS process and thus exhibits a much smaller storage density than state-of-the-art DRAM or FLASH devices.[USR$^+$13] This is partly due to the polarization degradation typically observed for perovskite ferroelectrics when scaled down to below 50 nm as well as due to its poor compatibility with Si-based CMOS technology, which gets pronounced especially in highly scaled devices and requires cost-intense fabrication steps.[PCL$^+$23] Furthermore, although its non-volatile nature, the readout event in FeRAM is destructive and requires restoring the actual state of the cell after each read operation. Thus, read operations are also write operation which can limit the endurance of the device and requires additional energy. Despite its lower displacement currents, the 3D-integration of the active layers in state-of-the-art DRAM allowed for decreasing the projected lateral dimensions (sub-20 nm CMOS process) without loosing the readout signal.[LLC$^+$23] Therefore, the storage density of DRAM and FLASH devices is much higher and the costs per bit much lower compared to perovskite-based FeRAMs. Consequently, commercially available FeRAM technology up to date serves a niche market which requires comparably low power consumption, fast access times and high reliability.

The emergence of the fluorite-type ferroelectrics in 2006 and the wurtzite-type ferroelectrics in 2019 raised expectations of advancing ferroelectricity-based devices, which are envisioned to eventually enhance information technology and serve a broader com-

mercial market.[PCL+23, KKOJ23, LLC+23, SPMH22] Both material classes are fully CMOS-compatible and their deposition is already well established in industry. Additionally, they feature unique properties such as a high E_c as well as a moderate to high P_r, which promises stable data retention and large memory windows (see chapter 2.2). This in combination with the thickness scalability down to the sub-5 nm regime, which for $Al_{1-x}Sc_xN$ was investigated during this doctoral thesis - see chapter 4.4 and 4.5), allows in principle for highly scaled devices operating at low power.

For HfO_2 -based FeRAMs a cycling endurance of up to 10^{14}, operation times of 10 ns, operation voltages of 2 V and data retention of 10 years at 85 °C are reported.[SSM18, OKK+20, KKOJ23] Highly scaled devices using a 1Xnm technology node consisting of 3D capacitor structures combined with 5 nm thin ferroelectric Hafnium-zirconium oxide (HZO) resulting in 8Gbit density were demonstrated.[SRK+21] The much faster read and write times compared to FLASH memory devices allow for reducing the latency gap between memory and computation. Furthermore, FeRAMs consume less power than conventional FLASH devices.[KKOJ23] FeRAMs are also interesting candidates for the replacement of DRAM. As mentioned above, the ferroelectric displacement currents are higher than the displacement currents of dielectrics. Very recently, Micron Technology Inc. demonstrated that this together with the ability of growing fluorite-type ferroelectrics (e.g. HZO) uniformly onto 3D structures by using atomic layer deposition (ALD), allows for a higher storage density as well as a reduction in manufacturing complexity and thus in a reduction of cost per bit compared to conventional DRAM. They presented a market-ready 32 Gbit dual-layer FeRAM device based on 3D-structured ferroelectric HZO, which they call non-volatile (NV)DRAM.[RCZ+23] The reported endurance greater than 10^{15} matches the endurance of conventional DRAM, while close to DRAM performance concerning write/read times is achieved, all combined with the non-volatile character for which retention times of more than 10 years are extrapolated. This enlarges the current memory landscape and demonstrates that highly scaled and in terms of costs per bit competitive FeRAM devices capable of serving a broad commercial market are from a technological point of view already available. Due to the relatively short development time of the wurtzite-type ferroelectrics, only very recently an FeRAM like selector free memory array consisting of 10 nm thin ferroelectric $Al_{1-x}Sc_xN$ was demonstrated.[CLL+24] The high P_r ($> 100\ \mu C/cm$) of the wurtzite-type ferroelectrics would allow in principle to reduce the lateral dimensions even more. However, up to date there is a lack of investigations on 3D growth (e.g. by using ALD) of the ferroelectric wurtzites. While the high crystallinity and textured growth promises uniform properties and ferroelectricity is present from the very first cycle, it could be a showstopper for the integration into 3D structures. The lower

cycling endurance (up to 10^{-7})[CHW+24] as well as the leakage currents appearing in $Al_{1-x}Sc_xN$ limits up to date the performance. On the other hand, the reported hysteretic leakage currents for $Al_{1-x}Sc_xN$ which add up to the ferroelectric displacement currents could allow for further cell size reduction.[SWI+23] Furthermore, when comparing the relative short development time of the wurtzite-type ferroelectrics with the history of the fluorite-type ferroelectrics, research resulting in a lowering of the non-hysteretic leakage current as well as an increase of the cycling endurance, e.g. by interface engineering or doping, is likely to occur. Additionally, the high temperature stability of $Al_{1-x}Sc_xN$ (up to at least 1100 °C)[IWY+21] makes this ferroelectric highly interesting for harsh environment memory applications (e.g. space or automotive). This is especially true if the ferroelectric capacitors are integrated into highly temperature stable SiC or Sapphire based field effect transistors (e.g. into HEMTs), which will be discussed in more detail below.[MAG+10]

Similar as for FeRAMs, the emergence of the fluorite-type ferroelectrics advanced significantly FeFET technology resulting in impressive device characteristics such as sub-nanosecond operation, 2-5 V write voltages, data retention of 10 years at 150 °C and a cycling endurance of up to 10^{11}.[SSM18, KKOJ23] In terms of applications, FeFETs are on one hand interesting for neuromorphic applications. The gradual switching capability of FeFETs allows for storing intermediate conduction states in an analogue-like fashion. Thus, FeFETs can mimic synaptic behaviour in the sense of that the intermediate conductivity states represent the weights of a synapse. Additionally, accumulative switching of FeFETs allows to mimic the integrate-and-fire functionality of neurons.[CMM+22] On the other hand, FeFETs offer faster read and write times and lower power consumption in comparison to FLASH devices, similar as for FeRAM but with the advantage of a non-destructive readout. Thus, they are also potential candidates for next-generation low-latency memory devices. However, the entrance of FeFETs into the commercial market is still pending, mainly due to device-to-device and cycle-to-cycle variability and the loss of multi-level storage capability in highly scaled devices. Both issues are related to the polymorphism and the polycrystallinity of the fluorite-type ferroelectrics - which is fundamentally different for the wurtzite-type ferroelectrics. The latter grow over a wide concentration range exclusively in the wurtzite phase with preferred texture and high crystallinity. Thus, compared to the fluorite-type ferroelectrics, more uniform properties can be expected also for highly scaled devices. Furthermore, during this thesis stable partial switching inside a single grain was experimentally observed which demonstrate multi-level storage capability also of small volumes in the range of $5x5x5nm^3$ - see chapter 4.5. This fundamental difference in switching dynamics and structure of the wurtzite-type- compared to the

fluorite-type ferroelectrics could potentially solve the current issues faced for state-of-the-art FeFETs. However, wurzite-type FeFETs are still in its infancy and similar as for FeRAM, the comparably lower cycling endurance, the lack of a 3D growth-method and especially the apparent leakage currents are severe issues which need to be addressed in order to compete with fluorite-type FeFET devices. The general feasibility of non-volatile wurtzite-type FeFET operation was demonstrated during this thesis in a cooperation with Fraunhofer ISIT by integrating 200 nm thin $Al_{1-x}Sc_xN$ into the gate stack of a silicon based NMOS FET.[FSD+23] Liu and Kim et al. demonstrated the integration of ferroelectric $Al_{1-x}Sc_xN$ with channel lengths and $Al_{1-x}Sc_xN$ film thicknesses down to 20 nm into a CMOS backend-of-line compatible 2D channel FeFET, thus guiding towards highly scaled $Al_{1-x}Sc_xN$ based FeFETs.[LWZ+20, KOF+23]

Similar as for FeFETs, ferroelectrics integrated into the gate-stack of a HEMT device allow in principle for dynamic non-volatile threshold voltage control, which is not only interesting for memory, but also for reconfigurable radio frequency applications. In contrast to FeFETs, the channel of a HEMT is formed due to the polarization discontinuity between the barrier (e.g. AlGaN) and the channel material (e.g. GaN), resulting in the formation of a two-dimensional electron gas (2DEG).[ASS+99] Since the polarization discontinuity is present right after the deposition, these transistors in its simplest form operate in depletion (D-)mode - meaning they behave as normally-on devices. Tuning dynamically the polarization discontinuity in a non-volatile manner by using ferroelectrics allows for changing from normally-on into normally-off operation.[HZL+12] The basic functionality of FeHEMTs was demonstrated for several ferroelectrics including the fluority-type as well as recently the wurtzite-type ferroelectrics.[SLS+02, SMMS06, WYS+20, WWH+23, YOY+23, CNN+22] However, HEMTs are typically based on III-N materials which grow in the wurtzite-structure. Thus, ferroelectric $Al_{1-x}Sc_xN$, which is a III-N material itself, offers not only ferroelectricity but also structural compatibility and similarities in the electrical properties, e.g. a wide bandgap and a high spontaneous polarization. Thus, independent of its ferroelectric properties, lattice-matched growth on GaN resulted in high performing HEMT devices with $Al_{1-x}Sc_xN$ used directly as barrier material.[HDN+17, AYY+22, CNC+22] Additionally, we demonstrated ferroelectricity of $Al_{1-x}Sc_xN$ sputter-deposited directly onto n-type doped GaN, which provides a base for the integration of wurtzite-type ferroelectricity into III-N heterostructures - see chapter 4.1. Thus, ferroelectric switching is in principle accessible directly in the barrier material, which, in addition to the enhanced electrical properties, could be beneficial from a manufacturing and cost perspective of view. This is especially true considering our study on MOCVD-grown ferroelectric $Al_{1-x}Sc_xN$ on n-GaN, which demonstrates that wurtzite-type ferroelectricity can

also be integrated by using the standard growth method for III-N devices - see chapter 4.3. This together with the outstanding temperature stability of $Al_{1-x}Sc_xN$ makes the ferroelectric heterostructures based exclusively on III-N materials highly interesting for high temperature (memory) applications as well as for enhanced HEMT operation.

The working principle of a classical ferroelectric tunnel junctions (FTJ) relies on the polarization dependent direct quantum mechanical tunnelling through an ultrathin (1-5 nm) ferreoelectric layer sandwiched between two electrodes (i.e. a capacitor).[TK06] The readout occurs at electric fields well below E_c, thus, in contrast to FeRAM, the readout is non-destructive. Thickness scaling below 5 nm film thickness of several ferroelectrics including the fluorite-type ones was achieved and FTJ operation based on direct tunneling was demonstrated in recent years.[GB14, AVKT$^+$17, YHS$^+$19] An endurance of 10^8, 10 years of data retention, switching at 20 ns, low power operation and multi-level storage capability was experimentally demonstrated for HfO_2 -based FTJs.[KKOJ23] Thus, such FTJs are already interesting candidates for non-volatile memory as well as for neuromorphic applications. The conductivity state of FTJs can typically be changed in an analogue-like fashion by switching partially the polarization, making them ideal candidates for the representation of synaptic weights. Thus, this two-terminal devices allow in principle for highly dense crossbar arrays to perform parallel weighted sum operations, which are very time consuming in conventional neural network implementations.[Yu18, CMM$^+$22] Furthermore, due to the time and electrical field dependence of the polarization switching, FTJs typically exhibit spike timing dependent plasticity (STDP). However, classical FTJs depend on ferroelectrics which can be scaled to below 5 nm film thickness. This remains challenging, e.g. in the case of HZO due the required crystallization and the associated favour for the non-polar tetragonal phase formation especially at such low thicknesses.[SPS$^+$20] Composite barrier or two-layer FTJs consist of a very thin dielectric layer in series with a ferroelectric layer, were latter can also be thicker than in classical direct tunneling FTJs.[MCPK04, WW19] In such devices, direct tunneling can appear only in the ultrathin dielectric layer which overlaps with a polarization dependent potential barrier modulation or/and results in a band bending of the whole stack.[MHSM18, SPS$^+$20] Similar to two-layer FTJs, in ferroelectric diodes (FE-diodes) the polarization dependent leakage currents, e.g. due to Schottky-barrier modulation,[BWCK94] allow for non-destructive readout without a specific requirement on the thickness of the ferroelectric layer.[KKOJ23] The FE-diode as well as the two-layer FTJs have in common that they typically exhibit a rectifying behaviour. In crossbar arrays this can suppress sneak currents, which potentially result in read failures.[PCL$^+$23, Gü19] One major concern of all of these two-terminal devices, especially in terms of non-volatile memory

applications, are the relatively low read currents. As a consequence, a trade-off between lateral scalability and the time required to accumulate a detectable amount of charges (i.e. read speed) has to be made.[SPS+20, KKOJ23] The read currents typically decrease with increasing film thicknesses and range in state-of-the-art devices between 100 A/cm² (3 nm thick HZO) down to 10^{-6} A/cm² (10 nm thick HZO).[CHC+21, HGJ23] For highly scaled devices with a footprint of 10 x 10 nm² this would result in a maximum current of 100 pA, which is orders of magnitudes lower than the desired μA range required for read speeds in the ns-range.[SM21] Furthermore, the device to device variability as well as the loss of multibit-capability faced in general for highly-scaled HfO_2 -based devices is a limiting factor also for FTJs and Fe-diodes. In this context, the wurtzite-type ferroelectrics promise advantages due to their single crystallographic phase without the need of post-deposition annealing as well as due to the demonstrated partial switching of ultralow volumes (see chapter 4.5). Furthermore, the comparably higher P_r of the wurtzite-type ferroelectrics allow in principle for higher On/Off ratios.[KKOJ23] Additionally, we could demonstrate ferroelectricity in 4 nm thin $Al_{1-x}Sc_xN$ and suggested the feasibility of further thickness downscaling (see chapter 4.5). However, while direct tunneling in HfO_2 -based FTJs was reported, the demonstration of direct tunneling through a wurtzite-type ferroelectric is still pending. Recently, several studies on ferroelectric $Al_{1-x}Sc_xN$ -based memristive devices (i.e. Fe-diode and FTJ-like metal-ferroelectric-semiconductor devices) were reported in literature.[WWM+23, HCF+23, WWM+22, LZW+21, Liu] Noticeably, an On/Off ratio of up to 10^5, operation voltages in the single-digit range and uniform properties over multiple cells and cycles were demonstrated for an $Al_{1-x}Sc_xN$ /GaN based two-terminal memristive device.[WWM+23] These devices are especially interesting for inference operation in FTJ-based crossbar arrays, since that does not require many write operations - from which the wurtzite-type ferroelectrics in its current state suffer due to the comparably low endurance and the leakage currents associated with ferroelectric switching at high fields.

Tow-terminal domain wall conduction (DWC) devices, similar to FTJS, exhibit memristive behaviour, i.e. intermediate analogue-like non-volatile conductivity states are achievable. Thus, also the possible applications are very similar as for FTJs, ranging from non-volatile memory to neuromoprhic applications (see above).[JZ19, SS23] The physics behind DWC-devices however are fundamentally different: the polarization discontinuity of two domains with different polarities can result in the accumulation of charge carriers at the interface resulting in a charged and conductive domain wall, similar as the 2DEG formation in HEMT devices.[EGMB20, STBS13, CSRS12] By partial ferroelectric switching, the domain wall density and thus the conductivity of

the ferroelectric layer can be modulated. The conductivity in such walls was demonstrated to have metallic character[STBS13] and could potentially result in high On/Off ratios combined with high on currents, which is an issue for FTJs limiting its lateral scalabilty.[WHB$^+$17] Furthermore, since domain-walls are almost 2D interfaces, i.e. they expand laterally only about 1 nm, they are very suitable for heavy scaling also from a structural point of view.[SLH$^+$24] On the other hand, in contrast to classical FTJs, there is no specific thickness requirement which could become cumbersome from an integration point of view. In recent years, DWC-devices based on several ferroelectric oxides such as the perovskites were demonstrated and impressive device characteristics such as fast access times $<$ 10 ns and huge On/Off ratios by nearly 12 orders of magnitude were demonstrated.[MS21, SLH$^+$24] At the moment of writing no report on domain wall conduction in fluorite-type ferroelectrics can be found in literature. For wurtzite-type ferroelectrics, despite the fact that a direct measurement of the domain wall conduction is still pending, we strongly suggested that domain wall conduction plays a major role in ferroelectric $Al_{1-x}Sc_xN$ (see publication 4.5 and 4.3). The high P_r of the wurtzite-type ferroelectrics and the associated high polarization discontinuity at inclined domain walls can be expected to result in a comparably high conductivity, as long as it can be accessed through the electrode-ferroelectric interface. On the other hand, the wide-band gap enables in principle low off currents (i.e. the monodomain state). This and the general properties of $Al_{1-x}Sc_xN$ such as CMOS compatibility in combination with the demonstrated partial in-grain switching of lowest volumes ($<$ 5x5x5 nm^3) at a film thicknesses of 4 nm makes $Al_{1-x}Sc_xN$ an attractive material for building DWC-devices.

Chapter 3

Experimental

In this chapter the fabrication of $Al_{1-x}Sc_xN$ based capacitors as well as its structural and electrical characterization methods are presented. While the exact experimental details of the individual studies performed during this doctoral work can be found in the respective publications (see chapter 4), a more general description is given here. This includes the optimization of the deposition process, the substrate dependent growth modes as well as details on wet-etching and dry-etching to structure and/or remove the top-electrodes.

3.1 Device fabrication

In the course of this thesis, the electrode material (Pt) and adhesion layer (AlN) as well as the ferroelectric $Al_{1-x}Sc_xN$ thin films were grown in-house by sputter-deposition. As templates Si wafers oxidized with 600 nm thick SiO_2, commercially bought n-type doped (Si, doping concentration $> 10^{18}$ $1/cm^3$) GaN/Sapphire as well as Pt(100 nm)/Ti(20 nm)/SiO_2/Si provided by Fraunhofer ISIT were used. All wafers were diced into 1x1 cm^2 chips and cleaned with acetone and isopropanol in an ultrasonic bath followed by rinsing with DI-water and drying with nitrogen. These chips were then laid on 8 inch Si carrier wafers and transferred into the sputter deposition chamber for further film growth.

Pt as well as AlN and the $Al_{1-x}Sc_xN$ thin films were deposited using an Oerlikon (now Evatec) MSQ 200 multisource magnetron sputtering system. A 20 nm thin AlN layer served as an adhesion promoter for Pt if SiO_2/Si was used as growth template, which was deposited by performing an established sputter process from Fichtner et al.[FRC+15] The deposition parameters for Pt are listed in table 3.1, resulting in a strong (111) texture if deposited onto AlN/SiO_2/Si. Interestingly, using

the same deposition process, epitaxial Pt (highly out-of-plane 111 as well as in-plane oriented grains) was grown when depositing directly onto epi-ready GaN/Sapphire templates. In comparison to non-epitaxial Pt, the eptiaxial growth enables high 111 orientation also for ultrathin (12 nm) Pt films, which in turn exhibit a low surface roughness. Epitaxial growth using sputtering is recognized in literature under the term *sputter-epitaxy* and typically involves high growth temperatures and an ultra-high vacuum.[HBA+10, PJS+02] However, in our deposition chamber we were limited to an only moderate base pressure and deposition temperature ($\approx 3x10^{-7}$ mbar and $T = 500C$).

Table 3.1: Deposition parameters of the bottom electrode and the respective growth mode.

Power (W)	Kr (sccm)	T (°C)	Thickness (nm)	Template	epitaxial growth
600	50	500	100	$AlN/SiO_2/Si$	no
600	50	500	12	n-GaN/Sapphire	yes

Table 3.2: Optimized deposition conditions for ferroelectric $Al_{1-x}Sc_xN$ grown on the respective template and the resulting growth mode. The deposition temperature was 450 °C in all cases.

Ar (sccm)	N_2 (sccm)	Template	epitaxial growth
7.5	15	$Pt/AlN/SiO_2/Si$	no
7.5	15	Pt/n-GaN/Sapphire	yes
0	15	n-GaN/Sapphire	yes

Prior to the $Al_{1-x}Sc_xN$ deposition, all Pt layers which were grown using the Si substrates (non-epitaxial growth) were cleaned by an established Ar/O_2-plasma-etching process in a Sentech Sl100 reactor.[FWK+17] The $Al_{1-x}Sc_xN$ thin films were deposited by reactive pulsed direct current (DC) co-sputtering of metallic 4 inch Sc and Al targets under pure nitrogen or under a mixture of nitrogen and argon atmosphere. The reactive gas (N_2) interacts chemically with the (sputtered) atoms from the Al and Sc targets. The targets were set into the poisoned state (i.e. insulating at the surface) by performing a chamber conditioning for several hours prior to the actual deposition and by the deposition conditions itself (i.e. nitrogen atmosphere). Pulsed DC sputtering allows to sputter from such poisoned targets. In comparison to DC sputtering, during the pulse-off time, may occurring charges at the targets get cleared, which in turn prevents the formation of arcs. Furthermore, the pulsed DC mode allows for sputtering at higher deposition rates compared to radio frequency (RF) sputtering. The scandium concentration was varied by changing the power ratio between the Al and the Sc target while keeping the total power constant at 1000 W. The deposition process was optimized in terms of texture, film stress and abnormally oriented grains (AOGs

- see below) by Fichtner et al. during his doctorate.[FRC+15, FWK+17] Further fine-tuning of the process, i.e. increasing the temperature from 300 °C to 450 °C and fixing the gas flow ratio to 15 sccm N2 and 7.5 sccm Ar (see table 3.2), allowed for reducing the thickness of ferroelectric $Al_{1-x}Sc_xN$ to the sub-5 nm regime. Interestingly, these films grow with the highly *c*-axis oriented wurtzite-structure required for ferroelectric switching from the very first atomic row, promising from a structural point of view ferroelectricity even in thinner films (see chapter 4.5).

Similar as for epitaxial Pt (epi-Pt), when depositing onto epi-Pt/n-GaN/Sapphire templates the $Al_{1-x}Sc_xN$ layer grows epitaxially (highly *c*-axes as well as in-plane oriented columnar grains) without any major modification of the deposition process. However, epitaxial $Al_{1-x}Sc_xN$ growth directly onto n-GaN/Sapphire was obtained only using a pure nitrogen atmosphere during deposition. This is likely related to the deposition process induced film stress which depends on the gas flow ratio[FWL+19] in combination with the Sc dependent lattice-mismatch between $Al_{1-x}Sc_xN$ and GaN (see chapter 4.1). A lower Ar flow results in more compressively in-plane strained films which match better the lower in-plane lattice of the GaN compared to the one of $Al_{1-x}Sc_xN$ ($x > 0.18$). Contrarily, epitaxial growth of $Al_{1-x}Sc_xN$ onto epi-Pt/GaN is likely not influenced by epitaxial strain due to the larger lattice-mismatch of Pt and $Al_{1-x}Sc_xN$. Similar as for epitaxial Pt, the degree of 0002 orientation of epitaxially grown $Al_{1-x}Sc_xN$ improves with decreasing film thickness, while the opposite is true for non-epitaxially grown $Al_{1-x}Sc_xN$ thin films.

Subsequently to the deposition of the Pt top layer at 400 W and 80 sccm Kr, the top electrodes where defined via standard lithography and structured by performing ion beam etching (Oxford Instruments Ionfab 300). The etching was stopped as soon as a constant Sc signal was recorded by the secondary ion mass spectrometer (SIMS) and thus only the Pt was patterned while the side areas of the capacitor structures are not open to the atmosphere. However, the SIMS signal is delayed and shadowing effects result in inhomogeneities especially around the defined top-electrodes. The capacitor structures and the respective layer stacks which were investigated mainly during the course of this thesis are sketched in Fig. 3.1.

When the $Al_{1-x}Sc_xN$ film thickness approaches the 20 nm regime, it was discovered that an in-situ capping with Pt is essential to exclude oxidation of the $Al_{1-x}Sc_xN$ layer and improve the ferroelectric response (see chapter 4.4). In particular, the coercive field of a with Pt in-situ capped 20 nm thin $Al_{0.72}Sc_{0.28}N$ film is $\approx 10\%$ lower than the E_c of an ex-situ capped film with the same thickness. This goes hand in hand with a more pronounced switching peak when capped in-situ. For 100 nm film thickness, the change in coercive field with respect to in-situ capping is reduced only by $\approx 2\%$ and a

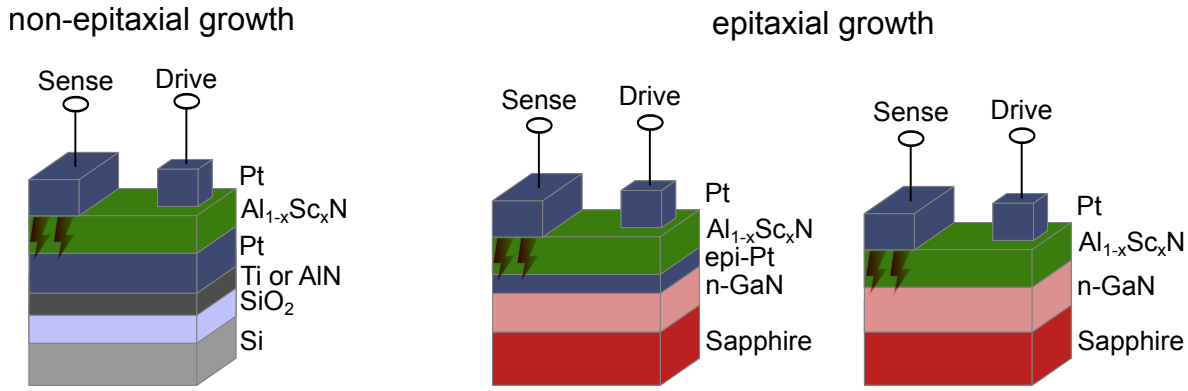

Figure 3.1: Sketch of the mainly investigated layer stacks, the capacitor structure and the electrical contacting. Epitaxial growth of the bottom Pt and the $Al_{1-x}Sc_xN$ layer was obtained when depositing onto GaN/Sapphire templates, non-epitaxial growth of the layers was obtained when depositing onto SiO_2/Si templates. Large top Pt structures at the edge of the 1x1 cm^2 chips are typically electrically shortened to the bottom layer (Pt or n-doped GaN) right after deposition (thunderbolts in the sketch) and served as electrical contact to the latter. The thickness proportions of the sketched layers do not match the real proportions of the deposited layers.

comparable switching peak for both variants is observed.

Wet-etching of wurtzite-type materials such as $Al_{1-x}Sc_xN$ and GaN is selective to the polarity. In general, the etch-rate is high for Nitrogen (N)-polarity and low for Metal (M)-polarity, thus allowing to investigate and proof the polarization reversal as already demonstrated by Fichtner et al.[FWL+19] In the course of this thesis, H_3PO_4 etching experiments were performed on Au/Cr/$Al_{1-x}Sc_xN$/n-GaN/Sapphire heterostructures to characterize the electrically discovered as-grown multipolarity (mixed M- and N-polarity) in $Al_{1-x}Sc_xN$ thin films if grown directly on M-polar n-GaN/Sapphire templates. The Au(10 nm)/Cr(30nm) electrodes, which were deposited using a von Ardenne CS730S sputtering tool, were selectively structured via wet-etching using a KI/I2 solution (Au) and TechniEtch Cr01 (Cr) solution. Thus, capacitors could be ferroelectrically switched by the application of an electric field with subsequent removal of the capacitors electrode with only minor (weak etching of Al reported for TechniEtch Cr01) structural impact on the $Al_{1-x}Sc_xN$ film beneath. Subsequent etching in 85% H_3PO_4 at 80 °C allowed for the investigation of the polarity in the capacitors region in comparison to the surrounding as-grown state of the $Al_{1-x}Sc_xN$ layer.

3.2 Methods for electrical and structural $Al_{1-x}Sc_xN$ thin film characterization

In this chapter a short overview of the characterization methods used in the course of this doctoral thesis is given. This chapter is not meant to give a detailed description of the working principle of each device and method. Instead, a general overview of ferroelectric $Al_{1-x}Sc_xN$ thin film characterization is given with special focus on the faced peculiarities and difficulties.

For recording the $J-E$ as well as the $P-E$ loops (see chapter 2.1) of the ferroelectric capacitors an aixACCT TF Analyzer 2000 with a maximum measurement frequency of 5 kHz as well as an aixACCT TF Analyzer 3000 which a maximum measurement frequency of 100 kHz were used. In general, due to the ferroelectric switching of $Al_{1-x}Sc_xN$ at comparably high electric fields leakage currents are contributing to the ferroelectric displacement currents. To clearly distinguish leakage from ferroelectric switching and thus to gain more insights into the switching process, it is useful to measure at the highest possible frequency. This lowers the current ratio between the frequency (f) independent leakage current and the f dependent ferroelectric displacement current, as the latter is increasing with increasing f. The correction methods DLCC and PUND for subtracting non-hysteretic leakage currents still present at higher f are described in detail in section 2.1 and allow in principle to determine the ferroelectric key properties such as the remanent polarization. However, in $Al_{1-x}Sc_xN$ thin films hysteretic leakage currents are appearing as well upon ferroelectric switching (see chapter 4.5). This currents are f independent and likely related to domain wall conduction upon ferroelectric switching. Thus, although correcting for non-hysteretic leakage using PUND, with decreasing measurement frequency the apparent remanent polarization increases to physically unrealistic values above 10000 $\mu C/cm$ (for 100 nm film thickness below 10 Hz - see chapter 5).

In general, the leakage currents increase with decreasing film thickness. Therefore, especially for the characterization of ultrathin $Al_{1-x}Sc_xN$ films it is helpful to record additionally $\varepsilon-E$ loops (see chapter 2.1 for a detailed description). While the remanent polarization can't be extracted from $\varepsilon-E$ loops, it gives insights into the ferroelectric switching process and allows for an accurate determination of E_c (quasi-DC). In the course of this thesis, a Hewlett Packard 4284 A Precision LCR meter was used, which allows to measure not only the capacitance, but also the electrical losses. The contribution of leakage currents are typically not visible in $\varepsilon-E$ loops. However, artefacts and noise starts to appear if the resistivity approaches 1 kOhm, which is the case for e.g. 4 nm thin $Al_{1-x}Sc_xN$ films at fields close to E_c. A high small signal measurement

frequency (between 100 kHz and 1 MHz) as well as a low small signal field amplitude (100 mV) are beneficial in terms of low noise and the capacitors resistance against electrical breakdown. Furthermore, as the film thickness decreases, the capacitors lateral dimensions were chosen to be close or smaller than 10 x 10 µm^2 to ensure electrical stability at high fields. This allowed to record very clear butterfly-shaped hysteresis loops also for sub-5 nm thin ferroelectric $Al_{1-x}Sc_xN$ films (see chapter 4.5).

Leakage currents were investigated by performing quasi-static $J-E$ measurements using a Keithley 6487 Picoammeter/Voltage Source. Here, similar as when recording $\varepsilon - E$ loops (see chapter 2.1), the field is increased stepwise with a delay of at least 100 ms in between each step. During the delay time the transient currents (e.g. i_c) have time to disappear and afterwards solely the steady-state leakage current is measured. Despite the long sweep time due to the delay, ferroelectric switching peaks were observed also in such quasi-static measurements. Similar as for the $P-E$ measurements at low f (see above), the clear appearance of switching peaks and the associated unrealistic high P_r values are likely related to domain wall conduction upon ferroelectric switching. This is supported by leakage current measurements with fields up to a maximum of $E_c/2$ (minor loops - without contributions from ferrolectric switching) in dependence of the prior polarization state of the films (see chapter 5). A high resistance state (HRS) is observed in the fully N-polar film (zero domain walls). Upon partially switching of the polarization, this transforms gradually (several intermediate conduction states corresponding to the respective domain wall densities) into a low resistance state (highest domain wall density). Further partial switching towards M-polarity results in an analog-like increase of resistivity until reaching the HRS again.

Structurally, the sputtered $Al_{1-x}Sc_xN$ thin films as well as the electrode materials are polycrystalline, yet they grow typically with preferred orientation, i.e. they are textured - see Fig. 3.2. To which crystallographic direction with respect to the substrates normal and to what extend the grains are aligned, is typically investigated by performing XRD measurements. In the course of this thesis, a Rigaku SmartLab diffractometer (9 kW, CuKα = 1.5406 Å, Hypix detector) as well as a Seifert XRD 3000 PTS using a monochromatic Kα radiation was used. By performing $\theta 2\theta$ and ω scans the out-of-plane texture of the respective films can be investigated. For out-of-plane ferroelectricity, i.e. applying the electric field along the growth direction, an 0002 oriented growth of the $Al_{1-x}Sc_xN$ thin films is required (c-plane oriented). The out-of-plane mosaicity, meaning the degree of tilt of the individually c-axes aligned columnar grains (see Fig. 3.2a), was investigated by performing rocking curve measurements (ω scans) of the 0002 reflection. The corresponding full-width at half-maximum (FWHM) was in between $\approx$ 0.3 (for epitaxially grown films) and 4° (for films grown using silicon substrates).

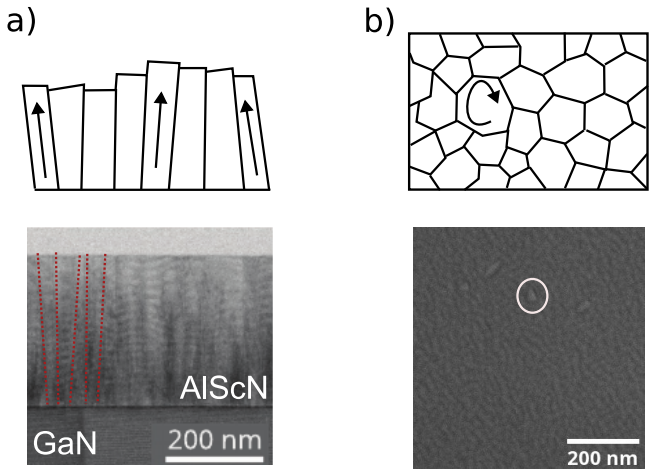

Figure 3.2: a) Sketched cross-section of columnar grains (top) - the crystallographic orientation of the individual grains is indicated by the arrows. Scanning transmission electron microscopy cross-section of 300 nm thin $Al_{0.72}Sc_{0.28}N$ grown on GaN (bottom) - the columnar grains are highlighted by dotted lines. b) Sketched topography of columnar grains (top) and their potential individual in-plane rotation as indicated by the arrow. Scanning electron microscope image of the surface of a 300 nm thin $Al_{0.72}Sc_{0.28}N$ film grown on GaN (bottom) revealing the grain structure as well as the occurrence of abnormally oriented grains (white circle). Adapted from [SPI+22] John Wiley & Sons. © 2022 The Authors. Advanced Functional Materials published by Wiley-VCH GmbH.

The in-plane mosaicity of the *c*-axes oriented $Al_{1-x}Sc_xN$ thin films was investigated by performing ϕ-scans of an in-plane reflection. For epitaxially grown films, six reflections corresponding to a six-fold symmetry are evident, meaning that the grains are in-plane oriented with respect to each other. The FWHM of such a reflection represents the degree of in-plane tilt between the individual columnar grains (see Fig. 3.2b). Contrarily, the grains of non-epitaxially grown films are randomly in-plane oriented, resulting in a constant signal while measuring an in-plane ϕ-scan.

The averaged lattice-parameters of the thin films were determined by in-plane as well as out-of-plane XRD scans. In the case of out-of-plane scans, for in-house sputtered $Al_{1-x}Sc_xN$ thin films with highest crystalline quality, reasonable signals were obtained down to $\approx$ 10 nm film thickness using a 9 kW radiation source. The in-plane scans, in which the beam hits the films surface at a very low angle, allow in principle to determine the in-plane lattice-parameter also of ultrathin films below 10 nm film thickness as well as they allow to obtain depth-dependent information by varying the incident angle. However, surface effects such as oxidation can have an impact on the surface near lattice-parameters which may differ from the bulk lattice parameter of the film. Further structural characterization was performed by recording reciprocal space maps and pole

figures. This allows the determination of all lattice-parameters, as well as it gives insights into the strain state and the in-plane relationship of the film with respect to the template in the case of epitaxial growth.

X-ray reflectometry (XRR) measurements allow in principle to determine the exact thickness of a thin film and were carried out to determine the thickness of the Pt electrode. However, the determination of the $Al_{1-x}Sc_xN$ thin film thickness using XRR is challenging. Films which were not capped in-situ are prone to oxidation, which may alters the total thickness especially of ultrathin films and complicates the spectra due to the presence of the signal from the oxidation layer. An in-situ capping with e.g. Pt right after the $Al_{1-x}Sc_xN$ deposition prevents oxidation, but comes with the downside of introducing a new material which is reflected in the spectra. In the case of Pt, the signal is much higher compared to the $Al_{1-x}Sc_xN$ signal and complicates the separation from it.

The microstructure and topography of the $Al_{1-x}Sc_xN$ layer was investigated using a scanning electron microscope (SEM, Zeiss GeminiSEM). This allows to estimate the grain size as well as to identify non-oriented protruding grains which are often called abnormally oriented grains (AOG) in literature - see Fig. 3.2b.[SPM+18] Additionally, the scandium concentration was determined by SEM energy dispersive X-ray spectroscopy (EDS, Oxford x-act). Interestingly, while determining the Sc concentration of $Al_{1-x}Sc_xN$ thin films grown directly on n-doped GaN, a charging of the surface was observed. This in turn led to a scattering of the electron beam towards the sample holder. In our case the sample holder is made up of Al and contributed therefore to the measured overall Al signal. Thus, the measured Sc content relative to Al was not reflecting the Sc concentration of the $Al_{1-x}Sc_xN$ thin film. This effect was prevented by capping the sample with a conductive metal such as Cu or Au and by tilting the sample further towards the EDS detector.

Transmission electron microscopy (TEM) is a sophisticated and diverse method to explore thin films down to the atomic level. In the course of this thesis, a Tecnai F30 typically operated in high-resolution mode (HRTEM) and lately also a JEOL (JEM200F) NEOARM typically operated in scanning mode (STEM) was used. Both devices were used to investigate the grain-like growth of sputtered $Al_{1-x}Sc_xN$ (see Fig.3.2a), the interface roughness, the may occurrence of Sc segregation (which in our case was never observed), the local crystallographic properties such as lattice-parameters as well as the elemental distribution using EDS. TEM appeared also to be an adequate technique to determine the exact thickness especially of ultrathin films ($<$ 10 nm thickness). Epitaxial strain could be determined locally by recording scanning nano-beam diffraction maps revealing the in-plane and out-of-plane strain propagation

in thickness direction (see chapter 4.1). Furthermore, the high crystal quality of epitaxial $Al_{1-x}Sc_xN$ thin films allowed to visualize the projection of the atoms in depth direction of the investigated cross-sections. This approach combined with the capabilities of the NEOARM STEM operated by dedicated experts enabled to determine the polarity as well as to identify and investigate for the first time polarization domains and their role in ferroelectric switching of $Al_{1-x}Sc_xN$.

Chapter 4

Publications

Ferroelectricity in $Al_{1-x}Sc_xN$ was discovered one year before the beginning of this doctoral thesis in 2020. Thus, at that time, there was not much knowledge on the thickness scalability, the appearing leakage currents at high electric fields, the temperature stability as well as the compatibility to other electrode materials than Mo and Pt available. However, all of these characteristics and properties are essential not only to gain a fundamental understanding of the material and its polarization inversion process but also to identify possible applications in terms of devices. A high cell density and a low power operation in competitive non-volatile memory or neuromorphic devices require low film thicknesses to reduce the operating voltage as well as small lateral dimensions. This fact is especially true considering the integration into Si-based advanced integrated circuits (ICs), where the switching voltage should match the on-chip voltage supply of about 1 V. On the other hand, the structural compatibility of $Al_{1-x}Sc_xN$ to III-N technology promises the integration of ferroelectric functionality into all-wurtzite-type III-N devices such as HEMTs. The five own publications included below address many of these aspects and reflect the most significant studies which were carried out during this doctoral thesis. In the following, a short summary of these publications and their relevance with respect to potential devices is given.

In the first publication, the feasibility of epitaxial growth of ferroelectric $Al_{1-x}Sc_xN$ in general as well as the integration onto the structurally compatible GaN/Sapphire templates was investigated. This not only resulted in the first demonstration of ferroelectric switching in sputtered-deposited $Al_{1-x}Sc_xN$ grown on n-doped GaN but also allowed to investigate the impact of epitaxy and structural quality on the electrical properties. Interestingly and contrary to classical ferroelectrics, the leakage current, the coercive field and the remanent polarization is similar as for non-epitaxially grown films. However, a thickness and Sc content dependent epitaxial strain was identified, allowing to investigate the impact of epitaxial in-plane strain on the coercive field. Furthermore,

the formation of a depletion region in the semiconducting GaN was linked to the peculiarities observed in the electrical response in the form of ferroelectric displacement current peak splitting and broadening at negative electric fields. Furthermore, the as-deposited polarity of $Al_{1-x}Sc_xN$ was determined to be pinned to the metal (M)-polarity of the underlying GaN template with a subsequent transition to nitrogen (N)-polarity (> 30 nm in growth direction). The polarity determines the polarization discontinuity and thus the functionality of III-N heterostructures, which can in principle be tuned by ferroelectric switching. On the other hand, the polarity is also of concern in terms of industrial integration, as wet-etching is highly selective to the polarity in $Al_{1-x}Sc_xN$.

In the second publication, epitaxial Pt was introduced as an intermediate layer into the $Al_{1-x}Sc_xN$ /GaN heterostructures. This resulted in an epitaxial growth of $Al_{1-x}Sc_xN$ while suppressing epitaxial strain, in a reduction of the leakage currents as well as in a fully N-polar as-deposited state. Furthermore, in comparison to $Al_{1-x}Sc_xN$ grown directly onto GaN, uniform ferroelectric displacement current peaks appeared due to the metallic nature of the bottom electrode. Detailed structural characterizations were performed revealing improvements in surface roughness and crystal quality when decreasing the epitaxial Pt film thickness. Furthermore, a correlation between these properties and the leakage currents appearing in the ferroelectric layer was identified. A comparison to Pt grown non-epitaxially on SiO_2/Si templates was performed, revealing opposite trends due to the different growth mode.

In the third publication ferroelectric switching in MOCVD-grown $Al_{0.85}Sc_{0.15}N$ is demonstrated and studied for the first time. The feasibility of growing ferroelectric $Al_{1-x}Sc_xN$ via MOCVD represents a big step towards its integration into III-N technology, as MOCVD is the standard growth method for III-N heterostructures. The single crystalline nature of the film and the high interface quality promises to use $Al_{1-x}Sc_xN$ not only to act as a functional layer due to ferroelectricity, but also to act directly as barrier layer required e.g. for building up a 2DEG in HEMTs. Additionally, the single crystal quality allowed for sophisticated STEM investigations which revealed the large-scale polarization domain pattern in $Al_{1-x}Sc_xN$. Electrically the films exhibit a wake-up like behaviour in the form of huge hysteretic currents appearing in the first cycles, which is likely related to the observed inclined (and thus in principle conductive) domain walls. After initial cycling, the electrical response including leakage currents, coercive field and remanent polarization is comparable to sputter-deposited as well as via molecular beam epitaxy (MBE) grown ferroelectric $Al_{1-x}Sc_xN$. Similar as for the study on sputter-deposited $Al_{1-x}Sc_xN$ on GaN, the as-deposited polarity is pinned to the M-polarity of the underlying GaN. Furthermore, this pinning resulted in a non-switching M-polar volume fraction close to the GaN interface and is focus of

ongoing studies. To summarize, the first three publications form a comprehensive base for the integration of ferroelectric $Al_{1-x}Sc_xN$ into III-N-based devices as well as they address fundamental questions related to the ferroelectric switching phenomena in the wurtzite-type materials.

The last two publications address the thickness scalability of ferroelectric $Al_{1-x}Sc_xN$. Firstly, due to the much better texture and lower interface roughness, epitaxial $Al_{0.72}Sc_{0.28}N$ grown on epi-ready Pt/GaN/Sapphire templates was considered to be superior to ultrathin $Al_{0.72}Sc_{0.28}N$ films grown non-epitaxially on $Pt/SiO_2/Si$ templates in terms of thickness scalability. Thus, in the fourth publication, ferroelectricity in epitaxial $Al_{0.72}Sc_{0.28}N$ down to 10 nm film thickness is demonstrated and surprisingly only a minor dependence of the coercive field on the film thickness was identified. This behaviour is discussed in detail and compared to classical models which predict a strong thickness dependence. Later, it was recognized that the epitaxial growth using sapphire substrates results in higher coercive fields compared to films grown using silicon substrates due to an unfavourable thermal expansion coefficient mismatch. Thus, despite the comparably lower crystal quality and interface roughness when using Si substrates, the higher coercive field to breakdown field ratio allowed for clear ferroelectric switching of 4 nm thin non-epitaxially grown $Al_{0.74}Sc_{0.26}N$ films, which is studied in detail in the fifth publication. Interestingly, the coercive field decreased below 10 nm film thickness and allowed for polarization switching at voltages as low as 1 V, which is already in the range of the on-chip voltage supply of advanced ICs. Furthermore, stable partial switching of volumes as low as 5 x 5 x 5 nm^3 is resolved atomically via STEM. The in this context visualized inclined (significant horizontal component) domain wall hints towards the appearance of domain wall conduction in ferroelectric $Al_{1-x}Sc_xN$, which is supported by electrical measurements. In terms of future devices, the results of the last two publications demonstrate the excellent thickness scalability and potential multi-level operation of ultralow volumes as well as the compatibility to advanced ICs. Furthermore, the suggested domain wall conduction in $Al_{1-x}Sc_xN$ paves the way towards memristive devices suitable for memory as well as for neuromorphic applications.

4.1 From Fully Strained to Relaxed: Epitaxial Ferroelectric $Al_{1-x}Sc_xN$ for III-N Technology

Own contributions

- Design of Experiment
- Data analysis & interpretation
- Sample fabrication
- Electrical characterization
- Etching experiments
- SEM investigations
- Structural characterization (partly)
- Manuscript preparation

RESEARCH ARTICLE

ADVANCED FUNCTIONAL MATERIALS
www.afm-journal.de

From Fully Strained to Relaxed: Epitaxial Ferroelectric $Al_{1-x}Sc_xN$ for III-N Technology

Georg Schönweger, Adrian Petraru, Md Redwanul Islam, Niklas Wolff, Benedikt Haas, Adnan Hammud, Christoph Koch, Lorenz Kienle, Hermann Kohlstedt, and Simon Fichtner**

The recent emergence of wurtzite-type nitride ferroelectrics such as $Al_{1-x}Sc_xN$ has paved the way for the introduction of all-epitaxial, all-wurtzite-type ferroelectric III-N semiconductor heterostructures. This paper presents the first in-depth structural and electrical characterization of such an epitaxial heterostructure by investigating sputter deposited $Al_{1-x}Sc_xN$ solid solutions with x between 0.19 and 0.28 grown over doped n-GaN. The results of detailed structural investigations on the strain state and the initial unit-cell polarity with the peculiarities observed in the ferroelectric response are correlated. Among these, a Sc-content dependent splitting of the ferroelectric displacement current into separate peaks, which can be correlated with the presence of multiple strain states in the $Al_{1-x}Sc_xN$ films is discussed. Unlike in previously reported studies on ferroelectric $Al_{1-x}Sc_xN$, all films thicker than 30 nm grown on the metal (M)-polar GaN template feature an initial multidomain state. The results support that regions with opposed polarities in as-grown films do not result as a direct consequence of the in-plane strain distribution, but are rather mediated by the competition between M-polar epitaxial growth on an M-polar template and a deposition process that favors nitrogen (N)-polar growth.

1. Introduction

Wide and tunable bandgaps, high electron mobility, good breakdown resistance, high thermal stability as well as advanced epitaxial deposition techniques have made the III-N compounds and their heterostructures one of the most successful semiconductor classes.[1] Commercial applications are wide ranging from radio frequency (RF) and power electronics to light emitting diodes (LEDs).[2–4] Current research focuses on extending these applications—next to the trend to expand beyond what are mainly discrete devices to fully integrated III-N solutions, either by integrating, e.g., GaN on CMOS or by developing fully GaN-based complementary circuits.[5–7] As the base technology has thus reached a high maturity, further innovation will require the integration of new compounds with increased functionality. Due to the predominance of the wurtzite-type structure in III-N compounds, its inherent spontaneous polarization is a crucial factor for core applications such as high electron mobility transistors (HEMTs) or LEDs.[8,9] Consequently, increased flexibility or even reconfigurability of the polarization direction will enable powerful new approaches for the continued development of III-N technology. This reconfigurability can readily be obtained through ferroelectricity, which becomes accessible since the formation of III-N based solid solutions such as $Al_{1-x}Sc_xN$ lead to a flattening of the wurtzite-type energy landscape.[10,11] Structurally, this increases the a/c-lattice parameter ratio as well as the internal parameter u (the distance from a metal to a nitrogen atom relative to the c-lattice parameter). Energetically, it will result in a lowering of the energy barrier between the two stable polarization states (metal (M)- and nitrogen (N)-polar, see **Figure 1**), until ferroelectric switching becomes possible by locally transitioning through the intermediate layered hexagonal structure.

G. Schönweger, A. Petraru, H. Kohlstedt
Institute of Electrical and Information Engineering
Kiel University
Kaiserstr. 2, D-24143 Kiel, Germany
E-mail: gmsc@tf.uni-kiel.de

The ORCID identification number(s) for the author(s) of this article can be found under https://doi.org/10.1002/adfm.202109632.

DOI: 10.1002/adfm.202109632

M. R. Islam, N. Wolff, L. Kienle, S. Fichtner
Institute for Material Science
Kiel University
Kaiserstr. 2, D-24143 Kiel, Germany
E-mail: simon.fichtner@isit.fraunhofer.de

B. Haas, C. Koch
Institute of Physics & IRIS Adlershof
Humboldt-Universität zu Berlin
Newtonstr. 15, D-12489 Berlin, Germany

A. Hammud
Department of Inorganic Chemistry
Fritz-Haber Institute of the Max-Planck Society
Faradayweg 4-6, D-14195 Berlin, Germany

S. Fichtner
Fraunhofer Institute for Silicon Technology (ISIT)
Fraunhoferstr. 1, D-25524 Itzehoe, Germany

ADVANCED SCIENCE NEWS
www.advancedsciencenews.com

ADVANCED FUNCTIONAL MATERIALS
www.afm-journal.de

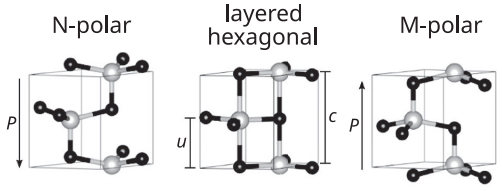

Figure 1. The two stable polarization (*P*) states in ferroelectric $Al_{1-x}Sc_xN$ and the intermediate layered hexagonal structure. Black dots depict nitrogen atoms, grey dots depict Al/Sc atoms.

Therefore, with the advent of wurtzite-type ferroelectrics such as $Al_{1-x}Sc_xN$ and $Al_{1-x}B_xN$ a clear pathway toward a tunable polarization in chemically and structurally matched III-N based material systems has emerged.[12,13] The key toward realizing such all-epitaxial, all-wurtzite-type ferroelectric/semiconductor heterostructures is in the thorough understanding of their structural as well as electrical properties to allow their knowledge driven engineering. Here, we present a detailed study of these properties for $Al_{1-x}Sc_xN$ films with Sc contents of 19, 24, and 28 at% relative to the total amount of metal atoms ($x = 0.19$, 0.24, 0.28) deposited by sputter epitaxy on doped n-GaN/sapphire substrates. In addition to the recently demonstrated ferroelectric switching of epitaxial $Al_{1-x}Sc_xN$ deposited on GaN by molecular beam epitaxy,[14] our study reveals that the interplay between the growth template and the structural properties of the film can lead to previously unknown peculiarities in the ferroelectric response of the $Al_{1-x}Sc_xN$ film which will play a crucial role in understanding the behavior of the spontaneous polarization in epitaxial wurtzite-type ferroelectric/semiconductor heterostructures.

This paper is structured into three sections, starting with a detailed structural characterization of our films using sophisticated techniques of X-ray diffraction (XRD) and dedicated scanning transmission electron microscopy (STEM), followed by the characterization of the ferroelectric response and finally an in-depth analysis of the initial polarization domain state of the samples.

The first section includes reciprocal space mappings (RSM) to confirm phase purity and epitaxial relationships, (a)symmetric XRD scans to deduce the $Al_{1-x}Sc_xN$ lattice parameters in dependence of Sc content and films thickness as well as complementary scanning nano-beam electron diffraction (NBED) maps of the strain distribution to illustrate the evolution of film strain at close to nm-resolution. Section 2 details the overall ferroelectric response of the films via polarization/displacement-current measurements in dependence on the electric field. Measurements are compared for the three different Sc contents and film thicknesses between 30 and 300 nm. The results are discussed on the basis of the microstructure as presented in Section 1. Finally, the as-deposited polarity of the $Al_{1-x}Sc_xN$ films is revealed to be strongly influenced by the interplay between the M-polar GaN template and a deposition process promoting N-polar films. The existence of horizontal inversion domain boundaries in $Al_{0.72}Sc_{0.28}N$ films with thicknesses above 30–40 nm is suggested by unipolar ferroelectric switching experiments and is supported by atomically resolved STEM to image the structure polarity in as-deposited, vertically separated regions of the film as well as by etching experiments.

2. Structural Characterization

Complementary structural characterization methods were employed to elucidate whether and to what degree the deposited $Al_{1-x}Sc_xN$ films are grown epitaxially on GaN templates and to what extent the GaN interface influences the local and average strain and orientation of the thin film—which could ultimately have a significant impact on the ferroelectric properties of the film. To investigate the quality of epitaxial growth, wide-range RSM of $Al_{1-x}Sc_xN/GaN/Al_2O_3$ heterostructures have been recorded on a laboratory-based diffractometer. $Al_{0.72}Sc_{0.28}N$ films with thicknesses ranging from 10 up to 300 nm as well as 100 nm thick $Al_{1-x}Sc_xN$ films with Sc contents of 19 and 24 at% were analyzed to understand the in-plane epitaxial strain distribution, whose analysis is complemented by scanning NBED derived strain maps of the 300 nm thick $Al_{0.72}Sc_{0.28}N$ film.

RSM provide a 2-dimensional representation of the *k*-space revealing the crystallographic relations of the $Al_{1-x}Sc_xN$ films to those of the underlying buffer layer and substrate. A wide-range RSM of a 300 nm thick $Al_{0.72}Sc_{0.28}N$ film, representative for our heterostructures, is shown in **Figure 2**.

All present reflections were identified and attributed to the $Al_{0.72}Sc_{0.28}N$ thin film (marked in yellow), the GaN buffer layer (marked in black), and the Al_2O_3 substrate (marked in red). Thus, we identify one crystallographic phase in our $Al_{1-x}Sc_xN$ films, which is the polar wurtzite-type phase (space group 186, $P6_3mc$) responsible for the ferroelectricity of the material. The films have been grown epitaxially on the underlying 4 µm thick doped n-GaN template, with no significant contribution from randomly oriented volume. They have thus the same crystallographic orientation as the GaN films, with the *c*-axis pointing out-of-plane and parallel hexagonal (0001) basal planes.

The in-plane epitaxial relationship between Al_2O_3, GaN, and $Al_{0.72}Sc_{0.28}N$ is also revealed by the pole figure measurement presented in **Figure 3**, showing almost coinciding 01–13 reflection intensities.

Thus, the epitaxial relationship between film and template is as expected: [1-100](0001)$Al_{1-x}Sc_xN$ ‖ [1-100](0001)GaN. The in-plane relation of the lattice orientation of GaN and sapphire is [1–100](0001)GaN ‖ [11–20](0001)Al_2O_3, meaning a 30° in-plane rotation of the GaN with respect to the Al_2O_3, as visible in the pole figure and reported also in literature.[15] In addition to the low resolution wide-range RSM, high-resolution data was obtained to determine the lattice parameters of the films more accurately and draw conclusions on their strain state. The *c*-lattice parameter of the $Al_{1-x}Sc_xN$ films could be obtained for film thicknesses down to 20 nm from the high-resolution specular scans using a two-bounce monochromator. For *a*-lattice parameter determination down to 30 nm film thickness, high-resolution asymmetric scans of non-specular 10–15, as well as –1013 reflections, were recorded. The in-plane rotation of the columnar grains with respect to each other was analyzed by high-resolution in-plane rocking curve (RC) scans using a two-bounce monochromator. We would like to mention here that the symmetric and asymmetric scans represent an average over the whole film thickness. Thus, the obtained lattice-parameters for films with epitaxially strained- as well as relaxed regions reflect an average of the present strain states. The in-plane RC measurements were performed at an incidence angle of about

ADVANCED SCIENCE NEWS
www.advancedsciencenews.com

ADVANCED FUNCTIONAL MATERIALS
www.afm-journal.de

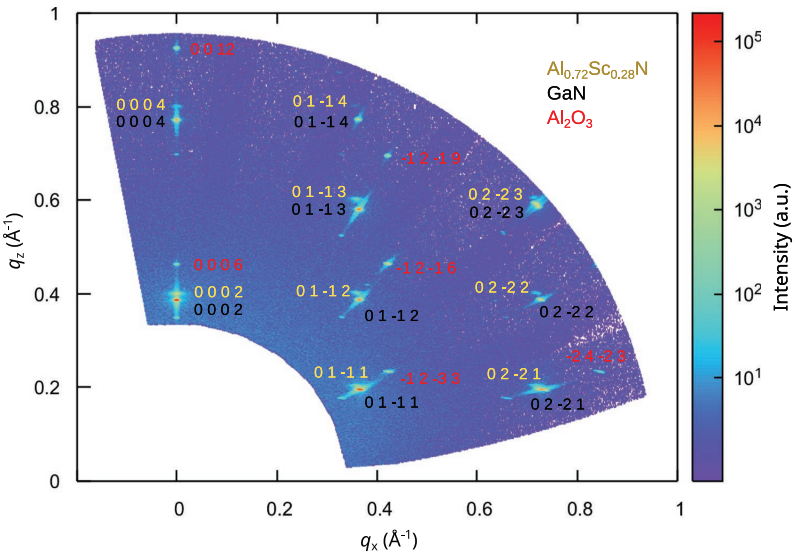

Figure 2. Wide-range RSM of the $Al_{0.72}Sc_{0.28}N$ (300 nm)/n-GaN/Al_2O_3(substrate) heterostructures. The intensities corresponding to Al_2O_3, GaN, and $Al_{0.72}Sc_{0.28}N$ are denoted respectively in red, black, and yellow. All non-labeled spots correspond to Cu K-beta (k_b) reflections.

0.3°, making them surface sensitive. Therefore, in this particular case, only a thin, surface near region was analyzed.

In **Figure 4**a, the evolution of the *a*-lattice parameter of 100 nm thick $Al_{1-x}Sc_xN$ is depicted for different Sc concentrations. With decreasing Sc content, the *a*-lattice parameter of $Al_{1-x}Sc_xN$ is decreasing and approaches the *a*-lattice parameter of GaN at 19 at% Sc. This decrease of the *a*-lattice parameter is expected due to the difference in preferred coordination and atomic radii between Al and Sc atoms, which is known to lead to a diminution of the wurtzite basal plane.[10,11] For epitaxial systems, a smaller *a*-lattice misfit between the film and the substrate leads to a higher critical thickness, meaning the transition from a fully strained epitaxial to a relaxed film shifts to a higher thickness. Thus, when decreasing the Sc content starting from 28 at%, the critical thickness is expected to increase until being infinite at 18 at% Sc due to lattice-matching with the GaN.[16] Hence, for a 100 nm thick film at 19 at% Sc, a uniform lattice without a significant strain gradient is expected. To study the in-plane strain state of the nearly lattice-matched film in more detail, a high-resolution RSM of the 10–15 reflections was recorded for 100 nm thick $Al_{0.81}Sc_{0.19}N$, as shown in Figure 4b. Both the 10–15 $Al_{0.81}Sc_{0.19}N$ and the 10–15 GaN reflections are distributed almost congruently on (q_x/q_z) space with their maxima located at identical q_x position, which also confirms that the $Al_{0.81}Sc_{0.19}N$ is in-plane lattice-matched to the GaN template.

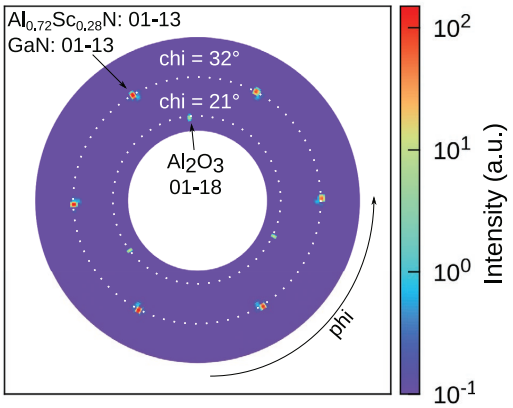

Figure 3. Pole figure of the 01–13 reflections from $Al_{0.72}Sc_{0.28}N$ (300 nm)/n-GaN/Al_2O_3(substrate) heterostructures.

A minor increase in the *c*-lattice parameter is observed while increasing the Sc content, as illustrated in Figure 4a. In relaxed films deposited on Si, an increase of the *c*-lattice parameter with lower Sc concentration was observed.[17] In the present case, the *c*-lattice parameter changes also due to elastic deformation of the unit cell imposed by the epitaxial strain which superimposes the change of the *c*-lattice parameter due to Sc variation.

Structural analysis of a thickness series of non-lattice-matched $Al_{0.72}Sc_{0.28}N$ films allows us to understand the strain relaxation in more detail. In this context, Figure 4c illustrates the *a*- and *c*-lattice parameter variation in dependence of the $Al_{0.72}Sc_{0.28}N$ film thickness. When reducing the film thickness, the *a*-lattice parameter is observed to be decreased until being close to be lattice-matched with the in-plane lattice of the GaN template. Thus, below ≈50 nm, $Al_{0.72}Sc_{0.28}N$ films appear to be fully strained to the GaN template. Between 40 and 100 nm, a steep increase of *a*-lattice parameter is observed, followed by a more constant plateau above 100 nm film thickness. Therefore, in-plane lattice relaxation occurs within a thickness range between 40 nm and 100 nm for 28 at% Sc. Using an energy

ADVANCED SCIENCE NEWS
www.advancedsciencenews.com

ADVANCED FUNCTIONAL MATERIALS
www.afm-journal.de

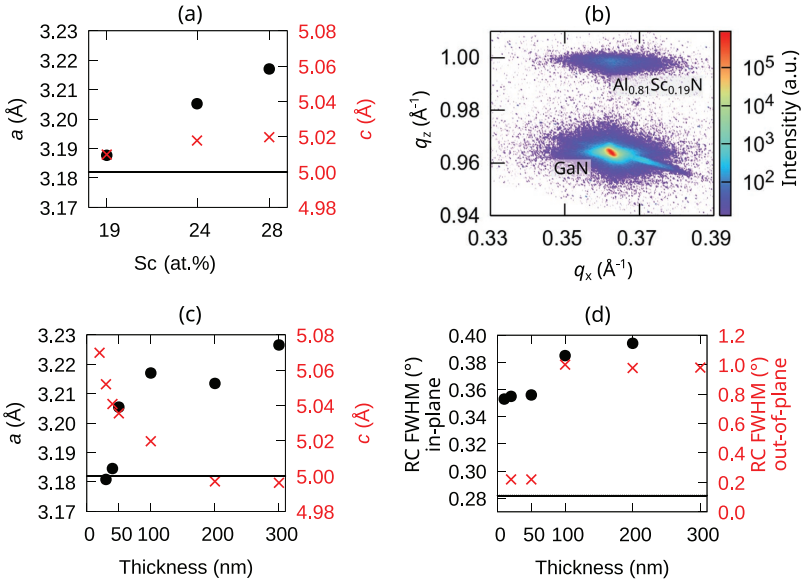

Figure 4. a) Evolution of *a*- and *c*-lattice parameters of 100 nm thick $Al_{1-x}Sc_xN$ in dependence of Sc content. b) High-resolution reciprocal space mapping of $Al_{0.81}Sc_{0.19}N$ 10-15 reflection. c) *a*- (black) and *c*-lattice parameter (red) of $Al_{0.72}Sc_{0.28}N$ films in dependence of film thickness. d) The corresponding FWHM of the 0002 RC (out-of-plane) and FWHM of the 10–10 RC (in-plane). For comparison the measured *a*-lattice parameter, as well as the measured FWHM of the 10–10 RC (in-plane) of the GaN, is illustrated as a solid black line in (a), (c), and (d), respectively. For lattice parameter determination we estimate an error of 1 pm.

balance model, the critical thickness for $Al_{1-x}Sc_xN$/GaN heterostructures was previously calculated to be ≈70 nm for 28 at% Sc.[16] Considering an estimated error for Scandium concentration determination in our films of 2 at%, this is in good agreement with the experimentally found critical thickness of ≈40 nm. By plotting the full-width at half maximum (FWHM) of the in-plane and out-of-plane rocking curves over the film thickness, as depicted in Figure 4d, a clear step is observed between 50 and 100 nm, thus providing yet more support that the transition from a fully strained to a partially relaxed lattice occurs at around 50 nm film thickness. At this particular thickness, the FWHMs of the rocking curves measured for in- and out-of-plane configurations change by 10% and 400%, respectively. Hence, a fully strained thin film below this transition regime exhibits an improved in-plane and out-of-plane alignment (tilt) of its nanoscale columnar grains. Noticeably, the in-plane mosaicity of our sputtered films is comparable to the GaN template itself with its in-plane FWHM of the rocking curve of 0.28°.

To complement the XRD measurements, we employed STEM imaging in combination with scanning NBED to resolve the local strain evolution with close to nm resolution on a 300 nm thick $Al_{0.72}Sc_{0.28}N$ film. STEM and electron diffraction (not shown) investigations confirm the results obtained by XRD on the epitaxial growth of the $Al_{1-x}Sc_xN$ films. As has to be expected from a sputtered film deposited at comparably low temperatures, the films do not form a single crystal but rather adjacent columnar grains with diameters in the range of < 10 nm in the nucleation zone expanding to about 20 nm at the top of the film (see **Figure 5**a). Despite epitaxial growth conditions providing a rigid in-plane orientation with sixfold symmetry, STEM imaging reveals that the individual columnar grains are presumably randomly in-plane rotated with respect to each other by about 20–30 mrad—as it is also apparent through the finite mosaicity of the films depicted in Figure 4d.

The powerful combination of STEM providing atomic resolution information and scanning NBED offering precise structural information was applied to the material system. From the nano-beam diffraction data, both in-plane (ε_{xx}) and out-of-plane (ε_{zz}) components of the strain matrix were calculated to determine the internal strain distribution from the interface toward the surface, including the related critical thickness for the film to relax from its fully strained state.

A cross-sectional view onto the $Al_{0.72}Sc_{0.28}N$(300 nm)/n-GaN layer structure is displayed in the annular bright-field (ABF) STEM image of Figure 5a and shows the aforementioned columnar character of the $Al_{0.72}Sc_{0.28}N$ film and extended vertical defects within the GaN buffer layer, which likely originate from the heavy doping of the n-GaN or its growth conditions on the sapphire substrate. The GaN polarity was determined to be M-polar at all examined positions left, right and in between the defects as indicated in the inset showing a high-resolution ABF STEM micrograph of the atomic structure of GaN.

Figure 5b displays a virtual dark-field (VDF) image of the scanning NBED experiment and the corresponding quantified strain maps and averaged profiles of the in-plane and out-of-plane components, both showing the local strain distribution

ADVANCED SCIENCE NEWS
www.advancedsciencenews.com

ADVANCED FUNCTIONAL MATERIALS
www.afm-journal.de

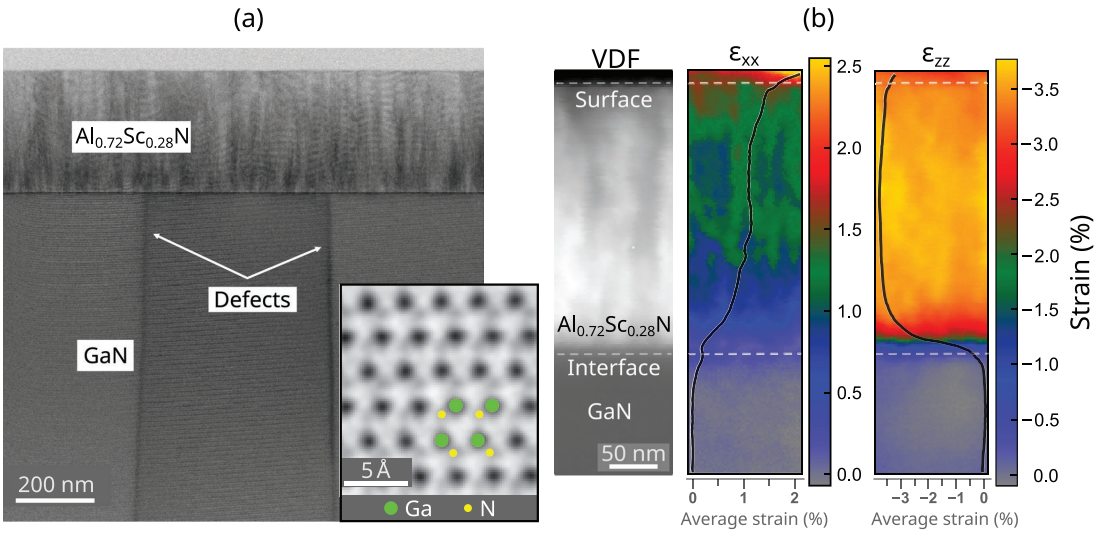

Figure 5. a) ABF STEM overview image of the $Al_{0.72}Sc_{0.28}N$/n-GaN layers showing the columnar grain structure within the $Al_{0.72}Sc_{0.28}N$ film and extended defects in the GaN single crystalline template. The inset shows an atomic resolution ABF STEM image of GaN and verifies its M-polar orientation (green: Ga atoms, yellow: N atoms). b) Virtual dark-field (VDF) image of the scanning NBED experiment and strain maps of the ε_{xx} and ε_{zz} strain components calculated in reference to the GaN template for the $Al_{0.72}Sc_{0.28}N$ film.

probed across the entire 300 nm $Al_{0.72}Sc_{0.28}N$ film in reference to the GaN buffer layer. The experimental resolution of about 5 nm limited the accuracy in determining the position of the interface to ±5 nm which was placed at the onset of rising material contrast in the VDF image. The in-plane strain component was calculated from the array of [11–20] diffraction patterns describing the distance between the (01–10) planes. From the bulk of the GaN (zero strain, reference), the strain value is observed to monotonously increase when approaching the interface, forming a small plateau of ≈0.2% strain. On the $Al_{0.72}Sc_{0.28}N$ side of the interface, the in-plane strain distribution forms a plateau within the first ≈30 nm with an average of 0.2% strain. With increasing thickness, the average strain distribution continues to increase slowly over a range of ≈80 nm up to 1.2%, where a second plateau starts to appear up to a thickness of ≈250 nm. This plateau at 1.2% strain corresponds to an *a*-lattice parameter of 3.22 Å (considering the measured *a*-lattice parameter of the GaN bulk corresponding to zero strain), which is in good agreement with the measured *a*-lattice parameter of 3.23 Å for 300 nm thick $Al_{0.72}Sc_{0.28}N$ via asymmetric XRD scans, whereas the latter represents an *a*-lattice parameter averaged over the whole thickness. Further relaxation to a value of 1.5% strain takes place within a range of ≈50 nm below the surface. Even higher values of strain beyond the surface are regarded as artifacts. The observed slow strain relaxation behavior of the in-plane lattice is in strong contrast to the rapid relaxation of the non-clamped *c*-lattice parameter, which tends to be fully relaxed after the first ≈50 nm from the interface.

In summary, all our $Al_{1-x}Sc_xN$ films can be expected to contain a fully strained region close to their n-GaN interface (Figure 5). The extent of this fully strained region is expected to decrease with increasing film thickness—so that for 300 nm it is considerably lower than the critical thickness of ≈40 nm which was determined via XRD measurements. The latter also reveals that films thinner than ≈40 nm are fully strained to the GaN substrate over their entire thickness.

3. Electrical Characterization

The foremost goal of the electrical characterization of our samples was to determine if they are ferroelectric and how their ferroelectricity compares to those films deposited on the common polycrystalline metal interfaces.[12,17] Displacement current density measurements in dependence of the electric field (*J–E* measurements) are at the core of ferroelectric characterization and were performed on capacitors with different $Al_{0.72}Sc_{0.28}N$ film thicknesses as well as different Sc concentrations with a constant thickness of 100 nm. If not stated otherwise, the contacted pad size was 50 × 50 µm^2 and the measurement frequency 1.5 kHz.

Figure 6a shows *J–E* and polarization over the electric field (*P–E*) loops to demonstrate clear ferroelectric switching for a 300 nm thick epitaxial $Al_{0.72}Sc_{0.28}N$ film deposited on doped n-GaN.

Additionally, ferroelectric switching is confirmed by strain over electric field measurements depicted in Figure 6b as well as capacitance over electric field measurements depicted in Figure S1 (Supporting Information). Leakage currents start to appear around E_c, similar to what is seen for highly textured non-epitaxial films on Pt/Si.[17] To separate leakage from switching current, we make use of dynamic leakage current compensation (DLCC).[18] Especially in thin $Al_{1-x}Sc_xN$ films, the

ADVANCED SCIENCE NEWS
www.advancedsciencenews.com

ADVANCED FUNCTIONAL MATERIALS
www.afm-journal.de

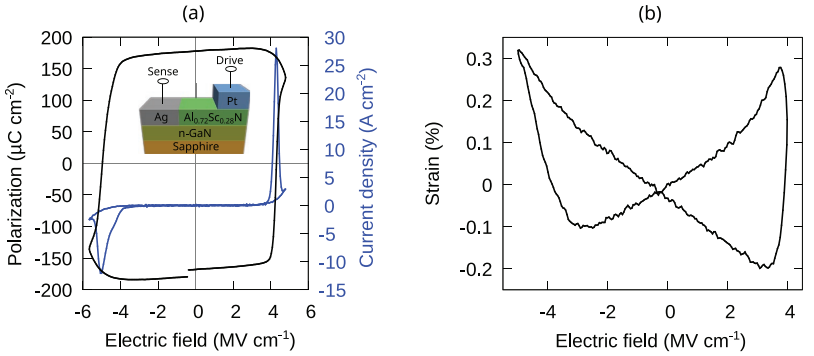

Figure 6. a) *J–E* and *P–E* loop for 300 nm thick $Al_{0.72}Sc_{0.28}N$ on n-GaN measured on a 100 × 100 μm² pad. The inset shows the layer structure and the electrical connections. b) Strain response in dependence of the applied electric field of 200 nm thick $Al_{0.72}Sc_{0.28}N$ on n-GaN measured at 711 Hz.

leakage currents for switching cycles are higher than for non-switching cycles. Therefore, it is typically not possible to fully compensate leakage currents by using positive-up negative-down (PUND) measurements as well as modified DLCC[12]—since both methods compensate using non-switching cycles. In DLCC, leakage is compensated using two successive switching cycles at different frequencies, thus overcoming the aforementioned issue. Therefore, DLCC better reflects the electrical features of our films. This comes however at the price of overlapping switching peaks due to the frequency dependence of the latter, which can lead to the minor artificial negative current response observed under positive fields, as visible in **Figure 7**b. In Figure 7a,b, DLCC *P–E* and *J–E* loops for different $Al_{0.72}Sc_{0.28}N$ film thicknesses are depicted. Although DLCC is not able to fully compensate for the leakage on the positive side, the remanent polarization (P_r) can be approximately determined from the negative half-cycle in Figure 7a. P_r values of roughly 125 μC cm^{-2} are in line with what is known from highly textured $Al_{1-x}Sc_xN$ on Pt/Si for similar Sc concentrations.[12]

Somewhat unexpected—and different to what has been previously observed in $Al_{1-x}Sc_xN$, the data displayed in Figure 7b reveals a broadening of the switching regime including the appearance of two peaks during sweeping negative half-cycles. From frequency-dependent measurements (see Figure S2, Supporting Information), both peaks behave like ferroelectric switching peaks—as expected, with increasing frequency the peak-heights are increasing as well as the peak centers are shifting to higher absolute fields. More gradual switching is also apparent during the negative half-cycle of the butterfly-shaped strain over the electric field loop displayed in Figure 6b, which gives additional evidence that both peaks are of ferroelectric origin. The clear observation of the double-switching phenomenon in our samples was facilitated by contacting the capacitor through the n-GaN, which results in an asymmetric current response that widens the negative side, especially for thinner films. This broadening of the displacement current peaks also occurs during switching two neighboring capacitors in series, i.e., by using the substrate for the series connection and therefore ruling out the influence of the Ag/n-GaN contact (see Figure S3, Supporting Information). Thus, although being highly doped, we expect a voltage drop on a built-up space charge region at the $Al_{1-x}Sc_xN$/n-GaN interface (a more detailed possible explanation for this observation is given at the end of this section). Due to the establishment of this space charge region, peak splitting effects are getting more pronounced with decreasing film thickness down to 100 nm. Below 50 nm, "peak

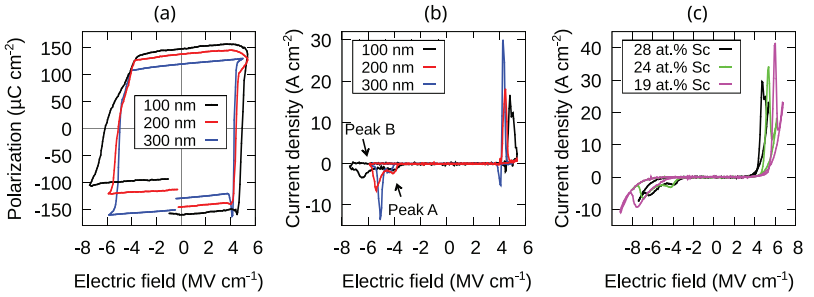

Figure 7. a) DLCC (1 kHz) *P–E* loops and b) corresponding DLCC (1 kHz) *J–E* curves for 100 nm (black), 200 nm (red), and 300 nm (blue) thick $Al_{0.72}Sc_{0.28}N$ films. Leakage compensation was calculated from measurements at 1 and 2 kHz. c) Uncorrected *J–E* curves showing the evolution of the double peak feature during the negative half-cycle for 100 nm thick $Al_{1-x}Sc_xN$ with varying Sc concentrations.

ADVANCED SCIENCE NEWS
www.advancedsciencenews.com

ADVANCED FUNCTIONAL MATERIALS
www.afm-journal.de

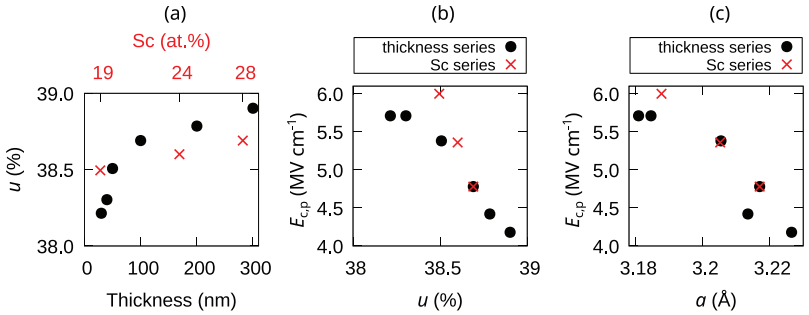

Figure 8. a) Internal parameter u in dependence of $Al_{0.72}Sc_{0.28}N$ film thickness and in dependence of Sc content for 100 nm thick $Al_{1-x}Sc_xN$. b) Positive coercive field ($E_{c,p}$) dependence on the internal parameter u and c) on the a-lattice parameter.

A" shrinks and finally disappears at 30 nm (see Figure S4, Supporting Information). As discussed in Section 2, $Al_{0.72}Sc_{0.28}N$ films with up to ≈40 nm thickness are fully strained to the GaN. Films with thicknesses in between ≈40 and 300 nm consist of a fully strained as well as a more relaxed volume. Since double peaks are only present in films thicker than 30 nm, we expect that they are related to the different strain regimes within the films. To further confirm that the switching peaks are indeed related to different strain regimes, the 100 nm thick samples with 24 at% Sc and 19 at% Sc were investigated. The a-lattice parameter and therefore the in-plane misfit to GaN is decreasing with decreasing Sc content and finally almost matches the GaN a-lattice parameter at 19 at% Sc, as discussed in Section 2. In Figure 7c *J–E* curves for the 100 nm thick $Al_{1-x}Sc_xN$ with different Sc concentrations are compared. It is evident that for 24 at% Sc "peak A" is shrinking at the cost of "peak B" while finally only one switching peak appears for the uniform fully strained 19 at% Sc film. Due to the compressively strained in-plane lattice of $Al_{1-x}Sc_xN$ at the GaN interface, it is reasonable to conclude that this volume fraction is switched at higher absolute electric fields, as it is known that compressive strain in $Al_{1-x}Sc_xN$ leads to higher coercive fields.[12] Therefore we expect "peak B" to be responsible for switching polarization of the fully strained region near the GaN interface and "peak A" to be responsible for switching the more relaxed region at lower absolute electrical fields. Since at 24 at% Sc the ratio between fully strained and relaxed volume is changing, also the area ratio of the two switching peaks is changing. Furthermore, the lower Sc content causes a higher coercive field, as it can be seen especially for the $Al_{0.81}Sc_{0.19}N$ film. As discussed in Section 2, the high-resolution RSM of the latter film (Figure 4b) is indicative of a largely uniform lattice over the entire film thickness, which can explain the occurrence of only one switching peak. Additional measurements that confirm that the switching behavior described above occurs independent of sample area and measurement setup are given in the supplement.

In order to investigate the effect of epitaxial strain on the coercive field, the internal parameter u was calculated according to $u = a^2/3c^2 + 0.25$[19–21] and is illustrated in **Figure 8**a for the various films investigated in this study. Due to the asymmetric voltage drop at the $Al_{1-x}Sc_xN$/GaN interface, only the positive coercive field ($E_{c,p}$) can be clearly determined and considered for the following evaluations.

As expected, u is decreasing with decreasing film thickness due to the compressively strained $Al_{0.72}Sc_{0.28}N$ close to the GaN interface. As previously shown, a reduction in Sc content leads to a drop in u as well.[10] In our particular case, the effect of epitaxial strain superimposes the distortion of the lattice due to Sc variation, resulting in relatively small changes for the different Sc concentrations. In Figure 8b the coercive field is correlated to the internal parameter u. Clearly, a decrease of the coercive field with increasing u is observed for both series due to a flattening of the energy landscape which facilitates ferroelectric switching.[12] Noticeably, the coercive field changes from 4.2 up to 5.7 MV cm^{-1} for $Al_{0.72}Sc_{0.28}N$ only as an effect of epitaxial strain. Although the trend is clear, a slightly different dependence of $E_{c,p}$ on u is observed for the thickness and the Sc series. This supports the assumption that u alone does not determine the coercive field. Besides distorting the lattice, Sc has an additional effect on the switching behavior, e.g., an introduction of local structural instability which facilitates switching.[22] Contrarily, the coercive field dependence on the a-lattice parameter is more congruent for the two series, as depicted in Figure 8c. To conclude, the coercive field is heavily influenced by epitaxial strain. Additional studies should therefore be conducted to investigate if the systematic introduction of epitaxial tensile strain can be used to further separate the coercive field from the onset of the leakage current.

To provide a possible explanation for the establishment of a space charge region under large negative fields, we rely on the following observation: The onset of the switching current occurs at roughly the same field for both polarities. This observation indicates that there is no large-scale depletion zone in the n-GaN and thus no space charge region at this point. For positive fields, there will be no additional depletion since the n-GaN is biased in the forward direction. For negative fields (and N-polar $Al_{1-x}Sc_xN$), the interface between the ferroelectric and the n-GaN will provide electrons from the charges screening the polarization of the ferroelectric. As soon as polarization switching occurs, this reservoir of charges will be substantially reduced through the rearrangement of the screening charges. Locally, there will no longer be sufficient screening charges to build up a field as high as the coercive field of $Al_{1-x}Sc_xN$. Therefore, the n-GaN will start to deplete when the first regions with M-polarity are formed and the remaining switching current will appear widened due to the additional voltage-drop over the depleted GaN.

ADVANCED SCIENCE NEWS
www.advancedsciencenews.com

ADVANCED FUNCTIONAL MATERIALS
www.afm-journal.de

4. Investigation of the Initial Film Polarity

The polarity of III-N heterostructures is of fundamental importance for, e.g., the carrier type in 2-dimensional electron gases (2DEGs) that form at their polarization discontinuities as well as their etching rate and selectivity—both of which are crucial from the integration point of view.[9,23] Sputtering of $Al_{1-x}Sc_xN$ usually favors N-polar growth, while most III-N heterostructures feature M-polar surfaces. Therefore, the as-deposited polarity of $Al_{1-x}Sc_xN$ grown on top of M-polar GaN is of special interest. To investigate the as-deposited polarity of the films, two successive unipolar triangular excitation signals at 1.5 kHz were applied on pristine pads. This allows distinguishing between switching (first signal, orange) and non-switching (second signal, green) currents, as depicted in **Figures 9**a,b for a 100 nm thick $Al_{0.72}Sc_{0.28}N$ film. Clear current peaks during positive and negative voltage sweeps are visible, meaning there are M-polar as well as N-polar regions inside the same, as-deposited film—unlike in the exclusively N-polar films deposited by similar processes on metal electrodes.[24]

Measurements of the piezoelectric coefficient $d_{33,f}$ on as-deposited pads in comparison to $d_{33,f}$ measured on pads with prior switching to full N-polarity by applying a field above the positive coercive field confirm the as-deposited multipolar state: The as-deposited $d_{33,f}$ for a 200 nm thick $Al_{0.72}Sc_{0.28}N$ capacitor is 19.4% smaller than after switching the same capacitor to full N-polarity. Furthermore, by looking at the full loop of the 100 nm film depicted in Figure 9a, it is apparent that the switching dynamics are completely different for the first unipolar excitation signal. This might not be related to a wake-up effect,[25] but rather an effect of the depleting GaN in the presence of M-polar AlScN and large negative electric fields, as explained in Section 3. The growth of M-polar $Al_{1-x}Sc_xN$ is promoted via the M-polar GaN template. This template-dependent polarity has also been observed for GaN grown by MOCVD—GaN grows N-polar on non-polar sapphire and M-polar on a template that exhibits M-polarity (AlN/sapphire).[26] For thicknesses $\gtrsim$40 nm, the film undergoes a transition to N-polarity, in accordance with the preference of the deposition process. This thickness-related transition from M- to N-polarity is confirmed by thickness-dependent as-deposited unipolar measurements, as depicted in Figure 9c. With decreasing film thickness the M-polar switching peak area is increasing, meaning the N-polar volume portion is shrinking. This increase in polarization when reducing the thickness of the non-switching layer is a common feature of dielectric/ferroelectric heterostructures.[27] Unipolar measurements on thinner as-deposited $Al_{0.72}Sc_{0.28}N$ films reveal full M-polarity for 30 nm film thickness, while at 40 nm film thickness a switching peak confirming the presence of N-polarity is observed (see Figure S5, Supporting Information). This confirms the aforementioned transition from M- to N-polarity at a thickness between 30 and 40 nm. Since also films with lower Sc concentrations and thus reduced built-in stress exhibit M- and N-polar as-deposited regions (see Figure S6, Supporting Information), we conclude that their presence is not predominantly related to the strain relaxation that is also observed to start at around 40 nm film thickness, but rather an independent effect due to the influence of the M-polar GaN at the interface. Conversely, the change in polarity necessarily induces an extended lateral defect (i.e., the domain wall), which might be the origin for the commencing stress relaxation at this particular thickness. To visualize the extent of the as-deposited M-polarity, etching experiments were conducted and are illustrated in **Figure 10**, since etchants like Phosphoric acid (H_3PO_4) are highly selective to the polarity of wurtzite-type crystals.[23] After switching the

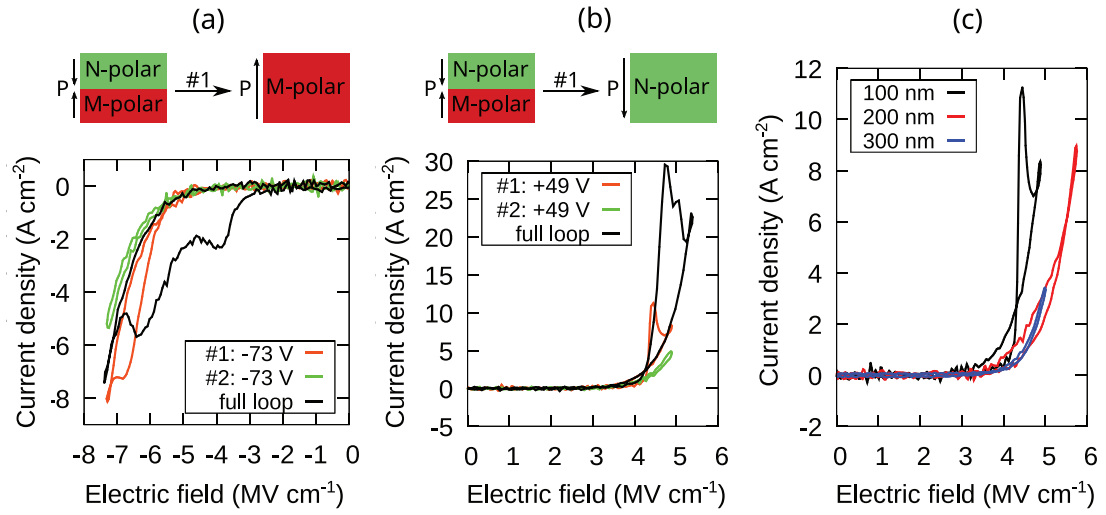

Figure 9. a) Negative and b) positive unipolar measurements on pristine 100 nm $Al_{0.72}Sc_{0.28}N$ capacitors to visualize the as-deposited polarization. The sketches above the respective figures represent the $Al_{1-x}Sc_xN$ polarization state before and after the first applied unipolar voltage. The *J–E* half-cycle after fully switching the same film to the respective opposite polarity is depicted in black c) Positive unipolar measurements on pristine $Al_{0.72}Sc_{0.28}N$ capacitors in dependence of film thickness to illustrate the extent of as-deposited M-polarity.

ADVANCED SCIENCE NEWS
www.advancedsciencenews.com

ADVANCED FUNCTIONAL MATERIALS
www.afm-journal.de

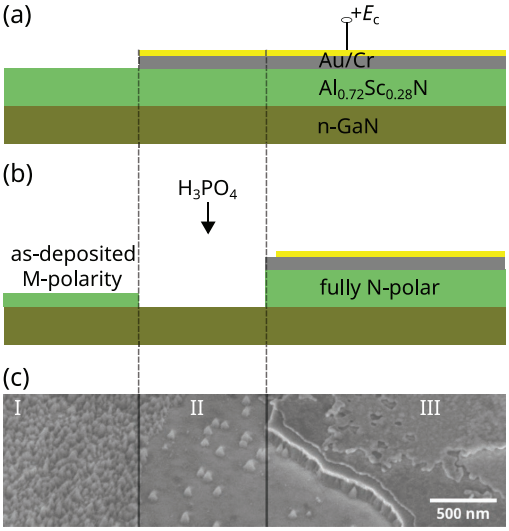

Figure 10. a) Schematic cross-section of a patterned Au(10 nm)/Cr(30 nm)/$Al_{0.72}Sc_{0.28}N$(100 nm)/n-GaN heterostructure with positive coercive field applied to the capacitor. b) Expected cross-section after removing part of the top-electrode and subsequent etching in phosphoric acid c) Scanning electron microscopy (SEM) image of the etched heterostructure sketched in (b). The three expected topographies marked with I, II, and III are clearly visible.

100 nm thick $Al_{0.72}Sc_{0.28}N$ below the patterned top-electrode to full N-polarity, as sketched in Figure 10a, the top electrodes were partially removed by wet-etching. Subsequent to the etching in 80 °C H_3PO_4, the etch-profile sketched in Figure 10b is expected and observed experimentally, as depicted in Figure 10c.

In region I, the as-deposited residual M-polar $Al_{0.72}Sc_{0.28}N$ volume fraction is visualized, followed by a clear transition to the neighboring almost fully etched region II, which was previously switched to full N-polarity. Noticeably, the topography in region I exhibits a rather complex three-dimensional structure. We presume the rough surface structure is a consequence of the M- to N-polarity transitions in the as-grown film taking place at different levels for the respective columnar $Al_{1-x}Sc_xN$ nanograins. In region II, only cone-like residuals on a very smooth surface are visible. These cone-like residuals are characteristic for N-polar $Al_{1-x}Sc_xN$, while the very smooth surrounding surface is indicative of an etch-stop at the $Al_{1-x}Sc_xN$/GaN interface.[23] The smooth etch-stop on the GaN surface allows the conclusion that the latter is not switched to N-polarity to a significant extend. This observation also gives additional support to our explanation that the double switching peak phenomenon originates in the $Al_{1-x}Sc_xN$ and is not a consequence of partial switching in GaN.

To further support this discussion, we confirmed the expected location of the M- and N-polar regions in the as-deposited $Al_{0.72}Sc_{0.28}N$ films by recording high-resolution STEM ABF micrographs at the interface and close to the surface, which were vertically aligned at a nearly identical lateral position. Registered STEM datasets were recorded with an aberration corrected electron probe allowing for the unambiguous

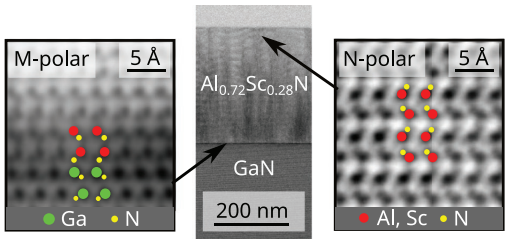

Figure 11. Registered and Gaussian-filtered STEM ABF micrographs of the 300 nm $Al_{0.72}Sc_{0.28}N$/GaN heterostructure in [11–20] zone axis. The structure is M-polar at the interface and N-polar close to the surface. The respective positions of the recorded micrographs are indicated by arrows. On the schematic models green dots depict Ga atoms, red dots Al/Sc atoms and yellow dots N atoms.

determination of $Al_{0.72}Sc_{0.28}N$ unit cell polarity at the atomic scale.[24] Although growing epitaxially, the nanoscale grain sizes and in-plane mosaicity of the investigated film implicated a challenging task for high-resolution STEM investigation. The small grain size causes overlapping orientations and irregularities in the field of view. Therefore, ABF as a very orientation angle sensitive technique resulted in unambiguous results only in certain regions.

The registered ABF datasets showing the atomic structure at the interface and at the top film region are presented in **Figure 11**, respectively. At the interface to the M-polar GaN buffer layer, the atomic structure of $Al_{0.72}Sc_{0.28}N$ exhibits also an M-polar configuration, which is illustrated by the schematics indicating the atomic species on their respective lattice positions. Conversely, the investigation of the relaxed region close to the surface revealed an N-polar structure.

Hence, the localized observations of position-dependent polarities in the $Al_{0.72}Sc_{0.28}N$ film confirm our initial hypothesis that the competition between an M-polar template and a deposition process that favors N-polar films leads to a transition between the polarities once a certain film thickness is reached. However, even with this initial multi-domain state, a single domain configuration can be obtained by either electrically polarizing the material or by keeping the film thicknesses below 30 nm.

5. Conclusion

Epitaxial ferroelectric $Al_{1-x}Sc_xN$ films with 19, 24 as well as 28 at% Sc and thicknesses ranging from 300 nm down to 10 nm were grown by sputter epitaxy on doped n-GaN/Al_2O_3 substrates. XRD, RSM, and pole-figures confirmed epitaxial growth and the expected [1–100](0001)$Al_{1-x}Sc_xN$ ‖ [1–100](0001) GaN relationship. At Sc concentrations above 19 at% the $Al_{1-x}Sc_xN$ lattice divides into a fully strained regime at the GaN interface and a relaxed regime above. Relaxation was further investigated combining aberration-corrected STEM and scanning NBED resulting in a strain map representing the whole thickness of the 300 nm $Al_{0.72}Sc_{0.28}N$ film. The aforementioned investigations reveal that $Al_{0.72}Sc_{0.28}N$ films up to ≈40 nm thickness are fully strained to the GaN, while for thicker films the

ADVANCED SCIENCE NEWS
www.advancedsciencenews.com

ADVANCED FUNCTIONAL MATERIALS
www.afm-journal.de

extent of the fully strained regime is decreasing with increasing film thickness.

By reducing the Sc concentration from 28 to 19 at%, lattice-matched growth conditions can be obtained that result in a more uniform strain state throughout the films. From the electrical response, it was found that two ferroelectric displacement current peaks appear for films with thicknesses >30 nm and Sc concentrations > 19 at%. This indicates that this distinct switching behavior is related to the respective strain states inside films consisting of a fully strained as well as a more relaxed volume. The compressively strained volume close to the GaN interface is expected to switch at higher coercive fields, while the relaxed volume distant from the GaN interface is expected to switch at lower coercive fields. The initial polarization state of all epitaxial $Al_{0.72}Sc_{0.28}N$ films investigated in this study was proven by electrical measurements to be M-polar near the interface up to ≈30 nm film thickness with a subsequent transition to N-polarity. In contrast to the double-switching phenomenon, this is not related to different strain regimes, but rather due to the competing influence of the M-polar GaN template and the sputter process for $Al_{1-x}Sc_xN$ favoring N-polarity. Hence two polarities are present also in the lattice-matched $Al_{0.81}Sc_{0.19}N$ films. STEM ABF imaging as well as the results of etching experiments confirmed the conclusions obtained from the electrical measurements: M-polarity in $Al_{0.72}Sc_{0.28}N$ was found near the GaN interface due to the impact of the M-polar template, while near the surface N-polar $Al_{0.72}Sc_{0.28}N$ was confirmed. Our results therefore give a conclusive overview regarding the effect of epitaxial growth on the ferroelectric response of heterostructures containing III-N based ferroelectrics and help to advance the pending integration of ferroelectric functionality to III-N technology.

6. Experimental Section

The substrates consisting of a 4.5 µm Si-doped epi-GaN top-layer and its corresponding buffer layers grown on Al_2O_3 (0002) were commercially bought. The dopant concentration was specified as $\geq 10^{18}$ cm^{-3} and the resistivity was specified as < 0.5 Ω cm. The as-grown 4-in. n-GaN wafers were protected by a photoresist and diced into 1 × 1 cm^2 pieces. Prior to deposition, the pieces were cleaned with acetone and isopropanol in an ultrasonic bath followed by rinsing in DI-water. The $Al_{1-x}Sc_xN$ films as well as the Pt top-electrodes were grown by sputter deposition in an Oerlikon (now Evatec) MSQ 200 multisource system. The $Al_{1-x}Sc_xN$ films were deposited by reactive pulsed DC co-sputtering at 450 °C and a nitrogen flow of 15 sccm. More details about the process are described elsewhere.[12,28] All electrically characterized samples were capped with 100 nm of Pt after a preceding vacuum break to clean the Pt-target. The top-electrodes were structured with lithography and ion beam etching (IBE, Oxford Instruments Ionfab 300). The n-GaN served as bottom-electrode by contacting it via applying a silver conductive paste. Etching experiments were conducted on 100 nm thick $Al_{0.72}Sc_{0.28}N$ samples with sputter-deposited 30 nm Cr and 10 nm Au capping in a von Ardenne CS730S sputtering tool. The electrodes were structured with lithography and wet-etched with a KI/I_2 solution (Au) and TechniEtch Cr01 (Cr). After switching certain pads to full N-polarity, the top-electrodes were removed using the aforementioned etchants followed by etching in 85% H_3PO_4 at 80 °C. The sample topography (see Figure S7, Supporting Information), especially the occurrence of non-*c*-axis oriented protruding grains as described in previous publications,[28,29] as well as the etched samples were analyzed using a scanning electron microscope (SEM, Zeiss GeminiSEM). The Sc content was determined by SEM energy dispersive X-ray spectroscopy (EDS, Oxford x-act) at 13 kV. XRD measurements were performed using a Rigaku SmartLab diffractometer (9 kW, $Cu_{K\alpha}$ = 1.5406 Å, Hypix detector). The in-plane lattice parameters were extracted from the asymmetric 10–15 reflection. The pole figure was measured with a 2-dimensional X-ray detector configuration, at a center $2\theta/\omega$ angle of 65° and a center χ angle of 30°. With these settings, the {01–13} family of reflections of the $Al_{1-x}Sc_xN$ and GaN films, as well as the {01-18} family of the sapphire substrate was detected. The high-resolution reciprocal space maps were recorded with a 0.5° Parallel Slit Analyzer on the detector side. Ferroelectric measurements were performed using an AixACCT TF Analyzer 2000. The longitudinal thin-film piezoelectric coefficient $d_{33,f}$ was measured using an AixACCT double beam laser interferometer (DBLI) with a signal amplitude of 30 V at 711 Hz. The strain response in dependence of the electric field was measured with the same setup. Capacitance over electric field measurements were conducted on a Hewlett Packard 4284A Precision LCR meter with a small signal of 1 V peak to peak at 100 kHz sweeping 1 V steps with a delay of 500 ms between each step. A cross-section specimen of the as-deposited 300 nm $Al_{0.72}Sc_{0.28}N$/n-GaN film was prepared for local nanostructure analysis by performing a standard focused ion beam (FIB) procedure on a FEI Helios NanoLab G3 FIB-SEM Dualbeam system. Special care has been taken to minimize damage and Gallium implantation into the structure and to prevent material re-deposition at the interfaces of interest during the final 5 and 2 keV cleaning steps. High-resolution scanning transmission electron microscopy (HRSTEM) capable of directly visualizing a projection of the atomic structure was performed on a Nion HERMES microscope operated at 200 kV (convergence semi-angle of 25 mrad) with aberration-correction up to 5th order, achieving a theoretical point resolution of 0.06 nm. In order to investigate the atomic structure, especially to visualize the positions of the lighter element N that determines the polarity of the material, the annular bright field (ABF) imaging mode was used, collecting the scattering regime of roughly 15–30 mrad on an annular scintillator detector. To reduce noise and the influence of sample drift during image acquisition, series of ABF micrographs from a given sample area have been recorded, rigidly registered, then summed into a single image and finally subjected to a small Gaussian blur filter. To calculate the strain distribution, a scanning nano-beam diffraction map was acquired with 200 × 200 scan points over a 400 × 400 nm^2 area and a convergence angle of ≈0.3 mrad. A 50 × 200 portion of the data was processed with a homemade DigitalMicrograph script to obtain the strain maps calculated from the diffraction spot distances for each scan point. Prior to STEM investigations, the specimen has been baked overnight at 120 °C in a high vacuum to remove residual hydrocarbons that can impair the investigation. This temperature was not high enough to lead to relaxation mechanisms in the material.[30]

Supporting Information

Supporting Information is available from the Wiley Online Library or from the author.

Acknowledgements

This work was supported by the project "ForMikro-SALSA" (Grant no. 16ES1053) from the Federal Ministry of Education and Research (BMBF) and the Deutsche Forschungsgemeinschaft (DFG) under the scheme of the collaborative research centers (CRC) 1261 and 1461.

Open Access funding enabled and organized by Projekt DEAL.

Conflict of Interest

The authors declare no conflict of interest.

Data Availability Statement

The data that support the findings of this study are available from the corresponding author upon reasonable request.

Keywords

aluminum-scandium-nitride ($Al_{1-x}Sc_xN$), epitaxial growth, ferroelectric, gallium nitride, semiconductors

Received: December 15, 2021
Revised: January 20, 2022
Published online:

[1] (Eds.: K. Takahashi, A. Yoshikawa, A. Sandhu), *Wide Bandgap Semiconductors*, Springer, Berlin, Heidelberg **2007**.
[2] S. Nakamura, T. Mukai, M. Senoh, *Appl. Phys. Lett.* **1994**, *64*, 1687.
[3] U. Mishra, S. Likun, T. Kazior, Y.-F. Wu, *Proc. IEEE* **2008**, *96*, 287.
[4] J. Millan, P. Godignon, X. Perpina, A. Perez-Tomas, J. Rebollo, *IEEE Trans. Power Electron.* **2014**, *29*, 2155.
[5] M. T. Hardy, B. P. Downey, N. Nepal, D. F. Storm, D. S. Katzer, D. J. Meyer, *Appl. Phys. Lett.* **2017**, *110*, 162104.
[6] M. Zhu, E. Matioli, in *Proc. IEEE 30th Int. Symp. on Power Semiconductor Devices and ICs (ISPSD)*, **2018**.
[7] N. Chowdhury, Q. Xie, M. Yuan, K. Cheng, H. W. Then, T. Palacios, *IEEE Electron Device Lett.* **2020**, *41*, 820.
[8] T. Takeuchi, S. Sota, M. Katsuragawa, M. Komori, H. Takeuchi, H. Amano, I. Akasaki, *Jpn. J. Appl. Phys.* **1997**, *36*, L382.
[9] O. Ambacher, J. Smart, J. R. Shealy, N. G. Weimann, K. Chu, M. Murphy, W. J. Schaff, L. F. Eastman, R. Dimitrov, L. Wittmer, M. Stutzmann, W. Rieger, J. Hilsenbeck, *J. Appl. Phys.* **1999**, *85*, 3222.
[10] F. Tasnádi, B. Alling, C. Höglund, G. Wingqvist, J. Birch, L. Hultman, I. A. Abrikosov, *Phys. Rev. Lett.* **2010**, *104*, 137601.
[11] S. Zhang, D. Holec, W. Y. Fu, C. J. Humphreys, M. A. Moram, *J. Appl. Phys.* **2013**, *114*, 133510.
[12] S. Fichtner, N. Wolff, F. Lofink, L. Kienle, B. Wagner, *J. Appl. Phys.* **2019**, *125*, 114103.
[13] J. Hayden, M. D. Hossain, Y. Xiong, K. Ferri, W. Zhu, M. V. Imperatore, N. Giebink, S. Trolier-McKinstry, I. Dabo, J.-P. Maria, *Phys. Rev. Mater.* **2021**, *5*, 044412.
[14] P. Wang, D. Wang, N. M. Vu, T. Chiang, J. T. Heron, Z. Mi, *Appl. Phys. Lett.* **2021**, *118*, 223504.
[15] N. Grandjean, J. Massies, P. Vennéguès, M. Laügt, M. Leroux, *Appl. Phys. Lett.* **1997**, *70*, 643.
[16] S. Zhang, W. Y. Fu, D. Holec, C. J. Humphreys, M. A. Moram, *J. Appl. Phys.* **2013**, *114*, 243516.
[17] S. Fichtner; G. Schönweger; T.-N. Kreutzer; A. Petraru; H. Kohlstedt; F. Lofink, B. Wagner, in *Proc. 2020 IEEE ISAF*, **2020**.
[18] R. Meyer, R. Waser, K. Prume, T. Schmitz, S. Tiedke, *Appl. Phys. Lett.* **2005**, *86*, 142907.
[19] G. A. Jeffrey, G. S. Parry, R. L. Mozzi, *J. Chem. Phys.* **1956**, *25*, 1024.
[20] H. Schulz, K. Thiemann, *Solid State Commun.* **1977**, *23*, 815.
[21] S. Yasuoka, T. Shimizu, A. Tateyama, M. Uehara, H. Yamada, M. Akiyama, Y. Hiranaga, Y. Cho, H. Funakubo, *J. Appl. Phys.* **2020**, *128*, 114103.
[22] K. H. Ye, G. Han, I. W. Yeu, C. S. Hwang, J.-H. Choi, *Phys. Status Solidi RRL* **2021**, *15*, 2100009.
[23] D. Zhuang, J. Edgar, *Mater. Sci. Eng., R* **2005**, *48*, 1.
[24] N. Wolff, S. Fichtner, B. Haas, M. R. Islam, F. Niekiel, M. Kessel, O. Ambacher, C. Koch, B. Wagner, F. Lofink, L. Kienle, *J. Appl. Phys.* **2021**, *129*, 034103.
[25] P. Jiang, Q. Luo, X. Xu, T. Gong, P. Yuan, Y. Wang, Z. Gao, W. Wei, L. Tai, H. Lv, *Adv. Electron. Mater.* **2020**, *7*, 2000728.
[26] M. Stutzmann, O. Ambacher, M. Eickhoff, U. Karrer, A. L. Pimenta, R. Neuberger, J. Schalwig, R. Dimitrov, P. Schuck, R. Grober, *Phys. Status Solidi B* **2001**, *228*, 505.
[27] M. Si, X. Lyu, P. D. Ye, *ACS Appl. Electron. Mater.* **2019**, *1*, 745.
[28] S. Fichtner, N. Wolff, G. Krishnamurthy, A. Petraru, S. Bohse, F. Lofink, S. Chemnitz, H. Kohlstedt, L. Kienle, B. Wagner, *J. Appl. Phys.* **2017**, *122*, 035301.
[29] C. Sandu, F. Parsapour, D. Xiao, R. Nigon, L. Riemer, T. LaGrange, P. Muralt, *Thin Solid Films* **2020**, *697*, 137819.
[30] M. R. Islam, N. Wolff, M. Yassine, G. Schönweger, B. Christian, H. Kohlstedt, O. Ambacher, F. Lofink, L. Kienle, S. Fichtner, *Appl. Phys. Lett.* **2021**, *118*, 232905.

4.2 A Comparative Study of $Pt/Al_{0.72}Sc_{0.28}N/Pt$-Based Thin-Film Metal-Ferroelectric-Metal Capacitors on GaN and Si Substrates

Own contributions

- Design of Experiment
- Data analysis & interpretation
- Sample fabrication
- Surface characterization
- Electrical characterization (partly)
- Structural characterization (partly)
- Manuscript preparation (partly)

ACS APPLIED MATERIALS & INTERFACES

www.acsami.org Research Article

A Comparative Study of $Pt/Al_{0.72}Sc_{0.28}N/Pt$-Based Thin-Film Metal-Ferroelectric-Metal Capacitors on GaN and Si Substrates

Md Redwanul Islam, Georg Schönweger, Niklas Wolff, Adrian Petraru, Hermann Kohlstedt, Simon Fichtner,* and Lorenz Kienle*

Cite This: https://doi.org/10.1021/acsami.3c05305 Read Online

ACCESS | Metrics & More | Article Recommendations | Supporting Information

ABSTRACT: $Al_xSc_{1-x}N$ is a nitride-ferroelectric compatible with both CMOS and GaN technology. The origin of ferroelectricity in these ternary nitrides relies on the full inversion of nitrogen atom positions, which is a significantly different structural mechanism than conventional perovskites. Therefore, its ferroelectric characteristics exhibit a high remanent polarization and a tunable coercive field but suffer heavily from leakage currents during the switching event. In this article, we studied epitaxially grown $Al_{0.72}Sc_{0.28}N$ thin films on epitaxial Pt electrode layers deposited on GaN/Al_2O_3 substrates. The results are compared both structurally and electrically with similar systems on SiO_2/Si substrates. Our X-ray diffraction analysis showed that $Al_{0.72}Sc_{0.28}N$/epi-Pt/GaN is always a complete epitaxial stack without any significant strain gradient. Electrically, this system has an overall lower leakage current and coercive field compared to directly grown, highly crystalline, strained epitaxial $Al_{0.72}Sc_{0.28}N$/GaN, despite having a lower crystalline quality of the ferroelectric layer. In addition, decreasing the epi-Pt thickness from 100 to 10 nm resulted in further improvement of the leakage profile, which we attribute to a decrease in surface roughness in the thinner Pt. In contrast, the dominant factor of leakage in a fiber-textured system on Si substrates is the Pt(111) texture. Finally, with the combination of in-plane X-ray diffraction and high-resolution scanning transmission electron microscopy, we have demonstrated an all-epitaxial 20 nm $Al_{0.72}Sc_{0.28}N/Pt/GaN$ MFM stack with a sharp interface thickness of less than 1 nm.

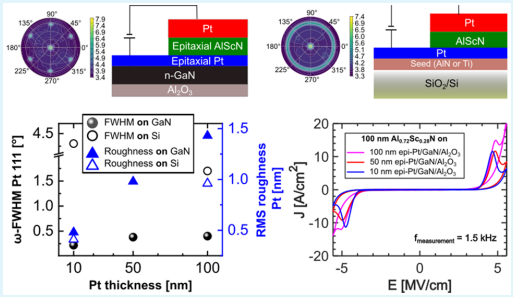

KEYWORDS: *ferroelectricity, AlScN, epitaxy, leakage, texture, interface*

1. INTRODUCTION

The experimental discovery of ferroelectricity in wurtzite-type aluminum scandium nitride (w-$Al_xSc_{1-x}N$) solid solutions is driving worldwide research on fundamental understanding and material optimization as well its device integration in silicon and nitride technologies.[1] Recently, the growth of highly textured or epitaxial ferroelectric (FE) w-$Al_xSc_{1-x}N$ on Si- and GaN-based heterostructures using magnetron reactive co-sputter deposition, molecular beam epitaxy, and metal−organic chemical vapor deposition has already been demonstrated.[2−5] In particular, the material's highly tunable coercive field (E_c) > 2 MV/cm and its large remanent polarization (P_r) up to 130 $\mu C/cm^2$, along with its fast and easy integration to devices, have attracted substantial interest for high-speed FE random-access memory and FE field effect transistor applications.[1,6,7]

Thin-film w-$Al_xSc_{1-x}N$ may also be integrated into GaN-based high-electron-mobility transistors and high-frequency power electronics.[8] The high temperature stability of the solid solution[9,10] and the ferroelectric Curie temperature crossing 1000 °C[11] can be appealing for microwave and harsh-environment electronics.[12] However, ferroelectricity in $Al_xSc_{1-x}N$ is not without limitations. One of the major issues is the high leakage current during switching.[13,14] With thickness downscaling, this issue becomes more severe, posing a significant obstacle to its usage in energy-efficient, ferroelectric-based electronics. In one of our recent works, we grew epitaxial $Al_xSc_{1-x}N$ on n-doped GaN/Al_2O_3 substrates.[15] While scaling down to a 20 nm film thickness was successful, the impact of the semiconducting GaN altered the ferroelectric response significantly. This impact consisted of significant depletion of the substrate under negative electric fields, a transition from M-polar to N-polar growth at a thickness of 40−70 nm, and the emergence of a more complex current-to-voltage response, consisting of two anomalous ferroelectric switching peaks in epitaxially strained films. In this study, we investigate a modified system by introducing an epitaxial (epi-) Pt electrode between the GaN substrate and the ferroelectric

Received: April 20, 2023
Accepted: August 7, 2023

ACS Applied Materials & Interfaces www.acsami.org Research Article

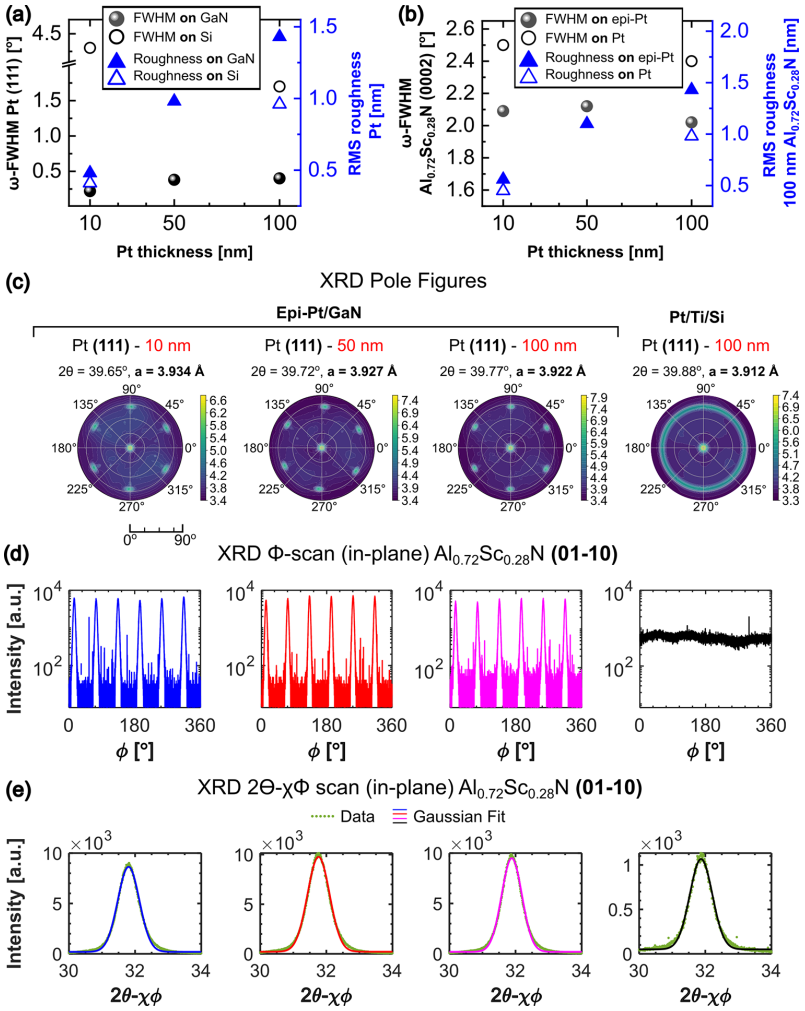

Figure 1. X-ray rocking curve fwhm (black spheres) and RMS roughness (blue triangles) of (a) Pt(111) and (b) 100 nm $Al_{0.72}Sc_{0.28}N$. The solid and hollow symbols represent the samples on GaN/Al_2O_3 and AlN(or Ti)/SiO_2/Si substrates, respectively. (For the sake of simplicity, the legend refers to GaN/Al_2O_3 as GaN and AlN (or Ti)/SiO_2/Si as Si.) The error bars are usually smaller than the data points and are therefore displayed as a table alongside the data values in Tables S1 (roughness) and S2 (XRC-fwhm). (c) X-ray pole figures centered at the Pt(111) reflection. In-plane AlScN [0,1,−1,0] reflection: (d) Φ scan and (e) 2Θ−χΦ scan. From (e), all cases yield an in-plane "*a*" lattice parameter around 3.25−3.24 Å.

w-$Al_{0.72}Sc_{0.28}N$. Pt was chosen as an electrode due to its high work function and its corresponding ability to limit charge leakage.[16] The aim of this experiment was to achieve an all-epitaxial system on GaN without a strain gradient in the ferroelectric layer, with no polarity transition, and with no depletion zone by introducing a metal contact. X-ray diffraction (XRD) analysis of these films showed highly crystalline epitaxial growth of Pt on GaN compared to Si substrates. Furthermore, we found that the growth of Pt on GaN is separated into a highly oriented interface and a slightly disordered bulk regime. Therefore, scaling down the Pt thickness from 100 to 10 nm enhances the overall high crystallinity of the electrode, resulting in a smoother surface for $Al_xSc_{1-x}N$ growth. This ultimately lowered the E_c and therefore the overall leakage current density. A high-resolution asymmetric reciprocal space map (RSM) showed that the metal-ferroelectric-metal (MFM) stack of Pt/AlScN/epi-Pt on GaN/Al_2O_3 grows epitaxially relaxed without any significant strain gradient. The electrical analysis confirmed that these relaxed epitaxial films on epi-Pt had an overall lower coercive field, less leakage, and a more symmetric FE response compared to directly grown strained films on GaN/Al_2O_3. Scanning transmission electron microscopy (STEM) of these Pt/AlScN/epi-Pt based metal-ferroelectric-metal (MFM) capacitors further demonstrated that even at smaller dimensions, such as 20 nm thick *w*-$Al_{0.72}Sc_{0.28}N$ on epi-Pt bottom electrodes, the local epitaxial growth holds with sharp interfaces less than 1 nm.

https://doi.org/10.1021/acsami.3c05305
ACS Appl. Mater. Interfaces XXXX, XXX, XXX−XXX

ACS Applied Materials & Interfaces www.acsami.org Research Article

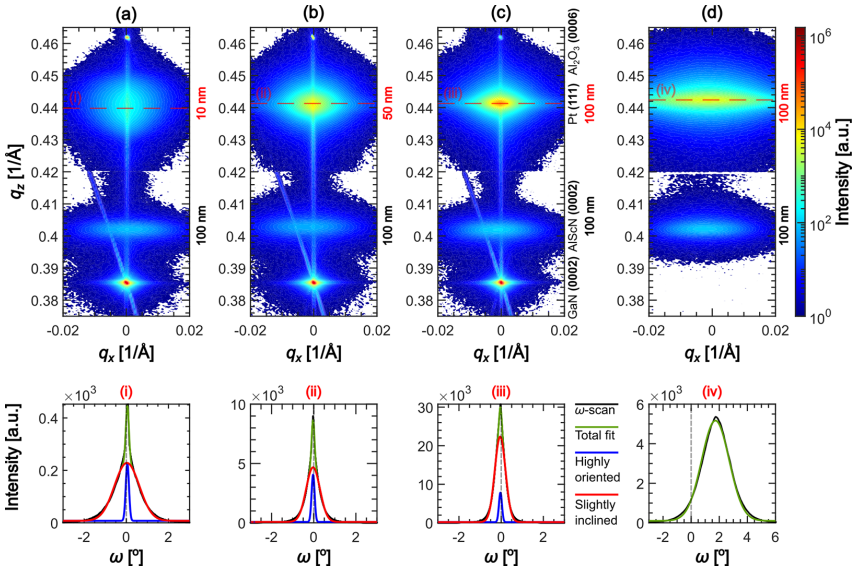

Figure 2. Reciprocal space mapping (RSM) of 100 nm $Al_{0.72}Sc_{0.28}N$ grown on (a) 10 nm, (b) 50 nm, and (c) 100 nm epi-Pt on GaN/Al_2O_3 substrates. (d) 100 nm Pt grown on AlN/SiO_2/Si. Panels i–iv show the corresponding cutline profiles across the Pt(111) reflections. The profiles (marked as red dashed lines in parts a–d) are taken with respect to the ω-axis of the goniometer.

2. RESULTS AND DISCUSSION

2.1. Growth of Pt(111) and $Al_{0.72}Sc_{0.28}N$(0002) on GaN and Si Substrates. The Pt bottom electrode on GaN for the ferroelectric AlScN-based MFM capacitor has a high crystalline quality and low film roughness. These analyses are summarized in Figure 1a, showing the comparison of the Pt(111) X-ray rocking curve (XRC) full width at half-maximum (fwhm) and the AFM root-mean-square (RMS) surface roughness values of as-grown Pt bottom electrodes on GaN and Si substrates. The AFM topographies are demonstrated in the Supporting Information. In terms of the crystalline quality of the Pt bottom electrodes, which is represented by its XRC fwhm, our result indicates a significant improvement of the Pt(111) crystalline quality on GaN (solid spheres) compared to Si (hollow spheres) substrates. For example, 100 nm Pt on Si has an XRC-fwhm of around 1.7°, while the value dropped close to 0.4° for Pt on GaN. The Pt(111) crystalline quality showed further improvement on GaN when its thickness is reduced from 100 to 10 nm (Table S2a). In contrast, identical variations in Pt electrode thickness on Si substrates resulted in a significant decline in crystalline quality from approximately 1.7° to 4.3° for the 100 and 10 nm electrodes, respectively. The RMS surface roughness of the Pt bottom electrodes improved with thickness reduction on both the GaN and Si substrates (blue triangles). Figure 1b displays the same characteristics for the AlScN RMS roughness, which improved from 1.5 to 0.5 nm on both the GaN and Si substrates. However, no significant change in the 100 nm $Al_{0.72}Sc_{0.28}N$-(0002) crystalline quality was observed across various Pt electrode thicknesses for either the GaN or Si substrates (Table S2b). Furthermore, the average Pt grain sizes determined from AFM (shown in Table S1a) decreased from ~30 to ~10 nm as the thickness decreased (measured via the watershed method). The average grain size of *w*-$Al_{0.72}Sc_{0.28}N$ reduced to about 3–10 nm on the thinner 10 nm Pt electrodes compared to the thicker 50 and 100 nm Pt electrodes. However, on Si substrates, after the Pt thickness was reduced from 100 to 10 nm, the average grain size for both Pt and the 100 nm $Al_{0.72}Sc_{0.28}N$ dropped significantly, from around 26 to 10 nm (Table S1b).

The opposite trends of the XRC fwhm that were observed for Pt(111) on both substrates in Figure 1a are interpreted to be two different kinds of growth mechanisms, which are evidenced by the Pt(111) X-ray pole figures presented in Figure 1c. Here, the epitaxial growth of Pt on GaN (epitaxial relation: [1,1,−2,0] (0001) $Al_{0.72}Sc_{0.28}N$ ∥ [1,−1,0] (111) Pt ∥ [1,1,−2,0] (0001) GaN) is demonstrated by the six-fold symmetry of the Pt (1−11) reflections (~79° tilted from Pt(111) planes) compared to the Si substrates, where the reflections are continuously distributed over a 360° Φ rotation showing fiber-textured grain growth. The improved structural quality of the epitaxially grown material also propagates to the 100 nm of $Al_{0.72}Sc_{0.28}N$ grown on the electrode. The in-plane Φ scans of the AlScN (01−10) reflection (Figure 1d) exhibit six-fold symmetry on epi-Pt/GaN. Nonetheless, the in-plane lattice parameter *a* of the *w*-$Al_{0.72}Sc_{0.28}N$ layers is around 3.24–3.25 Å for all cases, indicating a relaxed epitaxial growth of *w*-$Al_{0.72}Sc_{0.28}N$ on epi-Pt/GaN and a conventional, well-known, fiber-textured growth on the Si substrates.

2.2. Structural Analysis of 100 nm MFM Stacks on GaN and Si Substrates via Symmetrical RSMs. Figure 2 shows the GaN(0002), AlScN(0002), Pt(111), and Al_2O_3(0006) reflection spots in reciprocal space (marked in Figure 2c). The high crystallinity of the epi-Pt on GaN compared to the Pt on AlN/SiO_2/Si can be clearly evidenced from the Pt(111) intensity distribution in the RSMs. However, from the ω cutline profiles through all Pt(111) reflection centers (i–iv), it is evident that the direct growth of Pt grains on GaN results in very low average lattice tilt values $\Delta\omega \approx 0°$

https://doi.org/10.1021/acsami.3c05305
ACS Appl. Mater. Interfaces XXXX, XXX, XXX−XXX

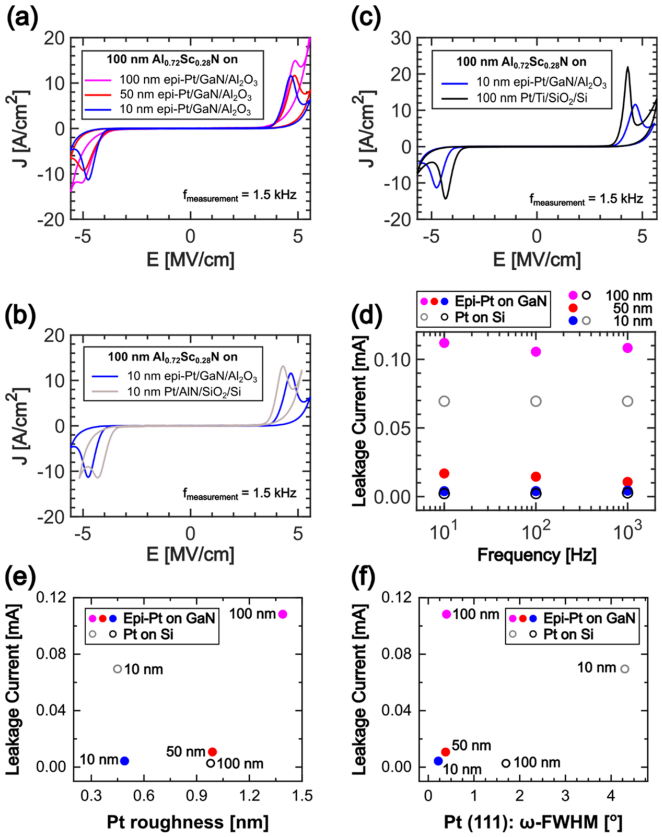

Figure 3. *J-E* characteristics of 100 nm $Al_{0.72}Sc_{0.28}N$ on (a) 100 (magenta), 50 (red), and 10 (blue) nm epi-Pt/GaN/Al_2O_3, (b) 10 nm epi-Pt/GaN/Al_2O_3 (blue) and Pt/AlN/SiO_2/Si (gray), and (c) 10 nm epi-Pt/GaN/Al_2O_3 (blue) and 100 nm Pt/Ti/SiO_2/Si (black). (d) The room temperature leakage current of 100 nm $Al_{0.72}Sc_{0.28}N$ (at 50 V, padsize ≈ 50 × 50 μm^2) via nonswitching measurements at 10, 100, and 1000 Hz. (e) Leakage current (at 1 kHz) vs Pt roughness . (f) Leakage current (at 1 kHz) vs Pt(111) ω fwhm.

from the GaN(0002) RSM center (ω = 0°, marked with a dashed black line in i–iv). These low-tilt mismatches for Pt on GaN substrates indicate a clear epitaxial relation of the layers with the smooth interface. However, the tilt mismatch is much bigger for Pt(111) (as shown in iv) on Si substrates from its normal direction, exceeding up to 1.7° on average. This is mostly due to the indirect growth of Pt through native amorphous SiO_2 and polycrystalline seed layers (Ti or AlN). In addition, the anisotropy of the deposition chamber, e.g., the angular distribution of the sputtered atoms, the substrate tilt, and the temperature gradient across the 8 in. SiO_2/Si wafer, may also contribute to the gradual tilt of the Pt(111) grains away from center of the wafer.[17,18] Further, the impact of epitaxial Pt growth on GaN is apparent from the shape of the cutline ω profiles of the Pt(111) reflections. The cutline profiles can be well-fitted by two functions corresponding to the highly oriented and slightly inclined regions, according to Miyake et al.[19] In contrast to the 50 and 100 nm epi-Pt on GaN, the combined fit of the Pt(111) reflection profile of the 10 nm film exhibits a larger fraction of the highly oriented region. We assume that the highly orientated Pt regions grown on GaN have the same crystalline quality, regardless of the overall Pt thickness. Therefore, the fitting was performed by keeping the fwhm of the highly oriented region constant at 0.16°. The analyses suggest that epi-Pt grains on GaN start to grow highly oriented up to a few monolayers and eventually relax by introducing additional out-of-plane tilt of the columnar grains with increasing thickness. However, we also considered the effect of the correlation peak according to Bläsing et al.;[20] therefore, the Pt(222) rocking curves were further recorded to confirm the high crystallinity of the 10 nm epi-Pt/GaN. From Figure S2b, the sharp intensity feature was also clearly visible at the ω scan, which further confirms our claim of an ultra-thin highly crystalline Pt interface on GaN.

2.3. Current Density vs Electric Field (*J-E*) Response with Varying Pt Thickness on GaN and Si Substrates. Figure 3a shows the *J-E* characteristics of 100 nm epitaxially grown $Al_{0.72}Sc_{0.28}N$ on 100, 50, and 10 nm epi-Pt, where the tail of the switching peak indicates the overall leakage current. The *P-E* responses at 5 kHz with positive-up-negative-down (PUND) measurements are depicted in Figures S3a and S3b. Here, the 100 nm $Al_{0.72}Sc_{0.28}N$ on the 10 nm epi-Pt showed the lowest overall leakage current density with a PUND corrected P_r value of ~147 $\mu C/cm^2$ (slightly overestimated due to switching-induced leakage).[21] Considering the structural data presented in Section 2.1, the lower leakage current density

https://doi.org/10.1021/acsami.3c05305
ACS Appl. Mater. Interfaces XXXX, XXX, XXX−XXX

ACS Applied Materials & Interfaces www.acsami.org Research Article

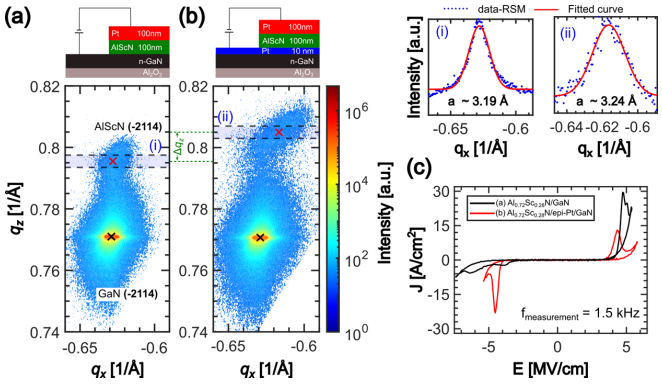

Figure 4. Asymmetric RSM of the 100 nm $Al_{0.72}Sc_{0.28}N$ grown directly on (a) GaN and (b) 10 nm epi-Pt/GaN. The black and red cross-marks in the RSMs indicate the evaluated center of gravity for the GaN (−2114) and AlScN (−2114) reflections, respectively. The horizontal dashed lines filled with a blue color indicate the averaged line profile area for parts i and ii. (c) Electrical *J-E* characteristics of the capacitor structures shown in a and b.

appearing in the 10 nm epi-Pt system can be attributed to the lower roughness and superior crystalline quality of the bottom electrode. The slight reduction of E_c (<0.2 MV/cm) in the 10 nm epi-Pt system could be the cause of minor compressive stress relaxation in the lattice through grain boundaries. However, small, unpredictable fluctuations in the deposition process, depending on the chamber conditioning history, could also have an impact on these minor E_c variations.[22]

In Figure 3b, we compare the electrical response of the epitaxial MFM structure with that of the fiber-textured MFM structure, both consisting of a 10 nm thin bottom electrode. The results show that the leakage current density was significantly lower in epitaxial systems, despite having higher E_c values. According to Section 2.1, the crystalline quality of Pt on Si improves as the thickness of fiber-textured Pt increases from 10 to 100 nm. Comparing Figures 3b and 3c, this enhancement results in a reduction in the overall leakage current density on fiber-textured systems on Si substrates. Figure 3d depicts the true leakage current at 10, 100, and 1000 Hz, determined via nonswitching measurements at room temperature. It shows that the leakage relation shown in parts a−c is frequency-independent.

Therefore, considering the negligible density of misaligned grains, the overall leakage current in structurally relaxed 100 nm $Al_{0.72}Sc_{0.28}N$ on Pt bottom electrodes is a rather complex function of the Pt(111) texture and surface roughness.[23] Figures 3e and 3f illustrate the relation of the leakage current to the surface roughness and the Pt(111) texture, respectively. Depending on the substrate and the growth type (i.e., epitaxial or fiber-textured), different mechanisms dominate. In highly textured epitaxial films on GaN, the overall leakage current decreased with improved Pt surface roughness. This improved roughness is the result of the improved epitaxial crystalline quality, as the overall ratio of the highly oriented regions increased in the thinner layers (as discussed in Section 2.2). In contrast, leakage in fiber-textured films on Si substrates (hollow data points) appears to be dominated by the Pt 111 texture. Here, even though Pt thickness downscaling resulted in improved surface roughness of the film (Figure 3e), the overall leakage current increased due to the loss of crystalline quality (Figure 3f). Additionally, we note that our results do not show a clear connection between the grain sizes and the leakage currents (Table S1) because the smallest average grains for epitaxial Pt and $Al_{0.72}Sc_{0.28}N$ showed the lowest leakage. In contrast, the opposite is true for fiber-textured films, as the smallest 10 nm Pt and $Al_{0.72}Sc_{0.28}N$ grains on Si showed higher leakage. Furthermore, the E_c for $Al_{0.72}Sc_{0.28}N$ grown on Si substrates is roughly ∼0.35 MV/cm lower compared to epi-Pt/GaN systems. As reported by Yasuoka et al., these lower E_c values correspond to the variations in thermally induced stress during deposition process for various substrates (in this study, silicon and sapphire).[24,25]

2.4. Study of the Epitaxial Strain in Directly Grown $Al_{0.72}Sc_{0.28}N$/GaN and $Al_{0.72}Sc_{0.28}N$/epi-Pt/GaN Systems.

Figure 4 shows the comparison between a 100 nm $Al_{0.72}Sc_{0.28}N$ film grown directly on GaN (a) without and (b) with an intermediate 10 nm Pt layer, as depicted in the corresponding layer diagrams. The difference in the center of gravity q_x of the AlScN and GaN (−2114) reflections indicates the epitaxial strain in the AlScN films. The average profiles of directly grown $Al_{0.72}Sc_{0.28}N$ on a GaN reflection center, depicted in Figure 4a(i), shows a strong epitaxial in-plane strain from the substrate to the film layer. The average in-plane lattice parameter a was found to be around 3.19 Å ($c \approx 5.02$ Å). From this, the relaxation parameter r can be calculated for the layer.[18]

$$r = \frac{a_{\text{film}} - a_{\text{sub}}}{a_{\text{film}}^{\text{relaxed}} - a_{\text{sub}}} \quad (1)$$

Therefore, direct growth of 100 nm thick $Al_{0.72}Sc_{0.28}N$ on GaN causes a strain relaxation of around 17% (assuming for $Al_{0.72}Sc_{0.28}N$, $a_{\text{film}}^{\text{relaxed}} = 3.24$ Å).[26] These films are considered to be epitaxially "strained" and have superior crystalline quality. This result is also in agreement with our previous work, where the critical thickness for strain relaxation in $Al_{0.72}Sc_{0.28}N$ was determined to be about 40 nm.[15] In contrast, from Figures 4b and 4b(ii), with the same $Al_{0.72}Sc_{0.28}N$ on epi-Pt/GaN, the relaxation is almost 100% as the calculated in-plane lattice parameter $a \approx 3.24$ Å $\approx a_{\text{film}}^{\text{relaxed}}$ ($c \approx 4.97$ Å).

Furthermore, due to the absence of epitaxial stress from the GaN substrate, the stress distribution inside the $Al_{0.72}Sc_{0.28}N$ layer on epi-Pt is significantly different from the directly grown case on GaN substrates. This can be observed from the shape

https://doi.org/10.1021/acsami.3c05305
ACS Appl. Mater. Interfaces XXXX, XXX, XXX−XXX

of the AlScN (−2,1,1,4) reflection in Figures 4a and 4b. The out-of-plane tensile stress in the strained $Al_{0.72}Sc_{0.28}N$/GaN is evaluated from the Δq_z shift between the AlScN (−2114) reflection center of the gravities, which is roughly 1.2%. As a result of the higher compressive stress,[1] Figure 4c shows that the E_c (positive field cycle) is roughly 0.5 MV/cm higher on strained $Al_{0.72}Sc_{0.28}N$/GaN compared to relaxed films on epi-Pt. The *J-E* response in the strained film is also leakier and more asymmetric. Therefore, it can be concluded that in terms of leakage current and symmetric response, the relaxed $Al_{0.72}Sc_{0.28}N$ on epi-Pt/GaN has a better claim for ferroelectric applications, despite having a lower crystalline quality.

2.5. Structural and Electrical Properties of Ultra-Thin $Al_{0.72}Sc_{0.28}N$. Following our work on describing the ferroelectric characteristics of ultra-thin 10 nm $Al_xSc_{1-x}N$ MFM capacitors lately,[27] in this article, we focus on the structural characterization of such thin MFM structures. Figure 5a shows

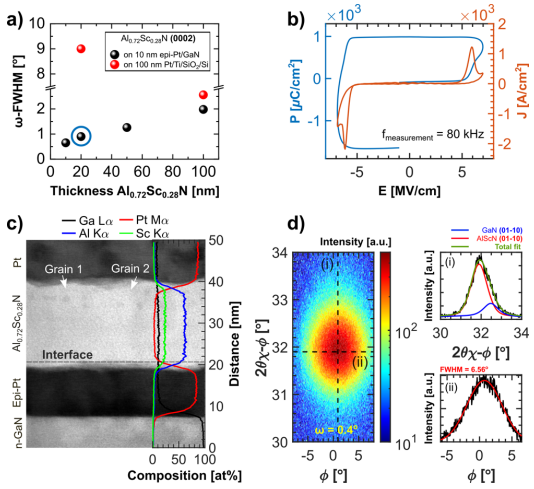

Figure 5. (a) AlScN(0002) rocking curve fwhm of different thicknesses on 10 nm epi-Pt/GaN/Al_2O_3 (black) and 100 nm Pt/Ti/SiO_2/Si (red) systems. The errors of the ω fwhm are noted in Tables S3a and S3b. Twenty nanometer $Al_{0.72}Sc_{0.28}N$ (marked inside the blue circle) (b) polarization and current density characteristics at 80 kHz, (c) STEM ABF micrograph with EDS profiles with Ga (black), Pt (red), Al (blue), and Sc (green), and (d) in-plane (01−10) reciprocal space map plotted in Φ vs $2\theta\chi-\Phi$ (in-plane incident angle $\omega = 0.4°$) ((i) $2\theta\chi-\Phi$ and (ii) Φ intensity profile of the dashed lines and their corresponding Gaussian fits from RSM).

a trend of improving the texture of epitaxial $Al_{0.72}Sc_{0.28}N$ with decreasing film thickness. Similar to the Pt texture on Si in Figure 1a, the texture of $Al_{0.72}Sc_{0.28}N$ also degrades with reducing film thickness on Si substrates. As an example, Figures 5b−5d show the FE polarization hysteresis, the cross-section scanning TEM, and the in-plane XRD, respectively, of a 20 nm $Al_{0.72}Sc_{0.28}N$ film grown on epi-Pt/GaN. The ferroelectric *P-E* and *J-E* responses shown in Figure 5b prove that the ferroelectric activity at this scale is consistent with our previous work.[20] Unfortunately, the assessment of realistic polarization values was not possible due to the high leakage current density, even after applying compensation methods. The ABF STEM micrograph in Figure 5c validates the successful growth of 20 nm *w*-$Al_{0.72}Sc_{0.28}N$ on epi-Pt with a sharp interface roughness of less than 1 nm. The overlaid EDS line scans validate a homogeneous subnanometer distribution of Sc within the FE layer. No trace of the fully strained region at the $Al_{0.72}Sc_{0.28}N$/epi-Pt interface was found, which is due to the large lattice mismatch of $Al_{0.72}Sc_{0.28}N$ with epi-Pt.[28] The STEM image further suggests a similar interface, also with epi-Pt and GaN. These sharp interfaces in the epitaxial films are known to reduce the overall leakage current for the capacitors.[29−31] In addition, the low contrast at the grain boundaries also indicates a relatively stronger grain-to-grain bond in epitaxial $Al_{0.72}Sc_{0.28}N$ films compared to the fiber-textured films grown on Si (previously published).[11,23,32] The in-plane X-ray diffraction scan proves that the $Al_{0.72}Sc_{0.28}N$ grows with an average lattice parameter of ∼3.24 Å, meaning a complete epitaxially relaxed 20 nm film on epi-Pt. The fitted $2\theta-\chi\Phi$ profile of the RSM (shown in Figure 5d(i)) shows the contributions of both the GaN and AlScN (01−10) reflections to the recorded peak intensity. The horizontal $2\theta-\chi\Phi$ profile from the in-plane XRD measurement at a higher incident angle ($\omega = 0.7°$) further confirms the presence of the GaN (01−10) reflection, along with its exact position at the $2\theta\chi-\Phi$ axis (Figure S4). The fwhm of the vertical Φ scan of the reflection in Figure 5d(ii) shows the mosaicity of the columnar grains on epi-Pt, which was found to be ∼6.56°, indicating a much larger average twist distribution of the grains compared to strained epitaxial films on GaN (0.82° for 30 nm $Al_{0.72}Sc_{0.28}N$/GaN, Figure S5).[16] This higher mosaicity values in epitaxially relaxed films can be associated with a large lattice mismatch between Pt and $Al_{0.72}Sc_{0.28}N$ compared to GaN and $Al_{0.72}Sc_{0.28}N$, causing more screw-type misfit dislocations originating at the epi-Pt/$Al_{0.72}Sc_{0.28}N$ interface during growth.

3. CONCLUSIONS

In this article, an in-depth structural characterization of GaN- and Si-substrate-based MFM capacitors with Pt electrodes and their ferroelectric properties were presented. The individual structural properties of Pt bottom electrodes grown on doped GaN and Si substrates were compared, and their interrelation with the ferroelectric properties of $Al_{0.72}Sc_{0.28}N$ were discussed. Using methods such as XRD pole figures and Φ scans, we demonstrated that the complete MFM capacitor stack with FE $Al_{0.72}Sc_{0.28}N$ and epi-Pt bottom electrodes successfully grows epitaxially relaxed on GaN, even down to 20 nm thickness. Hence, the developed MFM stack can remove strain gradients within the FE layer, which is electrically superior to AlScN/GaN heterostructures. This is demonstrated by a more symmetrical ferroelectric response with a lower average E_c of about 1 MV/cm and smaller leakage currents, despite having lower crystalline quality. The optimization of these properties in relation to the epi-Pt thickness was studied by high-resolution XRD analyses, pointing out the different growth regimes of epi-Pt on GaN, which are described by highly oriented and comparatively low-oriented zones. The highly oriented zone lies close to the GaN interface, where the directed growth of the Pt grain is almost defect-free. Hence, reducing the Pt thickness from 100 to 10 nm results in overall improved crystalline quality and surface roughness. This improvement is regarded as an active factor for reducing the overall leakage current density for epitaxial $Al_{0.72}Sc_{0.28}N$ on a 10 nm epi-Pt/GaN/Al_2O_3 stack, which showed the best leakage profile. Furthermore, we also confirmed relaxed epitaxy for a thinner 20 nm $Al_{0.72}Sc_{0.28}N$ on 10 nm epi-Pt. TEM analyses of these films showed a homogeneous composition at

https://doi.org/10.1021/acsami.3c05305
ACS Appl. Mater. Interfaces XXXX, XXX, XXX−XXX

the sub-nm scale with sharp interface roughness (<1 nm) between the layers, demonstrating a successful MFM design by magnetron sputter deposition.

4. EXPERIMENTAL METHODS

Thin-film depositions of Pt (100, 50, and 10 nm) and $Al_{0.72}Sc_{0.28}N$ (100, 50, 20, and 10 nm) were performed in an MSQ 200 multisource system (EVATEC AG). Epitaxial (111)-oriented Pt was deposited directly on commercial n-type 1 × 1 cm Si-doped (concentration ≥ 10^{18} cm^3) n-GaN/Al_2O_3 substrates. All Pt layers were deposited in DC sputter mode at 500 °C (600 W, 50 sccm Kr). For comparison purposes, (111)-orientated Pt was deposited on an 8 in. SiO_2/(100) Si wafer (SiO_2 thickness = 650 nm) with an additional 20 nm polycrystalline AlN or Ti seed layer predeposition step under the same condition. The preference of either the AlN or the Ti seed layer is only for Pt adhesion to SiO_2 and has no significant impact on the ferroelectric properties of $Al_xSc_{1-x}N$. After Pt deposition, the wafer was diced into 1 × 1 cm chips (DAD3350 dicing saw). Later, $Al_{0.72}Sc_{0.28}N$ was deposited via pulsed DC cosputtering from separate Al (680 W) and Sc (320 W) targets at 450 °C in a mixture of N_2 (15 sccm) and Ar (7.5 sccm) atmospheres. This deposition was performed simultaneously on 1 × 1 cm Pt/AlN(or Ti)/SiO_2/Si and epi-Pt/GaN/Al_2O_3 chips. At the final step, 100 nm Pt top electrodes were subsequently deposited at room temperature (with a vacuum break) and patterned with optical lithography and ion beam etching (Oxford Instruments Ionfab 300). The postdeposition electrical characterization was performed in an AixACCT TF Analyzer 2000. The surface topography of the films was analyzed using a SmartSPM 1000 scanning probe microscope from AIST-NT. The structural characterization, such as ω fwhm (without considering the instrumental broadening) along with symmetrical/asymmetrical RSM, was performed with parallel beam monochromatic X-ray diffraction (Rigaku SmartLab 9 kW, Cu Kα, Ge(220)2x with 5° Soller slits, Hypix-3000 pixel detector). Pole figures were recorded with a nonmonochromatic beam. All in-plane XRD measurements were performed by using a 0.5° parallel slit collimator at the incident side and a 0.5° parallel slit analyzer at the receiving side of the instrument. Local structural imaging and energy-dispersive X-ray spectroscopy (EDS) were performed with a probe-corrected scanning transmission electron microscope (JEM-ARM200F NEOARM, 200 kV) equipped with dual 100 mm^2 silicon drift detectors. All thicknesses mentioned in this paper are nominal, with an error of around ±1 nm.

■ ASSOCIATED CONTENT

Supporting Information

The Supporting Information is available free of charge at https://pubs.acs.org/doi/10.1021/acsami.3c05305.

AFM image of the Pt and $Al_{0.72}Sc_{0.28}N$ surfaces on GaN/Al_2O_3 and Si substrates; Pt(222) X-ray rocking curve on GaN/Al_2O_3 (100, 50, and 10 nm); polarization-electric field response of 100 nm w-$Al_{0.72}Sc_{0.28}N$ at 5 kHz with positive-up-negative-down (PUND) correction; in-plane RSM of 20 nm $Al_{0.72}Sc_{0.28}N$ on epi-Pt/GaN at ω = 0.7°; in-plane RSM of fully strained 30 nm $Al_{0.72}Sc_{0.28}N$ on GaN/Al_2O_3; RMS roughness values and their corresponding standard deviations; X-ray rocking curve fwhm's of Pt and 100 nm $Al_{0.72}Sc_{0.28}N$ with their corresponding fitting errors; epitaxial $Al_{0.72}Sc_{0.28}N$ (100, 50, 20, 10 nm) and fiber-textured (100, 20 nm) X-ray rocking curve fwhm's with corresponding fitting errors on 10 nm epi-Pt and 100 nm fiber-textured Pt bottom electrodes (PDF)

■ AUTHOR INFORMATION

Corresponding Authors

Simon Fichtner − *Microsystems and Technology Transfer, Institute for Material Science, Kiel University, D-24143 Kiel, Germany; Fraunhofer Institute for Silicon Technology (ISIT), 25524 Itzehoe, Germany;* orcid.org/0000-0003-1106-6868; Email: sif@tf.uni-kiel.de

Lorenz Kienle − *Synthesis and Real Structure, Institute for Material Science, Kiel University, D-24143 Kiel, Germany; Kiel Nano, Surface and Interface Science (KiNSIS), Kiel University, D-24118 Kiel, Germany*; Email: lk@tf.uni-kiel.de

Authors

Md Redwanul Islam − *Synthesis and Real Structure, Institute for Material Science, Kiel University, D-24143 Kiel, Germany;* orcid.org/0000-0003-1403-7173

Georg Schönweger − *Nanoelectronics, Institute of Electrical Engineering and Information Engineering, Kiel University, D-24143 Kiel, Germany; Fraunhofer Institute for Silicon Technology (ISIT), 25524 Itzehoe, Germany*

Niklas Wolff − *Synthesis and Real Structure, Institute for Material Science, Kiel University, D-24143 Kiel, Germany; Kiel Nano, Surface and Interface Science (KiNSIS), Kiel University, D-24118 Kiel, Germany*

Adrian Petraru − *Nanoelectronics, Institute of Electrical Engineering and Information Engineering, Kiel University, D-24143 Kiel, Germany*

Hermann Kohlstedt − *Nanoelectronics, Institute of Electrical Engineering and Information Engineering, Kiel University, D-24143 Kiel, Germany; Kiel Nano, Surface and Interface Science (KiNSIS), Kiel University, D-24118 Kiel, Germany*

Complete contact information is available at: https://pubs.acs.org/10.1021/acsami.3c05305

Notes

The authors declare no competing financial interest.

■ ACKNOWLEDGMENTS

Funded by the project "ForMikro-SALSA" (project ID: 16ES1053) from the Federal Ministry of Education and Research (BMBF). Funded by the Deutsche Forschungsgemeinschaft (DFG, German Research Foundation; project IDs: 434434223-SFB 1461, 286471992-SFB 1261, and 458372836). The authors gratefully acknowledge Christin Szillus for the FIB preparation of cross-section samples for TEM analysis.

■ REFERENCES

(1) Fichtner, S.; Wolff, N.; Lofink, F.; Kienle, L.; Wagner, B. AlScN: A III-V Semiconductor Based Ferroelectric. *J. Appl. Phys.* **2019**, *125* (11), 114103.

(2) Streicher, I.; Leone, S.; Kirste, L.; Manz, C.; Straňák, P.; Prescher, M.; Waltereit, P.; Mikulla, M.; Quay, R.; Ambacher, O. Enhanced AlScN/GaN Heterostructures Grown with a Novel Precursor by Metal-Organic Chemical Vapor Deposition. *Physica Status Solidi - Rapid Research Letters* **2023**, *17*, 2200387.

(3) Tsai, S. L.; Hoshii, T.; Wakabayashi, H.; Tsutsui, K.; Chung, T. K.; Chang, E. Y.; Kakushima, K. Roomerature Deposition of a Poling-Free Ferroelectric AlScN Film by Reactive Sputtering. *Appl. Phys. Lett.* **2021**, *118* (8), n/a DOI: 10.1063/5.0035335.

(4) Casamento, J.; Lee, H.; Maeda, T.; Gund, V.; Nomoto, K.; Van Deurzen, L.; Turner, W.; Fay, P.; Mu, S.; Van De Walle, C. G.; Lal, A.; Xing, H.; Jena, D. Epitaxial ScxAl1-XN on GaN Exhibits Attractive

High-K Dielectric Properties. *Appl. Phys. Lett.* **2022**, *120* (15), n/a DOI: 10.1063/5.0075636.
(5) Wang, P.; Wang, D.; Vu, N. M.; Chiang, T.; Heron, J. T.; Mi, Z. Fully Epitaxial Ferroelectric ScAlN Grown by Molecular Beam Epitaxy. *Appl. Phys. Lett.* **2021**, *118* (22), n/a DOI: 10.1063/5.0054539.
(6) Liu, X.; Wang, D.; Kim, K. H.; Katti, K.; Zheng, J.; Musavigharavi, P.; Miao, J.; Stach, E. A.; Olsson, R. H.; Jariwala, D. Post-CMOS Compatible Aluminum Scandium Nitride/2D Channel Ferroelectric Field-Effect-Transistor Memory. *Nano Lett.* **2021**, *21* (9), 3753−3761.
(7) Liu, X.; Zheng, J.; Wang, D.; Musavigharavi, P.; Stach, E. A.; Olsson, R.; Jariwala, D. Aluminum Scandium Nitride-Based Metal-Ferroelectric-Metal Diode Memory Devices with High on/off Ratios. *Appl. Phys. Lett.* **2021**, *118* (20), n/a DOI: 10.1063/5.0051940.
(8) Chen, S. M.; Tsai, S. L.; Mizutani, K.; Hoshii, T.; Wakabayashi, H.; Tsutsui, K.; Chang, E. Y.; Kakushima, K. GaN High Electron Mobility Transistors (HEMTs) with Self-Upward-Polarized AlScN Gate Dielectrics toward Enhancement-Mode Operation. *Jpn. J. Appl. Phys.* **2022**, *61* (SH), SH1007.
(9) Guido, R.; Lomenzo, P. D.; Islam, M. R.; Wolff, N.; Gremmel, M.; Schönweger, G.; Kohlstedt, H.; Kienle, L.; Mikolajick, T.; Fichtner, S.; Schroeder, U. Thermal Stability of the Ferroelectric Properties in 100 Nm-Thick Al $_{0.72}$ Sc $_{0.28}$ N. *ACS Appl. Mater. Interfaces* **2023**, *15* (5), 7030−7043.
(10) Wolff, N.; Islam, M. R.; Kirste, L.; Fichtner, S.; Lofink, F.; Žukauskaitė, A.; Kienle, L. Al1-xScxN Thin Films at High Temperatures: Sc-Dependent Instability and Anomalous Thermal Expansion. *Micromachines (Basel)* **2022**, *13* (8), 1282.
(11) Islam, M. R.; Wolff, N.; Yassine, M.; Schönweger, G.; Christian, B.; Kohlstedt, H.; Ambacher, O.; Lofink, F.; Kienle, L.; Fichtner, S. On the Exceptional Temperature Stability of Ferroelectric Al1-XScxN Thin Films. *Appl. Phys. Lett.* **2021**, *118* (23), n/a DOI: 10.1063/5.0053649.
(12) Drury, D.; Yazawa, K.; Zakutayev, A.; Hanrahan, B.; Brennecka, G. High-Temperature Ferroelectric Behavior of Al0.7Sc0.3N. *Micromachines (Basel)* **2022**, *13* (6), 887.
(13) Kataoka, J.; Tsai, S. L.; Hoshii, T.; Wakabayashi, H.; Tsutsui, K.; Kakushima, K. A Possible Origin of the Large Leakage Current in Ferroelectric Al1-XScxN Films. *Jpn. J. Appl. Phys.* **2021**, *60* (3), 030907.
(14) Nie, R.; Shao, S.; Luo, Z.; Kang, X.; Wu, T. Characterization of Ferroelectric Al0.7Sc0.3N Thin Film on Pt and Mo Electrodes. *Micromachines (Basel)* **2022**, *13* (10), 1629.
(15) Schönweger, G.; Petraru, A.; Islam, M. R.; Wolff, N.; Haas, B.; Hammud, A.; Koch, C.; Kienle, L.; Kohlstedt, H.; Fichtner, S. From Fully Strained to Relaxed: Epitaxial Ferroelectric Al1-XScxN for III-N Technology. *Adv. Funct Mater.* **2022**, *32*, 2109632.
(16) Baeg, K. J.; Khim, D.; Kim, D. Y.; Koo, J. B.; You, I. K.; Choi, W. S.; Noh, Y. Y. High Mobility Top-Gated Poly(3-Hexylthiophene) Field-Effect Transistors with High Work-Function Pt Electrodes. *Thin Solid Films* **2010**, *518* (14), 4024−4029.
(17) Sonklin, T.; Munthala, D.; Leuasoongnoen, P.; Janphuang, P.; Pojprapai, S. Effect of Substrate-Tilting Angle-Dependent Grain Growth and Columnar Growth in ZnO Film Deposited Using Radio Frequency (RF) Magnetron Sputtering Method. *Journal of Materials Science: Materials in Electronics* **2022**, *33* (21), 16977−16986.
(18) Engwall, A. M.; Bayu Aji, L. B.; Baker, A. A.; Shin, S. J.; Bae, J. H.; McCall, S. K.; Moody, J. D.; Kucheyev, S. O. Effect of Substrate Tilt on Sputter-Deposited AuTa Films. *Appl. Surf. Sci.* **2021**, *547*, 149010.
(19) Miyake, H.; Lin, C. H.; Tokoro, K.; Hiramatsu, K. Preparation of High-Quality AlN on Sapphire by High-Temperature Face-to-Face Annealing. *J. Cryst. Growth* **2016**, *456*, 155−159.
(20) Bläsing, J.; Krost, A.; Hertkorn, J.; Scholz, F.; Kirste, L.; Chuvilin, A.; Kaiser, U. Oxygen Induced Strain Field Homogenization in AlN Nucleation Layers and Its Impact on GaN Grown by Metal Organic Vapor Phase Epitaxy on Sapphire: An x-Ray Diffraction Study. *J. Appl. Phys.* **2009**, *105* (3), n/a DOI: 10.1063/1.3074095.
(21) Bernacki, S.; Jack, L.; Kisler, Y.; Collins, S.; Bernstein, S. D.; Hallock, R.; Armstrong, B.; Shaw, J.; Evans, J.; Tuttle, B.; Hammetter, B.; Rogers, S.; Nasby, B.; Henderson, J.; Benedetto, J.; Moore, R.; Pugh, C. R.; Fennelly, A. Standardized Ferroelectric Capacitor Test Methodology for Nonvolatile Semiconductor Memory Applications. *Integr. Ferroelectr.* **1993**, *3* (2), 97−112.
(22) Fichtner, S.; Reimer, T.; Chemnitz, S.; Lofink, F.; Wagner, B. Stress Controlled Pulsed Direct Current Co-Sputtered Al 1-x Sc x N as Piezoelectric Phase for Micromechanical Sensor Applications. *APL Materials* **2015**, *3*, 116102.
(23) Fichtner, S.; Wolff, N.; Krishnamurthy, G.; Petraru, A.; Bohse, S.; Lofink, F.; Chemnitz, S.; Kohlstedt, H.; Kienle, L.; Wagner, B. Identifying and Overcoming the Interface Originating C-Axis Instability in Highly Sc Enhanced AlN for Piezoelectric Micro-Electromechanical Systems. *J. Appl. Phys.* **2017**, *122* (3), 035301.
(24) Yasuoka, S.; Mizutani, R.; Ota, R.; Shiraishi, T.; Shimizu, T.; Uehara, M.; Yamada, H.; Akiyama, M.; Funakubo, H. Tunable Ferroelectric Properties in Wurtzite (Al0.8Sc0.2)N via Crystal Anisotropy. *ACS Appl. Electron Mater.* **2022**, *4* (11), 5165−5170.
(25) Lu, Y.; Reusch, M.; Kurz, N.; Ding, A.; Christoph, T.; Prescher, M.; Kirste, L.; Ambacher, O.; Žukauskaitė, A. Elastic Modulus and Coefficient of Thermal Expansion of Piezoelectric Al1-xScxN (up to x = 0.41) Thin Films. *APL Mater.* **2018**, *6* (7), 076105.
(26) Höglund, C.; Alling, B.; Birch, J.; Beckers, M.; Persson, P. O. Å.; Baehtz, C.; Czigány, Z.; Jensen, J.; Hultman, L. Effects of Volume Mismatch and Electronic Structure on the Decomposition of ScAlN and TiAlN Solid Solutions. *Phys. Rev. B Condens Matter Mater. Phys.* **2010**, *81* (22), n/a DOI: 10.1103/PhysRevB.81.224101.
(27) Schönweger, G.; Islam, M. R.; Wolff, N.; Petraru, A.; Kienle, L.; Kohlstedt, H.; Fichtner, S. Ultrathin Al1-xScxN for Low-Voltage-Driven Ferroelectric-Based Devices. *Physica Status Solidi - Rapid Research Letters* **2023**, *17*, 2200312.
(28) Kasai, M.; Dohi, H. Growth Temperature and Relaxation of Lattice Strain in Epitaxial Pt Films Exhibiting Diffraction Fringes. *Surf. Sci.* **2019**, *689*, 121461.
(29) Fishman, G.; Calecki, D. Surface-Induced Resistivity of Ultrathin Metallic Films: A Limit Law. *Phys. Rev. Lett.* **1989**, *62* (11), 1302−1305.
(30) Jamali, T.; Farahani, S. V.; Jannesar, M.; Palasantzas, G.; Jafari, G. R. Surface Coupling Effects on the Capacitance of Thin Insulating Films. *J. Appl. Phys.* **2015**, *117* (17), 175308.
(31) Schönweger, G.; Wolff, N.; Islam, M. R.; Gremmel, M.; Petraru, A.; Kienle, L.; Kohlstedt, H.; Fichtner, S. In-Grain Ferroelectric Switching in Sub-5 Nm Thin Al0.74Sc0.26N Films at 1 V. *Advanced Science* **2023**, 2302296.
(32) Vu, H. T.; Nguyen, M. D.; Houwman, E.; Boota, M.; Dekkers, M.; Vu, H. N.; Rijnders, G. Ferroelectric and Piezoelectric Responses of (110) and (001)-Oriented Epitaxial Pb(Zr0.52Ti0.48)O3 Thin Films on All-Oxide Layers Buffered Silicon. *Mater. Res. Bull.* **2015**, *72*, 160−167.

https://doi.org/10.1021/acsami.3c05305
ACS Appl. Mater. Interfaces XXXX, XXX, XXX−XXX

4.3 Demonstration and STEM Analysis of Ferroelectric Switching in MOCVD-Grown Single Crystalline $Al_{0.85}Sc_{0.15}N$

Own contributions

- Design of Experiment
- Data analysis & interpretation
- Electrical characterization
- Manuscript preparation

RESEARCH ARTICLE

ADVANCED PHYSICS RESEARCH Open Access
www.advphysicsres.com

Demonstration and STEM Analysis of Ferroelectric Switching in MOCVD-Grown Single Crystalline $Al_{0.85}Sc_{0.15}N$

Niklas Wolff, Georg Schönweger, Isabel Streicher, Md Redwanul Islam, Nils Braun, Patrik Straňák, Lutz Kirste, Mario Prescher, Andriy Lotnyk, Hermann Kohlstedt, Stefano Leone, Lorenz Kienle,* and Simon Fichtner**

Wurtzite-type $Al_{1-x}Sc_xN$ solid solutions grown by metal organic chemical vapor deposition are for the first time confirmed to be ferroelectric. The film with 230 nm thickness and $x = 0.15$ exhibits a coercive field of 5.5 MV cm^{-1} at a measurement frequency of 1.5 kHz. The single crystal quality and homogeneous chemical composition of the film are confirmed by X-ray diffraction and spectroscopic methods such as time of flight secondary ion mass spectrometry. Annular bright field scanning transmission electron microscopy serves to prove the ferroelectric polarization inversion at the unit cell level. The single crystal quality further allows to image the large-scale domain pattern of a wurtzite-type ferroelectric for the first time, revealing a predominantly cone-like domain shape along the *c*-axis of the material. As in previous work, this again implies the presence of strong polarization discontinuities along this crystallographic axis, which can be suitable for current transport. The domains are separated by narrow domain walls, for which an upper thickness limit of 3 nm is deduced but which can potentially be atomically sharp. The authors are confident that these results will advance the commencement of the integration of wurtzite-type ferroelectrics to GaN as well as generally III-N-based heterostructures and devices.

1. Introduction

Solid solutions with wurtzite-type crystal structure are one of the newest material classes to have been confirmed as possessing ferroelectric properties.[1,2] They are characterized by some of the largest spontaneous polarizations and coercive fields among ferroelectrics in general, extreme temperature stability, as well as compatibility to the major Si and GaN-based semiconductor platforms.[3–7] The fact that the wurtzite-type ferroelectrics share the same crystal structure and are most often III-nitrides themselves offers the perspective of introducing novel heterostructures with a sort of native ferroelectricity to engineer novel GaN-based devices. One of the first devices considered in this context is the ferroelectric high electron mobility transistor (FE-HEMT),[5–8] which could ultimately allow reconfigurable normally-off functionality in normally-on devices. Due to economic benefits like high yield and ease-of-operation as well as very good single crystal quality, metal organic chemical vapor deposition (MOCVD) is today the dominant method for III-nitride-based HEMT fabrication. The availability of MOCVD-grown wurtzite-type ferroelectric single crystal $Al_{1-x}Sc_xN$ thin films would therefore be of great benefit to advance the integration of said materials to GaN technology. However, although the MOCVD growth of $Al_{1-x}Sc_xN$ has already

N. Wolff, M. R. Islam, L. Kienle, S. Fichtner
Department of Material Science
Kiel University
Kaiserstr. 2, D-24143 Kiel, Germany
E-mail: lk@tf.uni-kiel.de; sif@tfuni-kiel.de

N. Wolff, H. Kohlstedt, L. Kienle, S. Fichtner
Kiel Nano, Surface and Interface Science (KiNSIS)
Kiel University
Christian-Albrechts-Platz 4, D-24118 Kiel, Germany

The ORCID identification number(s) for the author(s) of this article can be found under https://doi.org/10.1002/apxr.202300113

DOI: 10.1002/apxr.202300113

G. Schönweger, H. Kohlstedt
Department of Electrical and Information Engineering
Kiel University
Kaiserstr. 2, D-24143 Kiel, Germany

G. Schönweger, S. Fichtner
Fraunhofer Institute for Silicon Technology (ISIT)
Fraunhoferstr. 1, D-25524 Itzehoe, Germany

I. Streicher, P. Straňák, L. Kirste, M. Prescher, S. Leone
Fraunhofer Institute for Applied Solid State Physics (IAF)
Tullastr. 72, D-79108 Freiburg, Germany
E-mail: stefano.leone@iaf.fraunhofer.de

N. Braun, A. Lotnyk
Leibniz Institute of Surface Engineering (IOM)
Permoserstr. 15, D-04318 Leipzig, Germany

ADVANCED SCIENCE NEWS
www.advancedsciencenews.com

ADVANCED PHYSICS RESEARCH
Open Access
www.advphysicsres.com

been demonstrated in the last years, targeting either HEMT or RF-filters, no demonstration of ferroelectricity has been reported so far.[9–12] In this work, we demonstrate for the first time that single crystalline $Al_{0.85}Sc_{0.15}N$ films grown on GaN templates by MOCVD are indeed ferroelectric. Apart from standard electrical characterization to deduce the displacement current originating from the polarization inversion and to confirm a particularly high coercive field of 5.5 MV cm^{-1}, we focus on high resolution scanning transmission electron microscopy (STEM) for the imaging of the atomic structure. Annular bright field (ABF)-STEM is employed not only to confirm the electric field induced polarization inversion on unit cell level, but also to reveal the formation of cone-like shaped domain patterns, which we think could be the dominant domain shape in all wurtzite-type ferroelectrics in general.

2. Results and Discussion

MOCVD allows the conformal deposition of $Al_{1-x}Sc_xN$ thin films with high rates and single crystalline quality over industrial scale 300 mm substrates—unlike sputtering and molecular beam epitaxy (MBE).[13–15] For this study, a 230 nm thick $Al_{0.85}Sc_{0.15}N$ film was grown onto a Si-doped GaN layer deposited on a *c*-plane sapphire substrate at a temperature of 1000 °C using a novel precursor molecule with increased vapor pressure as described in the experimental details. As the high growth temperatures can potentially result in phase instability of the wurtzite-type metastable $Al_{1-x}Sc_xN$ solid solutions[16,17] the crystal structure and chemical composition of the film has been characterized by high-resolution X-ray diffraction (HRXRD), time of flight secondary ion mass spectrometry (ToF-SIMS), and STEM methods. X-ray diffraction (XRD) analysis from the single crystalline film demonstrates $Al_{1-x}Sc_xN$ *c*-axis texture with a narrow rocking curve full-width at half maximum of 252 arcsec (Figure S1, Supporting Information) and showed no secondary reflections from secondary crystal orientations or phases. The ToF-SIMS depth profile of the 230 nm thick $Al_{0.85}Sc_{0.15}N$ layer deposited on the n-GaN buffer is shown in Figure S2, Supporting Information. No fluctuations in the chemical composition along the growth direction were observed. The intensity ratio of the $AlCs^+$ and $ScCs^+$ signals obtained in positive-ion detection mode was used to determine the Sc concentration to be $x = 0.13$, which is in good agreement with the determined Sc content of $x = 0.15$ via energy dispersive X-ray spectroscopy (EDS) (see Section 4). Both the $^{12}C^-$ and $^{18}O^-$ signal intensities of the $Al_{1-x}Sc_xN$ are elevated with respect to those of the *n*-GaN layer. Carbon can be introduced as a residual impurity in the reactor by the hydrocarbon-based precursor molecule and act as an electron trap. Sc has a high oxygen affinity compared to that of Al and Ga and residual oxygen impurities in the precursor (research grade) and/or in the reactor can lead to higher oxygen incorporation.

In addition to the XRD analysis, which, for example, could be unable to localize or detect coherent nanoscale cubic domains, the present film was examined for local chemical variations with EDS and local structural irregularities using scanning transmission electron microscopy. Selected area electron diffraction (SAED) experiments covered the complete film thickness by selecting an aperture corresponding to an investigated circular area of 250 nm in diameter. The elemental maps (Figure S3a, Supporting Information) of the Pt/SiN/$Al_{1-x}Sc_xN$/GaN heterostructure show no variation of the Sc concentration along film growth direction, and the average Sc content was determined as $x = 0.15$ by multiple EDS measurements. In agreement with XRD data, the SAED experiments do not indicate structural variation (Figure S3b, Supporting Information) in the probed sample volume, confirming the single-crystalline structure of the film.

2.1. Electrical Characterization

The ferroelectric nature of the heterostructure is unveiled via current density over electric field ($J - E$) measurements. **Figure 1** depicts the ferroelectric current response of a Pt/SiN (10 nm)/$Al_{0.85}Sc_{0.15}N$ (230 nm)/GaN capacitor with a 20 µm diameter. The in situ-deposited SiN acts as a protection layer to prevent the $Al_{0.85}Sc_{0.15}N$ layer from oxidation during handling.

The hysteretic current contributions typical of the wurtzite-type ferroelectrics are clearly discernible at high electric fields with superimposed leakage contributions.[18,19] The hysteretic behavior of the switching event is further confirmed via recording non-hysteretic currents by applying two consecutive unipolar voltage sweeps with the same polarity (Figure 1a –black curves). Additionally, the coercive field as well as the hysteretic area increase with increasing frequency (see Figure S4, Supporting Information), as is expected for ferroelectricity. The coercive field ($E_c \approx 5.5$ MV cm^{-1} at 1.5 kHz) is in the range of what is typically reported for sputter-deposited as well as for MBE-grown ferroelectric $Al_{0.85}Sc_{0.15}N$ thin films.[18,19] In order to compare the leakage current of our MOCVD-derived films with sputtering and MBE, we analyzed the current flow of the backward (post-switching) current branch at the widest opening of the hysteretic current contribution (as an approximation of E_c) (see Figure 1b). With ≈12.5 A cm^{-2} and ≈11.5 A cm^{-2}, MOCVD and MBE have fairly similar levels of leakage current. Sputtered films, in contrast, have a lower leakage current flow around the coercive field of ≈7.0 A cm^{-2}, as already pointed out in ref. [19]. The direct comparison of leakage current contributions in between samples can only be done qualitatively, since they can be influenced by several factors such as film thickness, Sc concentration, the structural quality and the chemical and electronic nature of the film—(electrode) substrate interface.[20] Lately, also the defect concentration was reported to play a key factor for leakage observed within sputtered $Al_{0.7}Sc_{0.3}N$ thin film samples.[21]

These findings lead to the conclusion that the deposition method and the associated crystal quality (which for MOCVD-grown films is significantly higher than for sputter-deposited films—see structural analysis below) is not the major factor defining the coercive field and leakage in $Al_{1-x}Sc_xN$ solid solutions. This may be due to the fact that sputter-deposited films consist of columnar grains with diameters in the range of 5 to 30 nm, which are highly *c*-axis oriented.[22] As shown in Section 2.2, the horizontal grain size is in the same order of magnitude as the horizontal width (10–20 nm) of the domains imaged in the monocrystalline-like MOCVD film of this study. The coinciding length scale of typical sputter deposited grains and the ferroelectrically induced polarization domains can explain why, to date, no fundamental differences in the ferroelectric response of epitaxial and non-epitaxial wurtzite-type ferroelectrics have

ADVANCED SCIENCE NEWS
www.advancedsciencenews.com

ADVANCED PHYSICS RESEARCH
Open Access
www.advphysicsres.com

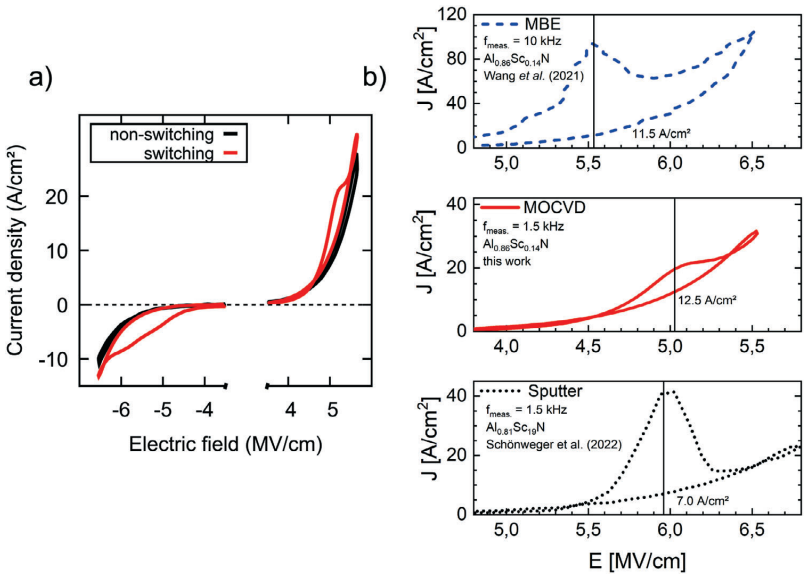

Figure 1. a) Current response of switching- and non-switching cycles measured at 1.5 kHz. Prior to the measurement, the capacitor was cycled for 2000 times, which favors the separation between leakage and ferroelectric displacement currents for this particular heterostructure—see discussion below. The unipolar non-switching response was measured by pre-poling the capacitor to the respective polarity. b) Comparison of switching current and leakage current contributions for MOCVD, MBE, and sputtered AlScN thin films on *n*-GaN.[18,19]

been observed. Thus, the absence of grain boundaries in the MOCVD-grown films (see Section 2.2) does not significantly impact the ferroelectric behavior and grain boundaries do not dominate the leakage mechanism of $Al_{1-x}Sc_xN$.

However, for this MOCVD-grown film, huge hysteretic currents at positive fields are observed when measuring as-deposited capacitors, while for negative fields the typical ferroelectric displacement current peak is present from the very first cycle (see Figure S5, Supporting Information). In one of our recent studies, we reported on hysteretic current contributions likely arising due to domain wall formation and conduction during polarization inversion.[23] Also in this MOCVD-grown film, polarization domain walls with horizontal components are evidenced in the cone-like shape domain patterns by STEM analysis (see Figure 4). However, in contrast to tail-to-tail domain walls (i.e., polarization direction of the adjacent domains pointing apart, resulting in a negatively charged domain wall) present in 5 nm thin films reported in our previous study,[23] in this heterostructure, head-to-head domain walls (i.e., polarization direction of the adjacent domains pointing toward each other, resulting in a positively charged domain wall) are forming during the switching process. Such head-to-head domain-walls typically exhibit a much higher conductivity as they can be compensated by electrons.[24,25] This could explain the huge hysteretic leakage current contributions observed during the first cycles. As visible in Figure S5, Supporting Information, for positive fields the hysteretic area decreases significantly with increasing number of switching cycles and the for $Al_{1-x}Sc_xN$ typical ferroelectric displacement current peaks also appear on the positive branch after cycling ≈1000 times. Positive-up negative-down (PUND) measurements of such a cycled sample, which correct for non-hysteretic leakage (see Figure S6, Supporting Information), suggest a remnant polarization of $P_{r,\,neg}$ = 154 μC cm^{-2} and $P_{r,\,pos}$ = 176 μC cm^2 for the negative and positive branches, respectively. Thus, the averaged P_r of this MOCVD-grown $Al_{0.85}Sc_{0.15}N$ ($P_r = (P_{r,\,neg} + P_{r,\,pos})/2 = 165$) is in the range of the typically reported P_r values of sputter-deposited as well as MBE-grown $Al_{1-x}Sc_xN$ films with similar Sc contents ($P_r \approx 150$ μ cm^{-2}).[26,27] However, the asymmetry suggests the presence of hysteretic leakage contributions likely arising due to domain-wall conduction upon ferroelectric switching, as discussed above. This can serve as an explanation as to why the measured remnant polarization exceeds theoretical expectations.

Similarly to epitaxially grown $Al_{1-x}Sc_xN$ on M-polar GaN templates via MBE or via sputter-deposition, the polarity of the as-deposited state of the MOCVD-grown $Al_{0.85}Sc_{0.15}N$ is M-polar, as evidenced by atomic resolution ABF-STEM (see Figure 3) and via the electrical measurements presented in **Figure 2**.[18,27] When applying an unipolar negative voltage sweep to an as-deposited capacitor (Figure 2a, red curve), no hysteretic current response and thus no ferroelectric switching of N-polar volume occurs. A subsequent negative voltage sweep results in exactly the same current response, confirming the absence of as-deposited N-polar volume (black curve). Contrarily, as depicted in Figures 1–3, when consecutively sweeping positive voltages on a pristine as-deposited capacitor, hysteretic current responses appear. The ferroelectric switching of as-deposited M-polar volume to N-polarity at positive voltage sweeps is confirmed by recording the current response of a subsequent negative voltage sweep on the same capacitor: A typical ferroelectric displacement

ADVANCED SCIENCE NEWS
www.advancedsciencenews.com

ADVANCED PHYSICS RESEARCH
Open Access
www.advphysicsres.com

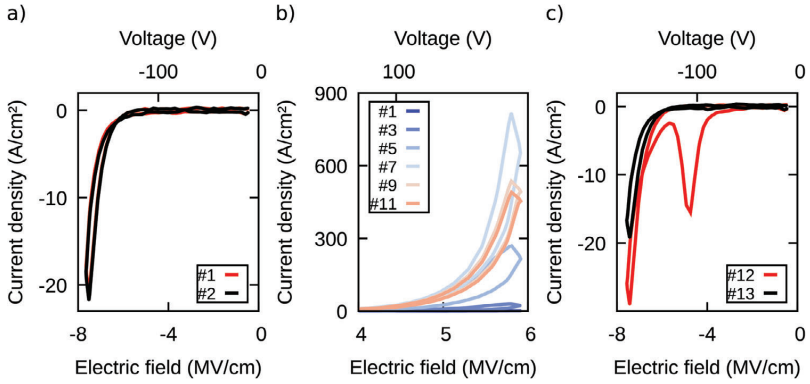

Figure 2. a) Two consecutive unipolar measurements performed on a pristine capacitor for negative electric fields reveal no as-deposited N-polarity. b) First eleven consecutive unipolar measurements performed on a pristine capacitor for positive electric fields. Hysteretic currents up to the 9th voltage pulse are visible, indicating as-deposited M-polarity which partially switches to N-polarity. c) Unipolar measurements for negative fields performed subsequently to the measurement described in (b). Clearly, a polarization switch from N-polarity to M-polarity is visible, which in turn gives evidence of prior switching from as-deposited M- to N-polarity. All measurements were performed at 1.5 kHz on capacitors with 20 µm diameter.

peak appears, evidencing the prior inversion of the full volume from the as-deposited M-polarity into N-polarity (Figure 2c).

In contrast to the typically N-polar growth of sputter-deposited $Al_{1-x}Sc_xN$ on non-polar templates,[1] retaining the polarity of the polar template lowers the polarization discontinuity and the associated energy at the interface. This driving force at the interface favoring M-polarity in $Al_{1-x}Sc_xN$ is likely the reason for the formation of the head-to-head domains present in this heterostructure. Due to that, when switching from full M-polarity to N-polarity, it is energetically more favorable to nucleate N-polar inversion domains at the top-interface (Pt/SiN), with subsequent domain growth toward the bottom interface (GaN). If this polarization reversal is not fully saturated, this results in N-polarity in the upper region of the film followed by M-polar domains in the lower region of the film, which corresponds to the head-to-head domain configuration confirmed by ABF-STEM experiments. This is in strong contrast to the aforementioned sputtered films grown on metal electrodes, with no driving force for M-polarity from the bottom interface. This results in N-polar residues at the latter when transitioning from M-polarity.[23,28] As a consequence, only tail-to-tail domain walls were observed.

2.2. Structural Characterization

As demonstrated in our previous works on sputtered $Al_{1-x}Sc_xN$ thin films, unambiguous evidence of ferroelectric polarization inversion can be reliably provided by the contrast produced by ABF-STEM.[18,23,28] This can be achieved by imaging the resulting unit cell inversion along the *c*-axis of the film parallel to the crystallographic $[2\bar{1}\bar{1}0]$ orientation. To understand the evolution of the atomic structure of MOCVD-grown $Al_{0.85}Sc_{0.15}N$ thin films subjected to large electric fields during cycling, both the as-deposited and the switched atomic states are compared. Unlike previous STEM investigations on sputtered material, the superior film quality enables the direct interpretation of the atomic polarization direction over large areas by the ABF-STEM image contrast examined in the as-deposited capacitor structure shown in **Figure 3**a. This structural quality is characterized by TEM examination showing single-crystalline areas with negligible in-plane tilt, which is in differentiation to in-plane tilt angles of 20–30 mrad for sputtered but epitaxial films on GaN or the allowed free in-plane rotation systems in the case of fiber textured films on electrode/Si substrates. This in-plane tilt strongly limited the field-of-view for on-atomic column STEM investigations in previous studies.[18,22,23,29,30]

The center ABF-STEM micrograph shows the $Pt/SiN/Al_{0.85}Sc_{0.15}N/GaN$ epitaxial heterostructure and the absence of structural defects, which would appear with darker contrast due to electron scattering and changes of the diffraction conditions. The atomic polarization of the as-deposited $Al_{0.85}Sc_{0.15}N$ film is determined to be M-polar growing from the GaN interface to the top of the film, consistent with the electrical data. Additionally, ferroelectric switching on unit cell level of a pre-cycled (400×) capacitor was investigated as well. Here, N-polarity is expected due to the prior application of four consecutive unipolar positive voltage signals with $E > E_c$. An ABF-STEM image of such a switched film is presented in Figure 3b, showing the appearance of cone-like contrast features within the switched part of the thin film that are absent in the pristine film.

Further STEM investigation of the switched film presented in **Figure 4** highlights the appearance of domains with N-polarity extending from the top Pt/SiN interface into the bulk of the film, providing direct confirmation for ferroelectricity in the MOCVD-grown $Al_{0.85}Sc_{0.15}N$ film. In more detail, the single crystal quality, which is not disturbed by visible grain boundaries, allowed the direct observation of electric-field induced structural modifications, for example, inversion domains and their boundaries. The appearance of these structures is observed in the overview ABF-STEM micrograph (Figures 3b and 4a, center) showing the formation of a zigzag and cone-like shaped contrast patterns in the bottom third of the film facing the GaN interface. The contrast patterns start to extend in ≈30–50 nm distance from the

ADVANCED SCIENCE NEWS
www.advancedsciencenews.com

ADVANCED PHYSICS RESEARCH
Open Access
www.advphysicsres.com

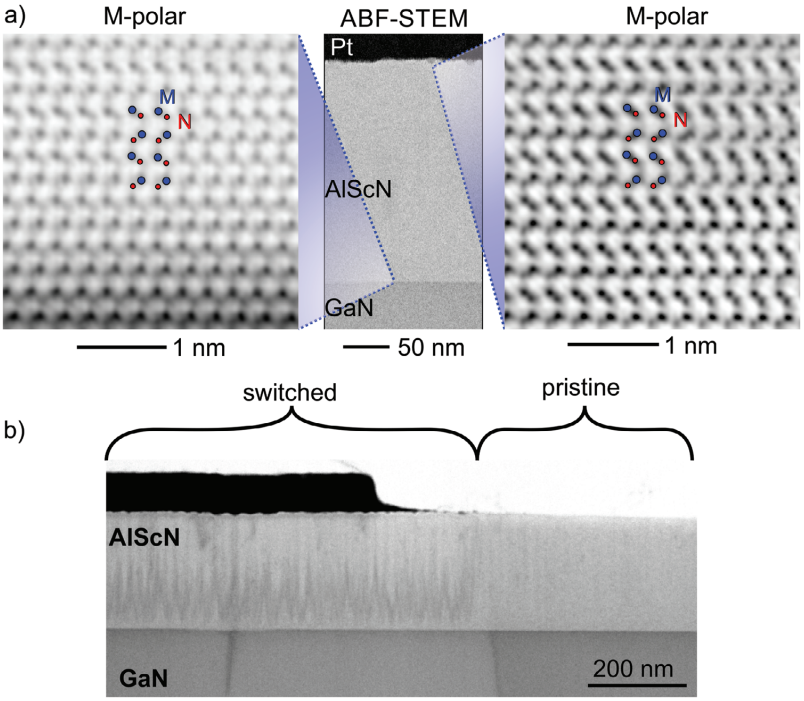

Figure 3. a) ABF-STEM investigation of the pristine MOCVD-grown $Al_{0.85}Sc_{0.15}N$ layer (center image). The atomic polarization of the pristine film under the capacitor is identified to grow completely M-polar from the bottom interface (left image) toward the top electrode (right image). b) ABF-STEM image showing the cone-like domain pattern in the switched region of the film in direct comparison to the pristine region.

GaN interface, are 10–20 nm wide and reach up to the center of the film. Atomic resolution ABF-STEM micrographs recorded in the top 50 nm show the full inversion of the atomic structure to N-polarity (Figure 4a, right). In contrast, atomic resolution ABF-STEM micrographs recorded at the GaN interface (Figure 4a, left) and within this 30–50 nm transition region show remaining domains with M-polarity. The formation of this domain pattern is expected from our observation of domain patterns in 5 nm $Al_{1-x}Sc_xN$ films with horizontal (cone-like) contributions.[23] The nucleation mechanism of the N-polar domain starts at the top electrode and subsequently progresses into the bulk of the film, forming cone-like shapes toward the pinned M-polar domain at the substrate interface.

The boundaries between the M- and N-polar regions were studied in more detail by ABF-STEM. This revealed a discontinuity of the M-polar domain displayed on the right side of Figure 4b, which changed incrementally across four unit cells to the N-polar configuration observed on the left side of the micrograph. In this transition region, the N-polar double spot pattern changes to a characteristic triplet of spots by superposition with the M-polar double spot pattern. The ABF intensity across the transition region is evaluated from profiles centered on the atomic positions of the metal atoms of N- (red line) and M-polar (blue line) unit cells. Apparently, the metal atom position of the N-polar unit cell is horizontally leveled with the nitrogen atom position of the M-polar unit cell, meaning the two atomic planes switched their position along the *z*-direction. This corresponds to a shift of the metal atom position by $\Delta d \approx 0.75$ Å and is consistent with experimental data on face-to-face inversion domain boundaries in GaN.[31] However, in this observation, no direct face-to-face boundary but subtle changes of ABF intensity between both domains are displayed within the individual spots of the triple spot pattern. The decrease in intensity of the N-polar metal atom position (red line) suggests the reduction of atom density in the probed metal atom column (first spot) and the change to the nitrogen atom column of the M-polar unit cell (second spot). The same consideration holds true for the blue profiles starting on the N-polar nitrogen atom column, which intensity decreases in favor of the metal atom position belonging to the M-polar domain in the upper left spot of the triplet. Hence, the view onto an inclined inversion domain boundary (i.e., two overlapping wedge-like domain volumes) leading to the observed intensity distributions is suggested.

For rationalization of this assumption, a structure model containing a regular inclined inversion domain boundary was constructed. First, the wurtzite-type unit cell was transformed into an orthohexagonal (*P*1, 5*a* 6*b c*) unit cell to create a model with a transition region spanning four unit cells. The M-polar cell was constructed from the N-polar cell by inversion of the axes *b* and *c*. Next, a (110)-inclined boundary was constructed by

ADVANCED SCIENCE NEWS
www.advancedsciencenews.com

ADVANCED PHYSICS RESEARCH
Open Access
www.advphysicsres.com

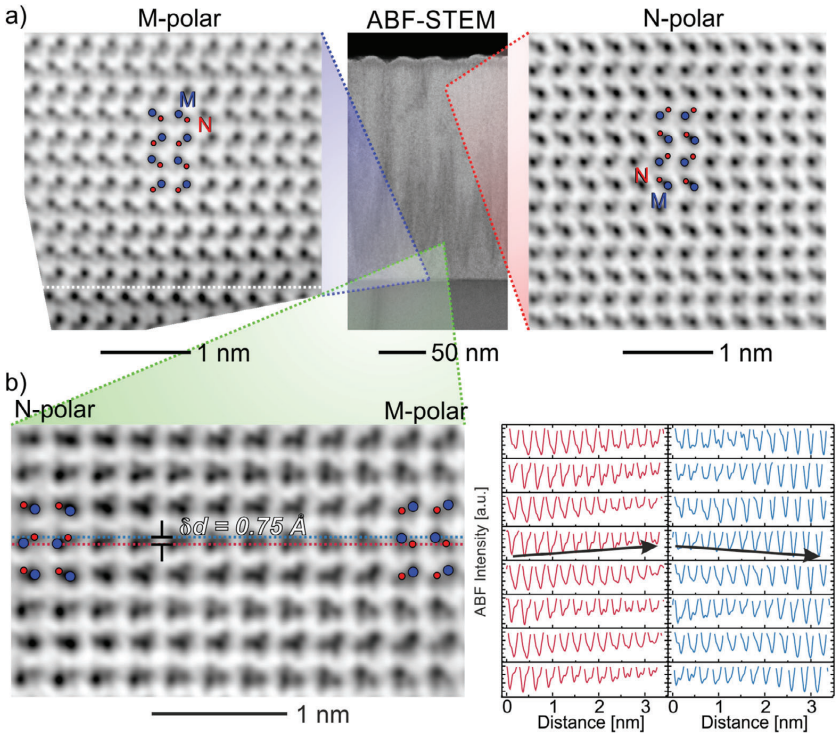

Figure 4. ABF-STEM investigation of the MOCVD-grown $Al_{0.85}Sc_{0.15}N$ layer switched to N-polarity. a) Atomic resolution micrographs showing the remaining M-polar domains at the GaN interface (dotted white line) and the inversion of the unit cell to N-polarity in areas toward the top electrode. Distinct structural features are observed in the ABF-STEM image assigned to the introduction of domain walls between domains with opposite polarity. b) ABF-STEM image of a horizontal discontinuity of the M-polar domain changing to the N-polar domain across a span of four unit cells. Intensity profiles drawn across this transition region from left to right are centered on the metal atom position of the of N- and M-polar unit cells in each row of atoms.

systematically deleting unit cells from the supercell, as shown in Figure S7, Supporting Information. Next, both cells were combined, and simulations of the ABF-contrast were conducted along the *b*–*c* projection orientation presented in **Figure 5**. The overlap of atoms in the projection direction resembles a structure motif consisting of nitrogen and metal atom dumbbells across the constructed transition region, similar to the low energetic transition structure reported for AlN.[32] Although the simulated contrast distribution does not perfectly resemble the more pronounced intensity within the experimentally observed triple spot structure, the intensity profiles do provide a decent match regarding the gradient of the intensity distribution across the transition region. A similar structural motif has been lately reported in the context of a proposed intermediate structure occurring during polarization switching in wurtzite-type $Al_{1-x}B_xN$.[33] In this structure, the Al-tetrahedra are iteratively inverted, resulting in a total non-polar structure and a comparable triple spot structure in experimental and simulated STEM images of the atomic structure. If this intermediate were spread evenly throughout the observed transition zone, no contrast variation would have been observed from left to right, unlike in our measurements. If,

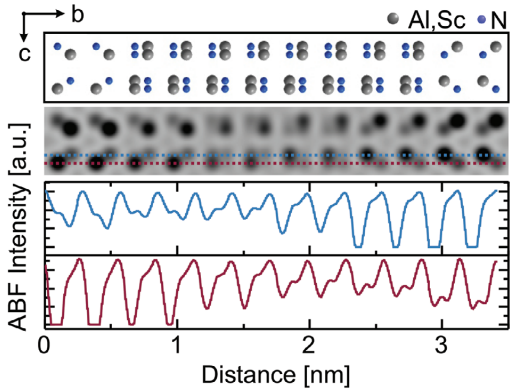

Figure 5. Supercell structure model of a simple inclined inversion domain boundary viewed along the *b*–*c* plane ($[2\bar{1}\bar{1}0]$ zone axis) and the corresponding simulated image and intensity profiles.

ADVANCED SCIENCE NEWS
www.advancedsciencenews.com

ADVANCED PHYSICS RESEARCH Open Access
www.advphysicsres.com

on the other hand, this intermediate would be stabilized with a defined gradient of switched Al-tetrahedra across the transition region, it would be almost impossible to discriminate between wedge-shaped domains of single polarity or a mixed polar intermediate structure. Nonetheless, the inclined superposition of the two wedge-shaped polar domains is currently the most likely explanation, especially considering that no stable non-polar state has been predicted for $Al_{1-x}Sc_xN$ yet.[34] Still, more experimental STEM work has to be carried out to understand the atomic structures of the inversion domain boundaries and the dynamics during the switching processing of $Al_{0.85}Sc_{0.15}N$ and wurtzite-type ferroelectric materials in general.

3. Conclusion

The ferroelectric operation of single crystal quality 230 nm thin MOCVD-grown $Al_{0.85}Sc_{0.15}N$ deposited onto a GaN template was demonstrated. Electrical $J-E$ measurements reveal a high coercive field of $E_c \approx 5.5$ MV cm^{-1} at 1.5 kHz and PUND measurements suggest a remnant polarization of $P_r = 165\,\mu C\,cm^{-2}$. The as-grown polarity of the $Al_{0.85}Sc_{0.15}N$ layer was determined to be fully M-polar. Furthermore, during the first switching cycles, large hysteretic currents are contributing to the ferroelectric displacement currents at positive fields. Both effects are most likely related to the growth onto the M-polar GaN template. Retaining M-polarity in $Al_{0.85}Sc_{0.15}N$ minimizes the polarization discontinuity at the interface. Contrarily, the introduction of polarization domain boundaries with horizontal components, as evidenced via STEM, implies the presence of strong polarization discontinuities in $Al_{0.85}Sc_{0.15}N$ along the crystallographic *c*-axis, which could be suitable for current transport. Due to the driving force for M-polarity at the interface to the GaN, these discontinuities are in a head-to-head like configuration with typically associated enhanced conductivity. Therefore, domain-wall formation and conduction during the first switching cycles could explain the observed high hysteretic currents. ABF-STEM investigations of as-deposited and switched thin films resolved the evolution of the nanostructure from a single M-polar domain state into M-polar and N-polar domains after ferroelectric cycling of the material. The single crystal quality of the grown film further allowed us to image the large-scale domain pattern for the first time, due to the absence of grain boundaries. The change of ABF-contrast after switching revealed a predominantly cone-like domain shape along the *c*-axis of the material, which is consistent with our previous observations of domain boundaries with horizontal components in 5 nm thin $Al_{1-x}Sc_xN$ films. These cone-like structures were identified as 2–3 nm-wide boundaries between the original M-polar and switched N-polar regions via resolving the atomic structure change by ABF-STEM and supercell simulation. In the projection direction, the visible triple spot structure and the progressing change in contrast intensity across the individual spots within the boundary region were explained by the simulation of an inclined superposition structure. These films are ideal candidates for future experiments targeting the atomic structure of the inversion domain boundaries in more detail and in situ switching experiments. As an outlook, the demonstration of ferroelectricity in $Al_{1-x}Sc_xN$ thin films grown by MOCVD will advance the commencing integration of wurtzite-type ferroelectrics to GaN as well as generally III-N-based heterostructures and devices due to its cost-effectiveness and conformal deposition on large-scale substrates.

4. Experimental Section

A close-coupled showerhead MOCVD reactor equipped with a proprietary setup for the generation of an adequate molar flow of the low-vapor pressure scandium precursor was used for growth.[35] A 230 nm-thick $Al_{0.85}Sc_{0.15}N$ layer was grown on a 2 µm-thick Si-doped GaN layer deposited on a 4″ *c*-plane sapphire substrate. The new Sc precursor $(EtCp)_2Sc(bdma)$ provided by Dockweiler Chemicals GmbH that, thanks to its increased vapor pressure, allowed for increased growth rates was employed and heated to 100 °C. Ammonia (NH_3) was used as N source, trimethylaluminum as the group 13- or IIIA-precursor. The carrier gas was hydrogen. A 10 nm-thick SiN_x in situ passivation layer was deposited on top of the $Al_{0.85}Sc_{0.15}N$ to protect the layer from oxidation during ex situ handling. The growth temperature was 1000 °C and the Sc/Al flow ratio was 50, similar to the descriptions in previous reports.[9,14] The chemical composition of the layers was characterized by ToF-SIMS. The ToF-SIMS depth profile of the MOCVD-grown heterostructure was obtained in a dual beam mode using a sputter beam of 1 keV Cs^+ ions together with a primary beam of 30 keV $^1Bi^+$ ions for the crater analysis. The Sc concentration was evaluated by relating the $AlCs^+/ScCs^+$ signal ratio to that of magnetron-sputtered AlScN reference samples, previously calibrated by energy elastic recoil detection analysis.[16] The average concentration of scandium in the AlScN layer was determined to be $x = 13.4$.

100 nm thick Pt was deposited on top of the heterostructure via magnetron sputtering (Von Ardenne CS 730S) and top-electrodes were structured via lithography and ion beam etching. Electrical measurements were performed using an AixACCT TF Analyzer 2000. The top-electrode was used as the drive contact and the bottom-electrode as the sense contact. The bottom electrode was accessed via an electrically shortened large-area capacitor. All $J-E$ measurements were performed using a triangular voltage signal starting from zero volt and sweeping first through the negative branch followed by a sweep of the positive branch. If not stated otherwise, the $J-E$ measurements were performed at 1.5 kHz. PUND measurements were performed using a triangular voltage signal.

XRD analysis of the sample was performed in a Rigaku Smartlab SE instrument (9 kW, Cu-Kα, Hypix-3000 pixel detector) equipped with a 2-bounce Ge(220) monochromator at the incident side.

Cross-section samples were cut and extracted from the $Pt/SiN/Al_{0.85}Sc_{0.15}N/GaN$ capacitor structures orthogonal to the $2\bar{1}\bar{1}0$ orientation and thinned to electron transparency by the focused ion-beam (FIB) method. Final polishing with 50 eV Ar^+-ions was performed using a Model1040 NanoMill system (Fischione Instruments). Atomic scale investigation of the local atomic polarization was conducted on a probe C_S-corrected JEOL (ARM200F) NEOARM scanning transmission electron microscope operated at an acceleration voltage of 200 kV. The ABF-STEM imaging mode was chosen for the identification of low-angle scattering nitrogen atom positions in the unit cell using a collection angle range of 10–20 mrad. Scan distortions and sample drift during image acquisition were minimized by fast serial recording of multi-frame images, followed by post-processing image alignment. The rigid and non-rigid image registration of typically 12 images recorded at a scan speed of 12 µs per row was performed using the Smart Align algorithm[36] (HREM Research Inc.) on the DigitalMicrograph v.3.5.1 (DM) (Gatan, Inc.) software. Fourier-filtering of non-rigidly processed ABF-STEM micrographs was applied using a simple radiance difference filter (lite version of the DM plug-in HREM-Filters Pro/Lite v.4.2.1, HREM Research Inc.) to remove high-frequency noise from the post-processed image. ABF image simulations were performed using the Dr.Probe software[37] and idealized microscope parameters (semi-coherent probe, probe forming aperture 35 mrad), setting all aberrations to zero. The film stoichiometry was determined by EDS using a dual silicon drift detector system with 100 mm^2 of active area each. The denoted scandium content *x* is defined as the number of Sc atoms relative to the total number of metal atoms (Sc + Al) with an estimated uncertainty of ±0.01.

ADVANCED SCIENCE NEWS
www.advancedsciencenews.com

ADVANCED PHYSICS RESEARCH
Open Access
www.advphysicsres.com

Supporting Information

Supporting Information is available from the Wiley Online Library or from the author.

Acknowledgements

N.W. and G.S. as well as the principal investigators S.L., L.K., and S.F. contributed equally to this work. This collaborative work is enabled through funding by the Federal Ministry of Education and Research (BMBF) in projects "ForMikro-SALSA" (Project-ID 16ES1053) and ProMat_KMU "PuSH" Grant Number 03XP0387B and the Deutsche Forschungsgemeinschaft (DFG, German Research Foundation)—Project-ID 434434223—SFB 1461; Project-ID 286471992—SFB 1261 as well as Project-ID 458372836 and Project-ID 448667535. The authors thank Lars Thormählen for the deposition of the Pt layer.

Open access funding enabled and organized by Projekt DEAL.

Conflict of Interest

The authors declare no conflict of interest.

Data Availability Statement

The data that support the findings of this study are available from the corresponding author upon reasonable request.

Keywords

AlScN, III-nitrides, nanostructure, STEM, wurtzite ferroelectrics

Received: October 9, 2023
Revised: November 13, 2023
Published online:

[1] S. Fichtner, N. Wolff, F. Lofink, L. Kienle, B. Wagner, *J. Appl. Phys.* **2019**, *125*, 114103.
[2] P. Wang, D. Wang, S. Mondal, M. Hu, J. Liu, Z. Mi, *Semicond. Sci. Technol.* **2023**, *38*, 043002.
[3] M. R. Islam, N. Wolff, M. Yassine, G. Schönweger, B. Christian, H. Kohlstedt, O. Ambacher, F. Lofink, L. Kienle, S. Fichtner, *Appl. Phys. Lett.* **2021**, *118*, 232905.
[4] S. Fichtner, G. Schönweger, F. Dietz, H. Hanssen, H. Züge, T.-N. Kreutzer, F. Lofink, H. Kohlstedt, H. Kapels, M. Mensing, in *2023 7th IEEE Electron Devices Technology and Manufacturing Conference (EDTM)*, IEEE, Piscataway, NJ **2023**, pp. 1–3.
[5] J. Casamento, K. Nomoto, T. S. Nguyen, H. Lee, C. Savant, L. Li, A. Hickman, T. Maeda, J. Encomendero, V. Gund, A. Lal, J. C. M. Hwang, H. G. Xing, D. Jena, in *2022 International Electron Devices Meeting (IEDM)*, IEEE, Piscataway, NJ **2022**, pp. 11.1.1–11.1.4.
[6] J. Y. Yang, S. Y. Oh, M. J. Yeom, S. Kim, G. Lee, K. Lee, S. Kim, G. Yoo, *IEEE Electron Device Lett.* **2023**, *4*, 1260.
[7] Z. Zhao, Y. Dai, F. Meng, L. Chen, K. Liu, T. Luo, Z. Yu, Q. Wang, Z. Yang, J. Zhang, W. Guo, L. Wu, J. Ye, *Appl. Phys. Express* **2023**, *16*, 031002.
[8] D. Wang, P. Wang, M. He, J. Liu, S. Mondal, M. Hu, D. Wang, Y. Wu, T. Ma, Z. Mi, *Appl. Phys. Lett.* **2023**, *122*, 090601.
[9] I. Streicher, S. Leone, C. Manz, L. Kirste, M. Prescher, P. Waltereit, M. Mikulla, R. Quay, O. Ambacher, *Cryst. Growth Des.* **2023**, *23*, 782.
[10] S. Krause, I. Streicher, P. Waltereit, L. Kirste, P. Brückner, S. Leone, *IEEE Electron Device Lett.* **2023**, *44*, 17.
[11] J. Ligl, S. Leone, C. Manz, L. Kirste, P. Doering, T. Fuchs, M. Prescher, O. Ambacher, *J. Appl. Phys.* **2020**, *127*, 195704.
[12] C. G. Moe, J. Leathersich, D. Carlstrom, F. Bi, D. Kim, J. B. Shealy, *Phys. Status Solidi A* **2023**, *220*, 2200849.
[13] C. Manz, S. Leone, L. Kirste, J. Ligl, K. Frei, T. Fuchs, M. Prescher, P. Waltereit, M. A. Verheijen, A. Graff, M. Simon-Najasek, F. Altmann, M. Fiederle, O. Ambacher, *Semicond. Sci. Technol.* **2021**, *36*, 034003.
[14] I. Streicher, S. Leone, L. Kirste, C. Manz, P. Straňák, M. Prescher, P. Waltereit, M. Mikulla, R. Quay, O. Ambacher, *Phys. Status Solidi RRL* **2023**, *17*, 2200387.
[15] D. Wang, P. Wang, S. Mondal, S. Mohanty, T. Ma, E. Ahmadi, Z. Mi, *Adv. Electron. Mater.* **2022**, *8*, 2200005.
[16] A. Zukauskaite, G. Wingqvist, J. Palisaitis, J. Jensen, P. O. Å. Persson, R. Matloub, P. Muralt, Y. Kim, J. Birch, L. Hultman, *J. Appl. Phys.* **2012**, *111*, 093527.
[17] X. Zhang, E. A. Stach, W. J. Meng, A. C. Meng, *Nanoscale Horiz.* **2023**, *8*, 674.
[18] G. Schönweger, A. Petraru, M. R. Islam, N. Wolff, B. Haas, A. Hammud, C. Koch, L. Kienle, H. Kohlstedt, S. Fichtner, *Adv. Funct. Mater.* **2022**, *32*, 2109632.
[19] D. Wang, P. Wang, B. Wang, Z. Mi, *Appl. Phys. Lett.* **2021**, *119*, 111902.
[20] M. R. Islam, G. Schönweger, N. Wolff, A. Petraru, H. Kohlstedt, S. Fichtner, L. Kienle, *ACS Appl. Mater. Interfaces* **2023**, *15*, 41606.
[21] L. Chen, Z. Wang, C. Liu, M. Li, W. Song, W. Wang, B. Varghese, H. K. Lee, H. Lin, Y. Zhu, in *2023 IEEE International Symposium on Applications of Ferroelectrics (ISAF)*, IEEE, Piscataway, NJ **2023**, pp. 1–3.
[22] G. Schönweger, M. R. Islam, N. Wolff, A. Petraru, L. Kienle, H. Kohlstedt, S. Fichtner, *Phys. Status Solidi RRL* **2022**, *17*, 2200312.
[23] G. Schönweger, N. Wolff, M. R. Islam, M. Gremmel, A. Petraru, L. Kienle, H. Kohlstedt, S. Fichtner, *Adv. Sci.* **2023**, *10*, 2302296.
[24] T. Sluka, A. K. Tagantsev, P. Bednyakov, N. Setter, *Nat. Commun.* **2013**, *4*, 1808.
[25] E. A. Eliseev, A. N. Morozovska, G. S. Svechnikov, V. Gopalan, V. Y. Shur, *Phys. Rev. B* **2011**, *83*, 235313.
[26] S. Yasuoka, T. Shimizu, A. Tateyama, M. Uehara, H. Yamada, M. Akiyama, Y. Hiranaga, Y. Cho, H. Funakubo, *J. Appl. Phys.* **2020**, *128*, 114103.
[27] P. Wang, D. Wang, N. M. Vu, T. Chiang, J. T. Heron, Z. Mi, *Appl. Phys. Lett.* **2021**, *118*, 223504.
[28] N. Wolff, S. Fichtner, B. Haas, M. R. Islam, F. Niekiel, M. Kessel, O. Ambacher, C. Koch, B. Wagner, F. Lofink, L. Kienle, *J. Appl. Phys.* **2021**, *129*, 034103.
[29] D. Wang, P. Musavigharavi, J. Zheng, G. Esteves, X. Liu, M. M. A. Fiagbenu, E. A. Stach, D. Jariwala, R. H. Olsson III, *Phys. Status Solidi RRL* **2021**, *15*, 2000575.
[30] J. Su, S. Fichtner, M. Z. Ghori, N. Wolff, M. R. Islam, A. Lotnyk, D. Kaden, F. Niekiel, L. Kienle, B. Wagner, F. Lofink, *Micromachines* **2022**, *13*, 5.
[31] F. Liu, R. Collazo, S. Mita, Z. Sitar, S. J. Pennycook, G. Duscher, *Adv. Mater.* **2008**, *20*, 2162.
[32] N. Stolyarchuk, T. Markurt, A. Courville, K. March, J. Zúñiga-Pérez, P. Vennéguès, M. Albrecht, *Sci. Rep.* **2018**, *8*, 14111.
[33] S. Calderon, J. Hayden, S. M. Baksa, W. Tzou, S. Trolier-McKinstry, I. Dabo, J.-P. Maria, E. C. Dickey, *Science* **2023**, *380*, 1034.
[34] Z. Liu, X. Wang, X. Ma, Y. Yang, D. Wu, *Appl. Phys. Lett.* **2023**, *122*, 122901.
[35] S. Leone, J. Ligl, C. Manz, L. Kirste, T. Fuchs, H. Menner, M. Prescher, J. Wiegert, A. Žukauskaitė, R. Quay, O. Ambacher, *Phys. Status Solidi RRL* **2020**, *14*, 1900535.
[36] L. Jones, H. Yang, T. J. Pennycook, M. S. J. Marshall, S. V. Aert, N. D. Browning, M. R. Castell, P. D. Nellist, *Adv. Struct. Chem. Imaging* **2015**, *1*, 8.
[37] J. Barthel, *Ultramicroscopy* **2018**, *193*, 1.

4.4 Ultrathin $Al_{1-x}Sc_xN$ for Low-Voltage-Driven Ferroelectric-Based Devices

Own contributions

- Design of Experiment
- Data analysis & interpretation
- Sample fabrication
- Surface characterization
- Electrical characterization
- Structural characterization (partly)
- Manuscript preparation

RESEARCH ARTICLE

physica status solidi rrl
www.pss-rapid.com

Ultrathin $Al_{1-x}Sc_xN$ for Low-Voltage-Driven Ferroelectric-Based Devices

Georg Schönweger, Md Redwanul Islam, Niklas Wolff, Adrian Petraru, Lorenz Kienle, Hermann Kohlstedt, and Simon Fichtner**

Thickness scaling of ferroelectricity in $Al_{1-x}Sc_xN$ is a determining factor for its potential application in neuromorphic computing and memory devices. In this letter, ultrathin (10 nm) $Al_{0.72}Sc_{0.28}N$ films that are ferroelectrically switchable at room temperature are reported on. All-epitaxial $Al_{0.72}Sc_{0.28}N$/Pt heterostructures are grown by magnetron sputtering onto GaN/sapphire substrates followed by an in situ Pt capping approach to avoid oxidation of the $Al_{0.72}Sc_{0.28}N$ film surface. Structural characterization by X-Ray diffraction and transmission electron microscopy reveals the established epitaxy. The thus-obtained high-quality films in combination with in situ capping facilitate ferroelectric switching of $Al_{1-x}Sc_xN$ in the ultrathin regime. The analysis of the relative permittivity and coercive field dependence on $Al_{0.72}Sc_{0.28}N$ film thicknesses in the range from 100 nm down to 10 nm indicates only moderate scaling effects, suggesting that the critical thickness for ferroelectricity is not yet approached. Furthermore, the deposited layer stack demonstrates the possibility of including ultrathin ferroelectric $Al_{1-x}Sc_xN$ into all-epitaxial GaN-based devices using sputter deposition techniques. Thus, the integration and scaling potential of all-epitaxial ultrathin $Al_{1-x}Sc_xN$ offering high storage density paired with low-voltage operation desired for state-of-the-art ferroelectric memory devices are highlighted.

1. Introduction

The high coercive field (E_c) and the high, stable remanent polarization separate the ferroelectric properties recently discovered in materials with wurtzite-type structure from classical ferroelectrics.[1–4] This raises hopes for particularly good scalability of wurtzite-type-based ferroelectric devices. In addition, the complementary metal-oxide semiconductor compatibility and the well-established industrial deposition process make $Al_{1-x}Sc_xN$ thin films highly attractive for building novel neuromorphic computing and memory devices such as ferroelectric field-effect transistors (FeFET) and ferroelectric tunnel junctions (FTJs).[5–9] Furthermore, it is expected that wurtzite-type ferroelectrics such as $Al_{1-x}Sc_xN$ introduce ferroelectricity into III-N technology, resulting in a straightforward approach to realize, for example, GaN-embedded memory. Such ferroelectric all-epitaxial all-wurtzite type $Al_{1-x}Sc_xN$/GaN heterostructures were demonstrated recently.[10,11] However, a very low film thickness of the ferroelectric layer is needed for following the general trend of miniaturization and increasing storage density in all of the aforementioned devices. In this context, $Al_{1-x}Sc_xN$ offers high scalability due to its high E_c, making it possible to tailor the film thickness to the ultrathin regime to achieve reasonable memory windows and low operating voltages.[12] Furthermore, in terms of device design, ultrathin ferroelectric films are a prerequisite for building FTJs.[7] Reducing the thickness to the ultrathin regime (<30 nm) is often accompanied by a material-specific diminution of remanent polarization (P_r), a drastic increase of E_c, or results in a total loss of ferroelectricity.[13–15] To our best knowledge, up to now, no thickness scaling study on ferroelectric epitaxial $Al_{1-x}Sc_xN$ heterostructures was conducted. Also for nonepitaxial heterostructures, only a small number of studies were performed. Below 20 nm film thickness, measurements that suggest ferroelectricity at elevated temperatures or indirectly through scanning nonlinear dielectric microscopy are accessible.[16,17] Very recently, partly ferroelectric switching of ≈12 nm-thick $Al_{1-x}Sc_xN$ was reported by performing positive-up-negative-down (PUND) measurements at room temperature.[18] The availability of ferroelectric sub-20 nm films is however crucial in order to reach switching voltages in the low-single-digit volt range that is desired for advanced circuits as

G. Schönweger, A. Petraru, H. Kohlstedt
Institute of Electrical and Information Engineering
Kiel University
Kaiserstrasse 2, 24143 Kiel, Germany
E-mail: gmsc@tf.uni-kiel.de

M. R. Islam, N. Wolff, L. Kienle
Institute for Material Science
Kiel University
Kaiserstrasse 2, 24143 Kiel, Germany

G. Schönweger, S. Fichtner
Fraunhofer Institute for Silicon Technology (ISIT)
Fraunhoferstr. 1, D-25524 Itzehoe, Germany
E-mail: sif@tf.uni-kiel.de

The ORCID identification number(s) for the author(s) of this article can be found under https://doi.org/10.1002/pssr.202200312.

DOI: 10.1002/pssr.202200312

ADVANCED SCIENCE NEWS
www.advancedsciencenews.com

physica status solidi rrl
www.pss-rapid.com

well as sufficiently small line widths for large-scale integration. Here we present our recent results on the thickness scaling (from 100 nm down to 10 nm) of epitaxial $Al_{0.72}Sc_{0.28}N$ grown on epitaxial Pt via sputter deposition on GaN/sapphire substrates. This epitaxial growth enables significantly better crystal properties of $Al_{1-x}Sc_xN$ compared with previous studies on materials with cylindrical symmetry.[11,16,17,19] In addition, as reported in several studies, epitaxial growth of $Al_{1-x}Sc_xN$ induced an improved coupling coefficient and quality factor in resonators as well as a reduction of the coercive field due to strain effects.[11,20–22] In our study, the low root mean square (RMS) roughness (see Figure S1, Supporting Information) and the sharp interfaces combined with an in situ Pt capping result in an improved ferroelectric response. Consequently, we were able to record typical butterfly-shaped capacitance–voltage (C–U) loops as well as current density over the electric field (J–E) loops at room temperature, demonstrating clearly distinguishable ferroelectric switching down to 10 nm film thickness. Therefore, the general feasibility of ultrathin $Al_{1-x}Sc_xN$ for future device integration and low voltage operation is demonstrated. In addition, this integration of epitaxial ultrathin ferroelectric $Al_{1-x}Sc_xN$ into a III-N heterostructure further highlights the viability of introducing new functionality into III-N-based devices.

2. Device Fabrication and Characterization Methods

All films were grown by sputter deposition in an Oerlikon (now Evatec) MSQ 200 multisource system on top of commercially available GaN/sapphire substrates. A 12 nm-thick epitaxial Pt layer (bottom electrode) was DC-sputtered at 500 °C and 600 W under Krypton atmosphere at a deposition pressure of 5.4×10^{-3} mbar. The base pressure was below 5×10^{-7} mbar. The X-ray diffraction (XRD) measurements were carried out using monochromatic K_α radiation in a Seifert XRD 3000 PTS system (θ–2θ scan) as well as in a Rigaku SmartLab diffractometer (in-plane phi-scan, θ–2θ scan, rocking curve). The $Al_{0.72}Sc_{0.28}N$ thin films were grown by pulsed DC cosputtering at 450 °C. Details about the process can be found in other studies.[23,24] The 10- and 20 nm-thick $Al_{0.72}Sc_{0.28}N$ layers were capped in situ with 100 nm-thick Pt, while 50 and 100 nm were capped after vacuum break. The in situ Pt top electrode was deposited at 450 °C and 400 W under Krypton atmosphere at a deposition pressure of 6.7×10^{-3} mbar after reaching a base pressure of 5×10^{-7} mbar. Square top electrodes were structured via lithography and ion-beam etching (IBE, Oxford Instruments Ionfab 300). Dry etching stopped abruptly after detecting Sc via a secondary-ion mass spectrometer (SIMS), thus not etching through the $Al_{0.72}Sc_{0.28}N$ layer. Capacitance measurements were performed on a Hewlett Packard 4284 A Precision LCR meter. High-frequency J–E loops were measured using an AixACCT TF Analyzer 3000. A cross-section specimen of the in situ-capped 10 nm-thick $Al_{0.72}Sc_{0.28}N$ sample was prepared using a standard focused ion beam (FIB) procedure and analyzed using high-resolution transmission electron microscopy (HRTEM, Tecnai F30, operated at 300 kV, field emission gun) and fast Fourier-transform (FFT) patterns.

3. Results and Discussions

The current response depending on the applied electric field for capacitors with various $Al_{0.72}Sc_{0.28}N$ film thicknesses is depicted in **Figure 1**a. Ferroelectric switching peaks appear for film thicknesses down to 10 nm. Leakage currents commonly present in thin $Al_{1-x}Sc_xN$ films are emerging also in our all-epitaxial heterostructures.[17,19,25] In this context, a comparably low tan δ for the respective film thickness was found to be crucial to ferroelectrically switch films below 20 nm film thickness before electrical breakdown occurs.

Noticeably, with decreasing film thickness, an increase in the area of the current peaks in the $J - E$ loops as well as an increase in the total area of the dynamic leakage current compensated (DLCC) $P - E$ loops (Figure S2, Supporting Information) are visible.[26] However, as discussed in the Supporting information, the corrected $P - E$ loops of the ultrathin films are not fully leakage compensated, leading to unrealistically high P_r values. Thus, the apparent increase in P_r with decreasing film thickness could be due to a dynamic leakage contribution which is closely correlated to the switching event.

The coercive field slightly increases with decreasing film thickness. Therefore, especially for ultrathin films, we had to increase the maximum electric field applied. This goes hand in hand with an increase in the leakage currents as well as an

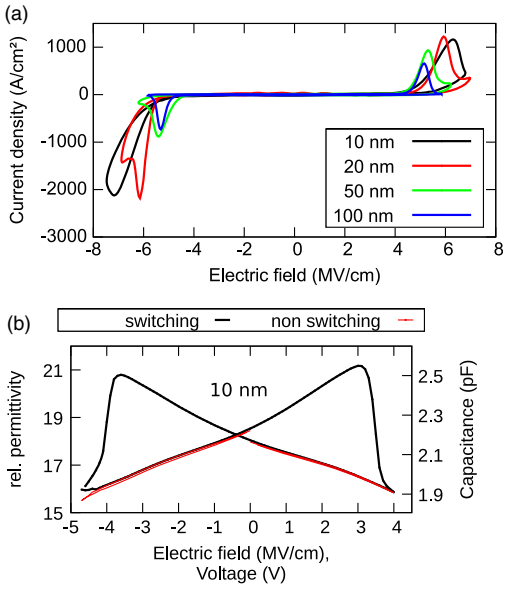

Figure 1. a) J–E loops of Pt(100 nm)/$Al_{0.72}Sc_{0.28}N$/Pt(12 nm) capacitors deposited on GaN/sapphire templates with varying $Al_{0.72}Sc_{0.28}N$ film thickness. All loops were measured at 80 kHz on $10 \times 10\,\mu m^2$ pads. b) Relative permittivity and capacitance as a function of the applied voltage and electric field for 10 nm-thick $Al_{0.72}Sc_{0.28}N$. The nonswitching half loops (red) were recorded by previously switching the capacitor to the respective polarity. Measured on $10 \times 10\ \mu m^2$ pads with a small signal of 0.1 V_{pp} at 100 kHz swept in 0.1 V steps with a delay of 300 ms per step.

ADVANCED SCIENCE NEWS
www.advancedsciencenews.com

physica status solidi rrl
www.pss-rapid.com

asymmetry in the current response, making it hard to identify clearly the switching peak at negative fields for the 10 nm-thick $Al_{0.72}Sc_{0.28}N$ film. However, the as-deposited polarization state of our films is nitrogen (N)-polar.[1] Consequently, ferroelectric switching at positive fields (from metal (M)-polar to N-polar) can only result after prior switching from N-Polarity to M-polarity at negative fields.

To further confirm ferroelectric switching of 10 nm-thick $Al_{0.72}Sc_{0.28}N$, *C–U* loops were recorded and are depicted in Figure 1b. The butterfly-shaped curve (black) demonstrates distinguishable ferroelectric switching.

In addition, nonswitching half loops (red) were recorded by measuring twice with the same polarity. No hysteretic behavior is observed for the nonswitching half-loops, thus giving additional evidence that the butterfly-shaped hysteresis for the switching loop originates from true ferroelectric switching. Previously, the coercive field in $Al_{1-x}Sc_xN$ thin films was observed to be almost independent of thickness for films thicker than ≈20 nm.[16,17,25] Similarly, in this study, E_c determined via *C–U* as well as via *J–E* loops, as depicted in **Figure 2**, does not change considerably when decreasing the film thickness from 100 to 50 nm. When decreasing the film thickness further to 20 nm and especially to 10 nm, a moderate increase of the coercive field by about 25% is observed. The difference in the coercive field determined via *C–V* and *J–E* curves for the respective thickness is a result of the frequency dependence of E_c. In *C–V* loops the electric field is swept very slowly (≈20 mHz), while in *J–E* loops the measurement frequency is much higher (80 kHz).

The coercive field scaling in $Al_{1-x}Sc_xN$ is in strong contrast to classical ferroelectrics, as illustrated in **Figure 3**. In the perovskites (e.g., $BaTiO_3$, $SrBi_2Ta_2O_9$, PZT) E_c is generally proportional to $d^{-2/3}$, according to the domain nucleation model elaborated from Kay–Dunn.[27] Dawber et al. included

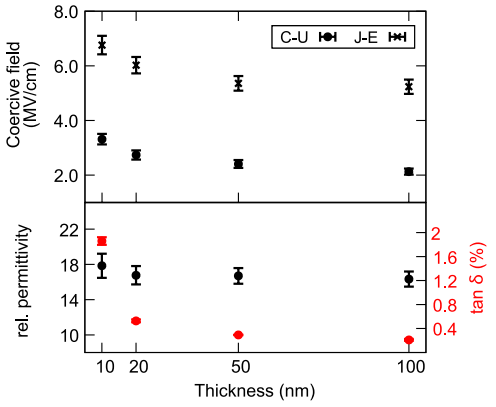

Figure 2. E_c, ε_r, and the loss tangent (tan δ) depending on $Al_{0.72}Sc_{0.28}N$ film thickness. ε_r and tan δ were measured at 100 kHz and 100 mV at 0 V bias. E_c was determined via measuring *C–U* loops, keeping the time for a full sweep constant for the various film thicknesses as well as via *J–E* using a sinus signal at 80 kHz. The error bars for E_c and ε_r were calculated using an estimated capacitor side-length error of 0.4 µm and an estimated thickness error of 5%. In addition, for E_c determination via *C–U* loops, the step width of the respective voltage sweep was included in the error calculation.

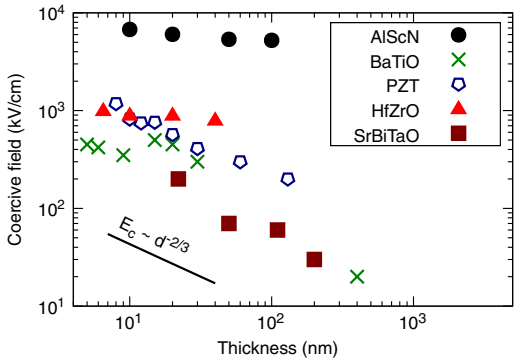

Figure 3. Coercive field scaling of PZT,[14,29–32] $BaTiO_3$, $SrBi_2Ta_2O_9$, Zr-doped HfO_2,[33] and of our $Al_{0.72}Sc_{0.28}N$ films.

contributions from the depolarization field due to incomplete screening at the electrodes to the Kay–Dunn model, being in good agreement with experimental data of ultrathin films.[28]

However, both models are apparently not able to describe the scaling behavior of the relatively new ferroelectrics HfO_2 and $Al_{1-x}Sc_xN$. For HfO_2, the nonscaling of E_c is explained by nanometer-scale confinement of the ferroelectric domains due to the grain-like multiphase structure, which is independent of film thickness.[33] Although the wurtzite phase of $Al_{1-x}Sc_xN$ is very stable and thus only one phase exists, a different domain shape as assumed by Kay and Dunn could explain the deviations from the classical E_c scaling. However, a low to moderate increase of E_c with decreasing film thickness is observed in our films and was reported recently also in other studies. For nonepitaxial films, this was attributed to a change of *c*-to-*a* lattice parameter ratio with decreasing $Al_{1-x}Sc_xN$ film thickness.[18] As a consequence, the internal parameter *u* decreased, which is known to result in an increase of the coercive field.[11] However, XRD measurements (not shown here) of our films reveal no scaling of *u*. Very recently the low E_c scaling of nonepitaxial $Al_{1-x}Sc_xN$ down to 20 nm film thickness was related to charge-injection effects through a very thin interfacial dielectric layer.[34,35] The lowering of E_c due to in situ capping of ultrathin films, as depicted in Figure S3, Supporting Information, supports this explanation. In addition, the prevention of an oxide layer formation in ultrathin films results in a lowering of the leakage currents, highlighting the improved ferroelectric response due to in situ Pt capping.

For Zr-doped HfO_2, a lower thickness limit for ferroelectricity of 5 nm was found and attributed to the formation of a dead layer if deposited on TiN or W bottom electrodes, while on a Pt bottom electrode, the dead layer formation could be suppressed and ferroelectric switching was demonstrated down to 2.5 nm thickness.[36] On the other hand, when HfO_2-based ferroelectrics become thicker (>≈50 nm), ferroelectricity becomes unstable due to the energetically more favourable paraelectric phase.[33] In general, the dramatic degradation or total loss of ferroelectric properties in ultrathin films due to such a nonswitching interfacial layer (dead layer[37]) is typically accompanied by a decrease of ε_r.[14,36,38] The moderate scaling

ADVANCED SCIENCE NEWS
www.advancedsciencenews.com

physica status solidi rrl
www.pss-rapid.com

of E_c and nonscaling of ε_r with thickness leads to our conclusion that the lower thickness limit in $Al_{1-x}Sc_xN$ is not yet approached at 10 nm, and stable ferroelectricity can be expected also for films <10 nm thickness. This highlights the thickness scalability of ferroelectric $Al_{1-x}Sc_xN$, ranging from at least 600 nm down to the single-digit nanometer range.[1]

Since, together with in situ capping, the bottom Pt interface can be considered crucial in order to obtain ferroelectric $Al_{1-x}Sc_xN$ films with very low thicknesses, we confirmed that our epitaxial electrodes are of significantly better texture than what can be expected of Pt films grown nonepitaxially over, for example, c-Si.[19,39] The structure of Pt grown on GaN/sapphire templates is revealed via the θ–2θ scan depicted in **Figure 4**a. The expected out-of-plane 111 orientation for Pt and 0002 orientation for GaN is visible. Laue oscillations, which are sensitive to crystalline disorder, appear for the Pt 111 reflection.[40]

The thus expected high crystallinity is confirmed by rocking curve (RC) measurements (not shown here) of the 111 Pt reflection; the full-width at half-maximum (FWHM) of 0.1° is indicative of a strain and defect-poor crystalline phase with high out-of-plane orientation. Furthermore, the distinct Laue oscillations allow for determining the thickness (t) of the ordered crystal volume.[40]

$$t = \frac{3\lambda}{2(\sin\theta_1 - \sin\theta_{-1})} \quad (1)$$

Using Equation (1), with θ_1 and θ_{-1} corresponding to the maximum of the peaks right and left from the center of the Pt 111 reflection, an average film thickness of 11 nm is determined.

The in-plane ordering was resolved by recording a phi-scan of the nonspecular 131 Pt reflection as well as the nonspecular 01–10 $Al_{0.72}Sc_{0.28}N$ reflection, as depicted in Figure 4b. A sixfold symmetry is visible, evidencing epitaxial (in-plane ordered) growth. The expected 0002 orientation of 10 nm-thick $Al_{0.72}Sc_{0.28}N$ grown on epitaxial Pt is revealed by the θ–2θ scan depicted in Figure 4c.

The intensity profile across the HRTEM micrograph of the Pt(100 nm)/$Al_{0.72}Sc_{0.28}N$(10 nm)/Pt(12 nm)/GaN/sapphire heterostructure is shown in **Figure 5** and film thicknesses of 10 nm for $Al_{0.72}Sc_{0.28}N$ and 12 nm for Pt are determined on local average. The latter is in excellent agreement with the Pt thickness calculated using Equation (1). The blurred interfaces present in the HRTEM image are attributed to the finite roughness of the heterostructure. The FFT pattern clearly reveals an epitaxial growth for both layers.

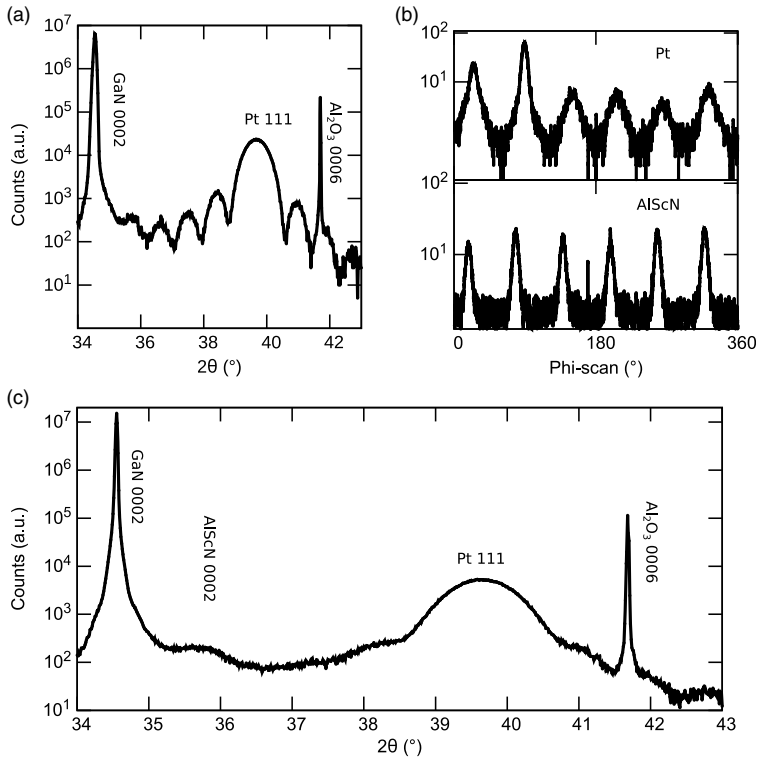

Figure 4. a) θ–2θ scan and b) (top) smoothed phi-scan for the nonspecular Pt 131 reflection of 12 nm Pt on GaN/sapphire as well as (bottom) smoothed phi-scan for the nonspecular $Al_{0.72}Sc_{0.28}N$ 01–10 reflection of 20 nm $Al_{0.72}Sc_{0.28}N$ on Pt(12 nm)/GaN/sapphire. c) θ–2θ scan of the film shown in (a) after deposition of 10 nm $Al_{0.72}Sc_{0.28}N$ followed by 5 nm in situ capping with Pt.

ADVANCED SCIENCE NEWS
www.advancedsciencenews.com

physica status solidi rrl
www.pss-rapid.com

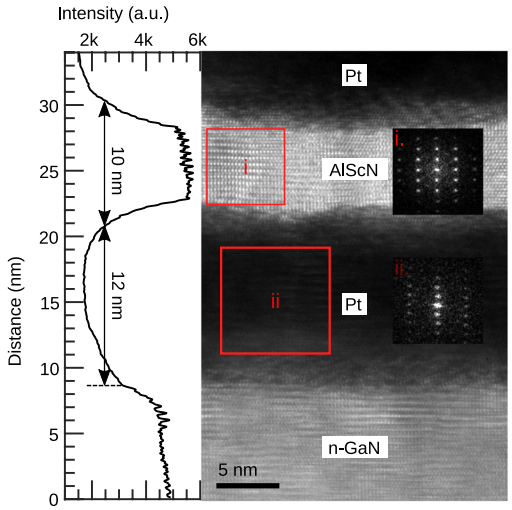

Figure 5. HRTEM image (right) and corresponding average thickness profile (left) of the Pt(100 nm)/$Al_{0.72}Sc_{0.28}N$(10 nm)/Pt(12 nm)/GaN/sapphire heterostructure. In the inset, the FFT pattern for i) $Al_{0.72}Sc_{0.28}N$ and ii) Pt is depicted.

The FWHM of the $Al_{1-x}Sc_xN$ 0002 RC decreases with decreasing film thickness, as illustrated in Figure S4, Supporting Information. This is in strong contrast to films grown on nonepitaxial Pt, where an increase of the RC with decreasing film thickness is observed.[16] Therefore, the crystal quality of the first few nanometers of $Al_{1-x}Sc_xN$ grown on epitaxial Pt is considerably higher than if grown on nonepitaxial Pt. Thus, the epitaxial growth in combination with the in situ capping of $Al_{1-x}Sc_xN$ to avoid oxidation has a significant impact on the ferroelectric switching behavior, especially for ultrathin films.

4. Conclusion

Distinguishable ferroelectric switching of 10 nm-thick $Al_{0.72}Sc_{0.28}N$ was demonstrated at room temperature. Only low-to-moderate changes in the coercive field and constant ε_r for films ranging from 100 nm down to 10 nm thickness were confirmed. Thus, no indications of instabilities of the ferroelectric phase or considerable contributions from dead layers are present. Therefore, it is expected that further potential remains to scale ferroelectric $Al_{1-x}Sc_xN$ to even lower thicknesses. This constitutes an important step toward integrated ferroelectric wurtzite-type thin films with low single-digit switching voltages. Thus, our results highlight the general feasibility of using $Al_{1-x}Sc_xN$ as an active layer for integrated electronic devices with low operating voltage and high storage density. Furthermore, the all-epitaxial growth on GaN/sapphire and the thus-obtained high-quality film and interfaces not only improve the ferroelectric response in the ultrathin regime but also make $Al_{1-x}Sc_xN$ highly attractive for the integration of ferroelectric functionality into all-epitaxial III-N devices.

Supporting Information

Supporting Information is available from the Wiley Online Library or from the author.

Acknowledgements

This work was supported by the project "ForMikro-SALSA" (grant no. 16ES1053) from the Federal Ministry of Education and Research (BMBF) and the Deutsche Forschungsgemeinschaft (DFG) under the scheme of the collaborative research centers (CRC) 1261 and 1461.
Open Access funding enabled and organized by Projekt DEAL.

Conflict of Interest

The authors declare no conflict of interest.

Data Availability Statement

The data that support the findings of this study are available from the corresponding author upon reasonable request.

Keywords

aluminum–scandium–nitride ($Al_{1-x}Sc_xN$), epitaxial growth, ferroelectrics, gallium nitride, ultrathin

Received: August 23, 2022
Revised: September 19, 2022
Published online:

[1] S. Fichtner, N. Wolff, F. Lofink, L. Kienle, B. Wagner, *J. Appl. Phys.* **2019**, *125*, 114103.
[2] K. Ferri, S. Bachu, W. Zhu, M. Imperatore, J. Hayden, N. Alem, N. Giebink, S. Trolier-McKinstry, J.-P. Maria, *J. Appl. Phys.* **2021**, *130*, 044101.
[3] J. Hayden, M. D. Hossain, Y. Xiong, K. Ferri, W. Zhu, M. V. Imperatore, N. Giebink, S. Trolier-McKinstry, I. Dabo, J.-P. Maria, *Phys. Rev. Mater.* **2021**, *5*, 044412.
[4] D. Wang, P. Wang, B. Wang, Z. Mi, *Appl. Phys. Lett.* **2021**, *119*, 111902.
[5] H. Mulaosmanovic, T. Mikolajick, S. Slesazeck, in *Topics in Applied Physics*, Springer, Singapore **2020**, pp. 399–411.
[6] T. Schenk, M. Pešić, S. Slesazeck, U. Schroeder, T. Mikolajick, *Rep. Progr. Phys.* **2020**, *83*, 086501.
[7] E. Y. Tsymbal, H. Kohlstedt, *Science* **2006**, *313*, 181.
[8] H. Kohlstedt, N. A. Pertsev, J. R. Contreras, R. Waser, *Phys. Rev. B* **2005**, *72*, 125341.
[9] X. Liu, D. Wang, J. Zheng, P. Musavigharavi, J. Miao, E. A. Stach, R. H. Olsson, D. Jariwala, *Nano Lett.* **2021**, *21*, 3753.
[10] P. Wang, D. Wang, N. M. Vu, T. Chiang, J. T. Heron, Z. Mi, *Appl. Phys. Lett.* **2021**, *118*, 223504.
[11] G. Schönweger, A. Petraru, M. R. Islam, N. Wolff, B. Haas, A. Hammud, C. Koch, L. Kienle, H. Kohlstedt, S. Fichtner, *Adv. Funct. Mater.* **2022**, *32*, 2109632.
[12] H. Mulaosmanovic, E. T. Breyer, T. Mikolajick, S. Slesazeck, *IEEE Trans. Electron Devices* **2019**, *66*, 3828.
[13] H. Qiao, C. Wang, W. S. Choi, M. H. Park, Y. Kim, *Mater. Sci. Eng.: R: Rep.* **2021**, *145*, 100622.

ADVANCED SCIENCE NEWS
www.advancedsciencenews.com

physica status solidi pss rrl
www.pss-rapid.com

[14] N. A. Pertsev, J. R. Contreras, V. G. Kukhar, B. Hermanns, H. Kohlstedt, R. Waser, *Appl. Phys. Lett.* **2003**, *83*, 3356.
[15] P. Chandra, M. Dawber, P. B. Littlewood, J. F. Scott, *Ferroelectrics* **2004**, *313*, 7.
[16] S. Yasuoka, T. Shimizu, A. Tateyama, M. Uehara, H. Yamada, M. Akiyama, Y. Hiranaga, Y. Cho, H. Funakubo, *J. Appl. Phys.* **2020**, *128*, 114103.
[17] R. Mizutani, S. Yasuoka, T. Shiraishi, T. Shimizu, M. Uehara, H. Yamada, M. Akiyama, O. Sakata, H. Funakubo, *Appl. Phys. Express* **2021**, *14*, 105501.
[18] S. Yasuoka, R. Mizutani, R. Ota, T. Shiraishi, T. Shimizu, S. Yasui, Y. Ehara, K. Nishida, M. Uehara, H. Yamada, M. Akiyama, Y. Imai, O. Sakata, H. Funakubo, *J. Ceram. Soc. Jpn.* **2022**, *130*, 436.
[19] D. Wang, J. Zheng, P. Musavigharavi, W. Zhu, A. C. Foucher, S. E. Trolier-McKinstry, E. A. Stach, R. H. Olsson, *IEEE Electron Device Lett.* **2020**, *41*, 1774.
[20] K. Yazawa, D. Drury, A. Zakutayev, G. L. Brennecka, *Appl. Phys. Lett.* **2021**, *118*, 162903.
[21] G. Wingqvist, F. Tasnádi, A. Zukauskaite, J. Birch, H. Arwin, L. Hultman, *Appl. Phys. Lett.* **2010**, *97*, 112902.
[22] M. Park, Z. Hao, R. Dargis, A. Clark, A. Ansari, *J. Microelectromech. Syst.* **2020**, *29*, 490.
[23] S. Fichtner, T. Reimer, S. Chemnitz, F. Lofink, B. Wagner, *APL Mater.* **2015**, *3*, 116102.
[24] S. Fichtner, N. Wolff, G. Krishnamurthy, A. Petraru, S. Bohse, F. Lofink, S. Chemnitz, H. Kohlstedt, L. Kienle, B. Wagner, *J. Appl. Phys.* **2017**, *122*, 035301.
[25] S. Fichtner, G. Schönweger, T.-N. Kreutzer, A. Petraru, H. Kohlstedt, F. Lofink, and B. Wagner, in *Proc. 2020 IEEE ISAF*, IEEE, Keystone, CO, USA **2020**.
[26] R. Meyer, R. Waser, K. Prume, T. Schmitz, S. Tiedke, *Appl. Phys. Lett.* **2005**, *86*, 142907.
[27] H. F. Kay, J. W. Dunn, *Philos. Mag.* **1962**, *7*, 2027.
[28] M. Dawber, K. M. Rabe, J. F. Scott, *Rev. Mod. Phys.* **2005**, *77*, 1083.
[29] J. Y. Jo, Y. S. Kim, T. W. Noh, J.-G. Yoon, T. K. Song, *Appl. Phys. Lett.* **2006**, *89*, 232909.
[30] N. Ogata, M. Nagata, K. Ishihara, H. Urashima, A. Okutoh, S. Yamazaki, S. Mitarai, J. Kudo, *Jpn. J. Appl. Phys.* **1998**, *37*, 3481.
[31] K. Hironaka, C. Isobe, B. ki Moon, S. Hishikawa, *Jpn. J. Appl. Phys.* **2001**, *40*, 680.
[32] T. Kijima, H. Ishiwara, *Jpn. J. Appl. Phys.* **2002**, *41*, L716.
[33] S. Migita, H. Ota, H. Yamada, K. Shibuya, A. Sawa, A. Toriumi, T. Kijima, H. Ishiwara, *Jpn. J. Appl. Phys.* **2002**, L716. 2018, *57*, 04FB01.
[34] S. K. Ryoo, K. D. Kim, H. W. Park, Y. B. Lee, S. H. Lee, I. S. Lee, S. Byun, D. Shim, J. H. Lee, H. Kim, Y. H. Jang, M. H. Park, C. S. Hwang, *Adv. Electron. Mater.* **2022**, 2200726.
[35] A. K. Tagantsev, I. A. Stolichnov, *Appl. Phys. Lett.* **1999**, *74*, 1326.
[36] S. Oh, H. Kim, A. Kashir, H. Hwang, *Appl. Phys. Lett.* **2020**, *117*, 252906.
[37] C. Zhou, D. M. Newns, *J. Appl. Phys.* **1997**, *82*, 3081.
[38] M. Stengel, N. A. Spaldin, *Nature* **2006**, *443*, 679.
[39] J.-E. Lim, D.-Y. Park, J. K. Jeong, G. Darlinski, H. J. Kim, C. S. Hwang, S.-H. Kim, C.-Y. Koo, H.-J. Woo, D.-S. Lee, J. Ha, *Appl. Phys. Lett.* **2002**, *81*, 3224.
[40] X. Castel, M. Guilloux-Viry, A. Perrin, J. Lesueur, F. Lalu, *J. Cryst. Growth* **1998**, *187*, 211.

4.5 In-Grain Ferroelectric Switching in Sub-5 nm Thin $Al_{0.74}Sc_{0.26}N$ Films at 1 V

Own contributions

- Design of Experiment
- Data analysis & interpretation
- Sample fabrication
- Electrical characterization
- Structural characterization (partly)
- Manuscript preparation

RESEARCH ARTICLE

ADVANCED SCIENCE Open Access

www.advancedscience.com

In-Grain Ferroelectric Switching in Sub-5 nm Thin $Al_{0.74}Sc_{0.26}N$ Films at 1 V

Georg Schönweger, Niklas Wolff, Md Redwanul Islam, Maike Gremmel, Adrian Petraru, Lorenz Kienle, Hermann Kohlstedt, and Simon Fichtner**

Analog switching in ferroelectric devices promises neuromorphic computing with the highest energy efficiency if limited device scalability can be overcome. To contribute to a solution, one reports on the ferroelectric switching characteristics of sub-5 nm thin $Al_{0.74}Sc_{0.26}N$ films grown on $Pt/Ti/SiO_2/Si$ and epitaxial Pt/GaN/sapphire templates by sputter-deposition. In this context, the study focuses on the following major achievements compared to previously available wurtzite-type ferroelectrics: 1) Record low switching voltages down to 1 V are achieved, which is in a range that can be supplied by standard on-chip voltage sources. 2) Compared to the previously investigated deposition of ultrathin $Al_{1-x}Sc_xN$ films on epitaxial templates, a significantly larger coercive field (E_c) to breakdown field ratio is observed for $Al_{0.74}Sc_{0.26}N$ films grown on silicon substrates, the technologically most relevant substrate-type. 3) The formation of true ferroelectric domains in wurtzite-type materials is for the first time demonstrated on the atomic scale by scanning transmission electron microscopy (STEM) investigations of a sub-5 nm thin partially switched film. The direct observation of inversion domain boundaries (IDB) within single nm-sized grains supports the theory of a gradual domain-wall driven switching process in wurtzite-type ferroelectrics. Ultimately, this should enable the analog switching necessary for mimicking neuromorphic concepts also in highly scaled devices.

1. Introduction

In recent years, ferroelectrics have become one of the main foci of advancing semiconductor technology toward higher performance and energy efficiency.[1–3] This applies especially to neuromorphic and in-memory computing, where the field-driven ferroelectric effect promises analog operation with the lowest input power. However, the entrance of ferroelectric functionality into the active areas of commercial devices other than binary ferroelectric random-access memories (FRAMs) is yet to take place. One of the major challenges in this context is an excess of device-to-device variability of key parameters like the threshold voltage in small devices as well as the loss of their capability to operate in an analog fashion. This variability becomes pronounced when the ferroelectrically active area of a device approaches the size of the grains inside the ferroelectric films and the domains therein. This grain size typically is in the range of tens of nanometers for the fluorite-type ferroelectrics, which have been at the focus of scientific attention in recent years.[4] The factors contributing to device variability are a lack of crystalline texture, stress inhomogeneities, and less than complete phase purity, which lead to different material parameters between different grains.[4,5] For fluorite-type ferroelectrics, the domain size can be considered equal to the grain size and thus has the same lower limit of tens of nanometers, which was shown to severely constrain analog operation in highly scaled devices.[6]

Since their discovery in 2019, the new wurtzite-type ferroelectrics have raised expectations of a possible solution to the aforementioned issues.[7] Wurtzite-type ferroelectric films can typically be grown phase pure, well textured and the narrow distribution of their displacement current response upon ferroelectric switching promises a narrow distribution of the local ferroelectric properties, all of which should contribute to improved device repeatability. At the same time, wurtzite-type films can

G. Schönweger, A. Petraru, H. Kohlstedt
Department of Electrical and Information Engineering
Kiel University
Kaiserstrasse 2, D-24143Kiel, Germany
E-mail: gmsc@tf.uni-kiel.de
The ORCID identification number(s) for the author(s) of this article can be found under https://doi.org/10.1002/advs.202302296

DOI: 10.1002/advs.202302296

G. Schönweger, S. Fichtner
Fraunhofer Institute for Silicon Technology (ISIT)
Fraunhoferstr. 1, D-25524Itzehoe, Germany
E-mail: sif@tf.uni-kiel.de
N. Wolff, M. R. Islam, M. Gremmel, L. Kienle, S. Fichtner
Department of Material Science
Kiel University
Kaiserstrasse 2, D-24143Kiel, Germany
N. Wolff, L. Kienle, H. Kohlstedt
Kiel Nano, Surface and Interface Science (KiNSIS)
Kiel University
Christian-Albrechts-Platz 4, D-24118Kiel, Germany

ADVANCED SCIENCE NEWS
www.advancedsciencenews.com

ADVANCED SCIENCE Open Access
www.advancedscience.com

easily be deposited at complementary metal oxide semiconductor (CMOS) back-end-of-line (BEOL) compatible conditions, feature extreme temperature stability themselves and thicker films are already in large-volume industrial production.[8,9] Further, for film thicknesses (d) above 100 nm, the switching kinetics of the material can be modeled to be domain-wall motion-limited,[10] which suggests that more than a single state can be stored per grain. Despite these conceptual advantages, major challenges remain to be solved until the material class is able to fully meet the demands of advanced microelectronic devices. In this context, it is highly necessary to further reduce the ferroelectric switching voltage of wurtzite-type thin films to meet the capabilities of typical on-chip voltage supplies (in the range of 1 V), while retaining the aforementioned advantages like phase purity and domain-wall motion-limited switching.

In this study, we demonstrate for the first time that wurtzite-type sub-5 nm thin (8 to 9 unit cells corresponding to 4 – 4.5 nm) $Al_{0.74}Sc_{0.26}N$ films sputter-deposited on silicon (Si) substrates retain ferroelectric functionality with switching voltages as low as 1 V and feature in-grain, nm-sized domains upon partial switching. We were thus able to reduce the switching voltage and film thickness of films on Si by around 50% compared to literature (5 nm thin films grown by non-BEOL compatible molecular beam epitaxy (MBE) and ≈10 nm thin films grown by sputtering on Si).[11–13] Further, by performing atomic resolution scanning transmission electron microscopy (STEM) on epitaxial sub-5 nm thin $Al_{0.74}Sc_{0.26}N$ films, we obtained the first images of domain walls in any wurtzite-type ferroelectric to confirm the presence of nm-sized domains within individual grains.

Our investigation starts with a structural as well as an electrical comparison of 10 nm thin $Al_{0.74}Sc_{0.26}N$ grown epitaxially on Pt/GaN/sapphire and grown non-epitaxially on $Pt/Ti/SiO_2/Si$ to demonstrate the improved ferroelectric properties of the latter. Further downscaling to the sub-5 nm range of ferroelectric $Al_{0.74}Sc_{0.26}N$ films grown on Si is investigated. The scaling of the coercive voltage, including a decrease of E_c below 10 nm film thickness ultimately allowed to achieve switching voltages as low as 1 V and is discussed in detail. Epitaxial growth was investigated as well, as it allows to resolve the ferroelectric polarization reversal on atomic level in partially switched sub-5 nm thin $Al_{0.74}Sc_{0.26}N$ layers via STEM. The identification of regions with opposite polarity inside a single grain and the necessary occurrence of a domain boundary in between gives first insights into the size, shape, location, and evolution of ferroelectric domains in $Al_{0.74}Sc_{0.26}N$ and potentially in the whole class of wurtzite-type ferroelectrics.

2. Results and Discussion

2.1. Effect of Non-Epitaxial Growth on Si versus Epitaxial Growth on GaN on the Ferroelectric Response of $Al_{0.74}Sc_{0.26}N$

For the direct integration of ferroelectric wurtzite-type films into CMOS technology, the possibility to deposit them on Si substrates without epitaxial templating is crucial. While one might assume that epitaxial growth and thus higher interface- and film quality will automatically result in improved electrical properties, this section motivates that the opposite can be the case for $Al_{1-x}Sc_xN$.

This can be concluded from the electrical response as well as from the interface quality investigations of 10 nm thin $Al_{0.74}Sc_{0.26}N$ films. In **Figure 1**a, the cross-sections of 10 nm thin $Al_{0.74}Sc_{0.26}N$ films grown epitaxially on Pt/GaN/sapphire as well as grown non-epitaxially on $Pt/Ti/SiO_2/Si$ are compared. All films were capped in situ to prevent oxidation of the $Al_{0.74}Sc_{0.26}N$ surface, which is crucial to obtain an undisturbed ferroelectric response especially of <10 nm thin films, where the thickness of the native oxide can be in the range of the total film thickness.[14–16]

For the epitaxially grown film stacks, the interfaces are smooth with an overall low surface roughness of the respective layers, which is known to result in a reduction of the leakage currents in capacitors.[17] Structurally, the epitaxial films with a 10 nm thin Pt bottom electrode layer also have superior crystalline quality compared to non-epitaxial ones, that is, higher c-axis texture, which we investigate in detail in a separate work.[18] Nonetheless, the films deposited on Si substrates exhibit more pronounced ferroelectric switching peaks (Figure 1b). Thus, despite their higher interface roughness and poorer interface texture compared to the epitaxial ones, a complete polarization inversion is demonstrated for the non-epitaxial 10 nm thin $Al_{0.74}Sc_{0.26}N$ grown on $Pt/Ti/SiO_2/Si$, yet not for the epitaxial films. This is apparent from the drop in current density (J) after ferroelectric switching at the coercive field (E_c) with maximum J followed by a local minimum before the contribution from leakage currents leads to a further increase in J. In comparison, no local minimum is observed for the epitaxial film. Although the leakage currents for the 10 nm thin epitaxial $Al_{0.74}Sc_{0.26}N$ grown on Pt/GaN/sapphire are lower (at a fixed voltage) compared to films grown on Si, E_c is also higher and approaches the electrical breakdown field. Thus, as demonstrated in our recent work, we were able to fully switch the polarization of 10 nm thin epitaxial films via capacitance versus electric field ($C-E$) measurements, but not via $J-E$ loops.[14] We attribute the improved E_c of the films grown on Si compared to the ones grown on sapphire to differences in the respective $Al_{0.74}Sc_{0.26}N$ film stress, which is well-known to result in a shift of E_c.[7] Despite the fact that both heterostructures were grown under exactly the same $Al_{0.74}Sc_{0.26}N$ deposition conditions (same run), the thermal expansion coefficients (α_{sub}) of the silicon substrate (non-epitaxial growth - $\alpha_{sub} = 2.6 \times 10^{-6}$ K^{-1}) and sapphire substrate (epitaxial growth - $\alpha_{sub} = 7.3 \times 10^{-6}$ K^{-1}) differ, leading to strong differences in the thermally induced film stress after cooling down from the $Al_{0.74}Sc_{0.26}N$ ($\alpha_{film} = 4.9 \times 10^{-6}$ K^{-1}) deposition temperature at 450 °C.[19–21] The resulting strain ($\epsilon_{thermal}$) in the basal plane of $Al_{0.74}Sc_{0.26}N$ can be calculated via Equation 1.

$$\epsilon_{thermal} = \int_{T_{RT}}^{T_{dep}} (\alpha_{film} - \alpha_{sub})\, dT \quad (1)$$

For induced epitaxial strain an in-plane lattice-misfit of ≈ 4% between $Al_{1-x}Sc_xN$ ($x = 0.38$) and GaN was calculated to result in a critical thickness of 2 nm.[22] Therefore, we do not expect induced epitaxial strain at the $Al_{0.74}Sc_{0.26}N$/Pt interface (misfit ≈ 18%) for both types of substrates. Thus, in addition to the film stress induced by grain boundaries and defects, tensile stress is thermally induced in $Al_{1-x}Sc_xN$ if grown on a silicon substrate

ADVANCED SCIENCE NEWS
www.advancedsciencenews.com

ADVANCED SCIENCE Open Access
www.advancedscience.com

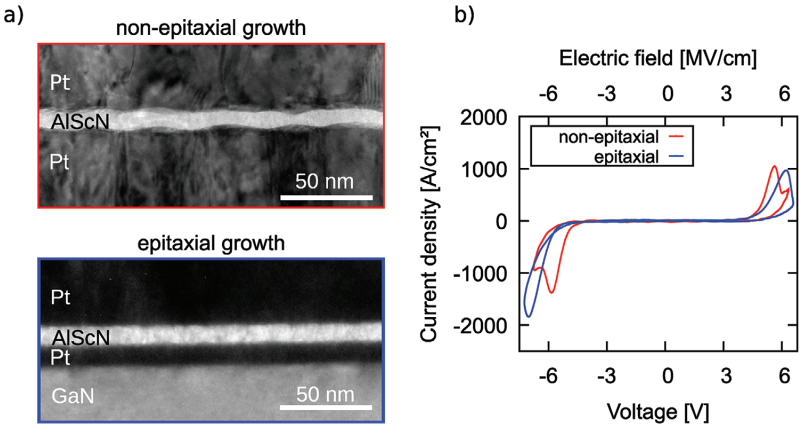

Figure 1. a) TEM cross-section of 10 nm thin $Al_{0.74}Sc_{0.26}N$ grown (top) non-epitaxially within a $Pt/Al_{0.74}Sc_{0.26}N/Pt/Ti/SiO_2/Si$ and (bottom) epitaxially within a $Pt/Al_{0.74}Sc_{0.26}N/Pt/GaN/sapphire$ capacitor stack. Only the capacitor structures are depicted. b) The $J-E$ loops of the capacitors depicted in (a), measured at 100 kHz.

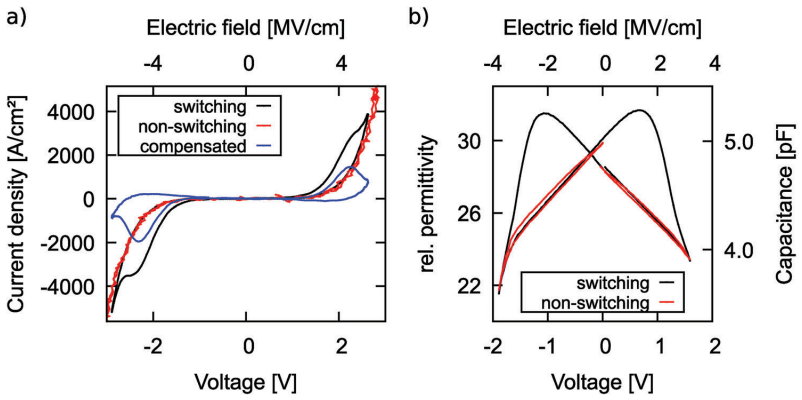

Figure 2. a) $J-E$ loops of sub-5 nm thin $Al_{0.74}Sc_{0.26}N$ grown on $Pt/Ti/SiO_2/Si$ measured at 100 kHz on 5 µm diameter pads. A leakage current compensated curve (blue) by subtracting the non-switching- (red) from the switching currents (black) is included. b) $C-V$ loop of the sub-5 nm thin $Al_{0.74}Sc_{0.26}N$ based capacitor described in (a) measured on a 10 µm diameter pad. Unipolar non-switching cycles (red) by measuring each branch (positive and negative voltages) twice with the same polarity are included to stress the non-volatile nature of the permittivity enhancement due to ferroelectricity.

($\varepsilon_{thermal} \approx 0.09\%$), while compressive stress ($\varepsilon_{thermal} \approx -0.10\%$) is thermally induced if grown on a sapphire substrate.

The ability to tune the coercive field of $Al_{1-x}Sc_xN$ exploiting the thermal expansion of varying substrates has also been reported recently by Yasuoka et al.[23] In consequence, thermal induced tensile stress extends the in-plane lattice resulting in the reduction of E_c, similar to an increase in Sc concentration. To conclude, we attribute the more pronounced ferroelectric displacement current peak of the non-epitaxial 10 nm thin $Al_{0.74}Sc_{0.26}N$ to a more favorable position of E_c compared to the onset of leakage (compare the local minima in the current response) and with respect to the breakdown strength.

2.2. Ferroelectric Properties of Sub-5 nm thin $Al_{0.74}Sc_{0.26}N$ Films Grown on Si

Next, we present and discuss the electric characterization results of sputter-deposited 8 to 9 unit cells (4 and 4.5 nm) thin $Al_{0.74}Sc_{0.26}N$ films grown on Si wafers. Details on the exact thickness determination by using STEM can be found in Section 2.4.

In **Figure 2**a, $J-E$ loops of sub-5 nm thin $Al_{0.74}Sc_{0.26}N$ grown on $Pt/Ti/SiO_2/Si$ are illustrated. In direct measurements (black curve), the clear hysteresis is already indicative of ferroelectric switching. The leakage current flow through the dielectric as well as the displacement current contributions due to the relative

ADVANCED SCIENCE NEWS
www.advancedsciencenews.com

ADVANCED SCIENCE Open Access
www.advancedscience.com

permittivity (ϵ_r) can be separated from the hysteretic (i.e., ferroelectric) displacement currents by recording non-switching loops (i.e., by pre-poling the respective measured positive and negative branch). After subtraction of the non-switching- (red curve) from the switching currents (black curve) the typical shape of ferroelectric displacement current peaks are obtained (blue curve), which allows the extraction of E_c.

The $C-V$ loop of the sub-5 nm thin $Al_{0.74}Sc_{0.26}N$ based capacitor depicted in Figure 2b further confirms the ferroelectric nature of the hysteretic event. A distinct butterfly-shaped loop, typical for ferroelectric switching, is visible. Clearly distinguishable, non-hysteretic non-switching loops are depicted as well for the $C-V$ loop. Furthermore, the polarization inversion of a sub-5 nm thin film is unambiguously demonstrated by atomically resolved STEM investigations discussed in Section 2.4. Thus, it is demonstrated that such thin ferroelectric wurtzite-type films can be grown by sputter deposition on oxidized silicon in a manner compatible with CMOS technology, which is a clear advantage over high-temperature (≥500 °C) MBE deposition processes on single crystal templates.[11,15] Furthermore, the ferroelectric switching of $Al_{0.74}Sc_{0.26}N$ films grown on silicon with, for wurtzite-type materials, record low voltages down to 1 V is a major milestone toward ferroelectric $Al_{1-x}Sc_xN$ based future devices operable with the on-chip voltage supply of integrated circuits.[24,25]

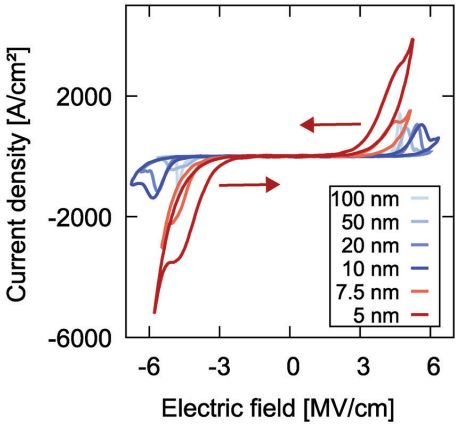

Figure 3. $J-E$ loops of 100 nm- down to sub-5 nm thin $Al_{0.74}Sc_{0.26}N$ based capacitors deposited on Pt/Ti/SiO_2/Si. All measurements were performed at 100 kHz on 5 µm diameter pads (< 10 nm $Al_{0.74}Sc_{0.26}N$ thickness) and 10 × 10 µm² pads (> 10 nm $Al_{0.74}Sc_{0.26}N$ thickness). The decreasing trend of E_c with decreasing film thickness below 10 nm is indicated by red arrows.

2.3. Coercive Field Scaling in Ultrathin $Al_{0.74}Sc_{0.26}N$

The low switching voltage down to 1 V reached in our films is not only due to a simple reduction in thickness but also due to the favorable scaling of E_c with thickness, which we will therefore discuss in more detail in this section. In particular, the appearance of a depolarization field (E_d) and its effects on the electrical response of films below 10 nm film thickness are discussed, as is the relative dielectric permittivity—which itself is related to the coercive field through the shape of the ionic potential wells.[3]

In **Figure 3**, $J-E$ loops of 100 nm- down to sub-5 nm thin $Al_{0.74}Sc_{0.26}N$ based capacitors are depicted. From 100 nm down to 10 nm the coercive field is increasing with decreasing film thickness, but interestingly, below 10 nm the coercive field is significantly decreasing again, as indicated by the red arrows in Figure 3. A comparable trend with thickness scaling down to sub-5 nm is also observed for epitaxial films grown on Pt/GaN/sapphire, although an almost thickness-independent shift of $\Delta E_c \approx 0.3$ MV cm^{-1} is visible (see Figure S2, Supporting Information). As discussed in the previous section, this shift in E_c results from the difference in thermally induced strain ($\Delta\epsilon_{thermal} \approx 0.2\%$ for the different substrates), which fits well to the literature where similar E_c shifts for similar strain differences are reported.[23,26] Thus, it is concluded that the scaling properties are rather independent of the substrate (silicon vs sapphire), crystalline quality and associated growth modes (non-epitaxial vs epitaxial).

A slight increase in E_c with decreasing film thickness down to 10 nm is consistent with the scaling properties reported so far for $Al_{1-x}Sc_xN$.[11–14] Yasuoka et. al. attributed this behavior to a change in the lattice-parameters for thinner films due to stress gradients arising from the lattice mismatch between Pt (2.78 Å) and $Al_{1-x}Sc_xN$ (3.22 Å for $x = 0.2$). Despite the high lattice mismatch, an epitaxial-like growth between Pt grains of the bottom-electrode layer and $Al_{1-x}Sc_xN$ grains is suggested, eventually resulting in an increase in compressive strain in the basal plane when reducing the film thickness. In our films, the lattice-parameters do not change significantly for thicknesses down to 10 nm. However, for sub-5 nm thickness, the $Al_{0.74}Sc_{0.26}N$ lattice-parameters determined via STEM are $a \approx 319$ pm and $c \approx 505$ pm (details on the determination can be found in Experimental Section). This implies (relative to the equilibrium a-lattice parameter of ≈324 pm at a Sc concentration of $x = 0.26$) an in-plane compressive strain of ≈1.5%.[26,27] However, we measure E_c to decrease below 10 nm film thickness down to less than 2 MV cm^{-1} in $C-E$ curves, as illustrated in **Figure 4**c. This decrease in E_c below 10 nm thickness differs from the very recently reported thickness scaling study down to 5 nm thin epitaxial films grown via MBE.[11] In this work, Wang et al. also attributed the increase in E_c to a stress gradient forming due to the smaller in-plane lattice-parameter of the Mo bottom electrode compared to the one of $Al_{1-x}Sc_xN$.

The reduction in the electric field necessary for switching in films thinner than 10 nm is especially pronounced when considering the onset of the hysteresis opening in the $J-E$ loops, as visible in Figure 3. For sub-5 nm film thickness the hysteresis opens at 2.1 MV cm^{-1}, while for 100 nm film thickness, the opening starts at 4.3 MV cm^{-1}. This implies a more gradual switching capability below 10 nm film thickness.

A decrease in E_c in ultrathin ferroelectrics was reported by Dawber et al., who included depolarization field corrections into the Janovec–Kay–Dunn (JKD) scaling.[28–30] The depolarization field resulting from a finite screening length in the electrodes adds up to the applied electric field if the condition $4\pi P_s >> \epsilon_r\epsilon_0 E$ is fulfilled. For $Al_{0.74}Sc_{0.26}N$, with a spontaneous polarization (P_s) of ≈110 µC cm^{-2} and electric fields up to 6 MV cm^{-1}, this

ADVANCED SCIENCE NEWS
www.advancedsciencenews.com

ADVANCED SCIENCE Open Access
www.advancedscience.com

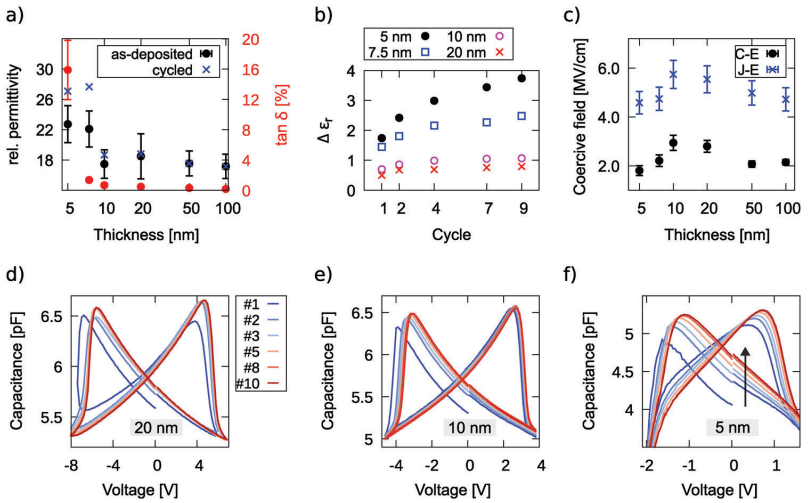

Figure 4. a) Relative permittivity as well as loss tangent as a function of $Al_{0.74}Sc_{0.26}N$ film thickness for as-deposited- and for pre-cycled (10 times) capacitors grown on Pt/Ti/SiO_2/Si. b) Absolute change of ϵ_r (state with full positive polarization, 0 V bias) with cycling in dependence of the $Al_{0.74}Sc_{0.26}N$ film thickness. c) The coercive field dependence on $Al_{0.74}Sc_{0.26}N$ thickness for the capacitors described in (a) determined via $J-E$ (100 kHz) and via $C-E$ (sweep time 20 s, small signal 100 mV and 900 kHz) loops. The coercive field determined via $C-E$ loops is approximated by the peak positions of the butterfly-loop. d) First ten $C-V$ cycles of pristine capacitors consisting of 20 nm thin-, e) 10 nm thin-, and f) sub-5 nm thin $Al_{0.74}Sc_{0.26}N$ used for determining the change of ϵ_r with cycling as depicted in (b). The capacitor area was 695 μm^2 (20 nm thickness), 341 μm^2 (10 nm thickness), and 99 μm^2 (sub-5 nm thickness). The drop in capacitance at negative fields for the sub-5 nm thin film depicted in (f) is due to the low and asymmetric resistivity (see Figure S4, Supporting Information).

condition is clearly satisfied (1507 >>14). Thus, similar to what was experimentally observed in ferroelectric PVDF films, a thickness dependent depolarization field qualitatively fits very well to the drop of E_c below 10 nm film thickness in $Al_{1-x}Sc_xN$.[31] Very recently, it has also been demonstrated by first-principles calculations that reducing the thickness of usually non-switchable Wurtzite III–V semiconductors (e.g., AlSb) could result in polarization switching capability (i.e., ferroelectricity), due to the depolarization field which scales with $\propto 1/d$.[32]

The decrease in E_c in our work is also reflected in the increase in ϵ_r below 10 nm film thickness, as illustrated in Figure 4a. In addition, ϵ_r increases to even higher values after cycling, which is especially pronounced for the thinner films (Figure 4b). A similar increase in the relative permittivity with cycling has also been observed for the wurtzite-type ferroelectric $Al_{1-x}B_xN$.[33] Through analysis of the Rayleigh parameters, this increase has been related to an increase in domain-wall area compared to pristine samples at 0 V bias. If persistent domain walls indeed form during cycling and these domain walls extend vertically in the film, similar to what is reported in the following section, an enhancement in permittivity with lower film thickness would be a natural consequence - due to an increase in the ratio of domain-wall area to film volume with reduced thickness. This change in the ratio would imply a larger relative volume that is frustrated by the domain-wall and in turn features a higher permittivity due to shallower ionic potential.

With decreasing film thickness not only the leakage current-, but also the hysteretic area is increasing especially for sub-5 nm film thickness, as illustrated in Figure 3. This increase in apparent displacement current can not be explained alone by polarization reversal, as it would imply a physically unlikely large spontaneous polarization above 1000 μC cm^{-2}. The enhanced apparent polarization has therefore to be attributed to a dynamic current contribution triggered by the polarization reversal of the $Al_{0.74}Sc_{0.26}N$ film. This is further supported by the fact that the remanent polarization determined via PUND measurements[34] can be frequency depended until it reaches saturation at frequencies > 10^4 Hz, as depicted in Figure S3 (Supporting Information). Currently, the most likely explanation of this behavior is the temporal formation of conductive domain walls during switching.[35] For higher frequencies, the time domain walls are present in the sample is reduced, and therefore their contribution to the apparent switching polarization. As discussed above, with decreasing film thickness, the relative domain-wall density will increase and domains are more likely to extend from the top to the bottom interface. Both effects can facilitate increased electrical current to flow in the form of compensation charges for the strong polarization discontinuity along the domain walls. This concept of conducting domains walls is closely related to the well-known polarization doping schemes in III-N semiconductors.[36–38] The model is further supported by non-switching quasi-static current response measurements demonstrating higher conductivity of partially switched capacitors at fields well below E_c, and for both positive and negative fields (see Figure S5, Supporting Information). Further analysis of this effect is the focus of ongoing work.

ADVANCED SCIENCE NEWS
www.advancedsciencenews.com

ADVANCED SCIENCE Open Access
www.advancedscience.com

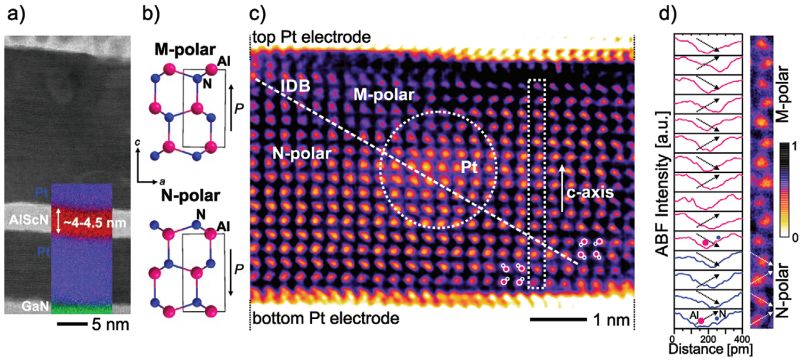

Figure 5. a) ABF-STEM micrograph showing the Pt/$Al_{0.74}Sc_{0.26}N$/Pt/GaN capacitor stack in cross-section. The inset shows the superimposed EDS maps of Pt, Al, and Ga. b) Sketches of the atomic structure in the M- and N-polar state along the line of sight. c) Inverted-ABF-STEM micrograph of the full $Al_{0.74}Sc_{0.26}N$ layer featuring an inclined inversion domain boundary separating regions of M-polarity (upper right) and N-polarity (lower left). Superimposed sketches of the (Al,Sc)-N dumbbells help to visualize the polarization direction. d) Intensity profile analysis of the polarization direction of individual (Al,Sc)-N dumbbells inside the single-column frame. Profiles are always drawn from left to right (see arrows on the unfiltered single column image); color code: M(-polarity) = pink, N(-polarity) = blue.

2.4. Atomic Scale Investigation of Ferroelectric Domains in Sub-5 nm thin $Al_{0.74}Sc_{0.26}N$

Analog-like ferroelectric switching is an elegant approach for emulating synapses and thus a stable partially switched state is an essential material property in the context of neuromorphic computing.[39,40] Hence, it is important to image and understand the atomistic switching processes and the evolution of polarization discontinuities (i.e., ferroelectric domain walls). This section explores the microscopic consequences of ferroelectric switching in sub-5 nm thin $Al_{0.74}Sc_{0.26}N$ films as well as their general structural properties via high-resolution STEM. The main focus of this study is the first observation of domain walls in individual $Al_{0.74}Sc_{0.26}N$ grains in any wurtzite-type ferroelectric. In order to clearly observe the local polarization on unit cell scale, the analysis was conducted on an epitaxial (in-plane ordered), yet still polycrystalline film (0002 oriented columnar grains), which allows for direct imaging conditions because of the identical film/substrate crystallographic orientation. An overview image of the sub-5 nm thin $Al_{0.74}Sc_{0.26}N$ film showing individual epitaxial grains with *c*-axis texture confirmed across the entire prepared area as well as $C-E$ loops demonstrating the ferroelectric switching in 10 nm- down to sub-5 nm thin epitaxially grown films is provided in Figures S1 and S6 (Supporting Information). While previous attempts to resolve the local polarization in wurtzite-type ferroelectrics were successful to identify the polarization direction of single unit cells, the observation of domain walls has so far been elusive.

The epitaxial nature of the heterostructure allowed for an accurate thickness determination on the level of monolayers due to the atomically sharp interfaces (c.f., Figure 1a). Despite the columnar growth mode of sputtered films, the good structural quality of the in-plane oriented growth enables the direct observation of the unit-cell polarity within single grains on the atomic scale.[41] In order to draw conclusions on the switching process itself (besides just confirming up and down polarization flips), the investigated capacitor was only partially switched from the nitrogen (N)-polar to the metal (M)-polar state. For this, the capacitor was pre-switched to full N-polarity by sweeping with a LCR-meter ($C-V$ measurement) to a positive field which is high enough to saturate the polarization reversal, with a subsequent sweep to a negative field which is ≈0.8 MV cm^{-1} below the saturation point.

The atomic scale STEM analysis of the partially switched capacitor is given in **Figure 5**. An annular bright-field (ABF)-STEM micrograph of the capacitor cross-section is depicted in Figure 5a. The individual thickness of the Pt electrodes is determined to be about 11 and 25 nm for the epitaxial Pt bottom electrode and the top electrode, respectively. They sandwich the $Al_{0.74}Sc_{0.26}N$ layer with a total thickness of 8 to 9 unit cells, which was determined by counting the number of monolayers. This corresponds to 4 to 4.5 nm at a *c*-lattice parameter of ≈505 pm. This number agrees well with the targeted thickness, considering the deposition rate calibrated on thicker films. Therefore, we conclude that there is no significant delay of film growth due to nucleation. The Sc content was verified by EDS analysis of a ≈10*x*4 nm^2 frame to be $x \approx 0.26$.

Atomic scale investigations of the polar domain structure were conducted using ABF-STEM imaging paired with multi-frame image alignment[42] on the partially switched $Al_{0.74}Sc_{0.26}N$ film. Here, the use of the ABF detector allows to routinely image atomic positions of light elements such as nitrogen, which is the crucial prerequisite to observe the polarity on the unit cell level in ferroelectric $Al_{1-x}Sc_xN$.[41] Figure 5b depicts atomic models of the N- and M-polar oriented wurtzite-type structures sketched along the [2-1-10] viewing direction required for the investigation of unit cell polarity. As already discussed in related work,[18,26,41] sputtered nanocrystalline films of $Al_{1-x}Sc_xN$ exhibit small grain diameters of 2 – 6 nm featuring an in-plane tilt between the individual grains in the order of 6° which restricts the observable area to single grains with exact orientation to the incident electron beam.[14] In this respect, the ABF-STEM image contrast formation crucially depends on exact orientation conditions.[43,44] In this investigation, the directly interpretable sample area was further limited by 1 to 2 nm large Pt agglomerates present evenly spaced in the center of the $Al_{0.74}Sc_{0.26}N$ layer. These Pt artifacts

ADVANCED SCIENCE NEWS
www.advancedsciencenews.com

ADVANCED SCIENCE Open Access
www.advancedscience.com

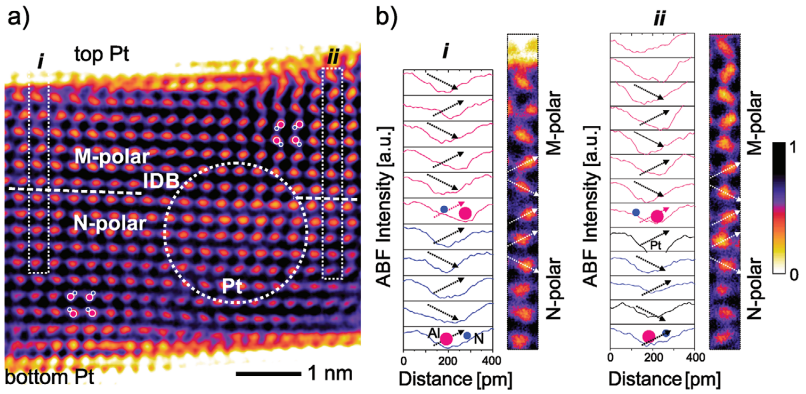

Figure 6. a) Inverted-ABF-STEM micrograph of the $Al_{0.74}Sc_{0.26}N$ layer featuring a horizontal inversion domain boundary separating regions of M-polarity within the top unit cells and N-polarity in the bottom film. Sketches of the (Al,Sc)-N dumbbells assist to visualize the polarity. b) Intensity profile analysis of the (Al,Sc)-N dumbbells inside the vertical single-column frames on the left (*i*) and right side (*ii*) of the grain. Both analyses hint toward the lateral progression of an IDB. Profiles are drawn from left to right (see arrows) on the unfiltered image; M(-polarity) = pink, N(-polarity) = blue.

were introduced during sample preparation using the FIB thinning method.

Individual grains with aligned zone axis orientation were identified in the $Al_{0.74}Sc_{0.26}N$ layer after centering the GaN crystal lattice into the [2-1-10] orientation. The unit cell polarity was identified from the non-rigidly registered multi-frame ABF-STEM data sets, by the analyses of intensity profiles drawn across the (Al,Sc)-N dumbbells (see Figure S7, Supporting Information, for a demonstration on the GaN substrate). The ABF-STEM micrograph contrast was inverted and a color scheme (inverted-cABF-STEM) was applied to enhance the image visibility as described in Experimental Section. No noise filter was applied for the analysis of intensity profiles to avoid potential artifacts by reducing the information limit. Intensity profile analysis is regularly performed to determine the polarity of materials with wurtzite-type crystal structure because of the strong contrast difference between metal and nitrogen or oxygen atoms.[45]

Using the described method, the presence of N-polar and M-polar regions within a single grain is observed in Figures 5c and **6**. They confirm the presence of inversion domain boundaries (IDB) with a varying, yet always significant horizontal component. This is highly surprising given the fact that the horizontal component should give rise to an extreme polarization discontinuity at the domain-wall, which likely requires an as-yet-unknown (charge) compensation or reconfiguration mechanism for stabilization. The nanocrystallinity of the film and thus the in-depth superposition of slightly in-plane rotated grains result in a less clear contrast compared to the single crystal material, for example, GaN. Furthermore, the expected 3D shape of the domains within the single grain itself adds certainly an additional level of diffusion to the atomic images and complicates the identification of the exact location of the IDB. On the other hand, the slightly in-plane rotated grains (6°) permit to focus on individual grains and reduce the interference to neighboring grains in-depth direction with a potentially different polarization state. Generally, M-polarity is clearly identified in the upper region in the inverted-ABF-STEM images, while the remaining N-polarity is predominantly located at the bottom interface. Figures 5d and 6b present the aforementioned profile analysis along the highlighted vertical atomic columns showing a clear N-polar (blue profiles) polarization near the bottom interface and a switch to M-polarity (pink profiles) closer to the upper interface. At the position of polarization inversion from N- to M-polarity (the profiles are drawn in the scheme "up-down" starting left of the (Al,Sc)-N dumbbell), the alternating dumbbell orientation (and so the drawn profiles) is intercepted, hence the polarity abruptly inverses to the M-polar state following an "up-down-down-up" scheme as indicated by the arrows. This change of the polarization within the sub-5 nm grains indicates that even in very thin films with grain diameters in the single-digit nanometer range, $Al_{1-x}Sc_xN$ can still feature more than two distinct polarization states. This suggests that the material, and possibly the wurtzite-type ferroelectrics in general, are potentially very suitable for multi-bit or even analog operation in single-digit nanometer scaled devices. Further, as already assumed for thicker films,[41] the nucleation of polar inversion domains switching from N to M-polarity is found to be initiated at the top electrode interface and from there propagates toward the bottom interface. These results demonstrate the first direct observation of IDBs in wurtzite-type ferroelectrics. From the application point of view, the in-grain switching and small domain size is highly attractive to address multiple states in lateral dimensions $< 10\ nm^2$, which emphasizes the potential of $Al_{0.74}Sc_{0.26}N$ for the realization of highly scaled synapse-emulating neuromorphic computing devices.[39]

3. Conclusion

In summary, ferroelectric switching in sputter-deposited, 8 to 9 unit cells (4 and 4.5 nm) thin $Al_{0.74}Sc_{0.26}N$ grown non-epitaxially on Pt/Ti/SiO_2/Si and epitaxially on Pt/GaN/sapphire is demonstrated. The ferroelectric nature of the switching event was independently confirmed by electric $J - E$ and $C - E$ measurements, as well as by STEM investigations, resolving the polarization inversion at the atomic scale. This is the first report on

a sub-5 nm thin wurtzite-type ferroelectric film switching fully on Si which also features record low switching voltages down to ≈1 V. Both aspects can be expected to greatly aid the future integration of the material class to advanced CMOS technology. Despite the better structural qualities of the thin film texture and interface structure of epitaxial films, the growth of sub-5 nm non-epitaxial $Al_{0.74}Sc_{0.26}N$ on silicon results in an improved ratio between coercive- and breakdown field. Hence, the structural quality is not a limiting factor for good ferroelectric performance. E_c in our films increased only slightly with decreasing film thickness down to 10 nm, while it decreased when the film thickness is further reduced down to sub-5 nm, thereby significantly lowering the required switching voltages. This behavior fits qualitatively to the depolarization-corrected JKD model described by Dawber et al.,[28] who explain the decrease in E_c by the increase in the depolarization field, resulting from the finite screening length of the electrodes. The increasing permittivity in thinner films supports this hypothesis. The permittivity is also found to increase with cycling, especially for thinner films, which we relate to an increase in the relative volume of domain walls with respect to the total film volume.

Our high resolution ABF-STEM investigation of epitaxially grown $Al_{0.74}Sc_{0.26}N$ for the first time allowed to resolve IDBs in a wurtzite-type ferroelectric. The resulting presence of nanoscale domains spanning only fractions of individual nm-sized grains suggests that domain-wall motion still limits the switching kinetics in wurtzite-type films thinner than 5 nm. The strong horizontal component of the observed domain walls further motivates the existence of a (charge) compensation mechanism for the strong polarization discontinuity at the boundary.

To conclude, the given evidence of in-grain switching of sub-5 nm thin films with sub-5 nm lateral grain dimensions demonstrates stable partial switching capabilities of extremely low volumes. This switching mechanism together with the positive effects of thickness downscaling on E_c that result in ferroelectric switching voltages as low as 1 V make ferroelectric $Al_{1-x}Sc_xN$ a highly interesting choice for nanoscale ferroelectric synaptic devices—as is the usage of a CMOS BEOL compatible deposition process already used in mass-production.

4. Experimental Section

As electrodes, 100 nm thick Pt layers on a 10 nm thick Ti seed layer sputter-deposited on SiO_2/Si wafers were provided by Fraunhofer ISIT, Germany. Epitaxy-ready templates consisting of GaN(4 µm)/sapphire were commercially bought. The substrates were diced into 1×1 cm^2 chips with prior surface protection using a photoresist. Cleaning in acetone and isopropanol using an ultrasonic bath was performed, followed by rinsing in DI-water. Subsequently, the non-epitaxial Pt templates were cleaned by performing an Ar/O_2-plasma-etching in a Sentech Sl100 reactor, details can be found elsewhere.[46] The $Al_{0.74}Sc_{0.26}N$ layers as well as the bottom epitaxial Pt and the Pt top layers were grown in-house by sputter deposition using an Oerlikon (now Evatec) MSQ 200 multisource system, details about the process can be found in a previous publication.[14] The epitaxial growth on Pt/GaN/sapphire as well as the non-epitaxial growth on Pt/Ti/SiO_2/Si was obtained by using the same deposition process. The Pt top layers were deposited in situ subsequently to the $Al_{0.74}Sc_{0.26}N$ deposition after reaching a base pressure of at least 5×10^{-7} mbar. Pt was choosen as electrode material due to its high work function, resulting in a high Schottky-barrier. This was expected to lower the leakage currents, which in turn facilitates the investigation of ferroelectric switching, especially in ultrathin films. Round- as well as square top electrodes were structured with lithography and ion-beam etching (IBE, Oxford Instruments Ionfab 300). The dry-etching was stopped right after the loss of Pt signal, detected via a secondary-ion mass spectrometer (SIMS). The capacitance and loss tangent measurements were performed using a Hewlett Packard 4284 A Precision LCR meter. If not stated otherwise, the small signal voltage and frequency were 0.1 V and 900 kHz, respectively. The sweep time for $C-E$ measurements of different $Al_{0.74}Sc_{0.26}N$ thickness was kept constant by adjusting the delay time between each step, as well as the step width of the voltage sweep. The TEM investigated sample was pre-switched by sweeping in 0.04 V steps with 100 ms delay in between. $J-E$ measurements were performed using an AixACCT TF 3000 analyzer. A cross-section sample of the partially switched film was extracted and thinned by the focused ion-beam technique using a Helios600 FIB-SEM machine and transferred into a JEOL (JEM200F) NEOARM scanning transmission electron microscope operated at 200 kV(cold-FEG). Atomic scale investigation of the unit-cell polarity within the sub-5 nm $Al_{0.74}Sc_{0.26}N$ layer was conducted using the ABF-STEM mode with 10 to 20 mrad collection angle and a spatial resolution limit of ≈70 pm. To minimize the effects of scan distortions and sample drift during image acquisition, the atomic-scale ABF-STEM micrographs were recorded using fast serial recording of multi-frame images followed by post-processing image alignment using rigid and non-rigid registration implemented in the Smart Align algorithm (HREM Research Inc.) on the DigitalMicrograph v.3.5.1 (DM) (GatanInc) software. If not stated otherwise, the non-registered ABF-STEM images were 1) Fourier filtered by a simple radiance difference filter using the lite version of DM plug-in HREM-Filters Pro/Lite v.4.2.1 (HREM Research Inc.) to remove high-frequency noise, and 2) the ABF contrast was inverted, a color scheme was applied and the contrast was slightly enhanced within DM, for presentation purposes (inverted-ABF-STEM). The in-plane and out-of-plane lattice parameters were estimated with ±2 pm accuracy by calculating the average atomic distance over minimum 8 and 6 unit cells, respectively, and are compared with the as-determined lattice parameter of the GaN substrate. For GaN, the as-determined lattice parameters are $a \approx 318$ pm and $c \approx 521$ and for $Al_{0.74}Sc_{0.26}N$ these are $a \approx 319$ pm and $c \approx 505$. Chemical analysis on the capacitor stack was conducted using energy-dispersive spectroscopy (EDS) with a dual silicon drift detector system with 100 mm^2 active area each. The denoted scandium content x was defined as the number of Sc atoms relative to the total number of metal atoms (Sc + Al) with an estimated uncertainty of ±0.02. Cross-section samples of 10 nm thin $Al_{0.74}Sc_{0.26}N$ based capacitor structures grown on Pt/GaN/sapphire and grown on Pt/Ti/SiO_2/Si were examined using a Tecnai F30 G^2 STwin microcsope operated at 300 kV.

Supporting Information

Supporting Information is available from the Wiley Online Library or from the author.

Acknowledgements

G.S. and N.W. contributed equally to this work. This work was funded by the project "ForMikro-SALSA" (Project-ID 16ES1053) from the Federal Ministry of Education and Research (BMBF). This work was also funded by the Deutsche Forschungsgemeinschaft (DFG, German Research Foundation)—Project-ID 434434223—SFB 1461; Project-ID 286471992—SFB 1261 as well as Project-ID 458372836. The authors gratefully acknowledge Christin Szillus for the FIB preparation of cross-section samples for TEM analysis.

Open access funding enabled and organized by Projekt DEAL.

Conflict of Interest

The authors declare no conflict of interest.

Data Availability Statement

The data that support the findings of this study are available from the corresponding author upon reasonable request.

Keywords

domains, ferroelectrics, neuromorphic computing, scandium, thin films

Received: April 13, 2023
Revised: May 26, 2023
Published online: June 29, 2023

[1] A. I. Khan, A. Keshavarzi, S. Datta, *Nat. Electron.* **2020**, *3*, 588.
[2] T. Mikolajick, U. Schroeder, S. Slesazeck, *IEEE Trans. Electron Devices* **2020**, *67*, 1434.
[3] T. Mikolajick, S. Slesazeck, H. Mulaosmanovic, M. H. Park, S. Fichtner, P. D. Lomenzo, M. Hoffmann, U. Schroeder, *J. Appl. Phys.* **2021**, *129*, 100901.
[4] U. Schroeder, M. H. Park, T. Mikolajick, C. S. Hwang, *Nat. Rev. Mater.* **2022**, *7*, 653.
[5] M. Lederer, T. Kämpfe, R. Olivo, D. Lehninger, C. Mart, S. Kirbach, T. Ali, P. Polakowski, L. Roy, K. Seidel, *Appl. Phys. Lett.* **2019**, *115*, 222902.
[6] H. Mulaosmanovic, J. Ocker, S. Müller, U. Schroeder, J. Müller, P. Polakowski, S. Flachowsky, R. van Bentum, T. Mikolajick, S. Slesazeck, *ACS Appl. Mater. Interfaces* **2017**, *9*, 3792.
[7] S. Fichtner, N. Wolff, F. Lofink, L. Kienle, B. Wagner, *J. Appl. Phys.* **2019**, *125*, 114103.
[8] M. R. Islam, N. Wolff, M. Yassine, G. Schönweger, B. Christian, H. Kohlstedt, O. Ambacher, F. Lofink, L. Kienle, S. Fichtner, *Appl. Phys. Lett.* **2021**, *118*, 232905.
[9] R. Aigner, G. Fattinger, presented at *20th Int. Conf. on Solid-State Sens., Actuators and Microsyst. Eurosensors*, Berlin, Germany **2019**, pp. 523–526.
[10] S. Fichtner, F. Lofink, B. Wagner, G. Schönweger, T.-N. Kreutzer, A. Petraru, H. Kohlstedt, presented at *2020 Joint Conf. of the IEEE Int. Frequency Control Sympos. and Int. Sympos. on Appl. of Ferroelectrics (IFCS-ISAF)*, Keystone, CO, USA **2020**, pp. 1–4.
[11] D. Wang, P. Wang, S. Mondal, M. Hu, D. Wang, Y. Wu, T. Ma, Z. Mi, *Appl. Phys. Lett.* **2023**, *122*, 052101.
[12] R. Mizutani, S. Yasuoka, T. Shiraishi, T. Shimizu, M. Uehara, H. Yamada, M. Akiyama, O. Sakata, H. Funakubo, *Appl. Phys. Express* **2021**, *14*, 105501.
[13] S. Yasuoka, R. Mizutani, R. Ota, T. Shiraishi, T. Shimizu, S. Yasui, Y. Ehara, K. Nishida, M. Uehara, H. Yamada, M. Akiyama, Y. Imai, O. Sakata, H. Funakubo, *J. Ceram. Soc. Jpn.* **2022**, *130*, 436.
[14] G. Schönweger, M. R. Islam, N. Wolff, A. Petraru, L. Kienle, H. Kohlstedt, S. Fichtner, *Phys. Status Solidi-RRL* **2022**, *17*, 2200312.
[15] D. Wang, J. Zheng, P. Musavigharavi, W. Zhu, A. C. Foucher, S. E. Trolier-McKinstry, E. A. Stach, R. H. Olsson, *IEEE Electron Device Lett.* **2020**, *41*, 1774.
[16] M. Li, K. Hu, H. Lin, V. Felmetsger, Y. Zhu, in *2022 IEEE Int. Ultrasonics Sympos. (IUS)*, IEEE, Piscataway, NJ, USA **2022**.
[17] Y.-P. Zhao, G.-C. Wang, T.-M. Lu, G. Palasantzas, J. T. M. D. Hosson, *Phys. Rev. B* **1999**, *60*, 9157.
[18] M. R. Islam, G. Schönweger, N. Wolff, A. Petraru, H. Kohlstedt, S. Fichtner, L. Kienle, *under review*.
[19] Y. Okada, Y. Tokumaru, *J. Appl. Phys.* **1984**, *56*, 314.
[20] W. M. Yim, R. J. Paff, *J. Appl. Phys.* **1974**, *45*, 1456.
[21] Y. Lu, M. Reusch, N. Kurz, A. Ding, T. Christoph, M. Prescher, L. Kirste, O. Ambacher, A. Žukauskaitė, *APL Mater.* **2018**, *6*, 076105.
[22] S. Zhang, W. Y. Fu, D. Holec, C. J. Humphreys, M. A. Moram, *J. Appl. Phys.* **2013**, *114*, 243516.
[23] S. Yasuoka, R. Mizutani, R. Ota, T. Shiraishi, T. Shimizu, M. Uehara, H. Yamada, M. Akiyama, H. Funakubo, *ACS Appl. Electron. Mater.* **2022**.
[24] C. M. Maxfield, in *FPGAs: Instant Access*, Elsevier, Amsterdam **2008**, pp. 13–48.
[25] X. Chen, N. A. Touba, in *Electronic Design Automation*, Elsevier, Amsterdam **2009**, pp. 39–95.
[26] G. Schönweger, A. Petraru, M. R. Islam, N. Wolff, B. Haas, A. Hammud, C. Koch, L. Kienle, H. Kohlstedt, S. Fichtner, *Adv. Funct. Mater.* **2022**, *32*, 2109632.
[27] O. Ambacher, B. Christian, N. Feil, D. F. Urban, C. Elsässer, M. Prescher, L. Kirste, *Jpn. J. Appl. Phys.* **2021**, *130*, 045102.
[28] M. Dawber, P. Chandra, P. B. Littlewood, J. F. Scott, *J. Phys.: Condens. Matter.* **2003**, *15*, L393.
[29] H. F. Kay, J. W. Dunn, *Philos. Mag.* **1962**, *7*, 2027.
[30] V. Janovec, *Czech. J. Phys.* **1958**, *8*, 3.
[31] S. Ducharme, V. M. Fridkin, A. V. Bune, S. P. Palto, L. M. Blinov, N. N. Petukhova, S. G. Yudin, *Phys. Rev. Lett.* **2000**, *84*, 175.
[32] C. Ke, Y. Hu, S. Liu, *Nanoscale Horiz.* **2023**, *8*, 616.
[33] W. Zhu, F. He, J. Hayden, Z. Fan, J. I. Yang, J.-P. Maria, S. Trolier-McKinstry, *Adv. Electron. Mater.* **2021**, *8*, 2100931.
[34] S. Bernacki, L. Jack, Y. Kisler, S. Collins, S. D. Bernstein, R. Hallock, B. Armstrong, J. Shaw, J. Evans, B. Tuttle, B. Hammetter, S. Rogers, B. Nasby, J. Henderson, J. Benedetto, R. Moore, C. R. Pugh, A. Fennelly, *Integr. Ferroelectr.* **1993**, *3*, 97.
[35] D. M. Evans, V. Garcia, D. Meier, M. Bibes, *Phys. Sci. Rev.* **2020**, *5*, 20190067.
[36] D. Jena, S. Heikman, D. Green, D. Buttari, R. Coffie, H. Xing, S. Keller, S. DenBaars, J. S. Speck, U. K. Mishra, I. Smorchkova, *Appl. Phys. Lett.* **2002**, *81*, 4395.
[37] L. Yan, Y. Zhang, X. Han, G. Deng, P. Li, Y. Yu, L. Chen, X. Li, J. Song, *Appl. Phys. Lett.* **2018**, *112*, 182104.
[38] O. V. Khokhlev, K. A. Bulashevich, S. Y. Karpov, *Phys. Status Solidi A* **2013**, *210*, 1369.
[39] R. Islam, H. Li, P.-Y. Chen, W. Wan, H.-Y. Chen, B. Gao, H. Wu, S. Yu, K. Saraswat, H.-S. P. Wong, *J. Phys. D: Appl. Phys.* **2019**, *52*, 113001.
[40] T. Shi, R. Wang, Z. Wu, Y. Sun, J. An, Q. Liu, *Small Struct.* **2021**, *2*, 2000109.
[41] N. Wolff, S. Fichtner, B. Haas, M. R. Islam, F. Niekiel, M. Kessel, O. Ambacher, C. Koch, B. Wagner, F. Lofink, L. Kienle, *J. Appl. Phys.* **2021**, *129*, 034103.
[42] L. Jones, H. Yang, T. J. Pennycook, M. S. J. Marshall, S. V. Aert, N. D. Browning, M. R. Castell, P. D. Nellist, *Adv. Struct. Chem. Imaging* **2015**, *1*, 1.

[43] D. Zhou, K. Müller-Caspary, W. Sigle, F. F. Krause, A. Rosenauer, P. A. van Aken, *Ultramicroscopy* **2016**, *160*, 110.
[44] E. Okunishi, H. Sawada, Y. Kondo, *Micron* **2012**, *43*, 538.
[45] M. de la Mata, C. Magen, J. Gazquez, M. I. B. Utama, M. Heiss, S. Lopatin, F. Furtmayr, C. J. Fernández-Rojas, B. Peng, J. R. Morante, R. Rurali, M. Eickhoff, A. F. i Morral, Q. Xiong, J. Arbiol, *Nano Lett.* **2012**, *12*, 2579.
[46] S. Fichtner, N. Wolff, G. Krishnamurthy, A. Petraru, S. Bohse, F. Lofink, S. Chemnitz, H. Kohlstedt, L. Kienle, B. Wagner, *J. Appl. Phys.* **2017**, *122*, 035301.

Chapter 5

Conclusion & Outlook

In this chapter, a short summary of the current work and an outlook with focus on device applications is given. Two major topics were investigated in the course of this doctoral thesis.

First, epitaxy and the integration of wurtzite-type ferroelectricity into III-N technology was addressed. The epitaxial sputter-deposition of ferroelectric $Al_{1-x}Sc_xN$ grown on single-crystal n-doped GaN/sapphire templates could be established and the dependence of the electrical response on the structure was explored.[SPI+22] This was followed by the demonstration and investigation of ferroelectricity in single crystal $Al_{1-x}Sc_xN$ /GaN heterostructures grown by MOCVD.[WSS+24] Interestingly, the comparison between single-crystal- (MOCVD), epitaxial columnar structured- (sputtering) and non-epitaxial $Al_{1-x}Sc_xN$ thin films (sputtering) revealed that the leakage current and the remanent polarization are in the same range and thus not directly related to the different structural qualities. Peculiarities such as a mixed and pinned as-grown polarity, epitaxial strain and a splitting of the ferroelectric switching peak as well as its prevention by introducing an intermediate epitaxial Pt electrode were investigated.[ISW+23] From the device perspective, the in-plane lattice-match of $Al_{1-x}Sc_xN$ (for $x \approx 0.18$) to GaN enables single crystal epitaxy without limitations regarding film thickness and enhanced 2DEG properties were reported already 2 years before the emergence of wurtzite-type ferroelectrics.[HDN+17]. In addition to that, ferroelectricy integrated into III-N devices can allow for a reconfigurable non-volatile threshold voltage control (non-volatile memory). Thus, the typical normally-on operation in HEMTs can be tuned dynamically into the more favourable normally-off behaviour.[YOY+23] Our fundamental studies on this heterostructures form a base for developing functional enhanced III-N devices suitable also for harsh environment (memory) applications, as we did not observe any destabilization of the ferroelectric phase of $Al_{1-x}Sc_xN$ up to 1100 °C.[IWY+21] Furthermore, our study of ferroelectric

epitaxial $Al_{1-x}Sc_xN$ grown by MOCVD[WSS+24] not only results in an extension of the repertoire of possible deposition methods, it can also facilitate the commercialisation of ferroelectric all-wurtzite-type III-N devices, for which MOCVD is the standard growth method.

Second, the scalability of ferroelectric $Al_{1-x}Sc_xN$ was addressed. Reducing the film thicknesses and the lateral dimensions enables low operating voltages and high storage densities. This not only results in a lower power consumption and lower costs per bit (memory), but it is also required to become compatible with the on-chip voltage supply of advanced integrated circuits, eventually facilitating the direct integration into the latter. The scaling studies of ferroelectric $Al_{1-x}Sc_xN$ performed during this doctoral thesis revealed a scalability down to at least 4 nm film thickness (8 to 9 unit cells).[SWI+23, SIF23] A clear ferroelectric response was achieved for epitaxial films grown on Pt/GaN/sapphire as well as for non-epitaxial films grown on $Pt/SiO_2/Si$ templates, thus demonstrating the availability of ferroelectricity at such low film thicknesses for III-N- as well as for silicon-technology. STEM investigations of a partially switched 4 nm thin film visualize the involvement of polarization domains in the switching process and demonstrate stable partial switching capabilities also of ultralow volumes (5 x 5 x 5 nm^3). A decrease of the coercive field below 10 nm film thickness was linked to depolarization field effects arising due to the finite screening length of the electrodes, which eventually allowed for a switching voltage of 1 V at 4 nm film thickness and demonstrates the compatibility to the on-chip voltage supply of advanced ICs. Surprisingly and contrary to reports on classical ferroelectrics, an increase in the apparent remanent polarization with decreasing film thickness was observed. This, together with the via STEM visualized inclined domain walls present in MOCVD-grown as well as in sputter-deposited $Al_{1-x}Sc_xN$ thin films, strongly suggests contributions from conductive domain walls upon ferroelectric switching.[SWI+23, WSS+24] This additional hysteretic currents which add up to the ferroelectric switching currents may allow for more aggressive scaling (e.g. in FeRAM due to a larger effective current response), as well as domain wall conduction in general allows to address additional device concepts such as two-terminal ferroelectricity-based memristive devices.

To conclude, these results highlight the suitability of ferroelectric $Al_{1-x}Sc_xN$ for next-generation memory devices operable also in harsh environments and capable of addressing neuromorphic concepts as well as in-memory computation. However, the comparably low cycling endurance and the presence of leakage currents at high electric fields limits the device performance in certain potential applications that require a large number of write-operations. Nevertheless, considering the short history as well as the at the moment of writing high interest of the ferroelectric community in wurtzite-type

ferroelectricity, research resulting in improvements of endurance and leakage can be expected.

Acknowledgments

This work would not have been possible without the help, advices, collaborative work and general support of many people.

First of all, I would like to thank Prof. Dr. Hermann Kohlstedt and Dr. Adrian Petraru for providing a friendly, motivating working environment and for the encouraging support especially in the most difficult part of probably any research topic - the beginning. The freedom to choose how, in what timeframe and in which direction to move on certainly was very self-motivating and contributed to the success of this work.

I would like to thank especially Dr. Simon Fichtner and Prof. Dr. Hermann Kohlstedt for creating the opportunity to research the exciting wurtzite-type ferroelectricity. Without the supervision and the guidance of Dr. Simon Fichtner, this work would not have been possible. The will of sharing his knowledge at any time, the ability of recognizing and ordering the importance of the individual findings as well as his encouraging view onto results is highly appreciated.

I would like to thank Dr. Adrian Petraru for being available and helpful at any time and for becoming a good (food) friend. I would also like to thank everybody from the nanoelectronics working group for providing a friendly and helpful environment.

I would also like to thank Prof. Dr. Lorenz Kienle for his persisting effort to improve the quality of our manuscripts as well as Prof. Dr. Fabian Lofink for coordinating the SALSA project, for his interest in AlScN and for bridging University and Fraunhofer ISIT.

The valuable expertise of Dr. Niklas Wolff for TEM together with his high motivation and persistence for understanding the fundamentals of wurtzite-type materials resulted in a very fruitful collaboration for which I would like to offer my thanks.

I would like to express my gratitude to my fellow PhD students Redwanul Islam, Tom-Niklas Kreutzer and Maike Gremmel (AlScN Team). The helping hands and minds, coffee breaks, conference companies and excursions helped to keep a good spirit up and move into the right direction.

I would also like to thank Katrin Brandenburg for always being helpful and for the professional assistance in complicated administrative issues.

My gratitude goes to Laura Gotthard and Sean Schulz for writing their master thesis under my supervision. Further gratitude goes to Vinay Lulla and Deik Dasenbrook for the helping hands and good work.

A special thanks goes to everybody living in room A-236 for the passion for high-quality coffee and for providing an excellent coffee machine and a nice coffee break atmosphere.

My deepest gratitude goes to my wife Maike and my two kids Alis and Hanna for being here with me and for exploring the small and enjoyable things of life with me. I also thank my whole family for the support from abroad. Despite living in different countries and some sporadic visits during the year, I always feel close and at home with you.

Full list of own publications

- Simon Fichtner, Fabian Lofink, Bernhard Wagner, **Georg Schonweger**, Tom-Niklas Kreutzer, Adrian Petraru, and Hermann Kohlstedt. *Ferroelectricity in AlScN: Switching, imprint and sub-150 nm films.* In 2020 Joint Conference of the IEEE International Frequency Control Symposium and International Symposium on Applications of Ferroelectrics (IFCS-ISAF). IEEE, jul 2020

- Md. Redwanul Islam, Niklas Wolff, Mohamed Yassine, **Georg Schönweger**, Björn Christian, Hermann Kohlstedt, Oliver Ambacher, Fabian Lofink, Lorenz Kienle, and Simon Fichtner. *On the exceptional temperature stability of ferroelectric alscn thin films.* Applied Physics Letters, 118(23):232905, jun 2021.

- **Georg Schönweger**, Adrian Petraru, Md Redwanul Islam, Niklas Wolff, Benedikt Haas, Adnan Hammud, Christoph Koch, Lorenz Kienle, Hermann Kohlstedt, and Simon Fichtner. *From fully strained to relaxed: Epitaxial ferroelectric $Al_{1-x}Sc_xN$ for III-n technology.* Advanced Functional Materials, page 2109632, feb 2022.

- **Georg Schönweger**, Md Redwanul Islam, Niklas Wolff, Adrian Petraru, Lorenz Kienle, Hermann Kohlstedt, and Simon Fichtner. *Ultrathin $Al_{1-x}Sc_xN$ for low-voltage-driven ferroelectric-based devices.* physica status solidi (RRL) – Rapid Research Letters, page 2200312, oct 2022.

- Roberto Guido, Patrick D. Lomenzo, Md Redwanul Islam, Niklas Wolff, Maike Gremmel, **Georg Schönweger**, Hermann Kohlstedt, Lorenz Kienle, Thomas Mikolajick, Simon Fichtner, and Uwe Schroeder. *Thermal stability of the ferroelectric properties in 100 nm-thick $Al_{0.72}Sc_{0.28}N$.* ACS Applied Materials & Interfaces, 15(5):7030–7043, jan 2023.

- Md Redwanul Islam, **Georg Schönweger**, Niklas Wolff, Adrian Petraru, Hermann Kohlstedt, Simon Fichtner, and Lorenz Kienle. *A comparative study of*

pt/$Al_{0.72}Sc_{0.28}N$/pt-based thin-film metal-ferroelectric-metal capacitors on GaN and si substrates. ACS Applied Materials & Interfaces, aug 2023.

- **Georg Schönweger**, Niklas Wolff, Md Redwanul Islam, Maike Gremmel, Adrian Petraru, Lorenz Kienle, Hermann Kohlstedt, and Simon Fichtner. *In-grain ferroelectric switching in sub-5 nm thin $Al_{0.74}Sc_{0.26}N$ films at 1 V.* Advanced Science, 10(25), jun 2023.

- **Georg Schönweger**, Md Redwanul Islam, and Simon Fichtner. *Structural and ferroelectric properties of $Al_{1-x}Sc_xN$*, pages 71–99. Elsevier, 2023.

- Simon Fichtner, **Georg Schönweger**, Frank Dietz, Henning Hanssen, Heiko Züge, Tom-Niklas Kreutzer, Fabian Lofink, Hermann Kohlstedt, Holger Kapels, and Michael Mensing. *Wurtzite-type ferroelectrics for microelectronic devices: Scalability and integration to silicon based ferroelectric fets.* In 2023 7th IEEE Electron Devices Technology & Manufacturing Conference (EDTM). IEEE, march 2023.

- Niklas Wolff, **Georg Schönweger**, Isabel Streicher, Md Redwanul Islam, Nils Braun, Patrik Straňák, Lutz Kirste, Mario Prescher, Andriy Lotnyk, Hermann Kohlstedt, Stefano Leone, Lorenz Kienle, and Simon Fichtner. *Demonstration and stem analysis of ferroelectric switching in mocvd-grown single crystalline $Al_{0.85}Sc_{0.15}N$.* Advanced Physics Research, february 2024.

- Haidong Lu, **Georg Schönweger**, Adrian Petraru, Hermann Kohlstedt, Simon Fichtner, Alexei Gruverman. *Domain Dynamics and Resistive Switching in Ferroelectric $Al_{1-x}Sc_xN$ Thin Film Capacitors.* Advanced Functional Materials, march 2024.

Own contributions

The following table declares the amount of own contribution for each article included in chapter 4.

	Conceptualization	Sample fabbrication	Measurements	Data analysis	Writing (original draft)	Review/Editing
From Fully Strained to Relaxed: Epitaxial Ferroelectric $Al_{1-x}Sc_xN$ for III-N Technology	H	H	H	H	H	H
A Comparative Study of $Pt/Al_{1-x}Sc_xN/Pt$-Based Thin-Film Metal-Ferroelectric-Metal Capacitors on GaN and Si Substrates	M	H	M	M	L	M
Demonstration and STEM Analysis of Ferroelectric Switching in MOCVD-Grown Single Crystalline $Al_{1-x}Sc_xN$	M	L	H	H	H	L
Ultrathin $Al_{1-x}Sc_xN$ for Low-Voltage-Driven Ferroelectric-Based Devices	H	H	H	H	H	H
In-Grain Ferroelectric Switching in Sub-5 nm Thin $Al_{0.74}Sc_{0.26}N$ Films at 1 V	H	H	H	H	H	H

Table 5.1: Own contributions for the respective article. H denotes High-, M denotes Medium- an L denotes Low contribution.

Bibliography

[AKK+08] Morito Akiyama, Toshihiro Kamohara, Kazuhiko Kano, Akihiko Teshigahara, Yukihiro Takeuchi, and Nobuaki Kawahara. Enhancement of piezoelectric response in scandium aluminum nitride alloy thin films prepared by dual reactive cosputtering. *Advanced Materials*, 21(5):593–596, dec 2008.

[AMMK18] Jackson D. Anderson, Jordan Merkel, David Macmahon, and Santosh K. Kurinec. Evaluation of si:HfO_2 ferroelectric properties in MFM and MFIS structures. *IEEE Journal of the Electron Devices Society*, 6:525–534, 2018.

[AP09] Mahmoud Al Ahmad and R. Plana. Piezoelectric coefficients of thin film aluminum nitride characterizations using capacitance measurements. *IEEE Microwave and Wireless Components Letters*, 19(3):140–142, mar 2009.

[ASS+99] O. Ambacher, J. Smart, J. R. Shealy, N. G. Weimann, K. Chu, M. Murphy, W. J. Schaff, L. F. Eastman, R. Dimitrov, L. Wittmer, M. Stutzmann, W. Rieger, and J. Hilsenbeck. Two-dimensional electron gases induced by spontaneous and piezoelectric polarization charges in n- and ga-face AlGaN/GaN heterostructures. *Journal of Applied Physics*, 85(6):3222–3233, mar 1999.

[AVKT+17] F. Ambriz-Vargas, G. Kolhatkar, R. Thomas, R. Nouar, A. Sarkissian, C. Gomez-Yáñez, M. A. Gauthier, and A. Ruediger. Tunneling electroresistance effect in a Pt/$Hf_{0.5}Zr_{0.5}O_2$/Pt structure. *Applied Physics Letters*, 110(9), February 2017.

[AYY+22] O. Ambacher, A. Yassine, M. Yassine, S. Mihalic, E. Wade, and B. Christian. Electron accumulation and distribution at interfaces of hexagonal

$Sc_xAl_{1-x}N$/GaN- and $Sc_xAl_{1-x}n$/InN-heterostructures. *Journal of Applied Physics*, 131(24):245702, jun 2022.

[AZH+21] Laith Alzubaidi, Jinglan Zhang, Amjad J. Humaidi, Ayad Al-Dujaili, Ye Duan, Omran Al-Shamma, J. Santamaría, Mohammed A. Fadhel, Muthana Al-Amidie, and Laith Farhan. Review of deep learning: concepts, cnn architectures, challenges, applications, future directions. *Journal of Big Data*, 8(1), March 2021.

[BBKK22] Maximilian T. Becker, Claus J. Burkhardt, Reinhold Kleiner, and Dieter Koelle. Impedance spectroscopy of ferroelectrics: The domain wall pinning element. *Journal of Applied Physics*, 132(4), jul 2022.

[BFPS21] Sergey V. Barabash, Simon Fichtner, Min Hyuk Park, and Tony Schenk. Emerging fluorite- and wurtzite-type ferroelectrics: From (Hf,Zr)O_2 to AlN and related materials. *physica status solidi (RRL) – Rapid Research Letters*, 15(5):2100201, may 2021.

[BJK+93] Steve Bernacki, Larry Jack, Yanina Kisler, Steve Collins, S. D. Bernstein, Rob Hallock, Bruce Armstrong, Jerry Shaw, Joe Evans, Bruce Tuttle, Bill Hammetter, Steve Rogers, Bob Nasby, Jack Henderson, Joe Benedetto, Randy Moore, Cpt Robert Pugh, and Al Fennelly. Standardized ferroelectric capacitor test methodology for nonvolatile semiconductor memory applications. *Integrated Ferroelectrics*, 3(2):97–112, jun 1993.

[BLGW99] Dierk Bolten, Oliver Lohse, Michael Grossmann, and Rainer Waser. Reversible and irreversible domain wall contributions to the polarization in ferroelectric thin films. *Ferroelectrics*, 221(1):251–257, January 1999.

[BMB+11] T. S. Böscke, J. Müller, D. Bräuhaus, U. Schröder, and U. Böttger. Ferroelectricity in hafnium oxide thin films. *Applied Physics Letters*, 99(10), September 2011.

[Bon90] David Bondurant. Ferroelectronic ram memory family for critical data storage. *Ferroelectrics*, 112(1):273–282, dec 1990.

[BWCK94] P. W. M. Blom, R. M. Wolf, J. F. M. Cillessen, and M. P. C. M. Krijn. Ferroelectric schottky diode. *Physical Review Letters*, 73(15):2107–2110, October 1994.

[Bö04] Ulrich Böttger. Dielectric properties of polar oxides, dec 2004.

[CBSB97] Francis K. Chai, J. R. Brews, R. D. Schrimpf, and D. P. Birnie. Domain switching and spatial dependence of permittivity in ferroelectric thin films. *Journal of Applied Physics*, 82(5):2505–2516, September 1997.

[CDLS04] P. CHANDRA, M. DAWBER, P. B. LITTLEWOOD, and J. F. SCOTT. Scaling of the coercive field with thickness in thin-film ferroelectrics. *Ferroelectrics*, 313(1):7–13, jan 2004.

[CHC+21] Yueh-Hua Chu, Hsin-Hui Huang, Yu-Hao Chen, Chien-Hua Hsu, Pei-Jer Tzeng, Shyh-Shyuan Sheu, Wei-Chung Lo, Chih-I Wu, and Tuo-Hung Hou. Ultra-thin hf0.5zr0.5o2 ferroelectric tunnel junction with high current density. In *2021 International Symposium on VLSI Technology, Systems and Applications (VLSI-TSA)*. IEEE, April 2021.

[CHW+24] Si-Meng Chen, Takuya HOSHII, Hitoshi WAKABAYASHI, Kazuo TSUTSUI, Edward Yi Chang, and Kuniyuki Kakushima. Reactive sputtering of ferroelectric alscn films with h2 gas flow for endurance improvement. *Japanese Journal of Applied Physics*, January 2024.

[CLL+24] Li Chen, Chen Liu, Hock Koon Lee, Binni Varghese, Ronald Wing Fai Ip, Minghua Li, Zhan Jiang Quek, Yan Hong, Weijie Wang, Wendong Song, Huamao Lin, and Yao Zhu. Demonstration of 10 nm ferroelectric $Al_{0.7}Sc_{0.3}N$-based capacitors for enabling selector-free memory array. *Materials*, 17(3):627, January 2024.

[CMM+22] Erika Covi, Halid Mulaosmanovic, Benjamin Max, Stefan Slesazeck, and Thomas Mikolajick. Ferroelectric-based synapses and neurons for neuromorphic computing. *Neuromorphic Computing and Engineering*, 2(1):012002, February 2022.

[CNC+22] Joseph Casamento, Thai-Son Nguyen, Yongjin Cho, Chandrashekhar Savant, Timothy Vasen, Shamima Afroz, Daniel Hannan, Huili (Grace) Xing, and Debdeep Jena. Transport properties of polarization-induced 2d electron gases in epitaxial AlScN/GaN heterojunctions. *Applied Physics Letters*, 121(19):192101, nov 2022.

[CNN+22] J. Casamento, K. Nomoto, T. S. Nguyen, H. Lee, C. Savant, L. Li, A. Hickman, T. Maeda, J. Encomendero, V. Gund, A. Lal, J. C. M. Hwang, H. G. Xing, and D. Jena. FerroHEMTs: High-current and high-speed all-epitaxial AlScN/GaN ferroelectric transistors. In *2022 International Electron Devices Meeting (IEDM)*. IEEE, dec 2022.

[CSRS12] G. Catalan, J. Seidel, R. Ramesh, and J. F. Scott. Domain wall nanoelectronics. *Reviews of Modern Physics*, 84(1):119–156, feb 2012.

[Dam98] Dragan Damjanovic. Ferroelectric, dielectric and piezoelectric properties of ferroelectric thin films and ceramics. *Reports on Progress in Physics*, 61(9):1267–1324, sep 1998.

[DEG13] Ruopeng Deng, Sarah R. Evans, and Daniel Gall. Bandgap in alscn. *Applied Physics Letters*, 102(11):112103, mar 2013.

[DMM95] R Douglas, M Mahowald, and C Mead. Neuromorphic analogue vlsi. *Annual Review of Neuroscience*, 18(1):255–281, March 1995.

[DRS05] M. Dawber, K. M. Rabe, and J. F. Scott. Physics of thin-film ferroelectric oxides. *Reviews of Modern Physics*, 77(4):1083–1130, oct 2005.

[DYZ+22] Daniel Drury, Keisuke Yazawa, Andriy Zakutayev, Brendan Hanrahan, and Geoff Brennecka. High-temperature ferroelectric behavior of $Al_{0.7}Sc_{0.3}N$. *Micromachines*, 13(6):887, 2022.

[EGMB20] Donald M. Evans, Vincent Garcia, Dennis Meier, and Manuel Bibes. Domains and domain walls in multiferroics. *Physical Sciences Reviews*, 5(9), apr 2020.

[Eit07] R.E. Eitel. Rayleigh law response in ferroelectric ceramics: Quantifying domain wall dynamics and structural relationships. In *2007 Sixteenth IEEE International Symposium on the Applications of Ferroelectrics*. IEEE, may 2007.

[FBZ+21] Kevin Ferri, Saiphaneendra Bachu, Wanlin Zhu, Mario Imperatore, John Hayden, Nasim Alem, Noel Giebink, Susan Trolier-McKinstry, and Jon-Paul Maria. Ferroelectrics everywhere: Ferroelectricity in magnesium substituted zinc oxide thin films. *Journal of Applied Physics*, 130(4):044101, jul 2021.

[FLW+20] Simon Fichtner, Fabian Lofink, Bernhard Wagner, Georg Schonweger, Tom-Niklas Kreutzer, Adrian Petraru, and Hermann Kohlstedt. Ferroelectricity in AlScN: Switching, imprint and sub-150 nm films. In *2020 Joint Conference of the IEEE International Frequency Control Symposium and International Symposium on Applications of Ferroelectrics (IFCS-ISAF)*. IEEE, jul 2020.

[FRC+15] Simon Fichtner, Tim Reimer, Steffen Chemnitz, Fabian Lofink, and Bernhard Wagner. Stress controlled pulsed direct current co-sputtered $Al_{1-x}Sc_xN$ as piezoelectric phase for micromechanical sensor applications. *APL Materials*, 3(11):116102, nov 2015.

[FSD+23] Simon Fichtner, Georg Schönweger, Frank Dietz, Henning Hanssen, Heiko Züge, Tom-Niklas Kreutzer, Fabian Lofink, Hermann Kohlstedt, Holger Kapels, and Michael Mensing. Wurtzite-type ferroelectrics for microelectronic devices: Scalability and integration to silicon based ferroelectric fets. In *2023 7th IEEE Electron Devices Technology & Manufacturing Conference (EDTM)*. IEEE, March 2023.

[FWK+17] Simon Fichtner, Niklas Wolff, Gnanavel Krishnamurthy, Adrian Petraru, Sascha Bohse, Fabian Lofink, Steffen Chemnitz, Hermann Kohlstedt, Lorenz Kienle, and Bernhard Wagner. Identifying and overcoming the interface originating c-axis instability in highly sc enhanced AlN for piezoelectric micro-electromechanical systems. *Journal of Applied Physics*, 122(3):035301, jul 2017.

[FWL+19] Simon Fichtner, Niklas Wolff, Fabian Lofink, Lorenz Kienle, and Bernhard Wagner. AlScN: A III-V semiconductor based ferroelectric. *Journal of Applied Physics*, 125(11):114103, mar 2019.

[GB14] Vincent Garcia and Manuel Bibes. Ferroelectric tunnel junctions for information storage and processing. *Nature Communications*, 5(1), July 2014.

[GLI+23] Roberto Guido, Patrick D Lomenzo, Md Redwanul Islam, Niklas Wolff, Maike Gremmel, Georg Schonweger, Hermann Kohlstedt, Lorenz Kienle, Thomas Mikolajick, Simon Fichtner, et al. Thermal stability of the ferroelectric properties in 100 nm-thick $Al_{0.72}Sc_{0.28}N$. *ACS Applied Materials & Interfaces*, 15(5):7030–7043, 2023.

[GSJ+18] N. Gong, X. Sun, H. Jiang, K. S. Chang-Liao, Q. Xia, and T. P. Ma. Nucleation limited switching (NLS) model for HfO2-based metal-ferroelectric-metal (MFM) capacitors: Switching kinetics and retention characteristics. *Applied Physics Letters*, 112(26), jun 2018.

[Gü19] Fatih Gül. Addressing the sneak-path problem in crossbar rram devices using memristor-based one schottky diode-one resistor array. *Results in Physics*, 12:1091–1096, March 2019.

[HBA+10] Carina Höglund, Jens Birch, Björn Alling, Javier Bareño, Zsolt Czigány, Per O. Å. Persson, Gunilla Wingqvist, Agne Zukauskaite, and Lars Hultman. Wurtzite structure $Sc_{1-x}Al_xN$ solid solution films grown by reactive magnetron sputter epitaxy: Structural characterization and first-principles calculations. *Journal of Applied Physics*, 107(12):123515, jun 2010.

[HCF+23] Yunfei He, Shangyi Chen, Merrilyn Mercy Adzo Fiagbenu, Chloe Leblanc, Pariasadat Musavigharavi, Gwangwoo Kim, Xingyu Du, Jiazheng Chen, Xiwen Liu, Eric A. Stach, Roy H. Olsson, and Deep Jariwala. Metal-ferroelectric alscn-semiconductor memory devices on sic wafers. *Applied Physics Letters*, 123(12), September 2023.

[HDN+17] Matthew T. Hardy, Brian P. Downey, Neeraj Nepal, David F. Storm, D. Scott Katzer, and David J. Meyer. Epitaxial ScAlN grown by molecular beam epitaxy on GaN and SiC substrates. *Applied Physics Letters*, 110(16):162104, apr 2017.

[HGJ23] Junghyeon Hwang, Youngin Goh, and Sanghun Jeon. Physics, structures, and applications of fluorite-structured ferroelectric tunnel junctions. *Small*, October 2023.

[HHX+21] John Hayden, Mohammad Delower Hossain, Yihuang Xiong, Kevin Ferri, Wanlin Zhu, Mario Vincenzo Imperatore, Noel Giebink, Susan Trolier-McKinstry, Ismaila Dabo, and Jon-Paul Maria. Ferroelectricity in boron-substituted aluminum nitride thin films. *Physical Review Materials*, 5(4):044412, apr 2021.

[HSO+23] Kota Hasegawa, Takao Shimizu, Takeo Ohsawa, Isao Sakaguchi, and Naoki Ohashi. Full polarization reversal at room temperature in unsubstituted aln. *Applied Physics Letters*, 123(19), November 2023.

[HZL+12] L.Z. Hao, J. Zhu, Y.J. Liu, X.W. Liao, S.L. Wang, J.J. Zhou, C. Kong, H.Z. Zeng, Y. Zhang, W.L. Zhang, and Y.R. Li. Normally-off characteristics of LiNbO3/AlGaN/GaN ferroelectric field-effect transistor. *Thin Solid Films*, 520(19):6313–6317, July 2012.

[ISW+23] Md Redwanul Islam, Georg Schönweger, Niklas Wolff, Adrian Petraru, Hermann Kohlstedt, Simon Fichtner, and Lorenz Kienle. A comparative

study of $Pt/Al_{0.72}Sc_{0.28}N/Pt$-based thin-film metal-ferroelectric-metal capacitors on GaN and Si substrates. *ACS Applied Materials &amp Interfaces*, aug 2023.

[IT71] Yoshihiro Ishibashi and Yutaka Takagi. Note on ferroelectric domain switching. *Journal of the Physical Society of Japan*, 31(2):506–510, aug 1971.

[IWY+21] Md. Redwanul Islam, Niklas Wolff, Mohamed Yassine, Georg Schönweger, Björn Christian, Hermann Kohlstedt, Oliver Ambacher, Fabian Lofink, Lorenz Kienle, and Simon Fichtner. On the exceptional temperature stability of ferroelectric alscn thin films. *Applied Physics Letters*, 118(23):232905, jun 2021.

[JLZ13] Li Jin, Fei Li, and Shujun Zhang. Decoding the fingerprint of ferroelectric loops: Comprehension of the material properties and structures. *Journal of the American Ceramic Society*, 97(1):1–27, dec 2013.

[JZ19] An Quan Jiang and Yan Zhang. Next-generation ferroelectric domain-wall memories: principle and architecture. *NPG Asia Materials*, 11(1), January 2019.

[KCJ21] Jae Young Kim, Min-Ju Choi, and Ho Won Jang. Ferroelectric field effect transistors: Progress and perspective. *APL Materials*, 9(2), February 2021.

[Kit46] Charles Kittel. Theory of the structure of ferromagnetic domains in films and small particles. *Physical Review*, 70(11-12):965–971, dec 1946.

[KKD20] Asif Islam Khan, Ali Keshavarzi, and Suman Datta. The future of ferroelectric field-effect transistor technology. *Nature Electronics*, 3(10):588–597, oct 2020.

[KKOJ23] Kwan-Ho Kim, Ilya Karpov, Roy H. Olsson, and Deep Jariwala. Wurtzite and fluorite ferroelectric materials for electronic memory. *Nature Nanotechnology*, 18(5):422–441, apr 2023.

[KL23] Ik-Jyae Kim and Jang-Sik Lee. Ferroelectric transistors for memory and neuromorphic device applications. *Advanced Materials*, 35(22), April 2023.

[KOF+23] Kwan-Ho Kim, Seyong Oh, Merrilyn Mercy Adzo Fiagbenu, Jeffrey Zheng, Pariasadat Musavigharavi, Pawan Kumar, Nicholas Trainor, Areej Aljarb, Yi Wan, Hyong Min Kim, Keshava Katti, Seunguk Song, Gwangwoo Kim, Zichen Tang, Jui-Han Fu, Mariam Hakami, Vincent Tung, Joan M. Redwing, Eric A. Stach, Roy H. Olsson, and Deep Jariwala. Scalable CMOS back-end-of-line-compatible AlScN/two-dimensional channel ferroelectric field-effect transistors. *Nature Nanotechnology*, may 2023.

[LBH15] Yann LeCun, Yoshua Bengio, and Geoffrey Hinton. Deep learning. *Nature*, 521(7553):436–444, May 2015.

[Liu] Liu. AlScN/n-GaN ferroelectric memristors with controllable on/off ratios and reversible bipolar resistive switching characteristics.

[LLC+23] Dong Hyun Lee, Younghwan Lee, Yong Hyeon Cho, Hyojun Choi, Se Hyun Kim, and Min Hyuk Park. Unveiled ferroelectricity in well-known non-ferroelectric materials and their semiconductor applications. *Advanced Functional Materials*, jun 2023.

[LS09] Huadong Li and G. Subramanyam. Capacitance of thin-film ferroelectrics under different drive signals. *IEEE Transactions on Ultrasonics, Ferroelectrics and Frequency Control*, 56(9):1861–1867, sep 2009.

[LWZ+20] Xiwen Liu, Dixiong Wang, Jeffrey Zheng, Pariasadat Musavigharavi, Jinshui Miao, Eric A. Stach, Roy H. Olsson III, and Deep Jariwala. Post-cmos compatible aluminum scandium nitride/2d channel ferroelectric field-effect-transistor, 2020.

[LZW+21] Xiwen Liu, Jeffrey Zheng, Dixiong Wang, Pariasadat Musavigharavi, Eric A. Stach, Roy Olsson, and Deep Jariwala. Aluminum scandium nitride-based metal–ferroelectric–metal diode memory devices with high on/off ratios. *Applied Physics Letters*, 118(20):202901, may 2021.

[MAG+10] David Maier, Mohammed Alomari, Nicolas Grandjean, Jean-Francois Carlin, Marie-Antoinette Diforte-Poisson, Christian Dua, Andrey Chuvilin, David Troadec, Christophe Gaquiere, Ute Kaiser, Sylvain L. Delage, and Erhard Kohn. Testing the temperature limits of gan-based hemt devices. *IEEE Transactions on Device and Materials Reliability*, 10(4):427–436, December 2010.

[MCPK04] R. MEYER, J. RODRIGUEZ CONTRERAS, A. PETRARU, and H. KOHLSTEDT. On a novel ferro resistive random access memory (frram): Basic model and first experiments. *Integrated Ferroelectrics*, 64(1):77–88, January 2004.

[MF53] Toshito Mitsui and Jiro Furuichi. Domain structure of rochelle salt and KH_2PO_4. *Physical Review*, 90(2):193–202, apr 1953.

[MHSM18] Benjamin Max, Michael Hoffmann, Stefan Slesazeck, and Thomas Mikolajick. Ferroelectric tunnel junctions based on ferroelectric-dielectric Hf0.5Zr0.5.O2/A12O3 capacitor stacks. In *2018 48th European Solid-State Device Research Conference (ESSDERC)*. IEEE, September 2018.

[MK22] A. Mehonic and A. J. Kenyon. Brain-inspired computing needs a master plan. *Nature*, 604(7905):255–260, April 2022.

[MLW+20] James P. V. McConville, Haidong Lu, Bo Wang, Yueze Tan, Charlotte Cochard, Michele Conroy, Kalani Moore, Alan Harvey, Ursel Bangert, Long-Qing Chen, Alexei Gruverman, and J. Marty Gregg. Ferroelectric domain wall memristor. *Advanced Functional Materials*, 30(28), may 2020.

[MMS20] Halid Mulaosmanovic, Thomas Mikolajick, and Stefan Slesazeck. FeFETs for neuromorphic systems. In *Topics in Applied Physics*, pages 399–411. Springer Singapore, 2020.

[MOM+17] Halid Mulaosmanovic, Johannes Ocker, Stefan Müller, Uwe Schroeder, Johannes Müller, Patrick Polakowski, Stefan Flachowsky, Ralf van Bentum, Thomas Mikolajick, and Stefan Slesazeck. Switching kinetics in nanoscale hafnium oxide based ferroelectric field-effect transistors. *ACS Applied Materials &amp Interfaces*, 9(4):3792–3798, jan 2017.

[MPG+23] Richard Marquardt, Deik Petersen, Ole Gronenberg, Finn Zahari, Rouven Lamprecht, George Popkirov, Jürgen Carstensen, Lorenz Kienle, and Hermann Kohlstedt. Domain wall movement in undoped ferroelectric HfO_2: A rayleigh analysis. *ACS Applied Electronic Materials*, 5(6):3251–3260, may 2023.

[MS21] Dennis Meier and Sverre M. Selbach. Ferroelectric domain walls for nanotechnology. *Nature Reviews Materials*, 7(3):157–173, October 2021.

[MSM+12] Stefan Mueller, Scott R. Summerfelt, Johannes Muller, Uwe Schroeder, and Thomas Mikolajick. Ten-nanometer ferroelectric Si:HfO_2 films for next-generation FRAM capacitors. *IEEE Electron Device Letters*, 33(9):1300–1302, sep 2012.

[MSM+21] T. Mikolajick, S. Slesazeck, H. Mulaosmanovic, M. H. Park, S. Fichtner, P. D. Lomenzo, M. Hoffmann, and U. Schroeder. Next generation ferroelectric materials for semiconductor process integration and their applications. *Journal of Applied Physics*, 129(10):100901, mar 2021.

[MWP+05] Rene Meyer, Rainer Waser, Klaus Prume, Torsten Schmitz, and Stephan Tiedke. Dynamic leakage current compensation in ferroelectric thin-film capacitor structures. *Applied Physics Letters*, 86(14):142907, apr 2005.

[NW23] Anam Nazir and Ze Wang. A comprehensive survey of chatgpt: Advancements, applications, prospects, and challenges. *Meta-Radiology*, 1(2):100022, September 2023.

[OKK+20] Jun Okuno, Takafumi Kunihiro, Kenta Konishi, Hideki Maemura, Yusuke Shuto, Fumitaka Sugaya, Monica Materano, Tarek Ali, Kati Kuehnel, Konrad Seidel, Uwe Schroeder, Thomas Mikolajick, Masanori Tsukamoto, and Taku Umebayashi. SoC compatible 1T1C FeRAM memory array based on ferroelectric $Hf_{0.5}Zr_{0.5}O_2$. In *2020 IEEE Symposium on VLSI Technology*. IEEE, June 2020.

[PCK+03] N. A. Pertsev, J. Rodriguez Contreras, V. G. Kukhar, B. Hermanns, H. Kohlstedt, and R. Waser. Coercive field of ultrathin $Pb(Zr_{0.52}Ti_{0.48})O_3$ epitaxial films. *Applied Physics Letters*, 83(16):3356–3358, oct 2003.

[PCL+23] Ju Yong Park, Duk-Hyun Choe, Dong Hyun Lee, Geun Taek Yu, Kun Yang, Se Hyun Kim, Geun Hyeong Park, Seung-Geol Nam, Hyun Jae Lee, Sanghyun Jo, Bong Jin Kuh, Daewon Ha, Yongsung Kim, Jinseong Heo, and Min Hyuk Park. Revival of ferroelectric memories based on emerging fluorite-structured ferroelectrics. *Advanced Materials*, mar 2023.

[PJS+02] J.-P. Palmquist, U. Jansson, T. Seppänen, P. O. Å. Persson, J. Birch, L. Hultman, and P. Isberg. Magnetron sputtered epitaxial single-phase Ti_3SiC_2 thin films. *Applied Physics Letters*, 81(5):835–837, jul 2002.

[PKH+17] Milan Pešić, Christopher Künneth, Michael Hoffmann, Halid Mulaosmanovic, Stefan Müller, Evelyn T. Breyer, Uwe Schroeder, Alfred Ker-

sch, Thomas Mikolajick, and Stefan Slesazeck. A computational study of hafnia-based ferroelectric memories: from ab initio via physical modeling to circuit models of ferroelectric device. *Journal of Computational Electronics*, 16(4):1236–1256, August 2017.

[PLH21] Hyeon Woo Park, Jae-Gil Lee, and Cheol Seong Hwang. Review of ferroelectric field-effect transistors for three-dimensional storage applications. *Nano Select*, 2(6):1187–1207, jan 2021.

[QWC+21] Huimin Qiao, Chenxi Wang, Woo Seok Choi, Min Hyuk Park, and Yunseok Kim. Ultra-thin ferroelectrics. *Materials Science and Engineering: R: Reports*, 145:100622, jul 2021.

[RCZ+23] N. Ramaswamy, A. Calderoni, J. Zahurak, G. Servalli, A. Chavan, S. Chhajed, M. Balakrishnan, M. Fischer, M. Hollander, D. P. Ettisserry, A. Liao, K. Karda, M. Jerry, M. Mariani, A. Visconti, B. R. Cook, B. D. Cook, D. Mills, A. Torsi, C. Mouli, E. Byers, M. Helm, S. Pawlowski, S. Shiratake, and N. Chandrasekaran. Nvdram: A 32gb dual layer 3d stacked non-volatile ferroelectric memory with near-dram performance for demanding ai workloads. In *2023 International Electron Devices Meeting (IEDM)*. IEEE, December 2023.

[RDL+] Karin M. Rabe, Matthew Dawber, Céline Lichtensteiger, Charles H. Ahn, and Jean-Marc Triscone. Modern physics of ferroelectrics: Essential background. In *Topics in Applied Physics*, pages 1–30. Springer Berlin Heidelberg.

[Sco07] J F Scott. Ferroelectrics go bananas. *Journal of Physics: Condensed Matter*, 20(2):021001, dec 2007.

[SDE+06] N. Setter, D. Damjanovic, L. Eng, G. Fox, S. Gevorgian, S. Hong, A. Kingon, H. Kohlstedt, N. Y. Park, G. B. Stephenson, I. Stolitchnov, A. K. Taganstev, D. V. Taylor, T. Yamada, and S. Streiffer. Ferroelectric thin films: Review of materials, properties, and applications. *Journal of Applied Physics*, 100(5):051606, sep 2006.

[SIF23] Georg Schönweger, Md Redwanul Islam, and Simon Fichtner. *Structural and ferroelectric properties of* $Al_{1-x}Sc_xN$, pages 71–99. Elsevier, 2023.

[SKN+05] Y. W. So, D. J. Kim, T. W. Noh, Jong-Gul Yoon, and T. K. Song. Polarization switching kinetics of epitaxial $Pb(Zr_{0.4}Ti_{0.6})O_3$ thin films. *Applied Physics Letters*, 86(9), feb 2005.

[SLH+24] Jie Sun, Yiming Li, Di Hu, Bowen Shen, Boyang Zhang, Zilong Wang, Haiyue Tang, and Anquan Jiang. Roadmap for ferroelectric domain wall memory. *Microstructures*, 4(1), January 2024.

[SLS+02] Bo Shen, Wei-ping Li, Takao Someya, Zhao-xia Bi, Jie Liu, Hui-mei Zhou, Rong Zhang, Feng Yan, Yi Shi, Zhi-guo Liu, You-dou Zheng, and Yasuhiko Arakawa. Influence of ferroelectric polarization on the properties of two-dimensional electron gas in $Pb(Zr_{0.53}Ti_{0.47})O_3/Al_xGa_{1-x}N/GaN$ structures. *Japanese Journal of Applied Physics*, 41(Part 1, No. 4B):2528–2530, April 2002.

[SM21] Tony Schenk and Stefan Mueller. A new generation of memory devices enabled by ferroelectric hafnia and zirconia. In *2021 IEEE International Symposium on Applications of Ferroelectrics (ISAF)*. IEEE, May 2021.

[SMMS06] Igor Stolichnov, Lisa Malin, Paul Muralt, and Nava Setter. Ferroelectric gate for control of transport properties of two-dimensional electron gas at AlGaN/GaN heterostructures. *Applied Physics Letters*, 88(4), January 2006.

[SPI+22] Georg Schönweger, Adrian Petraru, Md Redwanul Islam, Niklas Wolff, Benedikt Haas, Adnan Hammud, Christoph Koch, Lorenz Kienle, Hermann Kohlstedt, and Simon Fichtner. From fully strained to relaxed: Epitaxial ferroelectric $Al_{1-x}Sc_xN$ for III-N technology. *Advanced Functional Materials*, page 2109632, feb 2022.

[SPM+18] Cosmin Silviu Sandu, Fazel Parsapour, Stefan Mertin, Vladimir Pashchenko, Ramin Matloub, Thomas LaGrange, Bernd Heinz, and Paul Muralt. Abnormal grain growth in AlScN thin films induced by complexion formation at crystallite interfaces. *physica status solidi (a)*, 216(2):1800569, oct 2018.

[SPMH22] Uwe Schroeder, Min Hyuk Park, Thomas Mikolajick, and Cheol Seong Hwang. The fundamentals and applications of ferroelectric HfO2. *Nature Reviews Materials*, 7(8):653–669, mar 2022.

[SPS+20] T Schenk, M Pešić, S Slesazeck, U Schroeder, and T Mikolajick. Memory technology—a primer for material scientists. *Reports on Progress in Physics*, 83(8):086501, jul 2020.

[SRK+21] Minchul Sung, Kwangmyoung Rho, Jayong Kim, Junho Cheon, Kiyoung Choi, Dohee Kim, Hoseok Em, Gyeongcheol Park, Jungwook Woo, Yeongyu Lee, Jaehyeon Ko, Moonhoi Kim, Gwangyeob Lee, Seung Wook Ryu, Dong Sun Sheen, Yangsung Joo, Seiyon Kim, Chang Hyun Cho, Myung-Hee Na, and Jinkook Kim. Low voltage and high speed 1xnm 1t1c FE-RAM with ultra-thin 5nm HZO. In *2021 IEEE International Electron Devices Meeting (IEDM)*. IEEE, dec 2021.

[SRM98] Vladimir Shur, Evgenii Rumyantsev, and Sergei Makarov. Kinetics of phase transformations in real finite systems: Application to switching in ferroelectrics. *Journal of Applied Physics*, 84(1):445–451, jul 1998.

[SS23] Pankaj Sharma and Jan Seidel. Neuromorphic functionality of ferroelectric domain walls. *Neuromorphic Computing and Engineering*, 3(2):022001, may 2023.

[SSM18] Stefan Slesazeck, Uwe Schroeder, and Thomas Mikolajick. Embedding hafnium oxide based FeFETs in the memory landscape. In *2018 International Conference on IC Design &amp Technology (ICICDT)*. IEEE, jun 2018.

[STBS13] Tomas Sluka, Alexander K. Tagantsev, Petr Bednyakov, and Nava Setter. Free-electron gas at charged domain walls in insulating BaTiO3. *Nature Communications*, 4(1), may 2013.

[SWI+23] Georg Schönweger, Niklas Wolff, Md Redwanul Islam, Maike Gremmel, Adrian Petraru, Lorenz Kienle, Hermann Kohlstedt, and Simon Fichtner. In-grain ferroelectric switching in sub-5 nm thin $Al_{0.74}Sc_{0.26}N$ films at 1 V. *Advanced Science*, 10(25), jun 2023.

[SZS+17] Pankaj Sharma, Qi Zhang, Daniel Sando, Chi Hou Lei, Yunya Liu, Jiangyu Li, Valanoor Nagarajan, and Jan Seidel. Nonvolatile ferroelectric domain wall memory. *Science Advances*, 3(6), jun 2017.

[TK06] Evgeny Y. Tsymbal and Hermann Kohlstedt. Tunneling across a ferroelectric. *Science*, 313(5784):181–183, jul 2006.

[TSS+02] Alexander K. Tagantsev, Igor Stolichnov, Nava Setter, Jeffrey S. Cross, and Mineharu Tsukada. Non-kolmogorov-avrami switching kinetics in ferroelectric thin films. *Physical Review B*, 66(21):214109, dec 2002.

[USR+13] K. R. Udayakumar, T. San, J. Rodriguez, S. Chevacharoenkul, D. Frystak, J. Rodriguez-Latorre, C. Zhou, M. Ball, P. Ndai, S. Madan, H. McAdams, S. Summerfelt, and T. Moise. Low-power ferroelectric random access memory embedded in 180nm analog friendly CMOS technology. In *2013 5th IEEE International Memory Workshop*. IEEE, may 2013.

[Wan] Li-Mo Wang. Relationship between intrinsic breakdown field and bandgap of materials. In *2006 25th International Conference on Microelectronics*. IEEE.

[WHB+17] Christoph S. Werner, Simon J. Herr, Karsten Buse, Boris Sturman, Elisabeth Soergel, Cina Razzaghi, and Ingo Breunig. Large and accessible conductivity of charged domain walls in lithium niobate. *Scientific Reports*, 7(1), August 2017.

[WIK+22] Niklas Wolff, Md Redwanul Islam, Lutz Kirste, Simon Fichtner, Fabian Lofink, Agnė Žukauskaitė, and Lorenz Kienle. $Al_{1-x}Sc_xN$ thin films at high temperatures: Sc-dependent instability and anomalous thermal expansion. *Micromachines*, 13(8):1282, aug 2022.

[WMH+22] Jing Wang, Jing Ma, Houbing Huang, Ji Ma, Hasnain Mehdi Jafri, Yuanyuan Fan, Huayu Yang, Yue Wang, Mingfeng Chen, Di Liu, Jinxing Zhang, Yuan-Hua Lin, Long-Qing Chen, Di Yi, and Ce-Wen Nan. Ferroelectric domain-wall logic units. *Nature Communications*, 13(1), jun 2022.

[WML+23] Ding Wang, Shubham Mondal, Jiangnan Liu, Mingtao Hu, Ping Wang, Samuel Yang, Danhao Wang, Yixin Xiao, Yuanpeng Wu, Tao Ma, and Zetian Mi. Ferroelectric YAlN grown by molecular beam epitaxy. *Applied Physics Letters*, 123(3), jul 2023.

[WSS+24] Niklas Wolff, Georg Schönweger, Isabel Streicher, Md Redwanul Islam, Nils Braun, Patrik Straňák, Lutz Kirste, Mario Prescher, Andriy Lotnyk, Hermann Kohlstedt, Stefano Leone, Lorenz Kienle, and Simon Fichtner.

Demonstration and STEM analysis of ferroelectric switching in MOCVD-grown single crystalline $Al_{0.85}Sc_{0.15}N$. *Advanced Physics Research*, February 2024.

[WW19] Zheng Wen and Di Wu. Ferroelectric tunnel junctions: Modulations on the potential barrier. *Advanced Materials*, 32(27), October 2019.

[WWH+23] Ding Wang, Ping Wang, Minming He, Jiangnan Liu, Shubham Mondal, Mingtao Hu, Danhao Wang, Yuanpeng Wu, Tao Ma, and Zetian Mi. Fully epitaxial, monolithic ScAlN/AlGaN/GaN ferroelectric HEMT. *Applied Physics Letters*, 122(9):090601, feb 2023.

[WWM+22] Ding Wang, Ping Wang, Shubham Mondal, Subhajit Mohanty, Tao Ma, Elaheh Ahmadi, and Zetian Mi. An epitaxial ferroelectric ScAlN/GaN heterostructure memory. *Advanced Electronic Materials*, page 2200005, mar 2022.

[WWM+23] Ding Wang, Ping Wang, Shubham Mondal, Mingtao Hu, Yuanpeng Wu, Tao Ma, and Zetian Mi. Ultrathin nitride ferroic memory with large ON/OFF ratios for analog in-memory computing. *Advanced Materials*, 35(20), mar 2023.

[WWMM22] Ping Wang, Ding Wang, Shubham Mondal, and Zetian Mi. Ferroelectric n-polar ScAlN/GaN heterostructures grown by molecular beam epitaxy. *Applied Physics Letters*, 121(2):023501, jul 2022.

[WWV+21] Ping Wang, Ding Wang, Nguyen M. Vu, Tony Chiang, John T. Heron, and Zetian Mi. Fully epitaxial ferroelectric ScAlN grown by molecular beam epitaxy. *Applied Physics Letters*, 118(22):223504, may 2021.

[WWWM21] Ding Wang, Ping Wang, Boyu Wang, and Zetian Mi. Fully epitaxial ferroelectric ScGaN grown on GaN by molecular beam epitaxy. *Applied Physics Letters*, 119(11):111902, sep 2021.

[WYS+20] Chunlei Wu, Hansheng Ye, Nikhita Shaju, Jeffrey Smith, Benjamin Grisafe, Suman Datta, and Patrick Fay. $Hf_{0.5}Zr_{0.5}O_2$-based ferroelectric gate HEMTs with large threshold voltage tuning range. *IEEE Electron Device Letters*, 41(3):337–340, March 2020.

[YHM+23] Keisuke Yazawa, John Hayden, Jon-Paul Maria, Wanlin Zhu, Susan Trolier-McKinstry, Andriy Zakutayev, and Geoff L. Brennecka. Anoma-

lously abrupt switching of wurtzite-structured ferroelectrics: simultaneous non-linear nucleation and growth model. *Materials Horizons*, 2023.

[YHS+19] Jungkyu Yoon, Seunghyeon Hong, Yong Won Song, Ji-Hoon Ahn, and Seung-Eon Ahn. Understanding tunneling electroresistance effect through potential profile in $Pt/Hf_{0.5}Zr_{0.5}O_2/TiN$ ferroelectric tunnel junction memory. *Applied Physics Letters*, 115(15), October 2019.

[YIV+11] HAIXUE YAN, FAWAD INAM, GIUSEPPE VIOLA, HUANPO NING, HONGTAO ZHANG, QINGHUI JIANG, TAO ZENG, ZHIPENG GAO, and MIKE J REECE. The contribution of electrical conductivity, dielectric permittivity and domain switching in ferroelectric hysteresis loops. *Journal of Advanced Dielectrics*, 01(01):107–118, jan 2011.

[YMG+22] Keisuke Yazawa, John S. Mangum, Prashun Gorai, Geoff L. Brennecka, and Andriy Zakutayev. Local chemical origin of ferroelectric behavior in wurtzite nitrides. *Journal of Materials Chemistry C*, 10(46):17557–17566, 2022.

[YMO+22a] Shinnosuke Yasuoka, Ryoichi Mizutani, Reika Ota, Takahisa Shiraishi, Takao Shimizu, Masato Uehara, Hiroshi Yamada, Morito Akiyama, and Hiroshi Funakubo. Tunable ferroelectric properties in wurtzite $Al_{0.8}Sc_{0.2}N$ via crystal anisotropy. *ACS Applied Electronic Materials*, oct 2022.

[YMO+22b] Shinnosuke Yasuoka, Ryoichi Mizutani, Reika Ota, Takahisa Shiraishi, Takao Shimizu, Shintaro Yasui, Yoshitaka Ehara, Ken Nishida, Masato Uehara, Hiroshi Yamada, Morito Akiyama, Yasuhiko Imai, Osami Sakata, and Hiroshi Funakubo. Enhancement of crystal anisotropy and ferroelectricity by decreasing thickness in (Al,Sc)N films. *Journal of the Ceramic Society of Japan*, 130(7):436–441, jul 2022.

[YNF+22] M. Yassine, A. Nair, J. Fammels, E. Wade, Z. Fu, A. Yassine, L. Kirste, and O. Ambacher. Influence of structural properties on the ferroelectric behavior of hexagonal AlScN. *Journal of Applied Physics*, 132(11):114101, sep 2022.

[YOY+23] Jeong Yong Yang, Seung Yoon Oh, Min Jae Yeom, Seokgi Kim, Gyuhyung Lee, Kyusang Lee, Sungkyu Kim, and Geonwook Yoo. Pulsed e-/d-mode switchable GaN HEMTs with a ferroelectric AlScN gate dielectric. *IEEE Electron Device Letters*, pages 1–1, 2023.

[Yu18] Shimeng Yu. Neuro-inspired computing with emerging nonvolatile memorys. *Proceedings of the IEEE*, 106(2):260–285, February 2018.

[ZHH+21a] Wanlin Zhu, John Hayden, Fan He, Jung-In Yang, Pannawit Tipsawat, Mohammad D. Hossain, Jon-Paul Maria, and Susan Trolier-McKinstry. Strongly temperature dependent ferroelectric switching in AlN, $Al_{1-x}Sc_xN$, and $Al_{1-x}B_xN$ thin films. *Applied Physics Letters*, 119(6):062901, aug 2021.

[ZHH+21b] Wanlin Zhu, Fan He, John Hayden, Zhongming Fan, Jung In Yang, Jon-Paul Maria, and Susan Trolier-McKinstry. Wake-up in $Al_{1x}B_xN$ ferroelectric films. *Advanced Electronic Materials*, 8(6):2100931, dec 2021.

Appendix

A.1 Supplementary: From Fully Strained to Relaxed: Epitaxial Ferroelectric $Al_{1-x}Sc_xN$ for III-N Technology

ADVANCED FUNCTIONAL MATERIALS

Supporting Information

for *Adv. Funct. Mater.,* DOI: 10.1002/adfm.202109632

From Fully Strained to Relaxed: Epitaxial Ferroelectric $Al_{1-x}Sc_xN$ for III-N Technology

Georg Schönweger, Adrian Petraru, Md Redwanul Islam, Niklas Wolff, Benedikt Haas, Adnan Hammud, Christoph Koch, Lorenz Kienle, Hermann Kohlstedt, and Simon Fichtner**

WILEY-VCH

Supporting Information

From Fully Strained to Relaxed: Epitaxial Ferroelectric $Al_{1-x}Sc_xN$ for III-N Technology

Georg Schönweger, Adrian Petraru, Md Redwanul Islam, Niklas Wolff, Benedikt Haas, Adnan Hammud, Christoph Koch, Lorenz Kienle, Hermann Kohlstedt, Simon Fichtner**

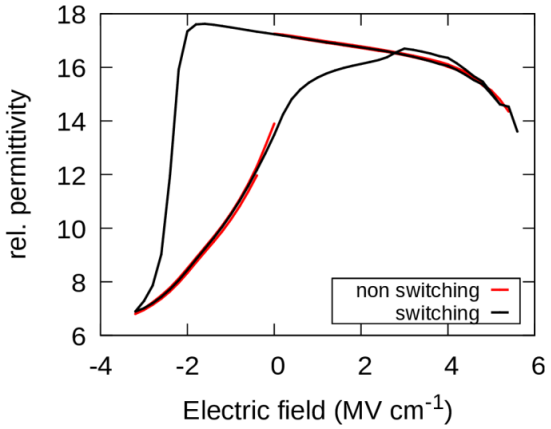

Figure S1. Relative permittivity in dependence of electric field for 50 nm thick $Al_{0.72}Sc_{0.28}N$ on n-GaN. In black the full loop shows a rather complex hysteresis at negative fields due to an expected depletion at the $Al_{0.72}Sc_{0.28}N$/n-GaN interface as discussed in section 3. To confirm ferroelectric switching at both sides, unipolar non-switching half-cycles were measured by pre-switching the film to the respective polarity and are depicted in red.

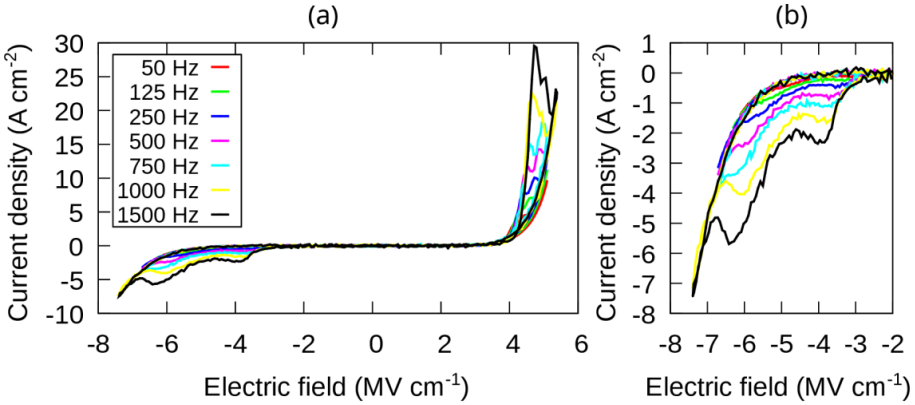

Figure S2. a) Uncorrected *J-E* curves measured at different frequencies for 100 nm thick $Al_{0.72}Sc_{0.28}N$. b) Zoom-in of the switching cycles for negative fields. With increasing frequency, the peak height is increasing as well as the peak center is shifting to higher absolute fields.

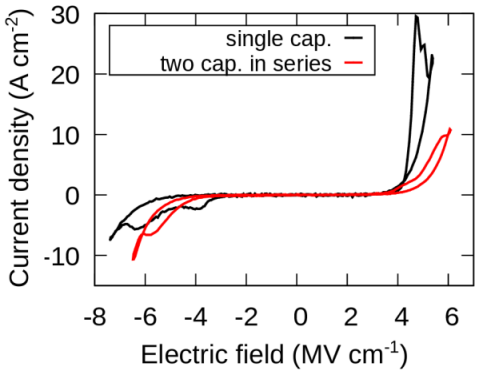

Figure S3. Uncorrected *J-E* loops of a 100 nm thick $Al_{0.72}Sc_{0.28}N$ on n-GaN sample measured a) through contacting the bottom electrode (n-GaN) via Ag and b) through contacting two capacitors in series and keeping the bottom electrode (n-GaN) floating.

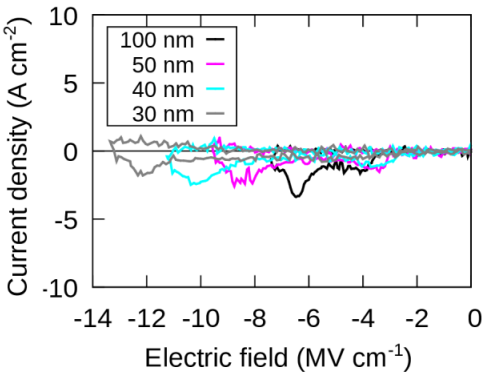

Figure S4. DLCC (1 kHz) *J-E* curves for different $Al_{0.72}Sc_{0.28}N$ thicknesses. 'Peak A' (lower coercive field) disappears at 30 nm film thickness. For clearer peak separation only the negative part of the cycle is illustrated. Leakage compensation was calculated using measurements at 1 kHz and 2 kHz.

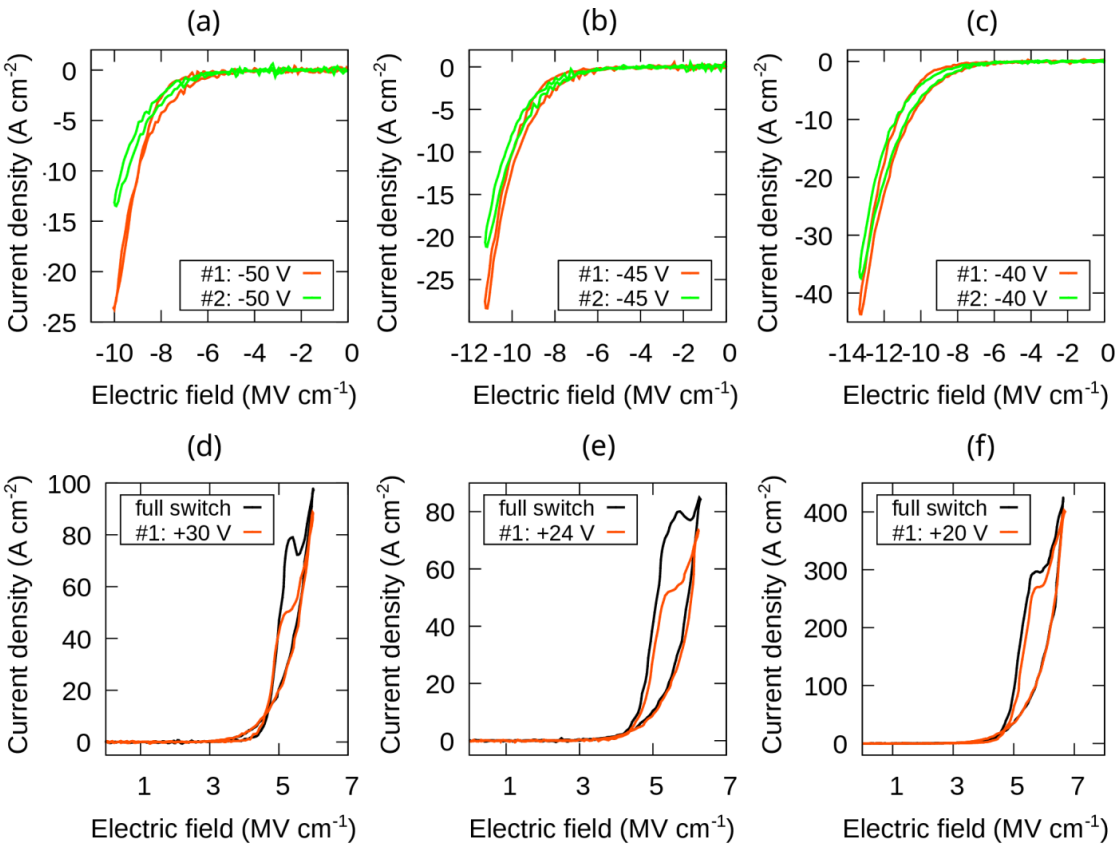

Figure S5. Unipolar measurements on pristine $Al_{0.72}Sc_{0.28}N$ capacitors to determine the initial polarization state in dependence of the film thickness for a), d) 50 nm, b), e) 40 nm and c), f) 30 nm thick films.

The unipolar measurements at negative fields in **Figure S5** compare the first- versus the second voltage signal applied to as-deposited capacitors with a), 50 nm b), 40 nm and c), 30 nm $Al_{0.72}Sc_{0.28}N$ film thickness. The first negative voltage applied (orange) switches as-deposited N-polar regions to M-polarity, while the current response from the second applied negative voltage (green) represents leakage currents. For the films with 50 nm and 40 nm thickness, switching of as-deposited N-polarity is still observed, while for the film with 30 nm thickness no significant difference between switching and leakage cycle is measured, meaning the latter film is fully M-polar after deposition. The positive loops in Figure S5 differentiate between the first unipolar positive switching cycle (orange) on as-deposited capacitors and a positive unipolar switching cycle (black) after pre-switching the capacitor to full M-polarity

by applying a negative voltage above the coercive field. The first applied positive voltage therefore switches the as-deposited M-polar regions to N-polarity, while the fully switching cycle inverts the fully M-polar film to N-polarity. Clearly, the area of as-deposited switching peaks converges to the area of the fully switching peaks with decreasing film thickness. Thus, at ~30 nm film thickness a horizontal inversion from as-deposited M-polarity to N-polarity is expected.

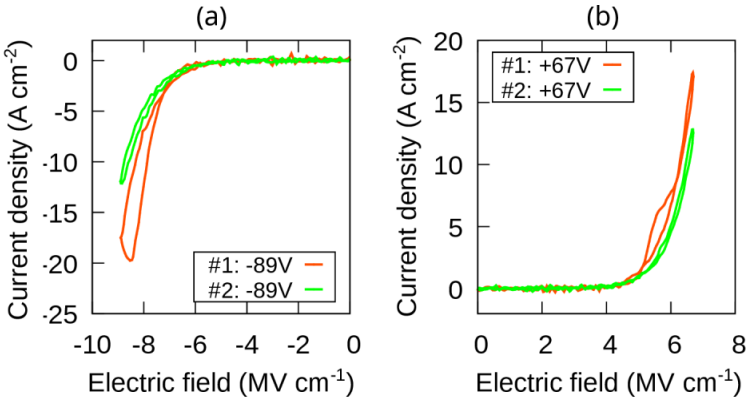

Figure S6. a) Negative and b) positive unipolar measurements on pristine 100 nm $Al_{0.81}Sc_{0.19}N$ capacitors to visualize the as-deposited polarization. As-deposited M- and N-polar regions are present also in lattice-matched films and are therefore not bound to different strain regimes.

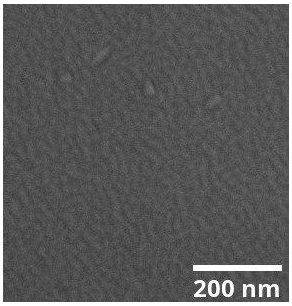

Figure S7. SEM image of the 300 nm $Al_{0.72}Sc_{0.28}N$ sample. The overall grain structure including four protruding grains is visible. The grain size is significantly lower than the grain size of $Al_{1-x}Sc_xN$ deposited on Pt/Si.[23]

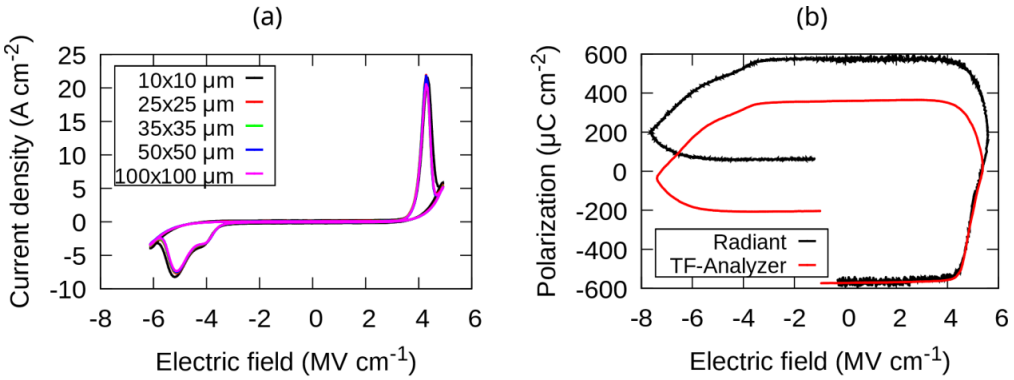

Figure S8. a) *J-E* loops for 200 nm thick $Al_{0.72}Sc_{0.28}N$ on n-GaN measured on different capacitor areas. b) *P-E* loops for 100 nm thick $Al_{0.72}Sc_{0.28}N$ on n-GaN measured with a TF-Analyzer 2000 (red) and a Radiant Precision Premiere II ferreoelectric tester (black). All loops were measured at 1.5 kHz.

The *J-E* loops presented in **Figure S8**a illustrate the independence of the displacement current response on the capacitor area. Thus, the appearing peak splitting at negative fields is not arising from fringing fields, which may ferroelectrically switch areas outside of the top metallization area. In Figure S8b *P-E* loops recorded via two different measurement devices are compared. Clearly both measurement devices reveal a broadening of the switching regime as well as the occurrence of the double-peaks (different slopes after switching starts) at negative fields. Therefore, the appearance of the double-peaks is not a measurement artifact originating from measurement-setup related issues. The higher polarization visible in the Radiant measurement at positive fields is a consequence of the higher maximum voltage leading to higher leakage currents (the *P-E* representation was chosen since the Radiant device features hardware integration of the displacement current and thus gives the polarization as its direct output).

A.2 Supplementary: A Comparative Study of Pt/$Al_{0.72}Sc_{0.28}$ Based Thin-Film Metal-Ferroelectric-Metal Capacitors on GaN and Si Substrates

Supporting Information

A Comparative Study of Pt/$Al_{0.72}Sc_{0.28}N$/Pt Based Thin-film Metal-Ferroelectric-Metal Capacitors on GaN and Si Substrates

Md Redwanul Islam[1], Georg Schönweger[2,4], Niklas Wolff[1,5], Adrian Petraru[2], Hermann Kohlstedt[2,5], Simon Fichtner[3,4]*, Lorenz Kienle[1,5]*

[1]Synthesis and Real Structure, Institute for Material Science, Kiel University, Kaiserstr. 2, D-24143 Kiel, Germany

[2]Nanoelectronics, Institute of Electrical Engineering and Information Engineering, Kiel University, Kaiserstr. 2, D-24143 Kiel

[3]Microsystems and Technology Transfer, Institute for Material Science, Kiel University, Kaiserstr. 2, D-24143 Kiel, Germany

[4]Fraunhofer Institute for Silicon Technology (ISIT), Fraunhoferstraße 1, 25524 Itzehoe, Germany

[5]Kiel Nano, Surface and Interface Science (KiNSIS), Kiel University, Christian-Albrechts-Platz 4, D-24118, Kiel, Germany.

Author to whom correspondence should be addressed: sif@tf.uni-kiel.de

Atomic Force Microscopy: Pt and $Al_{0.72}Sc_{0.28}N$ on GaN and Si substrates:

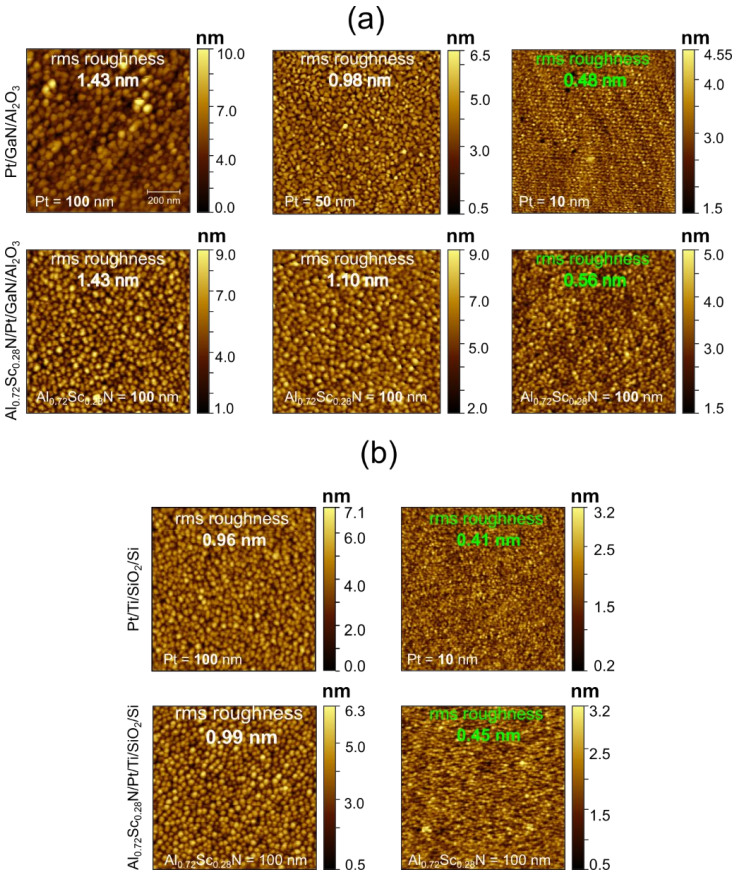

Figure S1: AFM surface profile with corresponding rms roughness values of (a) epi-Pt and $Al_{0.72}Sc_{0.8}N$ on GaN/Al_2O_3 substrates, (b) Fiber textured Pt and $Al_{0.72}Sc_{0.28}N$ on Si substrates.

Rocking curve Pt 222:

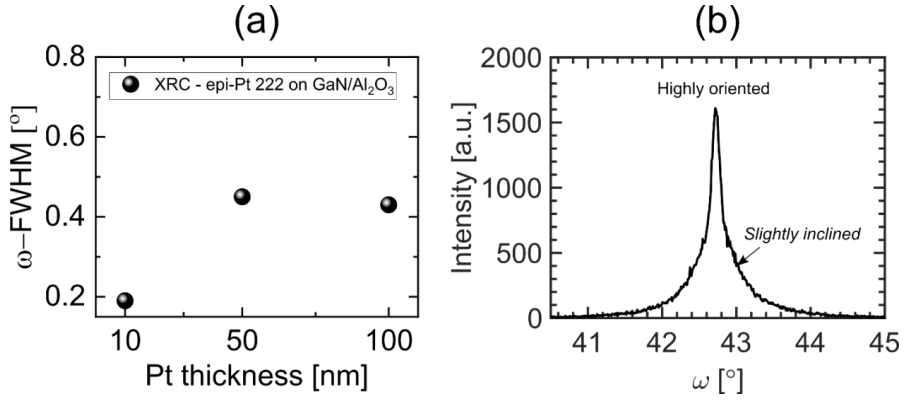

Figure S2: Epi-Pt on GaN/Al_2O_3: (a) Pt **222** ω-FWHM of 100, 50 and 10 nm epi-Pt films (b) ω-scan of a 10 nm epi-Pt

Figure S2 (a) shows the Pt 222 rocking curve FWHM of 10, 50, and 100 nm epi-Pt on GaN/Al_2O_3 substrate. The statistics clearly demonstrate that the crystalline quality improves as the epi-Pt electrode thickness decreases from 100 to 10 nm. In S2 (b), the ω-scan of Pt **222** reflection further reveals the highly crystalline and slightly disordered regions.

Polarization-Electric field (P-E) response of w-$Al_{0.72}Sc_{0.28}N$ on epi-Pt/GaN and Pt on Si substrates

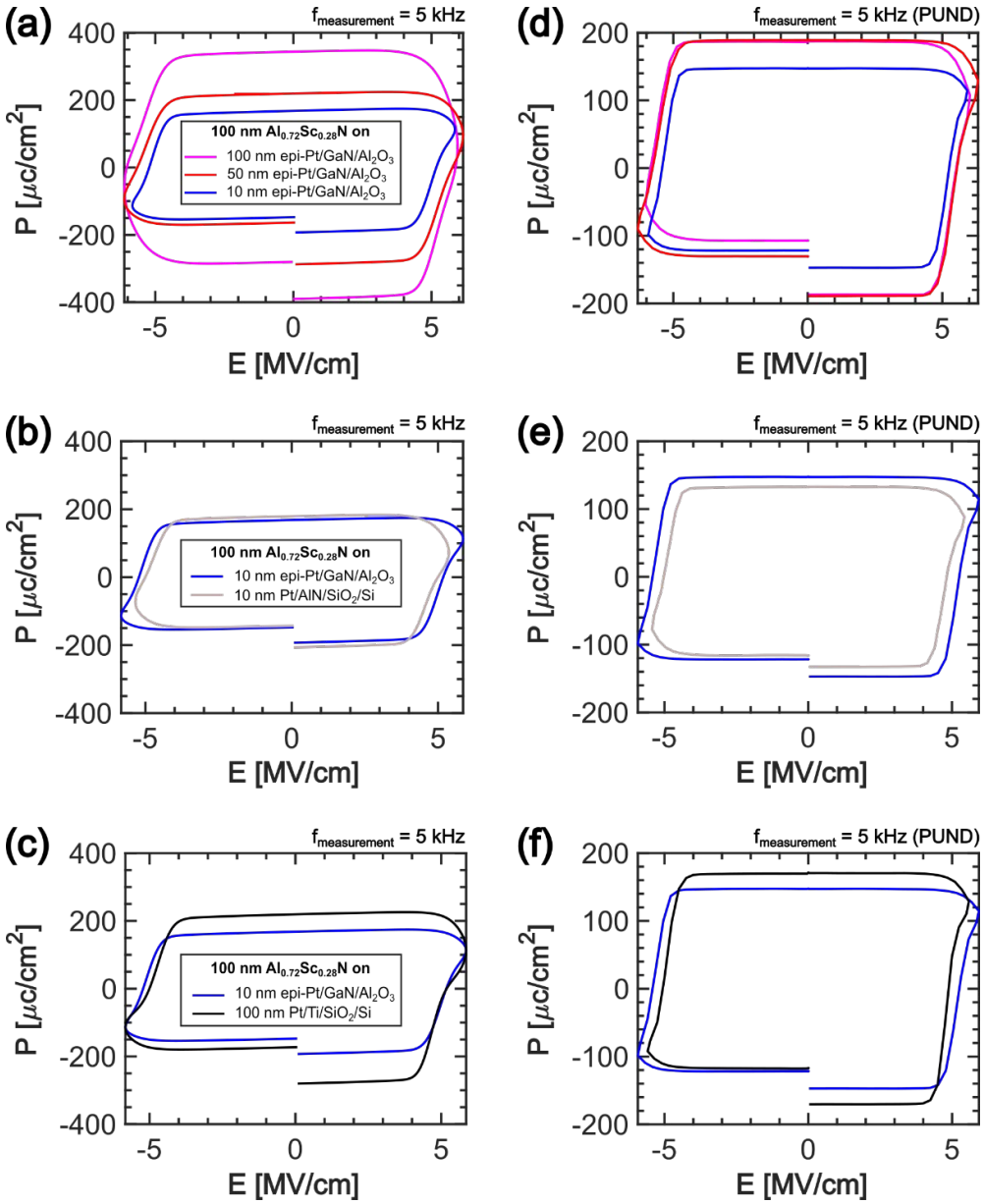

S-4

Figure S3: P-E response of $Al_{0.72}Sc_{0.28}N$ 100 nm at 5 kHz measurement frequency on (a) 100 (magenta), 50 (red), and 10 (blue) nm epi-Pt on GaN/Al_2O_3, (b) 10 nm $Al_{0.72}Sc_{0.28}N$ on epi-$Pt/GaN/Al_2O_3$ (blue) vs. $Pt/AlN/SiO_2/Si$ (gray), (c) 10 nm epi-$Pt/GaN/Al_2O_3$ (blue) vs. 100 nm $Pt/Ti/SiO_2/Si$ (black). (d-e-f) Corresponding Positive up negative down (PUND) measurements of (a-b-c).

Figure S3 (a) shows the polarization hysteresis loop at 5 kHz. The effect overestimation of the polarization due to leakage can be observed clearly for 100 nm $Al_{0.72}Sc_{0.28}N$ on 50 and 100 nm epi-$Pt/GaN/Al_2O_3$. From S3 (b-c) P-E loops of the 100 nm $Al_{0.72}Sc_{0.28}N$ on 10 nm epi-pt or 100 nm fiber textured Pt on Si are relatively less affected by leakage. However, still lacks required accuracy correct P_r estimation. Figure (d-f) shows the PUND corrected loops at the same measurement frequency. This measurement removes the switching independent leakage current, however the effect of switching induced leakage current still affects the overall polarization, therefore causes overestimation of real P_r values. This effect is frequency dependent and can be minimized by measuring at higher frequency.[1]

In-plane RSM 20 nm $Al_{0.72}Sc_{0.28}N$/epi-$Pt/GaN/Al_2O_3$ (ω = 0.7°):

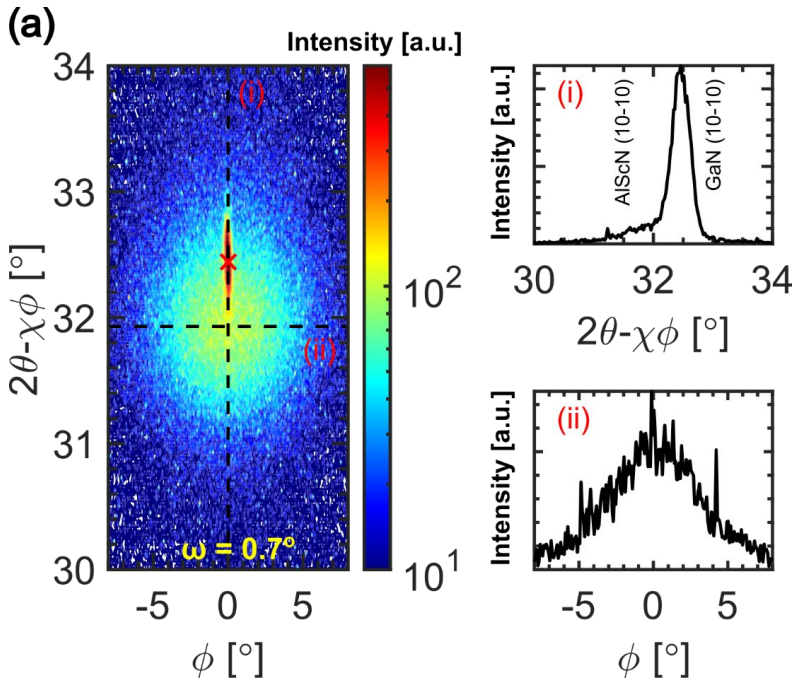

Figure S4: In-plane RSM of 20 nm $Al_{0.72}Sc_{0.28}N$ on 10 nm epi-$Pt/GaN/Al_2O_3$. (a) RSM with incident angle ω=0.7°. Cutlines through the reflection center are marked as (i) and (ii).

To provide further validity of our fitting in 5 (d)-i in-plane RSM measurements was taken of the same specimen at higher ω = 0.7° incident angle. This result further clarifies the position and the intensity spread of the GaN 10-10 reflection. Inside the reflection intensity distribution at S3 (a) the sharp spot (marked in red "x") belongs to GaN 10-10 reflection. The diffused intensity distribution aligned at the lower 2θχ-ϕ value is originating from the 20 nm top $Al_{0.72}Sc_{0.28}N$ thin film. The maximum GaN intensity was extracted from the RSM (S3-i) at 2θ-χϕ = 32.46°, yielding an in-plane lattice parameter of 3.183 Å. This value is fairly consistent with the literature.[2]

S-6

In-plane RSM 30 nm $Al_{0.72}Sc_{0.28}N$/GaN/Al_2O_3:

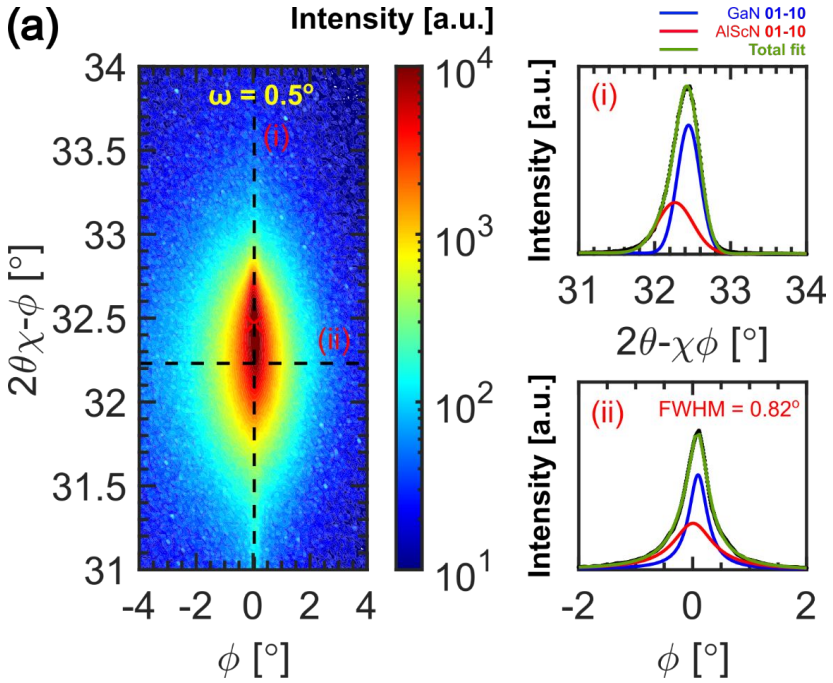

Figure S5: (a) In-plane RSM of 30 nm $Al_{0.72}Sc_{0.28}N$ grown directly on GaN at incident angle ω = 0.5°. Cutlines through the reflection center are marked as (i) and (ii).

Figure S4 shows a fully strained epitaxial 30 nm $Al_{0.72}Sc_{0.28}N$ grown directly on n-GaN/Al_2O_3 substrate. The effect of the strain is clearly visible from the much narrower intensity distribution compared to Figure 5 (a) and S3 (a) along ϕ-axis. This much narrower intensity spread indicates a much lower mosaicity (in-plane texture) of the strained $Al_{0.72}Sc_{0.28}N$ film compared to the same film grown with epi-Pt electrodes. Due to compressive strain from the GaN substrate to the $Al_{0.72}Sc_{0.28}N$, both GaN and AlScN 10-10 reflections almost overlaps causing a mixed intensity profile in both 2θχ-ϕ and ϕ direction. Fitting of the ϕ-reflection with 2 peaks (GaN and AlScN 10-10) yield the mosaicity around 0.82° for epitaxially grown 30 nm $Al_{0.72}Sc_{0.28}N$ on GaN.

Table S1

(a) Epitaxial Pt and *w*-$Al_{0.72}Sc_{0.28}N$ GaN/Al_2O_3 substrates

Epi-Pt thickness	Roughness [nm]	Standard deviation [nm]	Average Grain size [nm]	**$Al_{0.72}Sc_{0.28}N$ thickness [nm]**	Roughness [nm]	Standard deviation [nm]	Average Grain size [nm]
100	1.43	0.039	30	**100**	1.43	0.008	31
50	0.98	0.011	24	**100**	1.10	0.002	26
10	0.48	0.007	10	**100**	0.56	0.001	24

(b) fiber-textured Pt and *w*-$Al_{0.72}Sc_{0.28}N$ on Si substrates

Pt thickness	Roughness [nm]	Standard deviation [nm]	Average grain size [nm]	**$Al_{0.72}Sc_{0.28}N$ thickness**	Roughness [nm]	Standard deviation [nm]	Average grain size [nm]
100	0.96	0.002	26	**100**	0.99	0.005	26
10	0.41	0.008	10	**100**	0.45	0.003	10

Table S1: Roughness and average grain size of (a) Epitaxial Pt and $Al_{0.72}Sc_{0.28}N$ on GaN/Al_2O_3 substrates. (b) fiber textured Pt and $Al_{0.72}Sc_{0.28}N$ on Si substrates. Roughness measurement errors are given as standard deviations.

Table S2

(a) *w*-$Al_{0.72}Sc_{0.28}N$/Epi-Pt on GaN

Pt thickness	Pt 111, XRC-FWHM [°]	FWHM-Error [%]	Pt 222, XRC-FWHM [°]	FWHM-Error [%]	**$Al_{0.72}Sc_{0.28}N$ thickness [nm]**	$Al_{0.72}Sc_{0.28}N$ 0002, XRC-FWHM [°]	FWHM-Error [%]
100	0.40	0.3	0.44	0.41	**100**	2.02	0.5
50	0.38	0.5	0.48	0.53	**100**	2.12	0.5
10	0.22	0.2	0.12	0.40	**100**	2.09	0.4

(b) *w*-$Al_{0.72}Sc_{0.28}N$/Pt on Si

Pt thickness	XRC-FWHM Pt 111 [°]	FWHM-Error [%]	**$Al_{0.72}Sc_{0.28}N$ thickness [nm]**	XRC-FWHM $Al_{0.72}Sc_{0.28}N$ 0002 [°]	FWHM-Error [%]
100	1.7	0.2	**100**	2.41	0.3
10	4.3	9.5	**100**	2.56	0.3

Table S2: Rocking curve FWHM (a) $Al_{0.72}Sc_{0.28}N$/Epi-Pt on GaN (b) $Al_{0.72}Sc_{0.28}N$/Pt on Si. The pseudo-voigt peak fitting errors are given in percentage.

Table S3

(a) *w*-$Al_{0.72}Sc_{0.28}N$ on epi-Pt/GaN

Pt thickness [nm]	**$Al_{0.72}Sc_{0.28}N$ thickness [nm]**	XRC-FWHM [°]	Error [%]
10	**100**	2.09	0.5
10	**50**	1.26	1.4
10	**20**	0.9	1.9
10	**10**	0.65	1.9

(b) *w*-$Al_{0.72}Sc_{0.28}N$ on Pt/Ti/SiO_2/Si

Pt thickness [nm]	**$Al_{0.72}Sc_{0.28}N$ thickness [nm]**	XRC-FWHM [°]	Error [%]
100	**20**	9.00	7.2
100	**100**	2.41	0.3

Table S3: Rocking curve FWHM values for different *w*-$Al_{0.72}Sc_{0.28}N$ thicknesses (a) on 10 nm epi-Pt/GaN, (b) 10 nm fiber-textured Pt on Si substrates. The pseudo-voigt peak fitting errors are given in percentage.

References

(1) Yasuoka, S.; Mizutani, R.; Ota, R.; Shiraishi, T.; Shimizu, T.; Uehara, M.; Yamada, H.; Akiyama, M.; Funakubo, H. Tunable Ferroelectric Properties in Wurtzite (Al0.8Sc0.2)N via Crystal Anisotropy. *ACS Appl Electron Mater* **2022**, *4* (11), 5165–5170. https://doi.org/10.1021/acsaelm.2c00999.

(2) Darakchieva, V.; Monemar, B.; Usui, A. On the Lattice Parameters of GaN. *Appl Phys Lett* **2007**, *91* (3). https://doi.org/10.1063/1.2753122.

A.3 Supplementary: Demonstration and STEM Analysis of Ferroelectric Switching in MOCVD-Grown Single Crystalline $Al_{0.85}Sc_{0.15}N$

ADVANCED PHYSICS RESEARCH
Open Access

Supporting Information

for *Adv. Physics Res.*, DOI 10.1002/apxr.202300113

Demonstration and STEM Analysis of Ferroelectric Switching in MOCVD-Grown Single Crystalline $Al_{0.85}Sc_{0.15}N$

Niklas Wolff, Georg Schönweger, Isabel Streicher, Md Redwanul Islam, Nils Braun, Patrik Straňák, Lutz Kirste, Mario Prescher, Andriy Lotnyk, Hermann Kohlstedt, Stefano Leone, Lorenz Kienle* and Simon Fichtner**

Supporting Information

Demonstration and STEM Analysis of Ferroelectric Switching in MOCVD-Grown Single Crystalline $Al_{0.85}Sc_{0.15}N$

*Niklas Wolff**, *Georg Schönweger**, *Isabel Streicher*, *Md Redwanul Islam*, *Nils Braun*, *Patrik Straňák*, *Lutz Kirste*, *Mario Prescher*, *Andriy Lotnyk*, *Hermann Kohlstedt*, *Stefano Leone*[a], *Lorenz Kienle*[b], *Simon Fichtner*[c]
*Authors contributed equally to this work.

Dr. N. Wolff, Md R.Islam, Prof. Dr. L.Kienle ([b]lk@tf.uni-kiel.de), Dr. S. Fichtner ([c]sif@tfuni-kiel.de)
Department of Material Science, Kiel University, Kaiserstrasse 2, D-24143 Kiel, Germany

Dr. N. Wolff, Prof. Dr. L.Kienle, Dr. S. Fichtner, Prof. Dr. H. Kohlstedt
Kiel Nano, Surface and Interface Science (KiNSIS), Kiel University, Christian-Albrechts-Platz 4, D-24118 Kiel, Germany

G. Schönweger, Prof. Dr. H. Kohlstedt
Department of Electrical and Information Engineering, Kiel University, Kaiserstrasse 2, D-24143 Kiel, Germany

G. Schönweger, Dr. S. Fichtner
Fraunhofer Institute for Silicon Technology (ISIT), Fraunhoferstr. 1, D-25524 Itzehoe, Germany

N. Braun, Dr. A. Lotnyk
Leibniz Institute of Surface Engineering (IOM), Permoserstr. 15, D-04318 Leipzig, Germany

I. Streicher, P. Straňák, M. Prescher, Dr. L. Kirste, Dr. S. Leone ([a]stefano.leone@iaf.fraunhofer.de)
Fraunhofer Institute for Applied Solid State Physics (IAF), Tullastrasse 72, D-79108 Freiburg, Germany

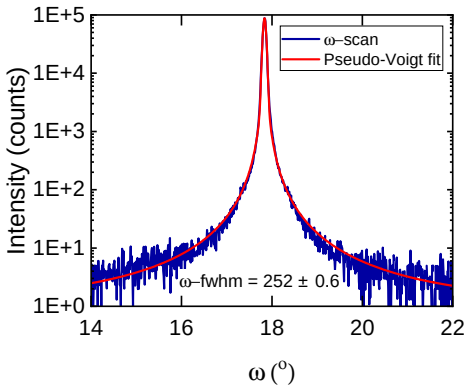

Figure S1: MOCVD grown $Al_{0.85}Sc_{0.15}N$: ω-scan of AlScN (0002) reflection with fwhm (in arcsec) from Pseudo-Voigt fitting.

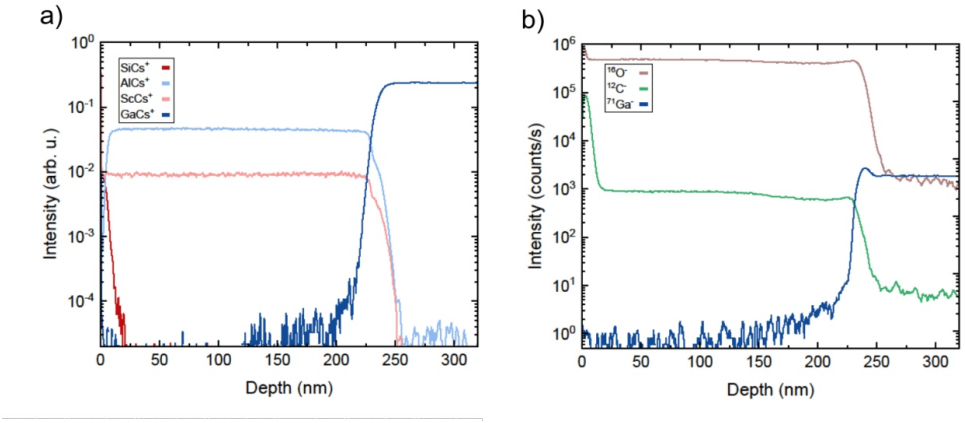

Figure S2: ToF-SIMS depth profiles of the MOCVD grown $Al_{0.85}Sc_{0.15}N$ thin film on n-GaN. The signals obtained in (a) positive-ion detection mode were normalized to Cs_2^+ signal to minimize the matrix effect. (b) Negative-ion mode was used to obtain $^{12}C^-$ and $^{16}O^-$ intensity signals.

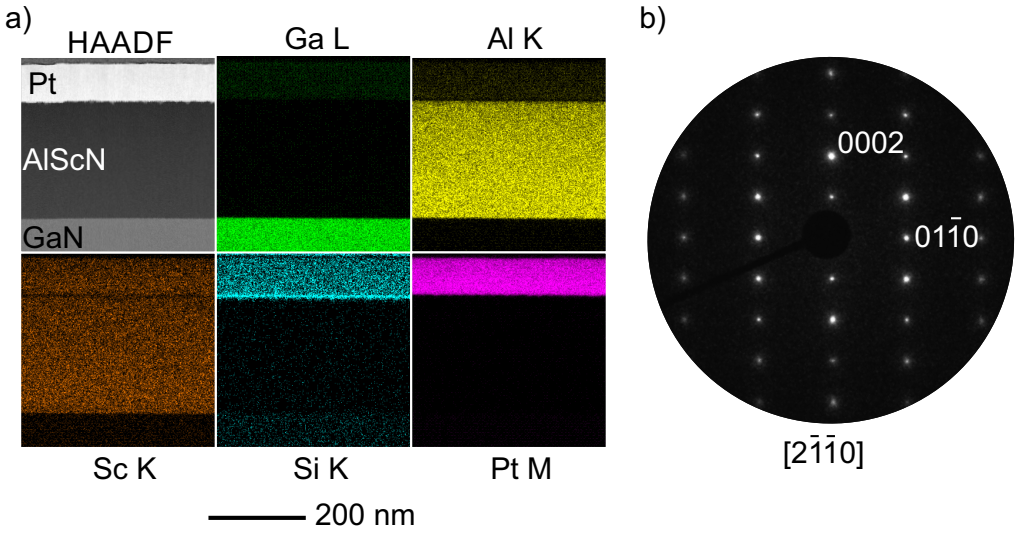

Figure S3: TEM analysis of the pristine Pt/SiN/$Al_{0.85}Sc_{0.15}N$/GaN heterostructure. a) HAADF-STEM micrograph of the heterostructure and the corresponding intensity maps recorded by EDS. b) Selected-area electron diffraction pattern recorded on the $Al_{0.85}Sc_{0.15}N$ layer. The analysis demonstrate the single-crystalline structure of the film showing no chemical separation nor cubic inclusions. Sc and Si signals at the position of the Pt layer are due to the increased intensity background. The average concentration of Sc in the layer is $x = 0.15$.

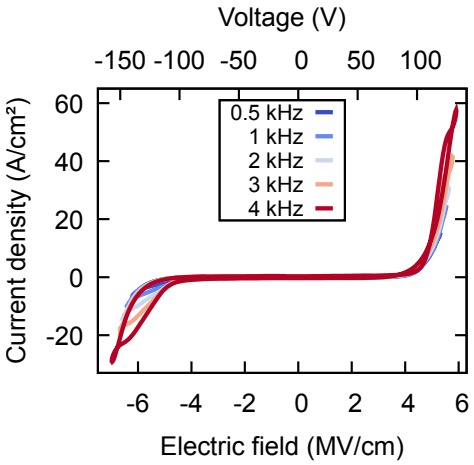

Figure S4: $J - E$ loops in dependence of measurement frequency. The coercive field as well as the peak area increases with increasing frequencies, as expected for true ferroelectricity. Prior to the measurement, the capacitor was cycled for 2000 times.

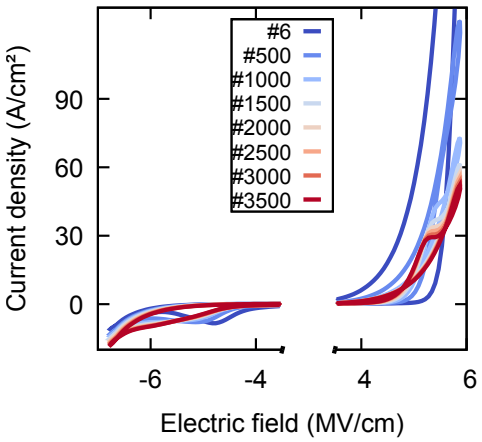

Figure S5: $J - E$ loop evolution with cycling measured at 1.5 kHz. The huge hysteretic area appearing on as-grown pads at positive fields disappears after some tens of cycles. Further cycling shifts the coercive field towards more negative fields. On the positive side this favours the separation between leakage and ferroelectric displacement currents and the typical ferroelectric switching peak appears.

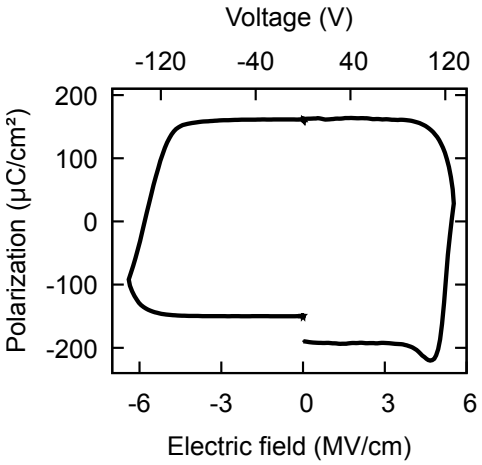

Figure S6: PUND corrected $P-E$ loop measured at 1.5 kHz.

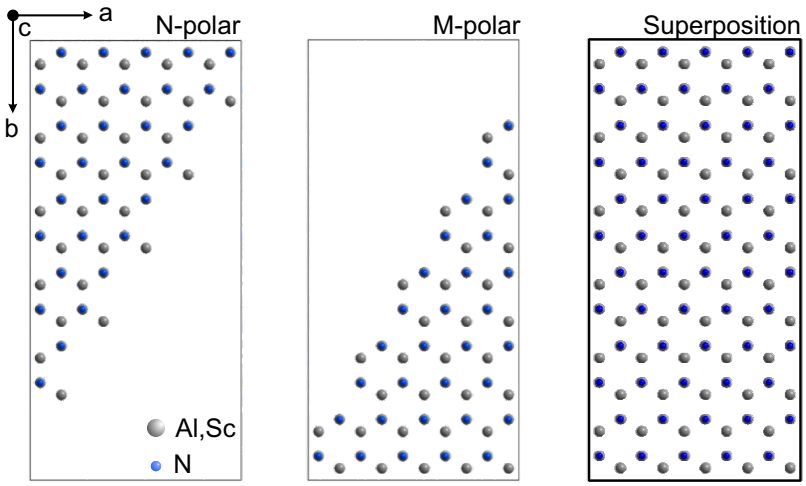

Figure S7: Supercell approach using two orthohexagonal cells of tapered N-polar and M-polar structure models viewed onto the *c*-plane. The combined superposition structure is used for simulation of the ABF scattering contrast along the *b*-*c* plane.

A.4 Supplementary: Ultrathin $Al_{1-x}Sc_xN$ for Low-Voltage-Driven Ferroelectric-Based Devices

1

Supporting information

Georg Schönweger*, Md Redwanul Islam, Niklas Wolff, Adrian Petraru, Lorenz Kienle, Hermann Kohlstedt, Simon Fichtner*

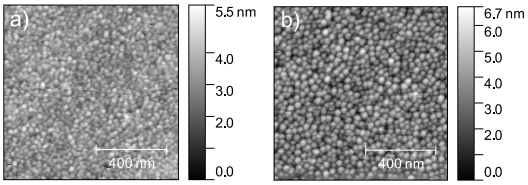

Fig. S1. Atomic force microscopy (AFM) image of 100 nm thick $Al_{0.72}Sc_{0.28}N$ a) deposited on epitaxial Pt and b) deposited on non-epitaxial Pt. A root mean square (RMS) roughness S_q of 0.58 nm (epitaxial) and of 0.96 nm (non-epitaxial) was determined.

In Fig. S1 an AFM image (a) of 100 nm thick $Al_{0.72}Sc_{0.28}N$ deposited on all-epitaxial Pt(12 nm)/GaN/sapphire is depicted and compared to the AFM image (b) of 100 nm thick $Al_{0.72}Sc_{0.28}N$ deposited on a non-epitaxial Pt(100 nm)/AlN/SiO/Si layer stack. The deposition parameters for the 100 nm thick $Al_{0.72}Sc_{0.28}N$ were the same for both templates. Furthermore, the area roughness of 12 nm thick epitaxial Pt is significantly lower than that of our previous 100 nm thick non-epitaxial Pt (0.2 nm vs. 1.6 nm for a 1x1 μm² area). Since the roughness determines the electrical field profile, this could be a crucial factor for the improvement of the ferroelectric response in ultrathin films.

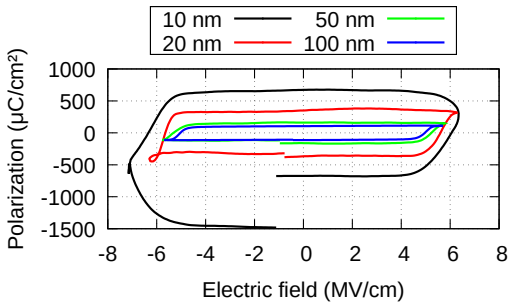

Fig. S2. Dynamic leakage current compensated (DLCC) $P-E$ loops in dependence of the $Al_{0.72}Sc_{0.28}N$ film thickness.

Fig. S2 depicts DLCC $P-E$ loops for the various film thicknesses [1]. We prefer DLCC over PUND because of the different leakage currents appearing for switching- and non-switching cycles, as already discussed elsewhere [2]. Although the leakage is compensated for films down to 50 nm film thickness, for thinner films this is not the case. An increase in P_r with decreasing film thickness was recently related to a decrease of the internal parameter u [3]. Latter amounts in our 20 nm thick $Al_{0.72}Sc_{0.28}N$ film to 38.8 % and is similar to the relaxed state for this specific Sc concentration [2]. Thus, such a drastic increase of P_r for films < 50 nm is unrealistic, meaning that even with DLCC we are at the moment not able to fully compensate for the leakage in ultrathin films.

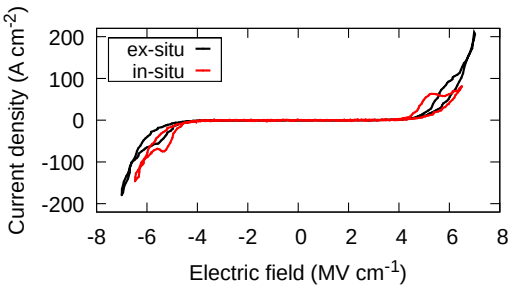

Fig. S3. $J-E$ loop of *in situ* capped- and *ex situ* capped 20 nm thick $Al_{0.72}Sc_{0.28}N$ deposited on epitaxial Pt.

Fig. S3 compares the electrical response of *in situ*- vs. *ex situ* capped $Al_{0.72}Sc_{0.28}N$ deposited on epitaxial Pt. Clearly the leakage current is smaller for the *in situ* capped sample. This can be explained by the absence of an oxide layer formation which could negatively affect the barrier height of the interface. Additionally, the coercive field is smaller for the *in situ* capped sample. An increase of E_c as well as the degradation of remanent polarization for 20 nm thick $Al_{1-x}Sc_xN$ was very recently attributed to the presence of a non-switching dielectric layer, e.g. an oxide layer that is forming if not capped in-situ [4].

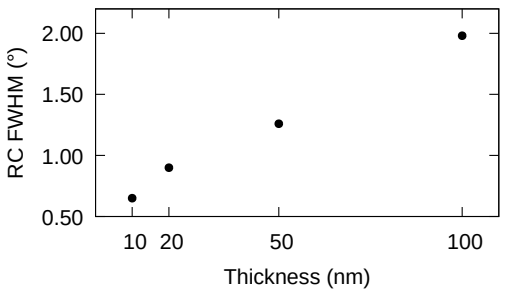

Fig. S4. FWHM of the $Al_{0.72}Sc_{0.28}N$ 0002 RC in dependence of film thickness for our all-epitaxial $Al_{0.72}Sc_{0.28}N$/Pt(12 nm)/GaN/sapphire heterostructures.

Fig. S4 illustrates the decrease of the full-width at half maximum (FWHM) of the $Al_{0.72}Sc_{0.28}N$ 0002 rocking-curve (RC) with decreasing $Al_{0.72}Sc_{0.28}N$ film thickness. This is in

strong contrast to films grown on non-epitaxial Pt, where an increases of RC with decreasing film thickness is observed [5]. Thus, the crystal quality of the first few nanometers of $Al_{1-x}Sc_xN$ grown on epitaxial Pt is considerably higher than if grown on non-epitaxial Pt. This in turn is expected to result in distinct ferroelectric switching of ultrathin films.

REFERENCES

[1] R. Meyer, R. Waser, K. Prume, T. Schmitz, and S. Tiedke, "Dynamic leakage current compensation in ferroelectric thin-film capacitor structures," *Applied Physics Letters*, vol. 86, no. 14, p. 142907, apr 2005.

[2] G. Schönweger, A. Petraru, M. R. Islam, N. Wolff, B. Haas, A. Hammud, C. Koch, L. Kienle, H. Kohlstedt, and S. Fichtner, "From fully strained to relaxed: Epitaxial ferroelectric al 1- x sc x n for III-n technology," *Advanced Functional Materials*, p. 2109632, feb 2022.

[3] S. Yasuoka, R. Mizutani, R. Ota, T. Shiraishi, T. Shimizu, S. Yasui, Y. Ehara, K. Nishida, M. Uehara, H. Yamada, M. Akiyama, Y. Imai, O. Sakata, and H. Funakubo, "Enhancement of crystal anisotropy and ferroelectricity by decreasing thickness in (al,sc)n films," *Journal of the Ceramic Society of Japan*, vol. 130, no. 7, pp. 436–441, jul 2022.

[4] S. K. Ryoo, K. D. Kim, H. W. Park, Y. B. Lee, S. H. Lee, I. S. Lee, S. Byun, D. Shim, J. H. Lee, H. Kim, Y. H. Jang, M. H. Park, and C. S. Hwang, "Investigation of optimum deposition conditions of radio frequency reactive magnetron sputtering of $al_{0.7}sc_{0.3}$)n film with thickness down to 20 nm," *Advanced Electronic Materials*, p. 2200726, sep 2022.

[5] S. Yasuoka, T. Shimizu, A. Tateyama, M. Uehara, H. Yamada, M. Akiyama, Y. Hiranaga, Y. Cho, and H. Funakubo, "Effects of deposition conditions on the ferroelectric properties of (al1-xScx)n thin films," *Journal of Applied Physics*, vol. 128, no. 11, p. 114103, sep 2020.

A.5 Supplementary: In-Grain Ferroelectric Switching in Sub-5 nm Thin $Al_{0.74}Sc_{0.26}N$ Films at 1 V

ADVANCED SCIENCE
Open Access

Supporting Information

for *Adv. Sci.*, DOI 10.1002/advs.202302296

In-Grain Ferroelectric Switching in Sub-5 nm Thin $Al_{0.74}Sc_{0.26}N$ Films at 1 V

Georg Schönweger, Niklas Wolff, Md Redwanul Islam, Maike Gremmel, Adrian Petraru, Lorenz Kienle, Hermann Kohlstedt and Simon Fichtner**

6 | SUPPLEMENT

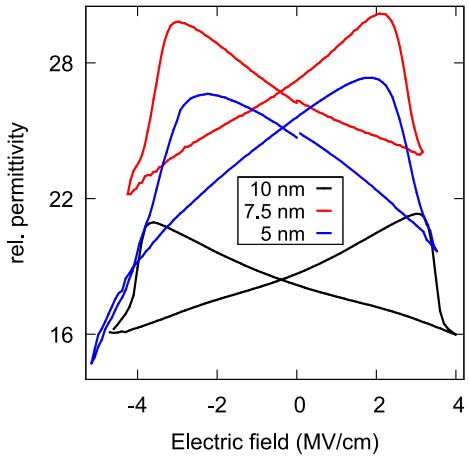

FIGURE S1 $C-E$ loops of 10 nm - down to sub-5 nm thin layers of $Al_{0.74}Sc_{0.26}N$ deposited epitaxially on Pt/GaN/sapphire. The sweep time for each thickness was kept constant. All measurements were performed on 10 µm diameter pads. No clear trend or ε_r with thickness can be observed from 10 nm down to sub-5 nm film thickness due to the error in relative permittivity of $\Delta(\varepsilon_r) \approx 4$, which mainly arises from variations in the capacitor area (nominal 10 µm diameter pads).

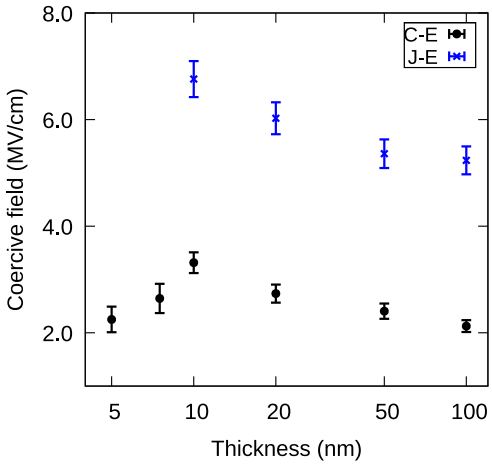

FIGURE S2 The coercive field of $Al_{0.74}Sc_{0.26}N$ epitaxially grown on Pt/GaN/sapphire in dependence on film thickness. E_c is determined via $J-E$ (80 kHz) and via $C-E$ (sweep time 20 s, small signal 100 mV and 900 kHz) loops. The breakdown field approaches the coercive field below 10 nm film thickness at high frequencies, thus not allowing to clearly determine E_c below that film thickness.

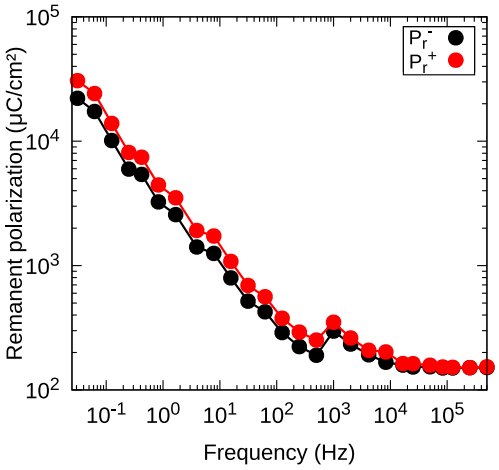

FIGURE S3 The remanent polarization of a 100 nm thin $Al_{0.74}Sc_{0.26}N$ based capacitor grown on Pt/Ti/SiO_2/Si in dependence of the measurement frequency. The positive-up negative-down (PUND) method[34] was used to correct for non-hysteretic leakage- as well as capacitive currents. The P_r values for positive half-loops (P_r^+) and negative half-loops (P_r^-) are determined separately. At higher frequencies, the displacement current due to polarization reversal increases, while leakage current flowing through conduction paths such as through domain walls should be time independent. Therefore, the apparent remanent polarization, which amounts to the integration over time of both currents, saturates at higher frequencies.

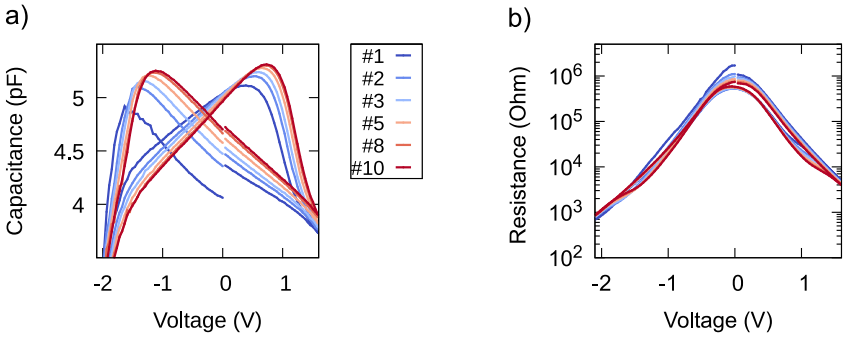

FIGURE S4 a) First ten $C-V$ cycles of pristine sub-5 nm thin $Al_{0.74}Sc_{0.26}N$ based capacitors grown on Pt/Ti/SiO_2/Si. b) Resistance of the respective curves shown in a). The decrease of the resistance to values below 1 kOhm at higher negative fields results in a capacitance drop.

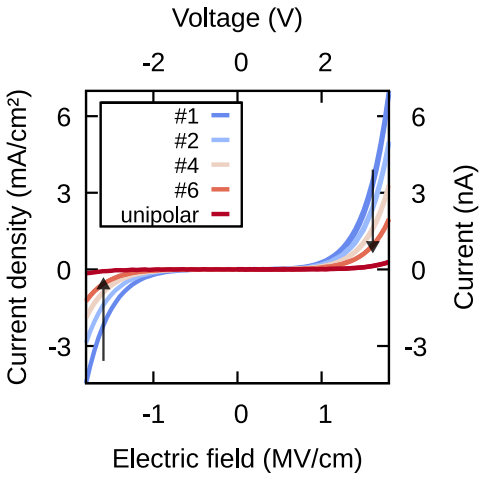

FIGURE S5 Quasi-static current response of minor non-switching loops (max. applied electric field below $E_c/2$) of a 20 nm thin $Al_{0.74}Sc_{0.26}N$ based capacitor grown on Pt/GaN/sapphire in dependence of the switching state. In the partially switched state, the capacitor is in a low resistance mode (blue curve). When switching more and more volume towards an unipolar state (transition from blue- to red curve, as indicated by the arrows), the resistance increases. This increase in resistance goes hand in hand with a decrease of ϵ_r. Both effects fit well to the model of conductive domain walls forming during switching - the domain-wall density decreases when switching the film partially towards the unipolar state and so does the current which flows through the conductive domain walls. The voltage was swept in steps of 0.1 V with a delay time between each step of 400 ms.

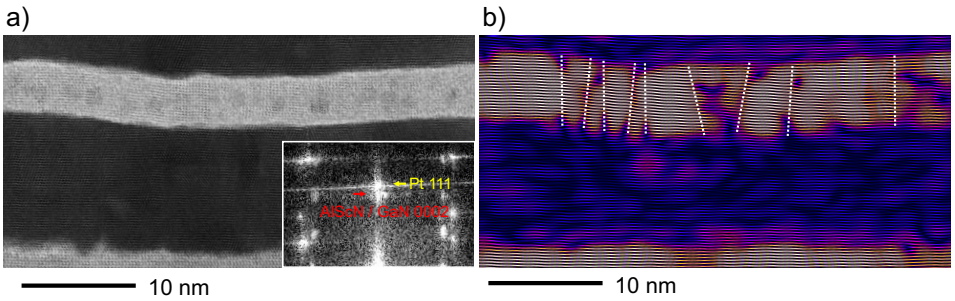

FIGURE S6 Nanoscale texture analysis of single-digit nanometer large columnar grains. a) ABF-STEM micrograph of the film cross section with Fast Fourier Transform (FFT) showing the aligned out-of-plane Pt 111 and $Al_{0.74}Sc_{0.26}N$ 0002 reflections. b) Inverse FFT image using an aperture to filter the spatial frequencies of the GaN and $Al_{0.74}Sc_{0.26}N$ out-of-plane 0002 reflections to demonstrate the crystal size and c-axis alignment. Dotted lines indicate the position of grain boundaries.

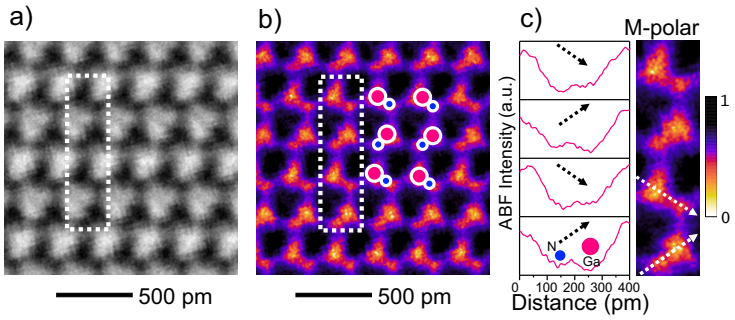

FIGURE S7 a) Unfiltered ABF-STEM micrograph of the GaN substrate and b) Inverted-ABF-STEM image featuring M-polarity. Sketches of the Ga-N dumbbells assist to visualize the M-polarity. c) Display of intensity profile analysis of the Ga-N dumbbells inside the vertical frame. Profiles are drawn from left to right (see arrows) on the unfiltered image; M(-polarity) = pink, N(-polarity) = blue.

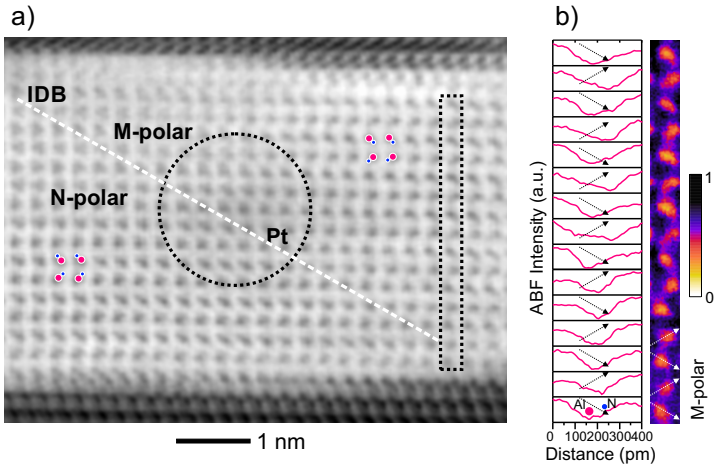

FIGURE S8 a) Unfiltered grayscale ABF-STEM micrograph of the inverted-ABF-STEM image shown in Figure 5 including the sketched position of the inclined inversion domain boundary. b) Profile analysis from the vertical single column frame where the M-polar domain reaches down to the bottom Pt interface. Profiles are drawn from left to right (see arrows) on the unfiltered image; M(-polarity) = pink, N(-polarity) = blue.